

## A free wake vortex model for floating wind turbine aerodynamics

Dong, J.

**DOI**

[10.4233/uuid:48b0221c-534f-4bdd-8b0f-b529375ec94a](https://doi.org/10.4233/uuid:48b0221c-534f-4bdd-8b0f-b529375ec94a)

**Publication date**

2021

**Document Version**

Final published version

**Citation (APA)**

Dong, J. (2021). *A free wake vortex model for floating wind turbine aerodynamics*. [Dissertation (TU Delft), Delft University of Technology]. <https://doi.org/10.4233/uuid:48b0221c-534f-4bdd-8b0f-b529375ec94a>

**Important note**

To cite this publication, please use the final published version (if applicable).  
Please check the document version above.

**Copyright**

Other than for strictly personal use, it is not permitted to download, forward or distribute the text or part of it, without the consent of the author(s) and/or copyright holder(s), unless the work is under an open content license such as Creative Commons.

**Takedown policy**

Please contact us and provide details if you believe this document breaches copyrights.  
We will remove access to the work immediately and investigate your claim.

# **A Free Wake Vortex Model for Floating Wind Turbine Aerodynamics**

**Jing Dong**

**董婧**



# A free wake vortex model for floating wind turbine aerodynamics



# A free wake vortex model for floating wind turbine aerodynamics

Dissertation

for the purpose of obtaining a degree of doctor  
at Delft University of Technology,

by the authority of the Rector Magnificus Prof.dr.ir. T.H.J.J. van der Hagen,  
chair of the Board for Doctorates,

to be defended publicly on Monday 13 September 2021 at 10:00 o'clock

by

Jing DONG

Master of Engineering in Design and Building of Ship and Ocean Structures,  
Dalian University of Technology, China.  
born in Beipiao, China.

This dissertation has been approved by the promoters

Composition of the doctoral committee:

Rector Magnificus,            chairperson  
Prof. dr. S.J. Watson,        Delft University of Technology, promotor  
Dr. ir. A. Viré,                Delft University of Technology, copromotor

Independent members:

Prof. dr. ir. D. von        Delft University of Technology  
Terzi  
Prof. dr. M. Graham        Imperial College London, UK  
Dr. W.G. Fruh,                Heriot Watt University, UK  
Dr. J.C. Gilloteaux,        Ecole Centrale Nantes, France



Keywords:            wind energy, floating offshore wind turbine, vortex ring method,  
vortex ring state, BEM

Printed by:            ProefschriftMaken

Front & Back:        Velocity field of the vortex ring state simulated with a free wake  
vortex method.

Copyright © 2021 by J. DONG

ISBN 978-94-6384-250-1

An electronic version of this dissertation is available at  
<http://repository.tudelft.nl/>.

To life



# Contents

Summary	xi
Samenvatting	xiii
1 Introduction	1
1.1 A brief retrospect of the development of wind energy	2
1.2 Floating offshore wind energy	3
1.2.1 Floating offshore wind turbine configurations	4
1.2.2 Offshore environmental loads	8
1.3 Rotor aerodynamics modeling methods	9
1.4 Problem description	12
1.5 Goals and contributions of this thesis	14
1.5.1 Research objectives and approach	14
1.5.2 Thesis outline	16
2 Prediction of the vortex ring state	19
2.1 Introduction	21
2.2 BEM method applied to floating offshore wind turbines	23
2.3 Theories for the prediction of the vortex ring state	25
2.3.1 VRS prediction based on the axial induction factor	26
2.3.2 VRS prediction based on Wolkovitch's criterion	27
2.3.3 VRS prediction based on Peters' criterion	28
2.4 OpenFAST simulation tool	30
2.4.1 NREL 5MW turbine and platforms	32
2.4.2 Load cases	33
2.5 Results for regular wave load cases	40
2.5.1 Results using the axial induction factor criterion	40
2.5.2 Results using Wolkovitch's criterion	41

2.5.3	Results using Peters' criterion . . . . .	47
2.5.4	Summary of regular wave load cases . . . . .	52
2.5.5	Reduced frequency analysis . . . . .	59
2.6	Results for irregular wave load cases . . . . .	62
2.6.1	NREL 5MW turbine mounted on a TLP . . . . .	62
2.6.2	NREL 5MW turbine mounted on the ITI Energy Barge . . . . .	62
2.6.3	NREL 5MW turbine mounted on the OC3-Hywind Spar . . . . .	69
2.6.4	Summary of the results under irregular wave load cases . . . . .	69
2.6.5	Coefficient of variation analysis . . . . .	77
2.7	Conclusions . . . . .	79
3	The free wake vortex ring method . . . . .	85
3.1	Introduction . . . . .	86
3.2	Vortex Ring Theory . . . . .	88
3.2.1	Velocity induced by a vortex filament . . . . .	88
3.2.2	Velocity induced by an axis-symmetric vortex ring . . . . .	90
3.2.3	Self induced velocity and induced velocity field of a vortex ring . . . . .	93
3.3	Numerical discretization . . . . .	100
3.3.1	Near wake models . . . . .	100
3.3.2	Far wake model . . . . .	105
3.3.3	Characteristics of the first rings shed in the wake . . . . .	110
3.3.4	Strength of the blade bound vortex . . . . .	112
3.3.5	Comparison and validation of the two trailing vortex models . . . . .	115
3.4	Computational cost description . . . . .	121
3.5	Conclusions . . . . .	123
4	Verification of the free wake vortex ring method . . . . .	125
4.1	Introduction . . . . .	126
4.2	NREL 5MW reference turbine parameters . . . . .	126
4.3	Results for a bottom-mounted wind turbine . . . . .	129
4.4	Floating wind turbine under a single-DoF motion . . . . .	133
4.5	Floating wind turbine under multiple-DoF motion . . . . .	145

---

4.6	Discussion on the wake structure . . . . .	150
4.7	Conclusions . . . . .	152
5	Working states of a floating offshore wind turbine in surge motion	155
5.1	Introduction . . . . .	157
5.2	Coordinate systems and load cases . . . . .	158
5.2.1	Floating offshore wind turbine coordinate systems . . . . .	158
5.2.2	Load cases . . . . .	159
5.3	Results and discussion . . . . .	162
5.3.1	Thrust coefficients on the rotor . . . . .	162
5.3.2	Prediction of VRS and associated rotor characteristics . . . . .	163
5.3.3	Velocity field around the rotor . . . . .	165
5.3.4	Angles of attack on the blade . . . . .	167
5.3.5	Velocity and thrust along the blade . . . . .	175
5.3.6	Working states within one surge period . . . . .	179
5.3.7	Wake structure . . . . .	181
5.4	Conclusion . . . . .	183
6	Conclusion and Recommendations	187
6.1	Conclusions . . . . .	188
6.1.1	Objective 1: Prediction of the vortex ring state . . . . .	188
6.1.2	Objective 2: Develop an aerodynamic model for the simulation of rotor-wake interactions . . . . .	189
6.1.3	Objective 3: Analyze the characteristics and impact of the rotor-wake interactions on the performance of floating offshore wind turbines . . . . .	191
6.2	Outlook . . . . .	192
6.2.1	Prediction of the vortex ring state . . . . .	192
6.2.2	Improvements in the numerical model . . . . .	192
6.2.3	Working state change of a moving rotor . . . . .	193
6.3	Final remarks . . . . .	193
	Bibliography	202
	Acknowledgement	203

Curriculum Vitæ	205
List of Publications	207

# Summary

In order to significantly increase the share of wind energy produced worldwide, wind energy technology is moving from onshore to offshore and from shallow water to deep water. Floating offshore wind turbines (FOWTs) are expected to be economically better than bottom-mounted turbines when placed in water deeper than 60 metres. Despite key initiatives such as the installation of the world's first floating wind farm off the coast of Scotland in 2017, many design and operational challenges need to be solved to make floating offshore wind turbines economically attractive.

In particular, the aerodynamics of floating offshore wind turbines can be largely different from its bottom-mounted counterpart due to platform motions. The existing literature identifies four working states for floating offshore wind turbines when these move back and forth, potentially strongly interacting with their own wake. However, it is still unclear when, and to what extent, do certain working states occur. The change of working state is potentially a problem for the aerodynamic performance and the lifetime of floating offshore wind turbines.

The aim of this research is twofold. First, it focuses on one of the most critical working states: the vortex ring state. This work defines criteria that can quantitatively predict the occurrence of this state during operation of a floating offshore wind turbine. These criteria are used with two different numerical frameworks in order to assess the influence of the vortex ring state on the aerodynamic performance of the rotor. Second, it uses a free wake vortex ring model developed in this work to identify the occurrence of different working states during a prescribed surge motion of the turbine.

The work is presented as follows.

Step 1. Prediction of the vortex ring state

- The vortex ring state prediction criteria originally used in the field of helicopters are investigated and adapted for the application to floating offshore wind turbines.
- The criteria defined above are used on the output of aero-hydro-servo-elastic coupled analyses of floating offshore wind turbines with different types of floating foundations. This leads to the prediction of the occurrence of the vortex ring state and its boundaries.

Step 2. The free wake vortex ring method

- The vortex theory, with a focus on vortex filament induction and vortex ring induction, is introduced and the numerical implementation of a simplified free wake vortex ring method is presented.
- The free wake vortex ring method is verified by executing a series of load cases on both fixed and moving rotors. The strengths and weaknesses of the model are identified and the results are compared with the literature.

Step 3. Analysis of rotor-wake interactions for a floating offshore wind turbine under surge motion

- The aerodynamic performance of a floating offshore wind turbine is analysed when the turbine moves under a prescribed surge motion. In particular, the occurrence of the four working states is assessed for a whole cycle of the rotor motion.

This thesis provides three main contributions to the floating offshore wind energy community. Firstly, it provides prediction methods for the occurrence of the so-called vortex ring state, as known in helicopter flights. These methods are adapted from those available in the helicopter community and used to identify the occurrence of a similar state during operation of floating offshore wind turbines. Secondly, a free wake vortex method is developed and verified for the simulation of both bottom-mounted and floating wind turbines. Thirdly, the occurrence of the four working states and their effect on aerodynamic performance are highlighted for a floating turbine under a forced surge motion. A quantitative way of identifying the boundary between the vortex ring state and the propeller working state is also proposed in this thesis.

# Samenvatting

Om het aandeel van wereldwijd geproduceerde windenergie aanzienlijk te vergroten, verschuift de windenergietechnologie van onshore naar offshore en van ondiep naar diep water. Drijvende offshore windturbines (FOWT's) zullen naar verwachting economisch beter zijn dan op de bodem gemonteerde turbines wanneer ze in water dieper dan 60 meter worden geplaatst. Ondanks belangrijke initiatieven zoals de installatie van 's werelds eerste drijvende windpark voor de kust van Schotland in 2017, zijn er veel ontwerpuitdagingen moeten worden opgelost om drijvende offshore windturbines economisch aantrekkelijk te maken.

Met name de aerodynamica van drijvende offshore windturbines kan door platformbewegingen sterk verschillen van die van bodemgemonteerde windturbines. De bestaande literatuur identificeert vier bedrijfstoestanden voor drijvende offshore windturbines wanneer deze heen en weer bewegen, mogelijk sterk in wisselwerking met hun eigen kielzog. Het is echter nog onduidelijk wanneer en in welke mate bepaalde werktoestanden zich voordoen. Deze verandering van werkstatus is mogelijk een probleem voor de aerodynamische prestaties en de levensduur van drijvende offshore windturbines.

Het doel van dit onderzoek is tweeledig. Ten eerste richt het zich op een van de meest kritieke werktoestanden: de vortexringtoestand. Dit werk definieert criteria die het optreden van deze toestand tijdens het gebruik van een drijvende offshore windturbine kwantitatief kunnen voorspellen. Deze criteria worden gebruikt met twee verschillende numerieke kaders om de invloed van de vortexringtoestand op de aerodynamische prestaties van de rotor te beoordelen. Ten tweede maakt het gebruik van een vrij kielzog-vortexringmodel, ontwikkeld in dit werk, om het optreden van alle vier de bedrijfstoestanden tijdens een voorgeschreven stijgbeweging van de turbine te identificeren. Het werk wordt als volgt gepresenteerd.

Stap 1. Voorspelling van de toestand van de vortexring

- De voorspellingscriteria van de vortexringtoestand die oorspronkelijk werden gebruikt op het gebied van helikopters, worden onderzocht en aangepast voor toepassing op drijvende offshore windturbines.
- De hierboven gedefinieerde criteria worden gebruikt voor de output van aero-hydro-servo-elastische gekoppelde analyses van drijvende offshore windturbines met verschillende soorten drijvende funderingen. Dit leidt tot de voorspelling van het optreden van de vortexringtoestand en zijn grenzen.

#### Stap 2. De gratis wake vortex ring-methode

- De vortex theorie, met een focus op vortex filament inductie en vortex ring inductie, wordt geïntroduceerd en de numerieke modellering van een vereenvoudigde free wake vortex ring methode wordt ontwikkeld.
- De vrije zogvortexringmethode wordt gevalideerd door een reeks belastinggevallen uit te voeren op zowel vaste als bewegende rotoren. De sterke en zwakke punten van het model worden geïdentificeerd en de resultaten worden vergeleken met de literatuur.

#### Stap 3. Analyse van rotor-zog-interacties voor een drijvende offshore windturbine onder golfbeweging

- De aerodynamische prestaties van een drijvende offshore windturbine worden geanalyseerd wanneer de turbine beweegt onder een voorgeschreven golfbeweging. In het bijzonder wordt het optreden van de vier bedrijfstoestanden beoordeeld voor een hele cyclus van de rotorbeweging.

Dit proefschrift levert de volgende drie belangrijke bijdragen aan de drijvende gemeenschap van offshore windenergie. Ten eerste biedt het voorspellingsmethoden voor het optreden van de zogenaamde vortexring-toestand, zoals bekend bij helikoptervluchten. Deze methoden zijn aangepast aan de methoden die beschikbaar zijn in de helikoptergemeenschap en worden gebruikt om het optreden van een vergelijkbare toestand tijdens de werking van drijvende offshore windturbines te identificeren. Ten tweede is een gratis wake vortex-methode ontwikkeld en gevalideerd voor de simulatie van zowel op de bodem gemonteerde als drijvende windturbines. Ten derde wordt het voorkomen van

de vier bedrijfstoestanden en hun effect van aerodynamische prestaties benadrukt voor een drijvende turbine onder een geforceerde golfbeweging. In dit proefschrift wordt ook een kwantitatieve manier voorgesteld om de grens tussen de vortexringtoestand en de werkende staat van de propeller te identificeren.



# 1

## Introduction

我注六经，六经注我。—陆九渊（宋）

One reads extensively to understand the original meanings of scriptures; one also uses the idea of scriptures to explain their own thoughts.

Lu Jiuyuan (Song dynasty)

## 1.1. A brief retrospect of the development of wind energy

The history of the application of wind power is age-old. Thousands of years ago, people already learned to use wind energy for propelling boats, grinding grain, pumping water, and cutting wood at sawmills <sup>1</sup>. Modern wind energy technology is represented by the development of wind turbines to generate electricity. The first known wind turbine used to produce electricity was created by Prof James Blyth in Scotland in 1887 <sup>2</sup>. An aircraft airfoil designed by Bilau and Betz was applied to a modern windmill in 1920 [1]. In the past one hundred years, great progress has been made in wind turbine design and manufacturing technology until it became what it is today — multi-megawatt capacity and large-scale commercial use.

Throughout history, we can see that the rapid developments of wind energy technology were often a result of the combination of external opportunities and its merits concerning sustainability, low environmental impact and affordability. For example, in the 1970s, when the oil crisis began and people faced shortages and skyrocketing oil prices, wind energy had the advantage that it would never run out and successfully gained support from governments. At that time, wind energy research agencies became established and the wind energy industry began to take shape<sup>3</sup>.

After the oil market stabilised, in the 1990s the wind energy entered a second phase of rapid development, with its clean energy reputation, driven by environmental concerns. In this stage, many countries introduced policies to support the development of wind energy [2]. The Tokyo protocol (1997) was an important instrument for promoting wind energy projects globally driven by concerns over climate change. The Paris Agreement (2015) was another global framework to ensure greenhouse gas reduction commitments, which many countries have used to highlight wind in their climate plans <sup>4</sup>. During the past two decades, the global wind power capacity increased from 10.2 gigawatt to 651.8 gigawatt, with a compound annualized growth rate of about 22%.

---

<sup>1</sup>Wind explained - History of wind power: <https://www.eia.gov/>

<sup>2</sup><https://www.renewableenergyworld.com/2014/11/21/history-of-wind-turbines/#gref>

<sup>3</sup><https://www.awea.org/wind-101/history-of-wind/1970s>

<sup>4</sup><https://windeurope.org/policy/topics/climate-change/>

Unlike fossil fuel energies where every kilowatt-hour of electricity produced is accompanied by the consumption of raw materials which increase expense, the wind resource is free and readily available, thus the more energy produced, the less the unit energy cost. All costs incurred throughout the life cycle of a wind turbine determine the price of wind energy. If the performance of the wind turbine is perfect and the service life is extremely long, the energy price can be very low. For this reason, the vast majority of wind energy research and development projects are dedicated to reducing the cost by making the equipment cheaper and more reliable. After years of policy-driven prosperity, which strongly depended on subsidies and tax benefits, the wind energy industry is about to move to a more mature phase, by further reducing electricity prices to make it more competitive in the market.

In recent years, wind energy technology has improved significantly, resulting in turbines that are larger and produce energy at reduced cost. So far, the price of onshore wind energy can already match that of fossil energy, or even be lower<sup>5</sup>. However, the cost of offshore wind energy is still higher. For waters deeper than 60 meters, floating offshore wind turbines could play a major role in reducing the cost of offshore wind and increasing the global wind energy capacity.

## 1.2. Floating offshore wind energy

A floating offshore wind turbine is able to generate electricity in water depths where fixed-foundation turbines are not economically feasible [3]. The world's first floating wind turbine prototype was deployed by Blue H Technologies from the Netherlands, which was installed 21.3 kilometers off the coast of Apulia, Italy in 2007<sup>6</sup>. As shown in Fig. 1.1, this prototype is a two-bladed turbine with a rated power of 80kW mounted on a tension-leg platform in a water depth of 113 meters. The first large-scale floating wind turbine was the 2.3MW Hywind turbine installed off the coast of Norway in 2009. Since 2017, the Hywind concept has been deployed in the world's first floating offshore wind farm, Hywind Scotland, 29 kilometers off Peterhead, Scotland. The farm has

<sup>5</sup><https://meic.org/issues/montana-clean-energy/cost-of-wind-vs-fossil-fuels/>

<sup>6</sup> [https://en.wikipedia.org/wiki/Floating\\_wind\\_turbine#cite\\_note-ge20110913-1](https://en.wikipedia.org/wiki/Floating_wind_turbine#cite_note-ge20110913-1)



Figure 1.1: World's first floating wind turbine<sup>6</sup>.

five 6 MW Hywind floating turbines with a total capacity of 30 MW. In its first two years of operation the facility has averaged a capacity factor in excess of 50%<sup>7</sup>. The technology of floating wind turbines is continuously maturing with several other concepts in the water or in development, for example, the WindFloat concept by Principle Power, which was first installed in 2011 as a standalone 2MW turbine, and is now part of a small farm of 25MW (WindFloat Atlantic). Today, floating offshore wind energy is a fast-maturing technology with more than 50 projects at different stages of development worldwide<sup>8</sup>. Although floating offshore wind represented only 84MW of installed capacity at the end of 2019 worldwide, there are currently 7.6GW in the pipeline [4], as shown by Fig. 1.2. In Europe alone, the installed capacity of floating offshore wind is planned to increase to 400MW by 2022<sup>9</sup>. Furthermore, projections show that floating offshore wind could be deployed at a utility scale by 2024<sup>10</sup>.

### 1.2.1. Floating offshore wind turbine configurations

Today, the most common design for floating offshore wind turbines is the upwind horizontal axis wind turbine (HAWT), where the axis of rotation is

<sup>7</sup>[https://en.wikipedia.org/wiki/Hywind\\_Scotland](https://en.wikipedia.org/wiki/Hywind_Scotland)

<sup>8</sup>WindEurope, Floating offshore wind energy: A policy blueprint for Europe

<sup>9</sup>WindEurope, Floating Offshore Wind (2020)

<sup>10</sup><https://www.nrel.gov/news/video/overview-of-floating-offshore-wind-text.html>

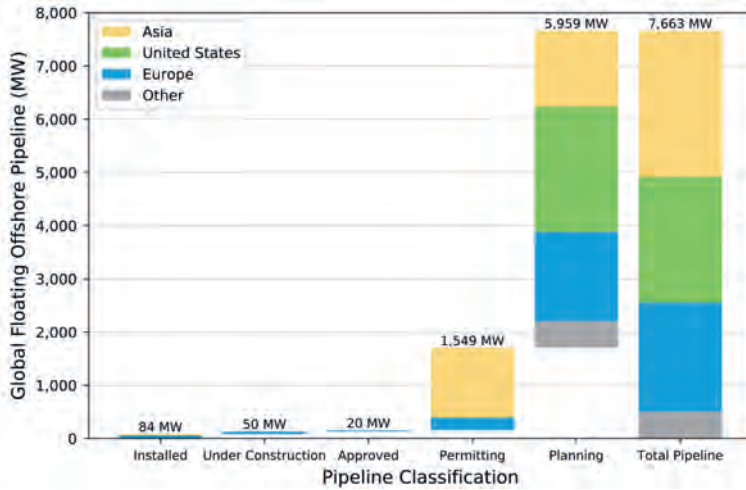


Figure 1.2: Global floating offshore wind pipeline (taken from [4]).

parallel to the sea level and the turbine faces the upcoming wind.

As shown in Fig. 1.3, the above-water part of these turbines looks very similar to a bottom-mounted offshore wind turbine. The main difference is that the tower is supported, below sea level, by a floating substructure that is moored via cables and lines with an anchor system<sup>10</sup>. The terminologies that are commonly used for engineering design are introduced here. The substructure, which is also called a platform or a foundation, is a part of the support structure. The support structure includes the tower, the floating platform as well as all the mooring lines and the anchor system.

Figure 1.4 shows the foundations currently available for both bottom-mounted and floating offshore wind turbine systems. The choice of the foundation strongly depends on the water depth. So far, all large-scale commercial offshore wind projects use bottom-mounted foundations as they are installed in water depths below 60 meters. The most common foundation is the monopile. It is a cylindrical steel tube driven into the seabed using a hydraulic impact hammer or vibratory device. The structure relies mainly on the lateral resistance of the soil to transfer the large moments induced by the wind and wave loads to the soil. This is in contrast to gravity-based foundations, which rely on the restoring moment provided by the self weight of the foundation and the

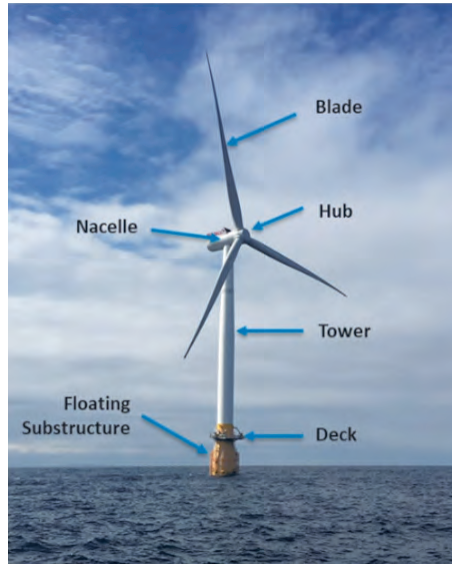


Figure 1.3: Siemens 6.0 MW wind turbine <sup>10</sup>(photo credit: Walt Musial (NREL)).

turbine to resist the overturning moments. These foundations are less effective at sea than on land because of buoyancy forces, so their use is less compared to other types of offshore foundations. In terms of deployment, the gravity bases are constructed on land and transported by barge to the offshore location. Due to crane lifting capacities, they are usually designed to be hollow, and are only filled with ballast material on site. Another popular type of foundation is the jacket, which forms a lighter alternative to the monopile and the gravity-based foundation in deeper waters. This is because the primary loading is resisted by much higher lever arms thanks to the wide separation of the legs. The consequent lightness of the structure forms one of its primary advantages, while the expensive fabrication and welding of many geometrically complex joints is an important disadvantage. Tripods and tri-piles also exist but are less popular. The main idea behind both of these concepts is that they are structurally more efficient than monopiles in resisting overturning moments. However, their installation and fabrication are often significantly more expensive than that of a monopile, which is why they are not very commonly used by the industry.

Floating foundations can be mainly categorised into three different types, as shown in Fig. 1.4: spar buoy, semi-submersible platform, and tension-leg

platform. These types of platform differs in the way they ensure static stability. The spar buoy achieves its stability through ballast weights that need to be installed very low. Thus, its application requires a deep draft. By contrast, the semi-submersible platform is a low draft system and ensures stability through a wide water plane area. This makes it highly sensitive to surface wave loads. The tension-leg platform mainly achieves its static stability through mooring line tension. This system is the lightest weight, but it is unstable until the mooring lines are hooked up and it requires very high vertical load mooring line capacity. Accordingly, the anchors have to provide about ten times the tensile force of the other two concepts, namely the spar or the semi-submersible. Additional concepts that do not fully fall under these three categories also exist. For example, the barge used by Ideol <sup>11</sup> has a pool that helps stabilise the system.

Today, many questions remain regarding the optimal type of floating support structure for floating turbines. For example, it is still unclear what the best floater design is for a given site and wind turbine architecture. Factors such as water depth (at site and port), distance to port, environmental conditions, etc, will influence design choices.

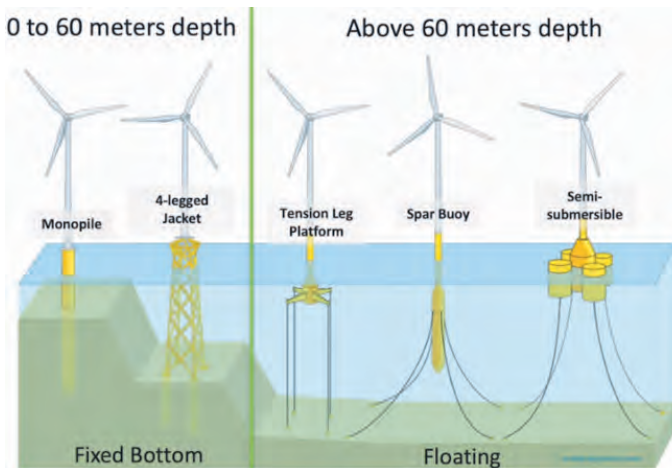


Figure 1.4: Offshore wind turbine substructures [5].

<sup>11</sup><https://www.bw-ideol.com/en/technology>

### 1.2.2. Offshore environmental loads

Floating offshore wind turbines are designed to work in an offshore environment several miles off the coast and in waters deeper than 60 meters [6]. One of the challenges to design these substructures is the ability to predict loads and resulting dynamic responses of the floating wind turbine system in combined wave and wind conditions. Figure 1.5 illustrates the different loading sources relevant for floating offshore wind turbines [5]. These are further described hereafter.

#### Aerodynamic Loads

Wind blowing over the blade airfoil generates aerodynamic lift and drag forces, which result in a torque rotating the blades and generating power. The aerodynamic loads on the rotor can be classified into three categories [6]:

- a. Steady aerodynamic loads generated by the mean wind speed.
- b. Periodic aerodynamic loads generated by rotor rotation, wind shear, tower shadow, and off-axis winds.
- c. Randomly fluctuating aerodynamic loads generated by turbulence, gusts, and dynamic effects.

#### Hydrodynamic Loads

Hydrodynamic loads are important for offshore floating turbines. The significance of hydrodynamic loads depends on the particular floating concept as mentioned earlier, as well as on the severity of the wind and wave conditions. Aerodynamic and hydrodynamic forces are correlated with the long-term statistical distributions of wind speed, wave height, and wave period. For example, load cases with high wind speeds usually are accompanied by high wave heights leading to greater loads on the floating platform [6].

#### Mooring Loads

The mooring system is an integral part of all floating platform concepts. It consists of cables attached to the floating platform at fairleads which connect with the anchors to the seabed. There are different types of cables available, such as chains, steel, synthetic fibers, or a combination of these. The mooring system is especially critical for a tension-leg platform design [6].

Hydrodynamic and mooring forces are additional sources of loads compared with land-based wind turbines. Accordingly, hydrodynamic and mooring line dynamic effects must be included within a comprehensive coupled analysis [7] for a floating offshore turbine.

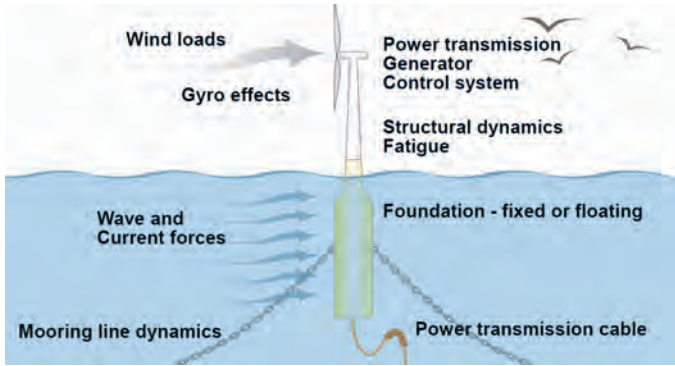


Figure 1.5: Floating offshore wind turbine system [5].

### 1.3. Rotor aerodynamics modeling methods

To numerically calculate the aerodynamic performance of a wind turbine rotor, several numerical modeling approaches (ranging from low to high fidelity) have been developed for wind energy applications. This section briefly introduces these modeling techniques.

#### Blade Element Momentum theory

The most classical model is the Blade Element Momentum (BEM) theory from Glauert in 1935 [8], which is still widely used in the wind energy academic and industrial communities. This method is a combination of the momentum theory and blade element theory. The momentum theory is the basis for the so-called "actuator-disc theory" or "one-dimensional slip-stream theory". The latter considers the wind turbine rotor as an ideal permeable disc, which exerts a uniform thrust force on the flow. The fluid flows through the disc in the form of a streamtube, as shown in Fig. 1.6. The fluid is assumed to be irrotational, inviscid and incompressible, which satisfies potential flow theory. Because the rotor disc extracts energy from the wind, the wind speed slows

down when it passes through the rotor disc as illustrated in the middle part of the figure. Accordingly, because of mass conservation, the downstream section of the streamtube (the wake) expands behind the rotor. Furthermore, there is a pressure difference at the disc, with the pressure being larger than the free-stream pressure in front of the disc and smaller than the free-stream pressure just behind the disc as illustrated in the lower part of the figure. By contrast,

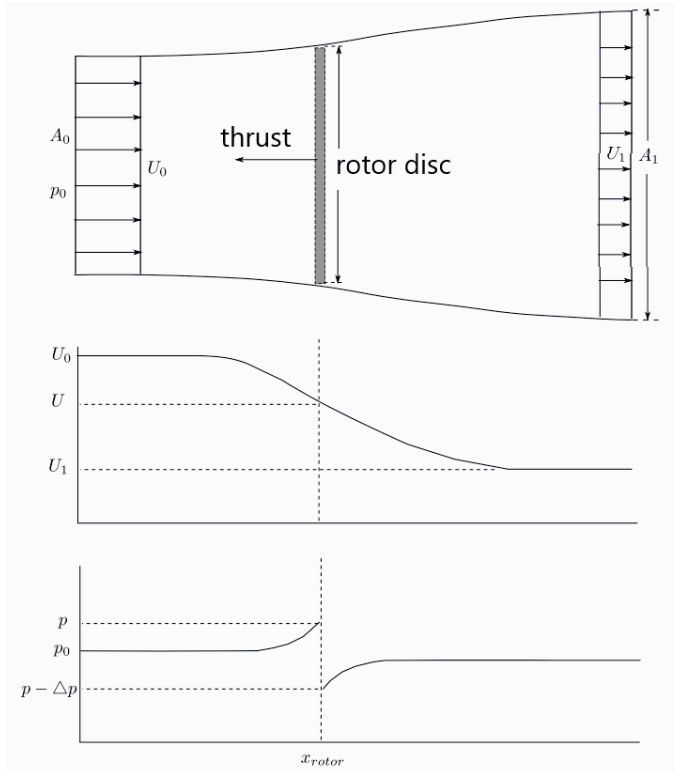


Figure 1.6: Sketch of flow through an ideal wind turbine rotor (adapted from Zhang [9]).

blade element theory uses lift and drag coefficient data for the airfoil sections along the blades, and the local flow conditions such as the angle of attack, to compute local values of the thrust force generated by the rotor. The blade element momentum equations are obtained by equating the aerodynamic loads from both the blade element theory and the momentum theory.

### Vortex-based method

Vortex-based methods focus on generating and tracking vorticity, a quantity that measures the local rotation of fluid particles. The level of accuracy of this type of method is usually higher than with BEM but lower than with computational fluid dynamics (CFD) methods [10]. Vortex-based method uses vortex elements to simulate the effect of the rotor blades and the wake. There are different types of vortex element, which includes vortex line, vortex ring and vortex particle. In vortex line methods, blade trailing vortices and shed vortices convect into the wake with a speed determined by the vectorial sum of the free stream velocity and the velocities induced by the other vortex elements in the field as well as themselves as shown in Fig. 1.7 . In vortex ring methods, vortex rings are taken as independent vortex elements which represent the vortex structure in the wake. In vortex particle methods, the vortices shed into the wake are represented by discrete vortex points.

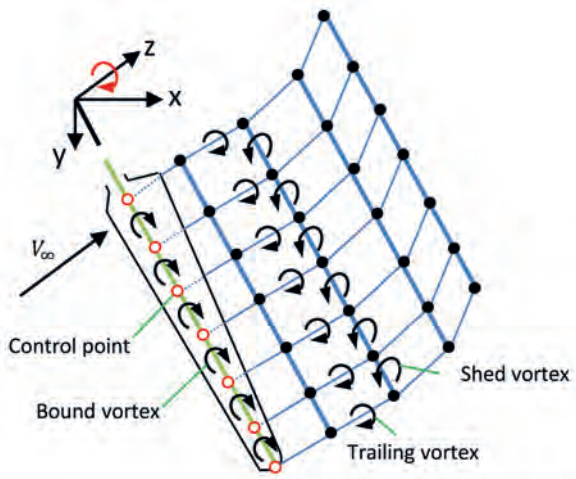


Figure 1.7: Vortex wake model of vortex line methods (adapted from Xu [11]).

### Panel method

Panel method is based on potential flow theory, where the rotor blade geometry is distributed with sources and doublets on the blade surface, and the wake is modeled as a sheet of distributed doublets.

## Computational fluid dynamics method

An alternative to advanced panel methods for wind turbine rotor aerodynamics is computational fluid dynamics (CFD), which involves solving the Navier-Stokes equations numerically. In theory, CFD provides the highest fidelity for simulating the dynamics of fluid flows. However, it is also the most time consuming method.

In this research, both the BEM method and the vortex-based method are applied to the coupled analysis of floating offshore wind turbines. Detailed information about these methods and their use in simulating the aerodynamics of floating offshore wind turbines are introduced in the relevant chapters.

### 1.4. Problem description

Due to the combined effects of wind and waves, floating offshore wind turbines (FOWT) often experience large amplitude motions. This means that the aerodynamics of FOWTs can differ from that of bottom-mounted wind turbines. In particular, it is shown in the literature that a FOWT can be subjected to four working states [12] when the floating platform undergoes a pitching motion: windmill state, turbulence state, vortex ring state, and propeller state. The windmill state is the initial operating state, when the turbine extracts energy from the flow field, as shown in the first frame of Fig. 1.8. In this figure, the yellow arrows represent the direction of the rotor motion. The turbulent state starts when the rotor reaches upwind maximum and begins to pitch downwind, interacting with its own wake, as shown in the second frame of Fig. 1.8. A vortex ring state (VRS) forms when the relative wind velocity drops significantly and a toroidal recirculation flow takes place normal to the rotor disc, as shown in the third frame of Fig. 1.8. Finally, the relative wind velocity reverses, and the wind turbine outputs energy in the flow like a propeller, as shown in the fourth frame of Fig. 1.8.

The vortex ring state is an interesting rotor flow state, assumed to be first recognized by de Bothezat [13], and is well-known in helicopter flight. In steep

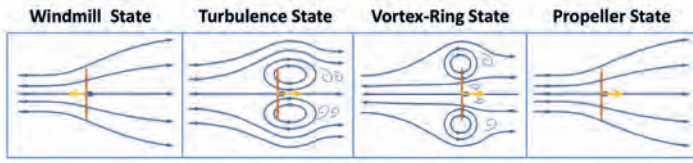


Figure 1.8: Four working states of FOWTs (adapted from Sebastian [12]).

descending flight of a helicopter, when the relative upward flow velocity at the rotor due to descent becomes a much larger fraction of the net inflow velocity downward induced by the rotor, the rotor can operate in a condition known as a vortex ring state [14], as shown in Fig. 1.9.

The vortex ring state of helicopters causes safety and operating problems for helicopter pilots. Research shows that the onset of the vortex ring state of an helicopter is accompanied by an increase in rotor thrust fluctuations. When in a deep vortex ring state, the rotor is engulfed in the vortex ring formed by the wake flow, which can cause a series of aerodynamic problems including thrust loss, significant rotor vibrations, and non-periodic blade flapping.

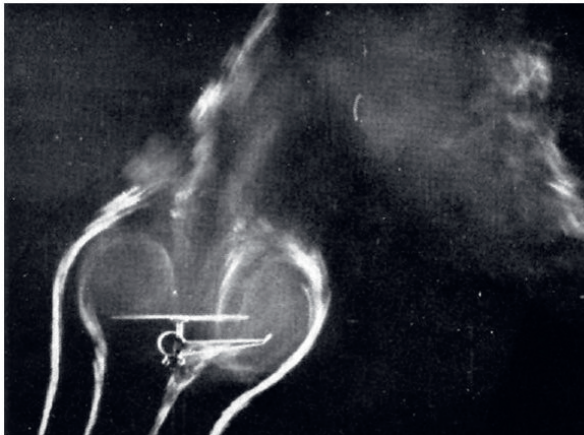


Figure 1.9: Vortex ring state occurring on a helicopter rotor [14].

Due to the platform motions, the rotor of a floating offshore wind turbine can interact with its own wake and potentially with the vortices shed at the blade tips. Such tip vortices are visualised in Fig. 1.10 using a smoke trail <sup>12</sup>.

<sup>12</sup><https://www.arising.com.au/aviation/windturbines/wind-turbine.html>

As documented in the literature, it seems that these interactions may give rise to a vortex ring state.

Although the occurrence of the vortex-ring state for FOWTs has been documented in previous works, the extend to which it occurs and its effect on turbine performance are still poorly understood. This work explores this problem through a series of tasks, as detailed in the next section.



Figure 1.10: Smoke visualisation of vortices being shed at the tip of a wind turbine rotor<sup>12</sup>.

## 1.5. Goals and contributions of this thesis

### 1.5.1. Research objectives and approach

The overarching goal of this research is to improve the physical understanding of the unsteady aerodynamics of floating offshore wind turbines due to platform motions, with a specific focus on the vortex ring state. This study aims at paving the way to better design and minimising the adverse effect of the vortex ring state on a floating wind turbine for the large-scale development of floating offshore wind turbines. Furthermore, three specific objectives are defined, as outlined below:

1. Find out whether, and to what extent, the vortex ring state occurs for floating offshore wind turbines.

This is the primary question to be answered in this research. The existence of the vortex ring state of floating offshore wind turbines has been theoretically identified. However, it is unclear whether the vortex ring state occurs during real operation of these turbines. It is important to understand if it does, and to what extent, so that appropriate mitigation measures can be developed. In light of this, the key research question is:

- What criteria can be used to identify the occurrence of the vortex ring state in floating offshore wind turbines?

In order to address this question, criteria to predict the occurrence of the vortex ring state are derived from the momentum theory and adapted for the application to floating offshore wind turbines. The open source aero-hydro-servo-elastic coupled analysis tool FAST/OpenFAST<sup>13</sup> is used to analyse the velocity profile through the rotor and the nature of rotor-wake interactions. Both regular and irregular wave load cases are investigated.

2. Build an aerodynamic model for the simulation of rotor-wake interactions of floating offshore wind turbines.

The simulation of the dynamic response of a floating wind turbine system requires aero-hydro-servo-elastic coupled analysis. Traditionally, the blade element momentum (BEM) method is a time-efficient aerodynamic method for performing such coupled analyses. However, its accuracy to simulate highly unsteady rotor-wake interactions can be limited. Also it only provides information on the rotor disc, without results on the velocity field in the wake. By contrast, computational fluid dynamics (CFD) models are capable of capturing the complex flow physics with high accuracy throughout a computational domain. However, the computational cost associated with such approaches limits their application to integrated coupled engineering analyses. Thus a key research question is:

- How to develop an accurate and computationally-efficient aerodynamic model for analysing rotor-wake interactions in FOWTs, including both the rotor and the wind field around it?

---

<sup>13</sup><https://www.nrel.gov/wind/nwtc.html>

In this work, a mid-fidelity free wake vortex ring method is developed for the aerodynamic analysis of moving rotors, which includes a near wake model and a far wake model. The near wake model uses vortex filaments and the far wake model uses vortex rings. It is shown that this approach is both suitable for the analysis of rotor-wake interactions of interest here and computationally attractive. This model is verified on both fixed and moving rotors.

3. Analyze the characteristics and impacts of rotor-wake interactions on the performance of floating offshore wind turbines.

To analyse rotor-wake interactions in more detail, the dynamic behaviour and transient response of the wind turbine system are of interest, as well as the wake structure and velocity field in the near-wake. Thus a series of aerodynamic parameters are analysed using both the vortex ring state (VRS) prediction methods and the numerical model developed in this work. The associated research questions are:

- How is the wind turbine performance affected by the vortex ring state?
- What is the impact of a change in working state during a whole cycle of the platform motion?

In order to address these questions, the present free wake vortex ring model is applied to the dynamics of a floating wind turbine subjected to a surge motion. The different working states of the rotor are identified and their effect on the aerodynamic performance of the rotor are quantified.

### 1.5.2. Thesis outline

This thesis addresses the research objectives in distinct – yet interrelated – chapters. First, prediction criteria are derived and used in the momentum theory framework to identify and assess the extent to which the vortex ring state occurs for floating wind turbines operating in real conditions. Then, a free wake vortex method is developed and presented to deal with unsteady aerodynamic problems. It is verified for both bottom-fixed and floating offshore wind turbines. Finally, this model is applied to further analyse rotor-wake interactions, and their role on performance, for a wind turbine rotor undergoing a prescribed platform motion in a more academic setting.

An overview of the content is as follows.

Chapter 2: Prediction of VRS for floating wind turbines.

The VRS prediction methods originally used in the field of helicopters are investigated and adapted for application to FOWTs. Then, an aero-hydro-servo-elastic coupled analysis of FOWTs with different types of floating foundations is executed and the VRS boundaries are evaluated using these criteria.

Chapter 3: The free wake vortex ring method.

Vortex theory, with a focus on vortex filament induction and vortex ring induction, is introduced and the numerical modeling of a simplified free wake vortex ring method is developed.

Chapter 4: Verification of the free wake vortex ring method.

The method introduced in the previous chapter is verified by executing a series of load cases on both fixed and moving rotors. The strengths and weaknesses of the model are identified and the results are compared with the literature.

Chapter 5: Working states of a floating offshore wind turbine in surge motion.

The vortex ring state of a floating offshore wind turbine during surge motion is simulated with the free wake vortex ring method and compared to the literature. More insight is given into the aerodynamic performance of floating offshore wind turbines through the different working states of the rotor over a whole cycle of the rotor motion.

Chapter 6: Conclusions based on the results presented in all the chapters are shown here and recommendations for future work are outlined.



# 2

## Prediction of the vortex ring state

他山之石，可以攻玉。 — 《诗经》

Stones from other mountains can be used to polish one's jade.

The Book of Songs

The aerodynamics of floating offshore wind turbines (FOWTs) can significantly differ from that of bottom-mounted wind turbines due to platform motion. The existing literature identifies four working states of FOWTs, one of them being the vortex ring state (VRS). This state may occur as the rotor moves into its own wake and can potentially be very detrimental to the aerodynamic performance and lifetime of FOWTs. It is still unclear when, and to what extent, the VRS occurs for floating offshore wind turbines. The aim of this chapter is to introduce the criteria that quantitatively predict the occurrence of VRS during the operation of FOWTs. In this chapter, three different criteria are derived: the axial induction factor, Wolkovitch's criterion and Peters' criterion. These criteria are then used to quantitatively predict the occurrence of VRS

during the operation of FOWTs. The results obtained from coupled analyses with OpenFAST show that the VRS phenomenon may occur for a large range of operating conditions and can be correlated with the minima in the relative wind speed normal to the rotor plane. Also, the probability of occurrence of a VRS is smallest for the floating platforms that exhibit the least motion, such as the TLP. Finally, Wolkovitch's criterion seems to be the most suitable one for VRS prediction, while Peters' criterion indicates the initial aerodynamic change associated with a VRS and is thus suitable for early warning of a VRS.

## 2.1. Introduction

As explained in the previous chapter, the literature outlines the existence of four working states for a FOWT: windmill state, turbulence state, vortex ring state, and propeller state [12]. Generally, when calculating the aerodynamics of onshore wind turbines with blade element momentum theory, only the windmill working state and the turbulent working state (TWS) are considered. This is acceptable because the foundation of bottom-mounted turbines is fixed and the rotor is only subjected to small amplitude vibrations. Thus the VRS and propeller state rarely occur. Glauert's correction [8] is often used to correct the rotor thrust coefficient when the rotor operates in a turbulent wake, which applies when the axial induction factor is  $a > 0.4$  or the thrust coefficient is  $C_T > 0.96$  [15]. By convention, the thrust coefficient  $C_T$  is defined as

$$C_T = \frac{T_x}{0.5\rho_{air}A_{rotor}V_\infty^2}, \quad (2.1)$$

where  $T_x$  is the force which is normal to the rotor,  $\rho_{air}$  is the air density taken as  $1.225 \text{ kg/m}^3$ ,  $A_{rotor}$  is the rotor swept area and  $V_\infty$  is the free stream velocity.

By contrast with onshore and bottom-mounted offshore wind turbines, the aerodynamics of floating wind turbines can be significantly affected by the VRS. From the literature on helicopter rotors, it is known that the VRS affects rotors in the following way [16]. First, the rotation becomes apparently unsteady and aperiodic. Second, the blades experience successive forward and backward velocities, which can lead to significant blade flapping and a loss of rotor control. Third, the level of thrust fluctuations is high. When the VRS occurs, the momentum theory stream tube assumption breaks down and BEM theory no longer holds true for the aerodynamic calculation. After Sebastian's hypothesis [12] that the VRS occurs as a transient phenomenon, several scholars performed some research concerning FOWT unsteady aerodynamics. Tran [17][18] studied the unsteady aerodynamics of FOWT platform motion using a computational fluid dynamics (CFD) model. Jeon et al [19] studied the unsteady aerodynamics of FOWTs in platform pitching motion using the vortex lattice method. Kyle [20] researched on the alleviation of the vortex ring state for FOWTs using a modified blade-tip shape using a CFD method. Additionally, Kyle [21] researched the propeller and vortex ring states of floating offshore wind turbines

during a prescribed surge motion. Finally, Mancini et al [22] studied the characterization of the unsteady aerodynamic response of a floating offshore wind turbine using experiments and CFD.

Despite these studies, two questions have yet to be answered: how often does the VRS happen for FOWTs and to what extent does it occur? The answer to these questions is important in order to assess if, and how, the VRS should be taken into account in the modeling and design of FOWTs. Moreover, the VRS is a transient phenomenon more likely to occur due to the pitch and surge motions of the turbine. Thus the simulation of the VRS must be integrated with the simulation of the other working states of the wind turbine. Traditionally, the unsteady aerodynamic analysis of wind turbines does not distinguish the VRS from the turbulence working state. It does not separately analyze its influence on the rotor either.

So far, there is no special criterion for the prediction of the VRS for FOWTs when the rotor interacts with its own wake. However, criteria exist for the prediction of the VRS in the context of helicopters during their descent. Basset [23] classified the prediction of the VRS boundaries in three different theories, i.e. zero transport velocity of rotor tip vortices, bifurcation of equilibria, and zero heave damping. Different methods are used to predict the VRS boundaries. For example, Drees [24] identified the VRS as a rough region based on the ratios between rotorcraft vertical or horizontal velocity and the hover induced velocity. Whashizu [25] experimentally researched on the VRS based on the fluctuations in the thrust force. By contrast, Xin and Gao [26] predicted the VRS with model tests taking the torque fluctuation as a reference, while Betzina [27] investigated the VRS with an experimental method taking the decrease of mean thrust as a reference. Wolkovitch [28] and Peters [29] predicted the VRS based on momentum theory with the assumption that the velocity of the tip vortices drops to zero. Leishman [30] predicted the VRS based on a free wake vortex method, which shows that the blade-flapping fluctuation can also be a feature of the VRS, besides the thrust and torque fluctuations. In particular, the angle of the blade-flapping fluctuation can be used to predict the VRS onset. Newman [31] devised a method for VRS prediction based on momentum theory, refined using measurement data from Drees [24], and made further reductions based on

the nature of the flow in the breakdown regime. Taghizad [32] researched the VRS with a flight test, during which the VRS boundary was identified using three criteria: first an increase of vibration, followed by a sudden increase in descent rate, and exiting the VRS when the descent rate was stable again. As shown by Basset [23], the different criteria can lead to different VRS boundaries. Generally speaking, the Peters' criterion covers relatively larger descent speeds of the rotor than Wolkovitch's criterion.

This chapter aims at quantitatively predicting the occurrence of what is commonly referred to as the vortex ring state in the literature on FOWTs, when supported by different floating foundations. The chapter is organized as follows. Firstly, since this chapter is based on blade-momentum element theory, the overall method is briefly presented in Section 2.2. Section 2.3 then derives the criteria used for the prediction of the vortex ring state of FOWTs. Section 2.4 introduces the simulation tools and the floating offshore wind turbines considered here. Section 2.5 shows results for regular wave load cases, whilst Section 2.6 focuses on irregular wave load cases. Finally, Section 2.7 summarises the main conclusion and discussion.

## 2.2. BEM method applied to floating offshore wind turbines

The most classical model is the Blade Element Momentum (BEM) theory from Glauert in 1935 [8], which is still widely used in the wind turbine industry and academia. Since the first introduction of BEM theory for wind turbine applications (Wilson and Lissaman, 1974 [33]), it has been widely used by the wind energy community for the aerodynamic and aero-servo-elastic coupled modeling of wind turbines. The original theory of the application of BEM in the open source software FAST and OpenFAST can be found in [34][35], which applies to bottom fixed wind turbines. Due to the floating platform motion, the mathematical model based on momentum theory for FOWTs is different than for bottom-fixed turbines. This is described in the literature [36][22][37] and summarised hereafter.

As shown in Fig. 2.1, in the rotor-fixed reference frame,  $V_0$  is the inflow velocity,  $V_i$  is the induced velocity and  $V_w$  is the far wake velocity. In the context of floating offshore wind turbines with low frequency platform motions,  $V_0$  equals

to  $V_\infty - V_p$ , where  $V_\infty$  is the free-stream velocity and  $V_p$  is the velocity of the rotor due to the floating platform motion.

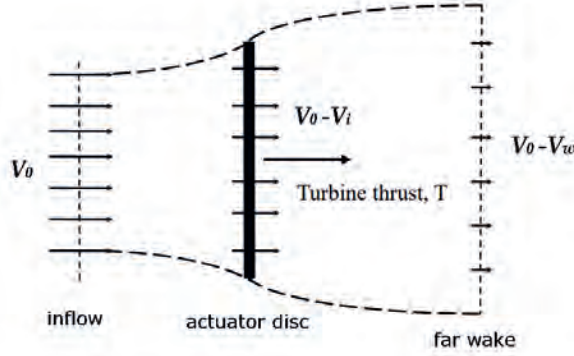


Figure 2.1: Flow model used for the momentum theory analysis of a floating wind turbine (modified from [38]).

According to the momentum conservation theory, the thrust on an annular cross-section can be expressed as:

$$dT = 2a(1 - a)\rho(V_\infty - V_p)^2 2\pi r dr \quad (2.2)$$

where  $a$  is the axial induction factor,  $r$  is the rotor radius,  $\rho$  is the air density.

According to the blade-element theory, the thrust on each blade section can be expressed as:

$$dT = \frac{1}{2} c \rho W^2 C_L(\alpha) \cos(\phi) dr \quad (2.3)$$

where

$$\phi = \arctan\left(\frac{(V_\infty - V_p)(1 - a)}{\Omega r(1 - a')}\right), \quad (2.4)$$

$$\alpha = \phi - \epsilon, \quad (2.5)$$

$$W = \sqrt{((V_\infty - V_p)(1 - a))^2 + (\Omega r(1 - a'))^2}. \quad (2.6)$$

where  $\phi$  is the inflow angle with respect to the rotor plane,  $a'$  is the angular induction factor,  $C_L$  is the lift coefficient which is a function of the angle of attack

$\alpha$ ,  $c$  is the chord length,  $W$  is the effective velocity at the blade element,  $\epsilon$  is the sum of the twist and pitch angles, and  $\Omega$  is the rotor speed.

The combination of the axial momentum and blade-element equations thus becomes [36][39]:

$$2a(1-a)\rho(V_\infty - V_p)^2 2\pi r dr = \sum_{\text{blade}} \frac{1}{2} c \rho W^2 C_L(\alpha) \cos(\phi) dr, \quad (2.7)$$

Additionally, the axial induction factor  $a$  (representing the fractional decrease between the velocity at the rotor and the velocity difference  $V_\infty - V_p$ ) is given by

$$a = \frac{V_i}{V_\infty - V_p}, \quad (2.8)$$

where  $V_i$  is the axial induced velocity at the operating point. In this context, the axial relative velocity at the rotor is given by

$$V_{rel} = (V_\infty - V_p)(1 - a), \quad (2.9)$$

and  $V_{rel} = V_\infty - V_p - V_i$ . Note that in Eq. (2.9), the induction factor is applied to both the free-stream velocity and the platform velocity[36][22].

### 2.3. Theories for the prediction of the vortex ring state

Numerous prediction methods for the vortex ring state of helicopter rotors have been developed. As shown in Fig. 2.2 [23], nine prediction criteria are listed with uniform pattern coordinates, where the vertical axis represents the non-dimensional relative speed normal to the rotor, the horizontal axis represents the non-dimensional relative speed parallel to the rotor, and the curves forms an envelop of the VRS region in each frame of the diagram. It can be seen that the VRS regions defined by different criteria are significantly different, which is mainly because the aerodynamic phenomenon constantly changes during the development of the VRS and different researchers describe the onset of the VRS differently in their studies. In this chapter, Wolkovitch's criterion and Peters' criterion are adapted to the study of VRS for FOWTs and their performances are compared. These two criteria are chosen as they represent extremes in the prediction of VRS: Wolkovitch predicting the narrowest area and Peters the

broadest one. The modifications associated with these criteria in the context of wind turbines are presented in this section. Additionally, the VRS prediction method based on the axial induction factor  $a$  is also introduced.

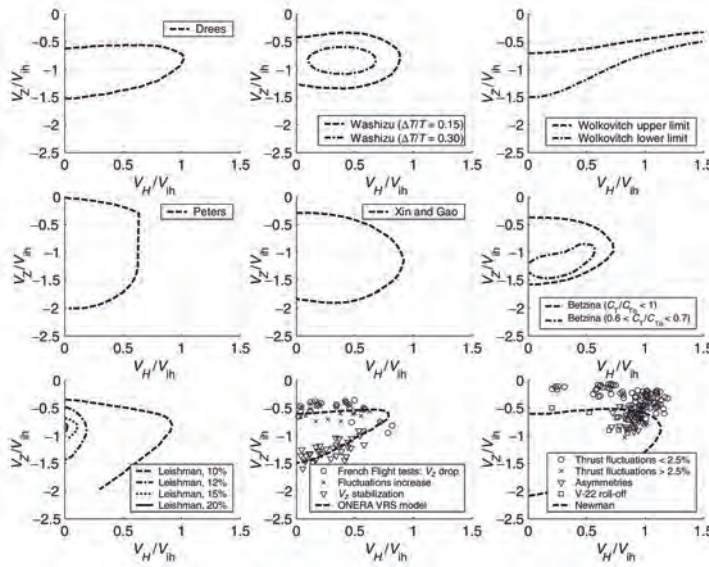


Figure 2.2: A summary of VRS boundaries from the literature, where  $V_z$  is the relative speed normal to the rotor,  $V_H$  is the relative speed parallel to the rotor,  $V_{th}$  is the rotor-induced velocity at hover [23]. (published with permission)

### 2.3.1. VRS prediction based on the axial induction factor

Figure 2.3 shows the rotor states of a fixed rotor corresponding to the measured thrust coefficient  $C_T$  as a function of the axial induction factor  $a$ , defined as (2.8) (assuming  $V_p = 0$ ). From Fig. 2.3, it can be seen that the vortex ring state is situated between the turbulent wake state and the propeller state, which are separated at  $a = 1$ . For  $a > 1$ , Glauert's empirical relation and momentum theory are invalid. In the context of wind turbines, vortices are generated on the blades and shed regularly into the wake, forming vortex rings. The VRS may occur on FOWTs as the rotor can move into its own wake, mainly due to the platform motions such as pitch and surge. At certain times during these motions, the rotor has a downwind speed approximately equal to the traveling

speed of the wake. Following Eq. (2.9), when  $a = 1$ ,  $V_{rel} = 0$ . Thus, the value  $a = 1$  can be taken as one criterion to predict the VRS.

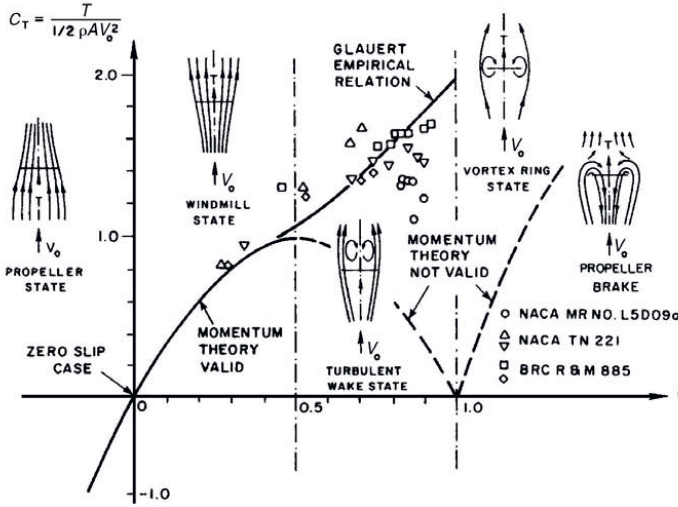


Figure 2.3: The rotor states corresponding to the measured thrust coefficient  $C_T$  as a function of the axial induction factor  $a$  (taken from [40]).

### 2.3.2. VRS prediction based on Wolkovitch's criterion

Even if momentum theory breaks down when the rotor enters the VRS, it can still be used to predict the occurrence of the VRS. Wolkovitch [28] developed a method based on momentum theory and the actuator disk concept to predict the vortex ring state during the descent of a powered helicopter. The flow model in this theory can be adapted to wind turbines, as illustrated in Fig. 2.4, in which  $\mathbf{V}_R$  is the vector of relative velocity,  $\mathbf{V}_I$  is the vector of the wake induced velocity at the rotor and  $\psi$  represents the angle between  $\mathbf{V}_R$  and the rotor disc. The rotor is surrounded by a streamtube which is also a vortex tube on the downstream side. The flow is uniform inside the tube, at any cross section. Outside the tube, the wind speed equals to  $\mathbf{V}_R$ . This vortex tube is formed of a series of vortex cores. Near the rotor and outside of the tube, the downwind component of the stream velocity is  $\mathbf{V}_R \sin \psi$ , while inside the tube the upwind

velocity component is  $(\mathbf{V}_I - \mathbf{V}_R \sin\psi)$ . The velocity of the vortex core center is the average between these velocities, i.e.  $(\mathbf{V}_I/2 - \mathbf{V}_R \sin\psi)$ , and points in the downwind direction. The vortex ring state is assumed to occur when the relative velocity of the vortex cores normal to the rotor disc falls to zero. Thus the critical velocity  $V_{crit}$  associated with Wolkovitch's criterion is given by

$$V_{crit} = \frac{|\mathbf{V}_I|}{2\sin\psi}. \quad (2.10)$$

When the velocity is smaller than the critical velocity, the rotor is in a vortex ring state. Different criteria predict the VRS with different aerodynamic conditions, and Wolkovitch's criterion predicts the VRS onset when the rotor has a speed that can catch up with the core center of the vortex ring.

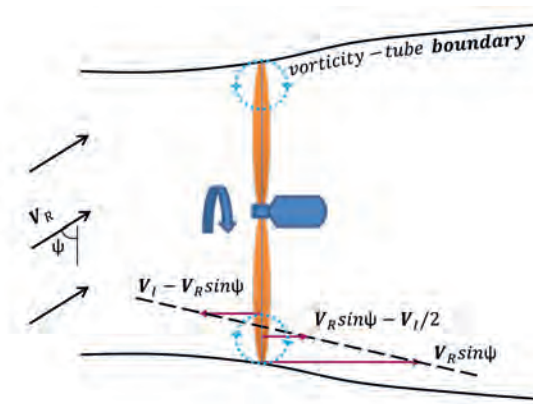


Figure 2.4: Illustration of a stream tube and components of the wind speed in the context of Wolkovitch's model.

### 2.3.3. VRS prediction based on Peters' criterion

Peters' criterion [29] can be used to predict the VRS of a rotor with both axial and in-plane velocities and was also developed based on momentum theory. The flow model of this theory adapted to wind turbines is shown in Fig. 2.5. It can be found that the component of the free stream velocity vector  $\mathbf{a}$  in the

direction of the wake stream velocity vector  $\mathbf{b}$  can be given by

$$\frac{\mathbf{a} \cdot \mathbf{b}}{|\mathbf{b}|} = \frac{\mu^2 + \eta^2 - v\eta}{\sqrt{\mu^2 + (v - \eta)^2}}, \quad (2.11)$$

where  $\eta$  is the non-dimensional axial component of free stream velocity, which is equal to  $|\mathbf{V}_R| \sin \psi / v_h$ ,  $v_h = |(T/2\rho A_{rotor})^{1/2}|$ , where  $T$  is thrust and  $A_{rotor}$  is the rotor swept area;  $v$  is the non-dimensional induced velocity, which equals  $|\mathbf{V}_i|/v_h$ , and  $\mu$  is the non-dimensional inplane component of the free stream velocity.

According to momentum theory, the induced velocity  $v$  inside the stream tube can be replaced by  $\kappa v$ , where the value  $\kappa$  varies from 1.0 at the rotor disc to 2.0 at infinity [28]. Following the same reasoning as before, i.e. the relative velocity should be zero for the VRS boundary, the condition becomes [29]

$$\mu^2 = (\kappa v - \eta)\left(\eta - \frac{\kappa v}{2}\right) = \frac{3}{2}\kappa v\eta - \frac{1}{2}\kappa^2 v^2 - \eta^2, \quad (2.12)$$

combined with the momentum equation which is given in terms of normalized flow-rates [29]

$$v^2[\mu^2 + (v - \eta)^2] = 1, \quad (2.13)$$

the boundary between windmill state and vortex ring state, for the case of  $\kappa = 1$ , is derived as

$$\begin{aligned} \mu^2 &= \frac{1}{v^2} - \frac{4}{v^6}, \\ \eta &= v - \frac{2}{v^3}, \end{aligned} \quad (2.14)$$

and the vortex ring boundary from vortex ring state to propeller state, for the case of  $\kappa = 2$ , is derived as

$$\begin{aligned} \mu^2 &= \frac{1}{v^2} - \frac{1}{v^6}, \\ \eta &= v + \frac{1}{v^3}. \end{aligned} \quad (2.15)$$

It is worth noting that the two vortex ring boundaries introduced above are opposite to those from the original paper of Peters [29] as the latter deals with helicopters, where the working state of the rotor changes from propeller

state to vortex ring state in the near wake (the wake directly connects to the rotor) and the rotor goes from vortex ring state to windmill state in the far wake (the rotor goes into the wake). For wind turbines, the near wake and the far wake boundaries are exactly opposite. The influence of wake expansion is always considered in the far wake which makes the two boundaries in  $\mu - \eta$  plane asymmetry along  $\mu$  axis [29]. Furthermore, assuming that the vortex ring state occurs when the velocity component normal to the rotor is negative, i.e.

$$\mu^2 + \eta^2 - v\eta < 0, \quad (2.16)$$

the vortex ring boundary between vortex ring state and windmill state is written as

$$\begin{aligned} \mu^2 &= \frac{1}{v^2} - \frac{1}{v^6}, \\ \eta &= v - \frac{1}{v^3}. \end{aligned} \quad (2.17)$$

Considering that the critical values of  $\mu$  on the propeller side and on the windmill side should be equal, the final criterion is taken as

$$\begin{aligned} \mu^2 &= \frac{1}{v^2} - \frac{1}{v^6}, \\ \eta &= v \pm \frac{1}{v^3}, \\ \lambda &= v - \eta = \mp \frac{1}{v^3}. \end{aligned} \quad (2.18)$$

When it is evaluated in the  $\mu - \lambda$  plane, the vortex ring state is located inside the envelop of the curve, whilst the upper half represents the boundary with the windmill state and the lower half represents the boundary with the propeller state as indicated in Fig. 2.2.

## 2.4. OpenFAST simulation tool

In this chapter, the comprehensive horizontal axis wind turbine simulation code OpenFAST [41] developed by NREL is used in order to apply the criteria

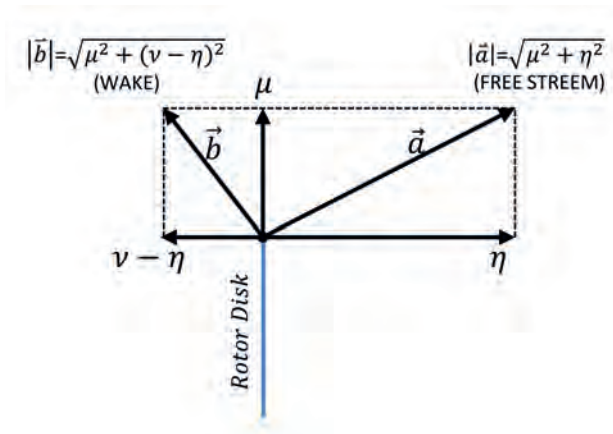


Figure 2.5: Illustration of the velocity components in Peters' flow model.

developed above and give a first assessment of the extent to which the VRS occurs for FOWTs. The code drives modules corresponding to different disciplines of the coupled aero-hydro-servo-elastic solution. The aim is to use OpenFAST to output the velocities on the blade sections when the wind turbine is subjected to both wind and waves. These values can be compared to the critical velocities introduced in the previous section, in order to assess whether a VRS occurs or not. In this work, the following OpenFAST modules are used: AeroDyn v15 to calculate aerodynamic loads based on blade element momentum theory and generalized dynamic wake theory [35]; InflowWind for processing wind-inflow including (but not limited to) uniform hub-height wind and full-field (FF) wind generated from TurbSim; HydroDyn to calculate hydrodynamic loads on a structure; MAP++ for mooring loads; ElastoDyn for the structural dynamics; and ServoDyn for control and electrical drive dynamics.

For the simulations conducted in this chapter, the floating platform is assumed to move in six degrees of freedom (DOFs). The tower and blades are considered as rigid. For Case I, the free stream wind is defined as constant, unidirectional and without shear, while for Case II, the free stream wind is defined as a full-field 3-component stochastic wind. The blade airfoil aerodynamics model is Beddoes-Leishman (B-L) model and the unsteady airfoil aerodynamic (UA) model is the B-L model developed by Minnema/Pierce [35]. The blade pitch and electrical-drive dynamics control are switched on. The total simula-

tion time is set to 1200s. The initial 300s of each simulation are omitted in the analysis.

#### 2.4.1. NREL 5MW turbine and platforms

The analysis is performed on the NREL offshore 5MW baseline wind turbine. The basic parameters of the turbine are shown in Table 2.1, and the reader can refer to the NREL report [42] for more information.

Table 2.1: Characteristics of the NREL 5MW reference turbine.

Rating	5MW
Rotor Orientation, Configuration	Upwind, 3 Blades
Control	Variable Speed, Collective Pitch
Drivetrain	High Speed, Multiple-Stage Gearbox
Rotor, Hub Diameter	126m, 3m
Hub Height	90m
Cut-In, Rated, Cut-Out Wind Speed	3m/s, 11.4m/s, 25m/s
Cut-In, Rated Rotor Speed	6.9rpm, 12.1rpm
Rated Tip Speed	80m/s
Overhang, Shaft Tilt, Precone	5m, 5°, 2.5°
Rotor Mass	110,000kg
Nacelle Mass	240,000kg
Tower Mass	347,460kg
Coordinate Location of Overall CM	[-0.2m, 0.0m, 64.0m]

Three types of floaters, namely barge, spar-buoy and TLP, have been modified to support the NREL 5MW turbine for realistic simulations. The main dimensions and hydrostatic data of these platforms are summarized in Table 2.2,

with the center of mass (CM) defined with respect to the still water level (SWL). The natural frequencies of the three floating systems are summarized in Table 2.3, which were calculated by NREL with an earlier version of FAST [43].

### 2.4.2. Load cases

Two types of FAST-simulated design load cases (DLCs) in terms of wind speeds and sea states are described below. The regular wave load cases aim at assessing the dependence of the VRS with wave and wind parameters. The irregular wave load cases aim at simulating real offshore environmental conditions to see whether the VRS is likely to happen on real wind turbines or not.

#### Regular wave states

In this group of DLCs, deep-water regular waves [44] are used and zero-degree heading angles are considered for wind, wave and current. The values of the constant wind speed  $V_\infty$  and sinusoidal wave with regular wave height  $H_{rw}$  and regular wave period  $T_{rw}$  are shown in Table 2.4. The wind speed range covers the cut-in wind speed and cut-out wind speed of the NREL 5MW turbine. The wave height range is determined according to the common sea states. The wave period range covers the natural period of the pitch motion of the three floating systems, as shown in Table 2.3. In order to reduce the set of combined load cases for  $H_{rw}$ ,  $T_{rw}$  and  $V_\infty$ , the wave steepness  $\delta$  is considered, i.e.

$$\delta = \frac{H}{V_{rw}T_{rw}} = 2\pi \frac{H_{rw}}{gT_{rw}^2}, \quad (2.19)$$

where  $V_{rw}$  is the regular wave speed and  $g$  is the acceleration of gravity taken as  $9.8 \text{ m/s}^2$ . Since the FAST hydrodynamic solver HydroDyn assumes linear wave theory [6], the present load cases are limited to  $\delta \leq 0.011$  (see Figure 3-4 in 'DNVGL-RP-C205' [45]). In Table 2.4 two sets of load cases are given: in set A,  $\delta = 0.007$ , the load cases are marked by 'LCA-m-n', and in set B,  $\delta = 0.01$ , the load cases are marked by 'LCB-m-n', where 'm' and 'n' are the serial numbers of the wind speed and the wave height respectively. The NREL 5MW turbine supported by a OC3-Hywind spar buoy is selected for the simulation with the regular wave load cases.

Table 2.2: Characteristics of the three floating platforms.

	MIT/NREL TLP	OC3-Hywind Spar
Diameter or width $\times$ length	18 m	6.5 to 9.4 m
Draft	47.89 m	120 m
Water displacement	12,180 m <sup>3</sup>	8,029 m <sup>3</sup>
Mass, including ballast	8,600,000 kg	7,466,000 kg
CM location below SWL	40.61 m	89.92 m
Roll inertia about CM	571,600,000 kg $\cdot$ m <sup>2</sup>	4,229,000,000 kg $\cdot$ m <sup>2</sup>
Pitch inertia about CM	571,600,000 kg $\cdot$ m <sup>2</sup>	4,229,000,000 kg $\cdot$ m <sup>2</sup>
Yaw inertia about CM	361,400,000 kg $\cdot$ m <sup>2</sup>	164,200,000 kg $\cdot$ m <sup>2</sup>
Number of mooring lines	8 (4 pairs)	3
Depth to fairleads, anchors	47.89 m, 200 m	70 m, 320 m
Radius to fairleads, anchors	27 m, 27 m	5.2 m, 853.9 m
Unstretched line length	151.7 m	902.2 m
Line extensional stiffness	1,500,000,000 N	384,200,000 N

	ITI Energy Barge
Width $\times$ length	40 m $\times$ 40 m
Draft	4 m
Water displacement	6,000 m <sup>3</sup>
Mass, including ballast	5,452,000 kg
CM location below SWL	0.2818 m
Roll inertia about CM	726,900,000 kg $\cdot$ m <sup>2</sup>
Pitch inertia about CM	726,900,000 kg $\cdot$ m <sup>2</sup>
Yaw inertia about CM	1,454,000,000 kg $\cdot$ m <sup>2</sup>
Number of mooring lines	8
Depth to fairleads, anchors	4 m, 150 m
Radius to fairleads, anchors	28.28 m, 423.4 m
Unstretched line length	473.3 m
Line extensional stiffness	589,000,000 N

Table 2.3: Natural frequencies of the three floating platforms [6].

Natural Frequencies of TLP System					
Mode	Frequency[Hz]	Period [s]	Mode	Frequency[Hz]	Period [s]
Surge	0.0165	60.6061	Roll	0.2229	4.4863
Sway	0.0165	60.6061	Pitch	0.2211	4.5228
Heave	0.4375	2.2857	Yaw	0.0972	10.2881

Natural Frequencies of ITI Energy Barge System					
Mode	Frequency[Hz]	Period [s]	Mode	Frequency[Hz]	Period [s]
Surge	0.0076	131.5789	Roll	0.0854	11.7096
Sway	0.0076	131.5789	Pitch	0.0849	11.7786
Heave	0.1283	7.7942	Yaw	0.0198	50.5051

Natural Frequencies of OC3-Hywind System					
Mode	Frequency[Hz]	Period [s]	Mode	Frequency[Hz]	Period [s]
Surge	0.0080	125.0000	Roll	0.0342	29.2398
Sway	0.0080	125.0000	Pitch	0.0343	29.1545
Heave	0.0324	30.8642	Yaw	0.1210	8.2645

### Irregular wave states

With irregular waves, we consider the NREL 5MW turbine supported by three different floaters, namely MIT/NREL TLP, ITI Energy Barge and OC3-Hywind Spar Buoy. The IEC design standard prescribes numerous DLCs. Here, in the power production situation, one set of fatigue-type DLCs (NTM+NSS) and one set of ultimate-type DLCs (NTM+ESS) are considered, where NTM stands for normal turbulence wind model, NSS is the normal sea state wave model and ESS is the extreme sea state wave model [46]. The other DLCs described in the design standards with idling or fault of the turbine are disregarded.

According to the requirement of the IEC 61400-3 design standard, the loads analysis shall be based on site-specific external conditions. The test site is located at  $61^{\circ} 20' N$  latitude,  $0^{\circ} 0' E$  longitude on the prime meridian northeast of the Shetland Islands, the northeast of Scotland<sup>1</sup>, as illustrated in Fig. 2.6. The environmental data as shown in Table 2.5 were extracted from the NREL technical report [47] at the same location. The NTM+NSS data set is the long-term joint-probability distribution of wind speed  $V_{\infty}$ , significant wave height  $H_s$ , and peak-spectral period of incident waves  $T_p$ . The NTM+ESS data set is the extreme waves with a 1-year return period ( $H_{s1}, T_{p1}$ ) and a 50-year return period ( $H_{s50}, T_{p50}$ ), respectively. The fifteen wind speeds of the NTM+NSS data set are also used for the calculations with the extreme wave data (NTM+ESS set).

---

<sup>1</sup>Web site: <http://www.waveclimate.com/>

Table 2.4: Case I: Regular wave + steady wind load cases.

		Set A, $\delta = 0.007$				
		Wind Speed [m/s]				
$H_{wv}$ (m)	$T_{wv}$ (s)	8	7	6	5	4
10	30.5	LCA-1-1	LCA-2-1	LCA-3-1	LCA-4-1	LCA-5-1
9	28.9	LCA-1-2	LCA-2-2	LCA-3-2	LCA-4-2	LCA-5-2
8	27.2	LCA-1-3	LCA-2-3	LCA-3-3	LCA-4-3	LCA-5-3
7	25.5	LCA-1-4	LCA-2-4	LCA-3-4	LCA-4-4	LCA-5-4
6	23.6	LCA-1-5	LCA-2-5	LCA-3-5	LCA-4-5	LCA-5-5
5	21.5	LCA-1-6	LCA-2-6	LCA-3-6	LCA-4-6	LCA-5-6
4	19.3	LCA-1-7	LCA-2-7	LCA-3-7	LCA-4-7	LCA-5-7
3	16.7	LCA-1-8	LCA-2-8	LCA-3-8	LCA-4-8	LCA-5-8
2	13.6	LCA-1-9	LCA-2-9	LCA-3-9	LCA-4-9	LCA-5-9
1	9.6	LCA-1-10	LCA-2-10	LCA-3-10	LCA-4-10	LCA-5-10
		Set B, $\delta = 0.01$				
10	25.3	LCB-1-1	LCB-2-1	LCB-3-1	LCB-4-1	LCB-5-1
9	24	LCB-1-2	LCB-2-2	LCB-3-2	LCB-4-2	LCB-5-2
8	22.6	LCB-1-3	LCB-2-3	LCB-3-3	LCB-4-3	LCB-5-3
7	21.1	LCB-1-4	LCB-2-4	LCB-3-4	LCB-4-4	LCB-5-4
6	19.6	LCB-1-5	LCB-2-5	LCB-3-5	LCB-4-5	LCB-5-5
5	17.9	LCB-1-6	LCB-2-6	LCB-3-6	LCB-4-6	LCB-5-6
4	16	LCB-1-7	LCB-2-7	LCB-3-7	LCB-4-7	LCB-5-7
3	13.8	LCB-1-8	LCB-2-8	LCB-3-8	LCB-4-8	LCB-5-8
2	11.3	LCB-1-9	LCB-2-9	LCB-3-9	LCB-4-9	LCB-5-9
1	8	LCB-1-10	LCB-2-10	LCB-3-10	LCB-4-10	LCB-5-10



Figure 2.6: Reference-site location.

Table 2.5: Case II: Irregular wave + full field wind load cases.

		NTM+NSS														
		LC1	LC2	LC3	LC4	LC5	LC6	LC7	LC8	LC9	LC10	LC11	LC12	LC13	LC14	LC15
$V_\infty$ [m/s]		4.2	5.6	7.0	8.4	9.8	11.2	12.6	14	15.4	16.8	18.2	19.6	21.0	22.4	23.8
$H_s$ [m]		1.7	1.8	1.9	2.0	2.2	2.4	2.7	3.0	3.4	3.7	4.1	4.5	4.8	5.2	5.5
$T_p$ [s]		12.7	12.7	12.8	14.8	14.1	13.4	12.7	12.1	13.4	13.4	15.5	14.1	13.4	16.2	15.5
		NTM+ESS 1-YEAR														
		LC16	LC17	LC18	LC19	LC20	LC21	LC22	LC23	LC24	LC25	LC26	LC27	LC28	LC29	LC30
$V_\infty$ [m/s]		4.2	5.6	7.0	8.4	9.8	11.2	12.6	14.0	15.4	16.8	18.2	19.6	21.0	22.4	23.8
$H_{s1}$ [m]		10.8	10.8	10.8	10.8	10.8	10.8	10.8	10.8	10.8	10.8	10.8	10.8	10.8	10.8	10.8
$T_{p1}$ [s]		17.6	17.6	17.6	17.6	17.6	17.6	17.6	17.6	17.6	17.6	17.6	17.6	17.6	17.6	17.6
		NTM+ESS 50-YEAR														
		LC31	LC32	LC33	LC34	LC35	LC36	LC37	LC38	LC39	LC40	LC41	LC42	LC43	LC44	LC45
$V_\infty$ [m/s]		4.2	5.6	7.0	8.4	9.8	11.2	12.6	14.0	15.4	16.8	18.2	19.6	21.0	22.4	23.8
$H_{s50}$ [m]		13.8	13.8	13.8	13.8	13.8	13.8	13.8	13.8	13.8	13.8	13.8	13.8	13.8	13.8	13.8
$T_{p50}$ [s]		19.2	19.2	19.2	19.2	19.2	19.2	19.2	19.2	19.2	19.2	19.2	19.2	19.2	19.2	19.2

## 2.5. Results for regular wave load cases

### 2.5.1. Results using the axial induction factor criterion

In this section, the criterion based on the axial induction factor  $a$ , abbreviated as 'a', as introduced in section 2.3.1, is used for the prediction of the VRS. An example of the time history curves of  $a$  from FAST v8 for 9 nodes spread equally along the blade of the OC3 Spar wind turbine is shown in Fig. 2.7. Due to tip loss and hub loss settings in FAST, the blade nodes r1, r2 on the root and r9 on the tip only have zero values of  $a$ . At the other blade nodes,  $a$  is positive and increases towards the blade tip. Fig. 2.7 shows that, for the load case  $V_\infty = 6\text{m/s}$ ,  $H_{rw} = 9\text{m}$ ,  $T_{rw} = 28.9\text{s}$ , the blade nodes  $r7 = 47.6\text{m}$  and  $r8 = 54.5\text{m}$  exhibit  $a > 1$  at certain times, which is considered to be in the VRS, while the blade nodes  $r6 = 40.8\text{m}$ ,  $r7 = 47.6\text{m}$  and  $r8 = 54.5\text{m}$  have  $0.5 < a < 1$ , the rotor operates in turbulent wake.

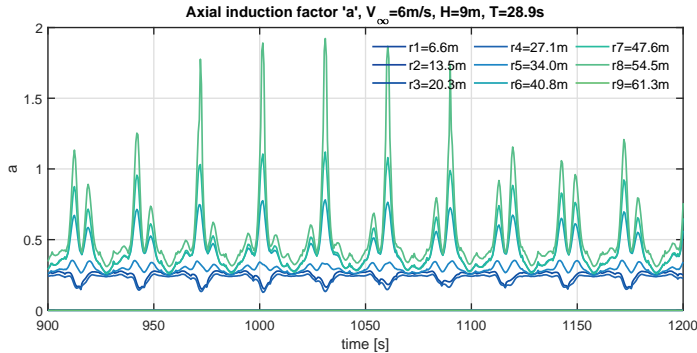


Figure 2.7: Values of the axial induction factor  $a$  on the different blade nodes (LCA32), ( $r_{1-9}$  indicates the location on the blade starting from the root).

Due to the sheer volume of results, only a small fraction is presented here. Eight samples of the VRS prediction results are shown from Fig. 2.8 to Fig. 2.15. All the figures are obtained with the same value of wind speed and wave height but differ in wave steepness. For the first four figures,  $\delta = 0.007$  whilst for the next four figures,  $\delta = 0.01$ . The area colored in purple represents  $0.5 \leq a < 1$ , where the rotor operates in turbulent wake, and the area colored in yellow represents  $a \geq 1$ , corresponding to the occurrence of the VRS. The velocity component normal to the rotor  $V_n$  of the relative wind speed  $V_{rel}$  and the 6-degree of freedom (DOF) platform motions are plotted as reference, with the

values shown on the right-hand-side vertical axis. The  $V_n$  curve represented by the green line directly determines the VRS prediction result which is a combined effect of the 6-DOF platform motions. The surge and pitch motions of the platform which are represented by the red line and the blue line, respectively, dominate the rotor motion along the wind direction. From the figures, it can be found that the VRS ( $a \geq 1$ ) areas are surrounded by the TWS ( $a \geq 0.5$ ) areas, with the TWS area being larger than the VRS area in both blade radial span and time span. The VRS only shows on the outboard part of the blade, except at the tip due to the tip-loss correction of the BEM theory. From Fig. 2.8 to Fig. 2.11, it can be seen that the VRS area becomes larger when the wind speed decreases. Furthermore, for identical values of wind speed and wave height, the VRS areas are wider for larger values of the wave steepness. Also, the VRS occurs periodically when  $V_n$  is negative. In some cases, such as in Fig. 2.8 and Fig. 2.9, there are two regions of the VRS in one period, and  $V_n$  is negative in two regions correspondingly.

### 2.5.2. Results using Wolkovitch's criterion

Wolkovitch's criterion, abbreviated as 'w', as introduced in section 2.3.2, uses an axial velocity parameter to predict the VRS. The examples of the VRS prediction results according to this criterion on individual sections of a rotor blade are shown in Fig. 2.16, in which (a) represents a typical case with VRS occurrence and (b) represents a typical case where the VRS does not occur. The blue dotted lines represent the relative velocities on the blade normal to the rotor disc and the red lines represent the critical velocities calculated based on Wolkovitch's criterion. Thus, when the blue dotted line is below the red line at a given time, the blade node enters the vortex ring state. It can be seen from Fig. 2.16a that, at the blade node  $r=54.5\text{m}$ , the VRS often occurs when the relative velocities drop rapidly. Fig. 2.16b shows that the change in relative velocities is similar than in Fig. 2.16a. However, the VRS never occurs at that blade node because the amplitude of the critical velocity is smaller than in Fig. 2.16a, whilst the magnitude of the relative velocity is larger.

Eight examples of the VRS prediction results according to Wolkovitch's criterion along the blade in time domain are shown from Fig. 2.17 to Fig. 2.24,

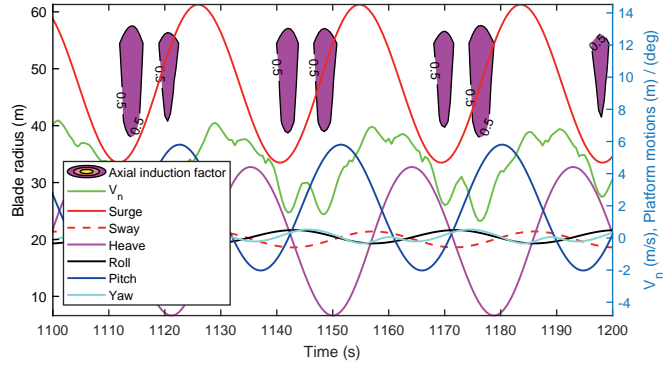


Figure 2.8: Regions of VRS predicted with 'a' (in yellow) together with  $V_n$  and platform motions (LCA-2-2)

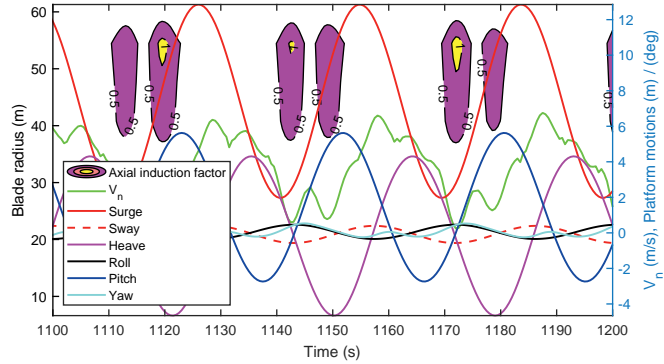


Figure 2.9: Regions of VRS predicted with 'a' (in yellow) together with  $V_n$  and platform motions (LCA-3-2)

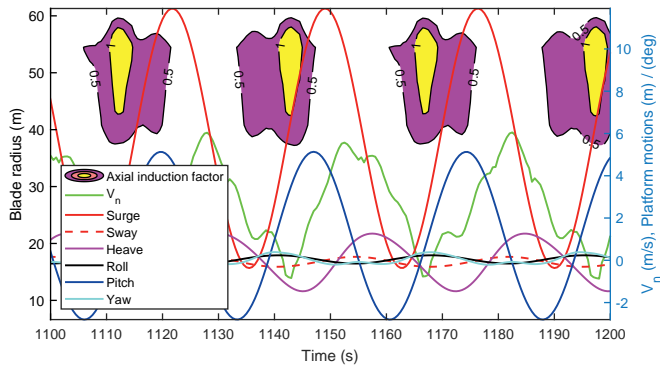


Figure 2.10: Regions of VRS predicted with 'a' (in yellow) together with  $V_n$  platform motions (LCA-4-3)

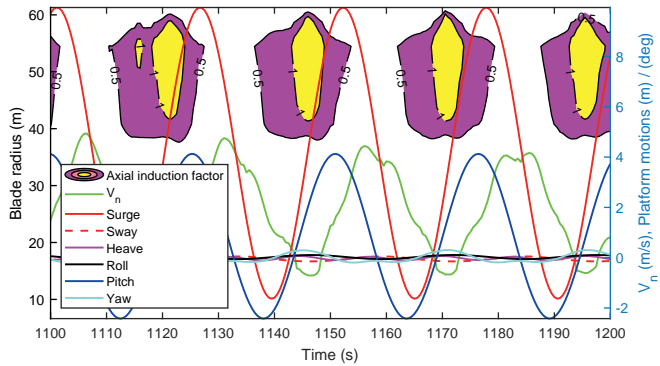


Figure 2.11: Regions of VRS predicted with 'a' (in yellow) together with  $V_n$  and platform motions (LCA-5-4)

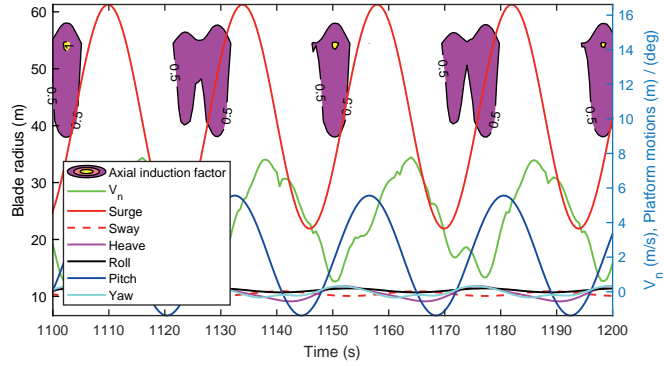


Figure 2.12: Regions of VRS predicted with 'a' (in yellow) together with  $V_n$  and platform motions (LCB-2-2)

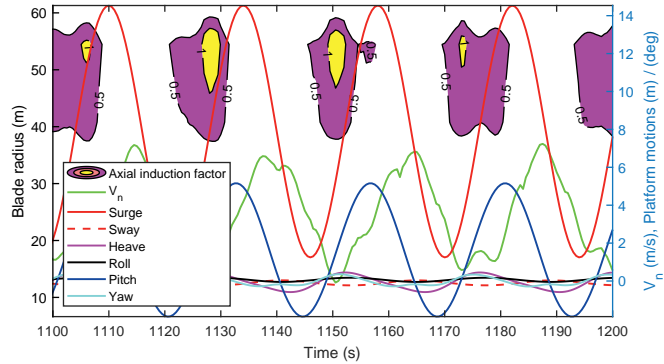


Figure 2.13: Regions of VRS predicted with 'a' (in yellow) together with  $V_n$  and platform motions (LCB-3-2)

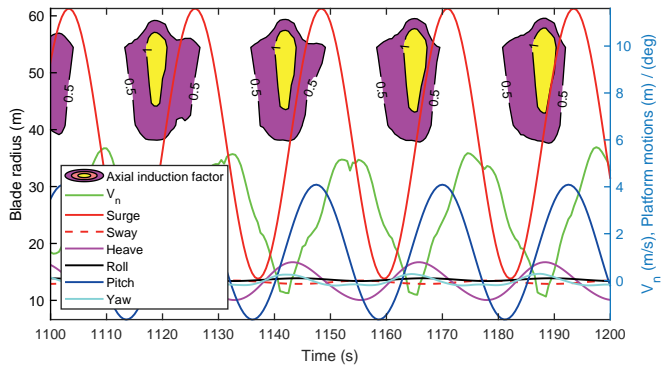


Figure 2.14: Regions of VRS predicted with 'a' (in yellow) together with  $V_n$  and platform motions (LCB-4-3)

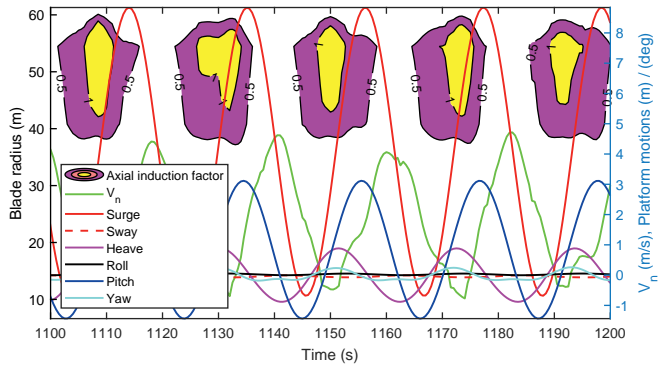
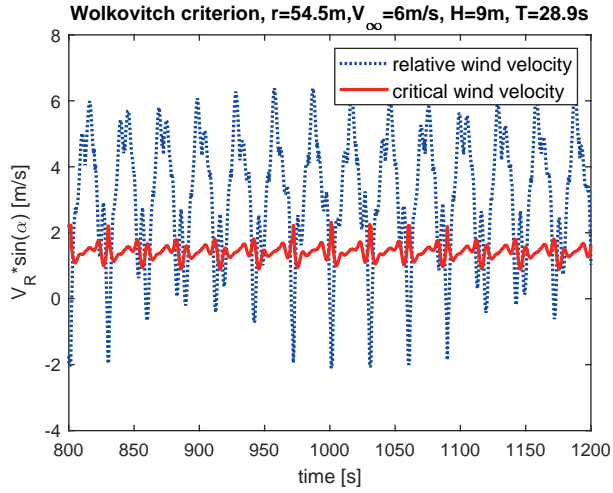
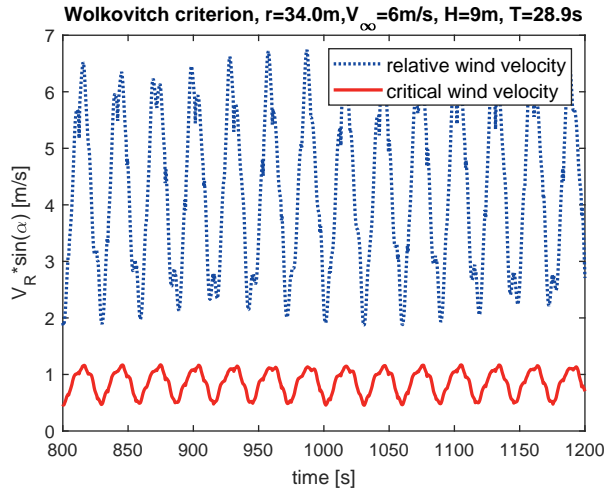


Figure 2.15: Regions of VRS predicted with 'a' (in yellow) together with  $V_n$  and platform motions (LCB-5-4)



(a)



(b)

Figure 2.16: VRS predicted with 'w' on two different blade nodes of the OC3 wind turbine: (a) node  $r = 54.5m$ , (b)  $r = 34m$ .

with the same load cases as the figures in Section 2.5.1. The shaded blue areas represent the regions of occurrence of the VRS according to Wolkovitch's criterion. The relative wind speed normal to the rotor plan  $V_n$  and the 6-degree of freedom platform motions are plotted for reference, with their values shown on the vertical axis on the right-hand-side. Although the exact regions of the VRS differ from those obtained with the criterion based on the induction factor, similar observations can be made. In particular, the VRS area increases when the wind speed decreases and widens as  $\delta$  increases. Also, the VRS occurs periodically when  $V_n$  reaches its minimum values. In some cases, such as Fig. 2.17, Fig. 2.18 and Fig. 2.19, the VRS occurs twice within a short period of time, which is because  $V_n$  has two valley points due to the phase differences of the surge and pitch motions of the platform. By contrast, Fig. 2.20 shows one large area of occurrence of the VRS per period of the platform motion, mainly because the surge and pitch motions have relatively small phase differences in this load case. It can also be found that the VRS area predicted with 'w' completely covers the area of  $a \geq 0$  in Section 2.5.1.

### 2.5.3. Results using Peters' criterion

Peters' criterion, abbreviated as 'p', as introduced in Section 2.3.3, uses one axial velocity parameter and one in-plane velocity parameter to predict the VRS. Examples of the VRS prediction results according to 'p' on single nodes of a rotor blade are shown in Fig. 2.25. The blue points in each sub-figure represent a set of non-dimensional coordinates of  $(\mu, \lambda)$  on a particular blade node, in a certain period of time, and the solid curves represent the critical velocities given by 'p'. When a blue point is located inside the region enclosed by the curves  $\lambda = \pm \frac{1}{v^3}$  ( $0 \leq \mu \leq 0.62$ ) in the  $\mu - \lambda$  plane, the blade node is considered to be in the vortex ring state. Figure 2.25 shows that the VRS does not occur on the two blade nodes located at  $r = 27.1m$  and  $r = 34.0m$ , as all the blue points fall outside of the region of interest. For the two blade nodes located at  $r = 40.8m$  and  $r = 47.6m$ , the sets of  $(\mu, \lambda)$  go across the upper branch of  $\lambda$  critical values and fall into the VRS region. The blade node  $r = 47.6m$  has some negative values of  $\lambda$ , whilst the blade node  $r = 40.8m$  has only positive values of  $\lambda$ . Moreover, the VRS is wider at  $r = 47.6m$  than

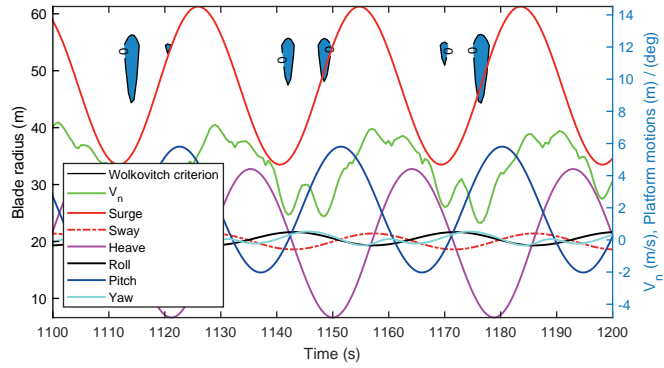


Figure 2.17: Regions of VRS according to 'w' (in blue) together with  $V_n$  and platform motions (LCA-2-2)

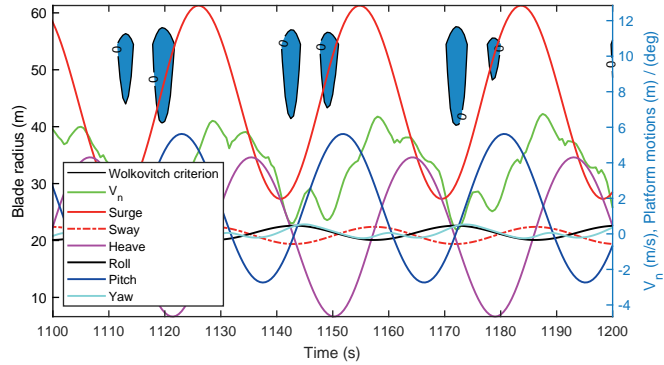


Figure 2.18: Regions of VRS according to 'w' (in blue) together with  $V_n$  and platform motions (LCA-3-2)

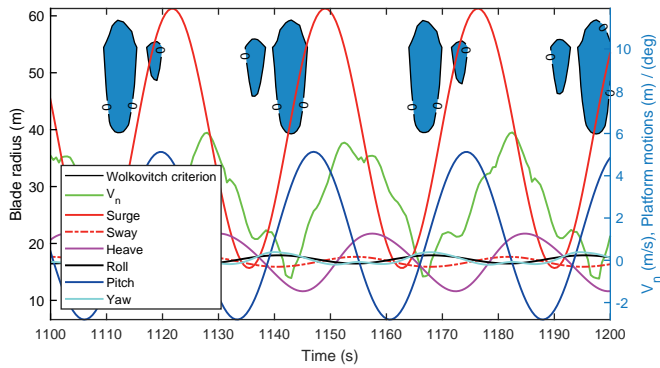


Figure 2.19: Regions of VRS according to 'w' (in blue) together with  $V_n$  and platform motions (LCA-4-3)

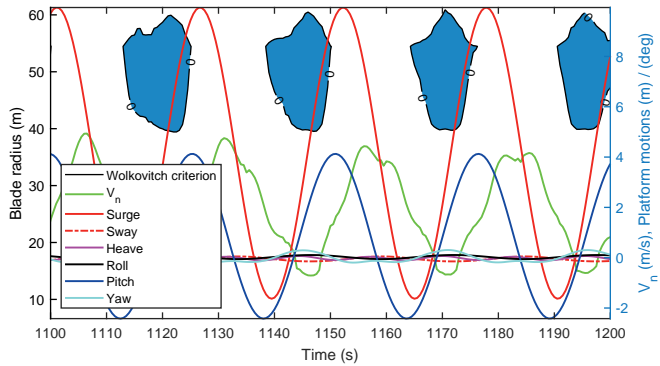


Figure 2.20: Regions of VRS according to 'w' (in blue) together with  $V_n$  and platform motions (LCA-5-4)

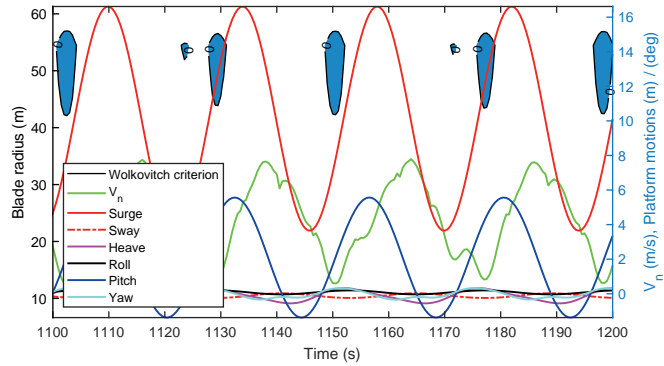


Figure 2.21: Regions of VRS according to 'w' (in blue) together with  $V_n$  and platform motions (LCB-2-2)

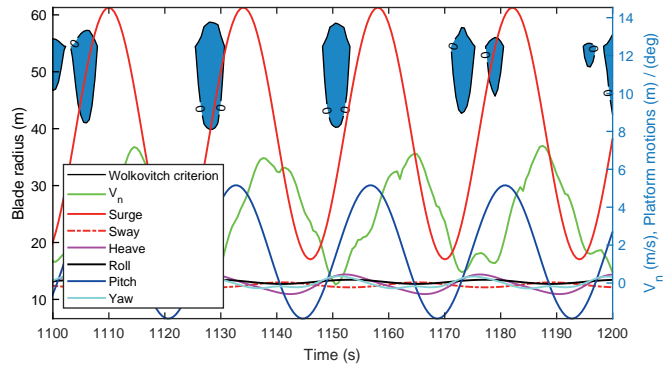


Figure 2.22: Regions of VRS according to 'w' (in blue) together with  $V_n$  and platform motions (LCB-3-2)

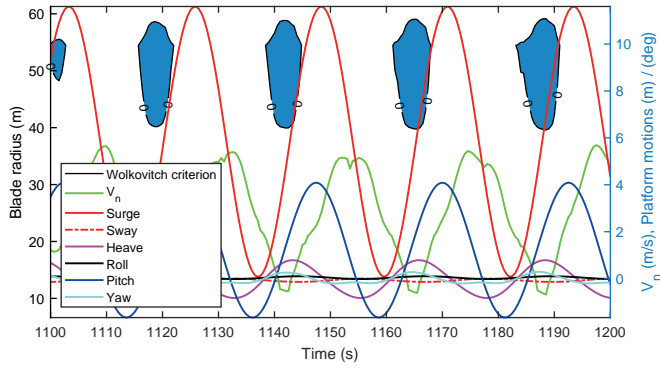


Figure 2.23: Regions of VRS according to 'w' (in blue) together with  $V_n$  and platform motions (LCB-4-3)

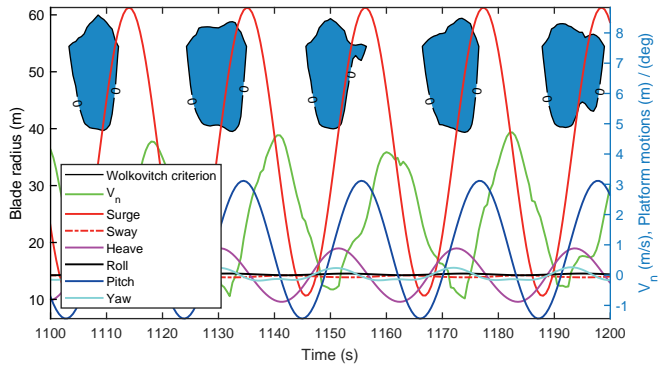


Figure 2.24: Regions of VRS according to 'w' (in blue) together with  $V_n$  and platform motions (LCB-5-4)

at  $r = 40.8m$ , which is mainly because the pitch motion of the platform can occasionally cause larger downwind velocities on the outboard part of the blade while the rotor rotates. The blade node located at  $r = 54.5m$  is the only one that has a set of  $(\mu, \lambda)$  that goes across both the upper branch and the lower branch of the critical values of  $\lambda$ . It also has the largest proportion of VRSs among all the six blade nodes. The blade node located at  $r = 61.3m$  also has a set of  $(\mu, \lambda)$  that goes across the upper branch of the critical values. However, it exhibits a smaller proportion of VRSs due to the tip loss correction effect. For all the six blade nodes,  $\mu \leq 0.6$  which is relatively small because only zero degree heading angles for wind, wave and current are considered in the design load cases.

Eight examples of the VRS predicted with 'p' along the blade in the time domain are shown from Fig. 2.26 to Fig. 2.33, with the same load cases as in the two previous sections. The green shaded area represent the region of occurrence of the VRS as predicted by 'p'. The figures show that the VRS only occurs at the outboard part of the blade and the VRS regions narrow down near the blade tip. The VRS occurs when the FOWT has downwind platform motions, which can be dominated by either surge or pitch motion. The VRS area predicted with 'p' completely encompasses that predicted with 'w'.

#### 2.5.4. Summary of regular wave load cases

The above analysis shows that the three different prediction criteria agree in that the VRS area increases significantly with a decrease in wind speed and an increase in wave steepness. Figure 2.34 and 2.35 further show the percentage of occurrence of the VRS for the OC3 Hywind Spar wind turbine with a wave steepness of  $\delta = 0.007$  and  $\delta = 0.01$ , respectively, over an operating time period of 1200s. The different colors show different wind speeds, while the symbols relate to the different VRS criteria: axial induction factor  $a$  ( $\circ$ ), Wolkovitch's criterion ( $\Delta$ ) and Peters' criterion ( $\times$ ). According to the criterion based on  $a \geq 1$ , the upper limits in terms of wind speeds for the VRS occurrence are  $V_\infty = 8m/s$  for  $\delta = 0.007$  and  $V_\infty = 9m/s$  for  $\delta = 0.01$ . The maximum percentage of VRS occurrence is 29.48% for  $\delta = 0.007$  and 30.14% for  $\delta = 0.01$ . Both

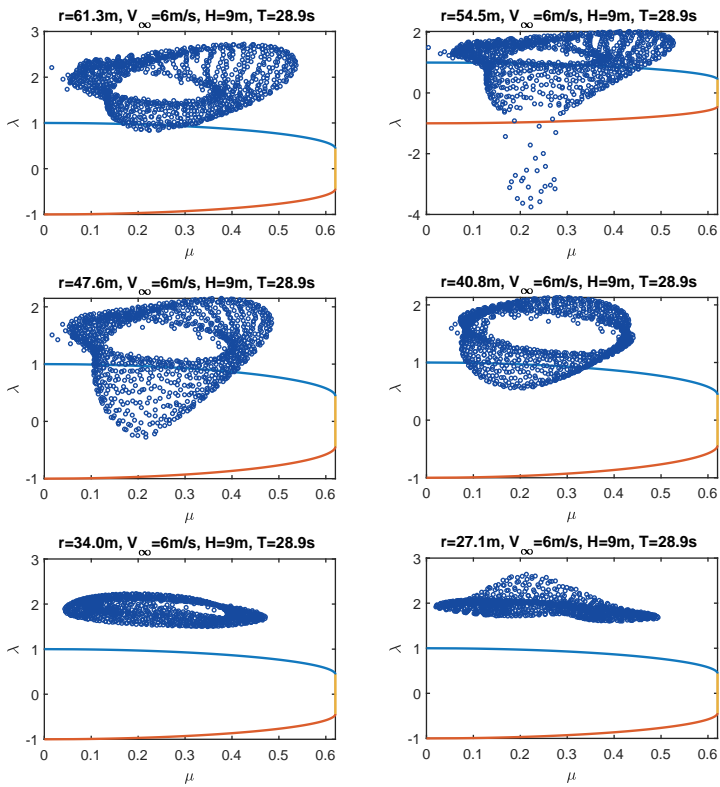


Figure 2.25: VRS predicted with 'p' criterion on blade nodes of OC3 wind turbine. The blue curve is the VRS boundary to the windmill state, the orange curve is the VRS boundary to propeller state, the yellow line corresponding to  $\mu = 0.62$

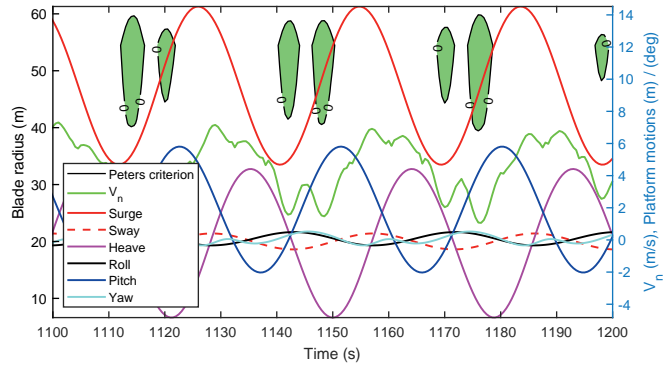


Figure 2.26: Regions of VRS according to 'p' (in green) together with  $V_n$  and platform motions (LCA-2-2)

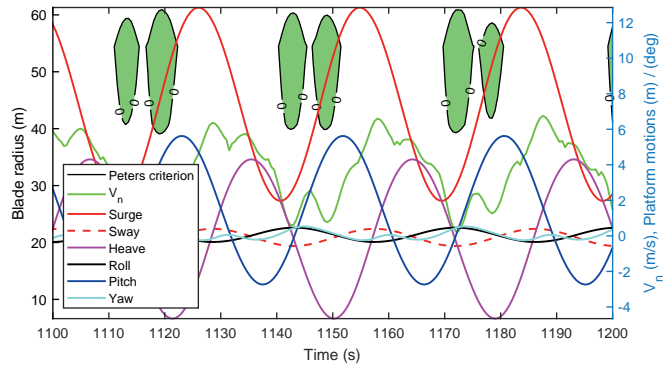


Figure 2.27: Regions of VRS according to 'p' (in green) together with  $V_n$  and platform motions (LCA-3-2)

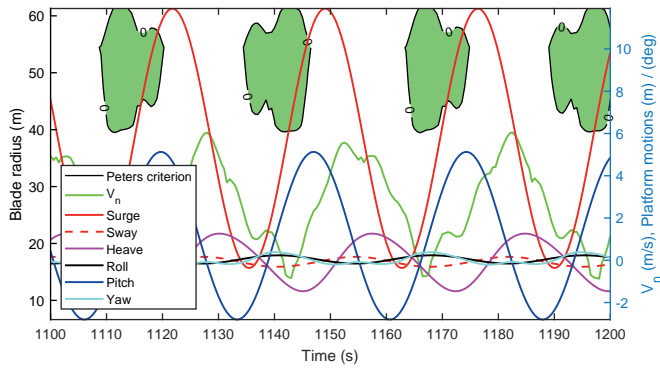


Figure 2.28: Regions of VRS according to 'p' (in green) together with  $V_n$  and platform motions (LCA-4-3)

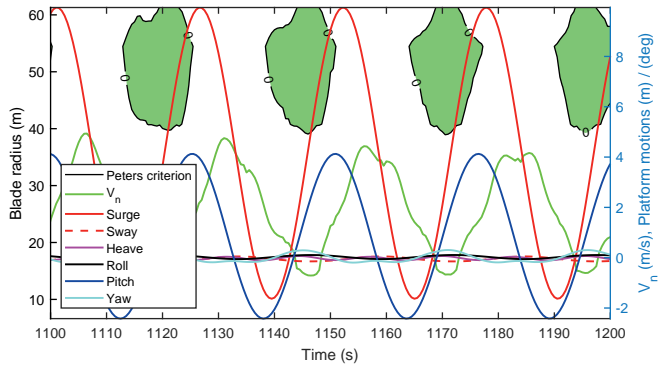


Figure 2.29: Regions of VRS according to 'p' (in green) together with  $V_n$  and platform motions (LCA-5-4)

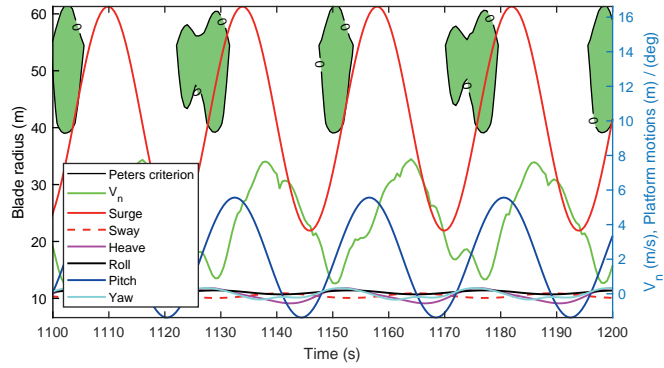


Figure 2.30: Regions of VRS according to 'p' (in green) together with  $V_n$  and platform motions (LCB-2-2)

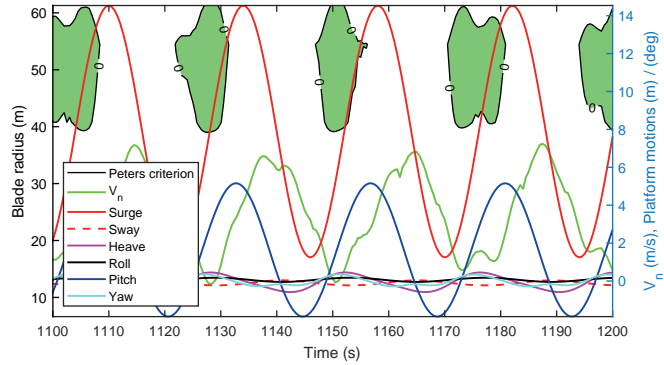


Figure 2.31: Regions of VRS according to 'p' (in green) together with  $V_n$  and platform motions (LCB-3-2)

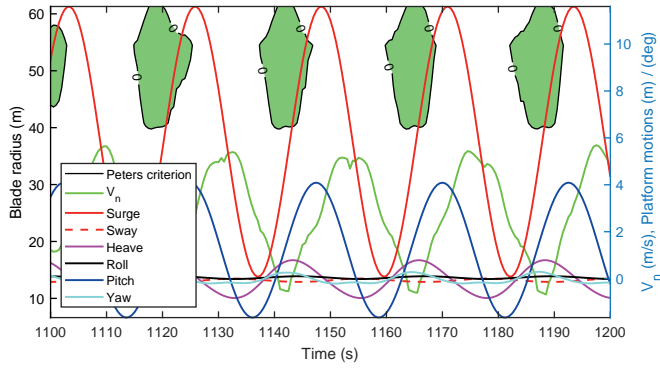


Figure 2.32: Regions of VRS according to 'p' (in green) together with  $V_n$  and platform motions (LCB-4-3)

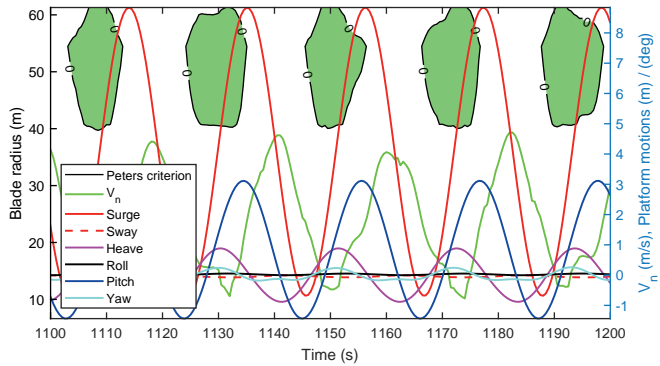


Figure 2.33: Regions of VRS according to 'p' (in green) together with  $V_n$  and platform motions (LCB-5-4)

these values occur when  $V_\infty = 4\text{m/s}$  and  $H_{rw} = 7\text{m}$ . According to Wolkovitch's criterion, the upper limit in terms of wind speeds for the VRS occurrence is  $V_\infty = 11\text{m/s}$  for both  $\delta = 0.007$  and  $\delta = 0.01$ . The maximum percentage for  $\delta = 0.007$  is 48.88% and for  $\delta = 0.01$  is 49.04%, and they both occur when  $V_\infty = 4\text{m/s}$  and  $H_{rw} = 7\text{m}$ . According to Peters' criterion, the upper limit in terms of wind speeds for the VRS occurrence is  $V_\infty = 12\text{m/s}$  for both  $\delta = 0.007$  and  $\delta = 0.01$ . The maximum percentage for  $\delta = 0.007$  is 50.96% and for  $\delta = 0.01$  is 50.79%, which both occur when  $V_\infty = 4\text{m/s}$  and  $H_{rw} = 7\text{m}$ .

It can also be noted that the VRS area predicted by Peters' criterion is larger than that predicted by Wolkovitch's criterion, which is also larger than that predicted by the criterion based on the axial induction factor. This is because the axial induction factor predicts the very center of the VRS, which is between the turbulent wake state and the propeller state at  $a = 0$ . By contrast, Wolkovitch's criterion predicts the VRS when the rotor enters the core of the vortex ring. Therefore, it covers a larger area than only  $a = 0$ . Finally, Peters' criterion leads to a larger region than Wolkovitch's criterion as it predicts the boundaries of the VRS region and not only the center of the region.

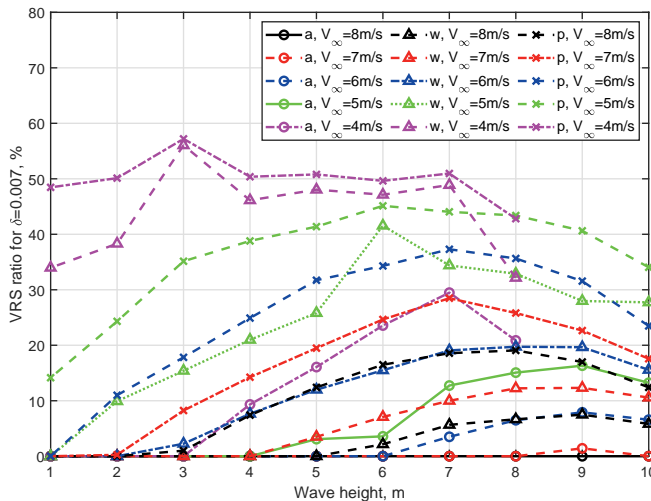


Figure 2.34: Percentages of occurrence of the VRS for a time interval of 1200s and a wave steepness  $\delta = 0.007$ .

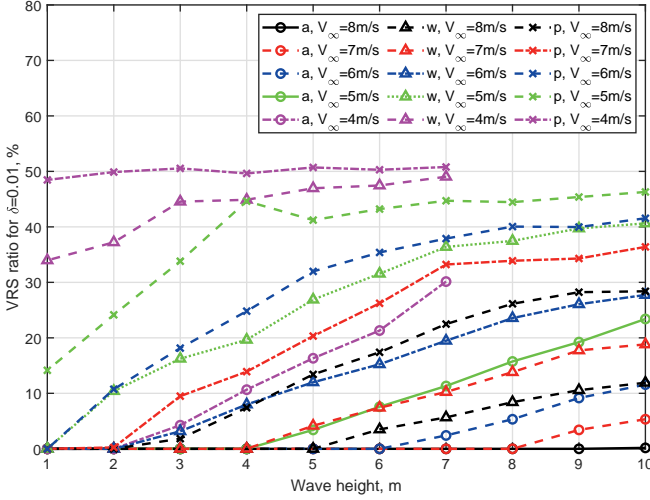


Figure 2.35: Percentages of occurrence of the VRS for a time interval of 1200s and a wave steepness  $\delta = 0.01$ .

### 2.5.5. Reduced frequency analysis

The reduced frequency,  $k$ , is a dimensionless parameter that can be used to characterise the level of unsteadiness in the flow. It is expressed as [12]

$$k = \frac{\omega c}{2V}, \tag{2.20}$$

where  $\omega$  is a disturbance frequency (in radians per second) taken as the weighted characteristic frequency of  $V_n$ ,  $c$  is the chord length of the airfoil under consideration, and  $V$  is the average relative flow velocity on the airfoil. The degree of flow unsteadiness is generally categorized via Table 2.6. Taking the regular wave load cases as an example, the reduced frequency  $k$  at the maximum VRS region (blade radius  $r \approx 55m$ ) is analyzed and the results are shown in Table 2.7. Above the red line are the load cases with VRS occurrence predicted with axial induction factor  $a$ , above the green line are the load cases with VRS occurrence predicted with Wolkovitch's criterion and above the brown line are the load cases with VRS occurrence predicted with Peters' criterion. From the results it can be seen that the reduced frequency  $k$  of all the design load cases lies in the region of quasi-steady flow according to Table 2.6, and the  $k$  values increase with an increase in wave frequency for the same wave steepness. This

Table 2.6: Degree of flow unsteadiness for different levels of reduced frequency,  $k$ 

Range	Flow type
$k = 0$	Steady
$0 < k \leq 0.05$	Quasi-steady
$0.05 < k \leq 0.2$	Unsteady
$k \geq 0.2$	Highly unsteady

is in agreement with the assumptions and findings available in the literature [48][22].

The VRS phenomenon is mainly driven by low frequency macroscopic floating motions and is not sensitive to the influence of high frequency motion. It should be noticed that for high frequency rotor motions, the BEM theory might not be applicable.

Table 2.7: The reduced frequency analysis of the design load cases.

Set A	$V_{\infty}$ [m/s]								Set B	$V_{\infty}$ [m/s]							
	8	7	6	5	4	3	2	1		8	7	6	5	4			
$H_{rw}$ (m)									$H_{rw}$ (m)								
10	0.012	0.011	0.011	0.011	-	10		0.009	0.009	0.009	0.009	0.009	0.009	0.009	0.009	0.009	-
9	0.010	0.010	0.010	0.010	-	9		0.008	0.009	0.009	0.009	0.009	0.009	0.009	0.009	0.009	-
8	0.009	0.010	0.009	0.009	-	8		0.009	0.009	0.009	0.009	0.009	0.009	0.009	0.009	0.008	
7	0.009	0.009	0.009	0.009	0.009	7		0.010	0.010	0.010	0.010	0.010	0.010	0.010	0.010	0.009	
6	0.010	0.010	0.010	0.009	0.009	6		0.010	0.010	0.010	0.010	0.010	0.010	0.010	0.010	0.010	
5	0.010	0.010	0.010	0.010	0.009	5		0.011	0.011	0.011	0.011	0.011	0.011	0.011	0.011	0.011	
4	0.011	0.011	0.010	0.011	0.011	4		0.010	0.011	0.011	0.011	0.011	0.011	0.011	0.011	0.012	
3	0.012	0.013	0.013	0.013	0.014	3		0.012	0.012	0.012	0.012	0.012	0.012	0.012	0.012	0.013	
2	0.012	0.013	0.016	0.016	0.014	2		0.014	0.014	0.014	0.014	0.014	0.014	0.014	0.014	0.015	
1	0.015	0.014	0.012	0.013	0.012	1		0.015	0.014	0.012	0.012	0.012	0.012	0.012	0.012	0.012	

T

## 2.6. Results for irregular wave load cases

### 2.6.1. NREL 5MW turbine mounted on a TLP

The examples of the VRS prediction results for the NREL 5MW turbine mounted on a TLP under irregular wave load cases are shown from Fig. 2.36 to Fig. 2.44 for the load cases LC1, LC16 and LC31, where the right axis in the figures represents the 6-DOF platform displacements with the units of either meter or degree. For the NSS load case (LC1), there is a large area of  $a > 0.5$  but no VRS predicted with the axial induction factor. With 'w', there are small areas of the VRS on the outboard of the blade, representing 11.74% of the time series. Finally, Peters' criterion lead to a larger area of the VRS on the outboard of the blade, representing 53.87% of the time series. In the ESS 1-Year load case (LC16), a small area of  $a > 1$  is shown representing 4.66% of the time, whilst 'w' gives a larger area representing a 39.22% of the time and 'p' leads to the largest area of the VRS representing 51.87% of the time. Similar trends can be found for the ESS 50-Year load case (LC31), with the percentages of occurrence of the VRS of 10.16%, 41.3% and 51.37% according to the 'a', 'w' and 'p', respectively. According to Table 2.3, the natural period of the surge motion for the TLP is 60.6s, which is larger than the wave periods of the load cases considered here (see Table 2.5) and the natural period of the pitch motion is 4.5s, which is smaller than the wave periods. The results show that the low frequency surge motion of the TLP platform is more sensitive to the wave loads than the high frequency pitch motion. A further sensitivity analysis could help to confirm this more broadly.

### 2.6.2. NREL 5MW turbine mounted on the ITI Energy Barge

The examples of the VRS prediction results for the NREL 5MW turbine mounted on the ITI Energy Barge under irregular wave load cases are shown from Figure 2.45 to Figure 2.53. For LC1, there is a large area of  $a > 0.5$  and smaller areas of  $a > 1$  with representing 5.83% of the time. The percentages become 40.38% and 56.62% based on 'w' and 'p', respectively. These percentages increase for LC16 to 21.32%, 49.46% and 54.87% based on 'a', 'w' and 'p', respectively. A similar trend is found with LC31, with percentages of 19.48%,

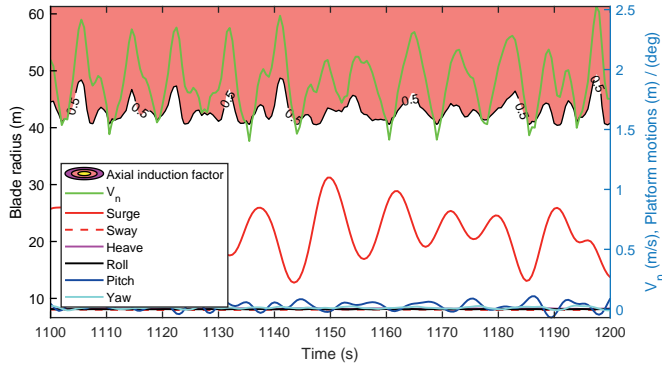


Figure 2.36: TLP with irregular waves (LC1): VRS predicted with 'a'.

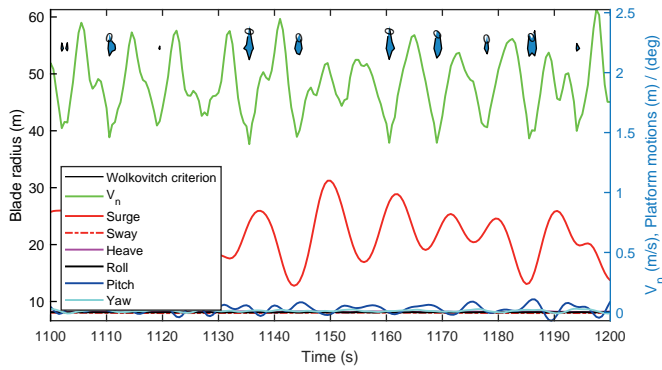


Figure 2.37: TLP with irregular waves (LC1): VRS predicted with 'w'.

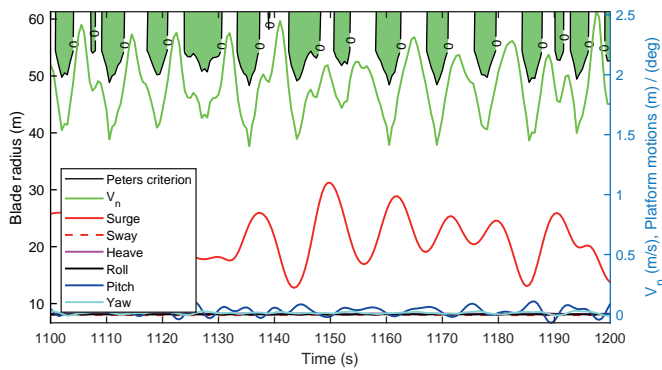


Figure 2.38: TLP with irregular waves (LC1): VRS predicted with 'p'.

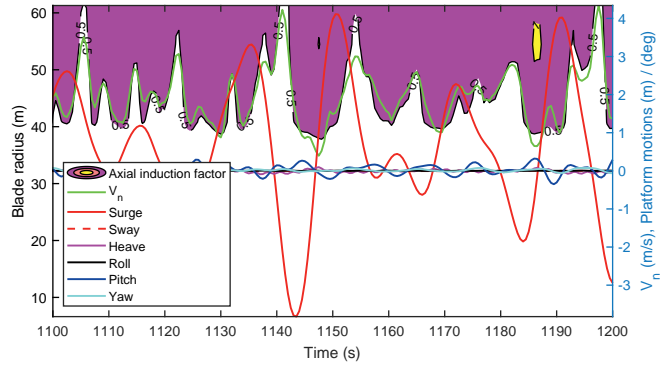


Figure 2.39: TLP with irregular waves (LC16): VRS predicted with 'a'.

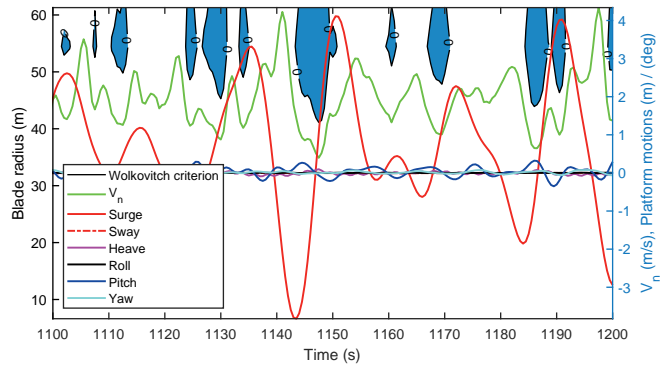


Figure 2.40: TLP with irregular waves (LC16): VRS predicted with 'w'.

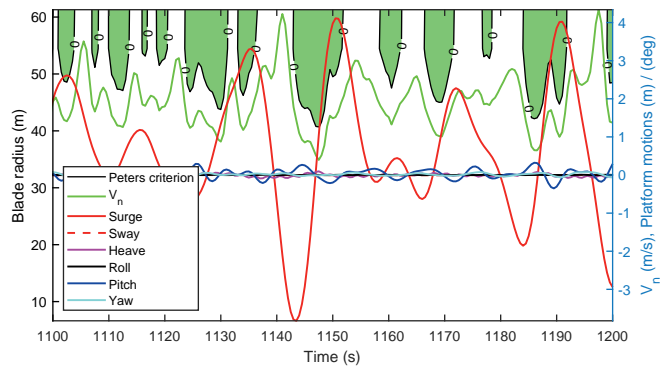


Figure 2.41: TLP with irregular waves (LC16): VRS predicted with 'p'.

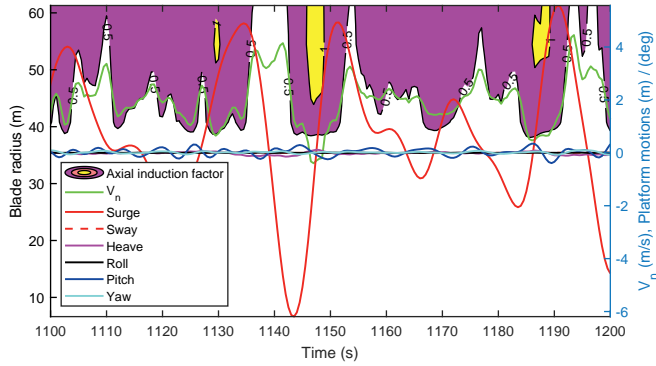


Figure 2.42: TLP with irregular waves (LC31): VRS predicted with 'a'.

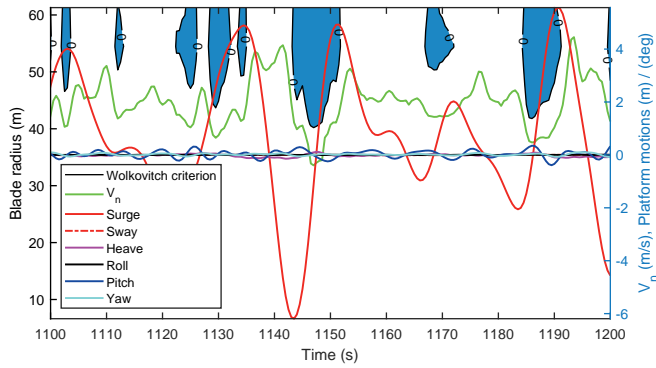


Figure 2.43: TLP with irregular waves (LC31): VRS predicted with 'w'.

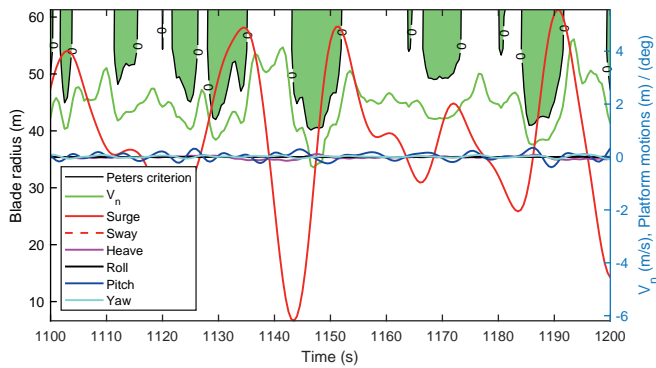


Figure 2.44: TLP with irregular waves (LC31): VRS predicted with 'p'.



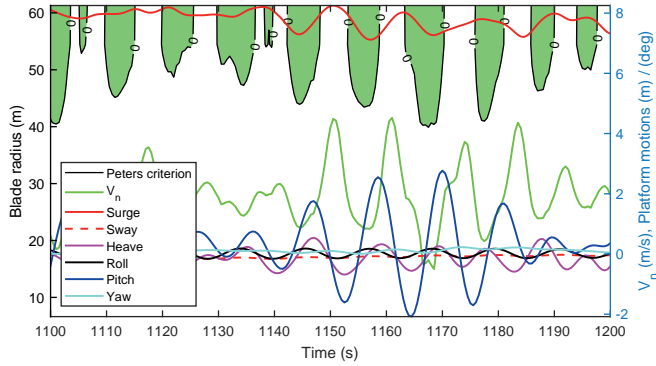


Figure 2.47: Barge with irregular waves (LC1): VRS predicted with 'p'.

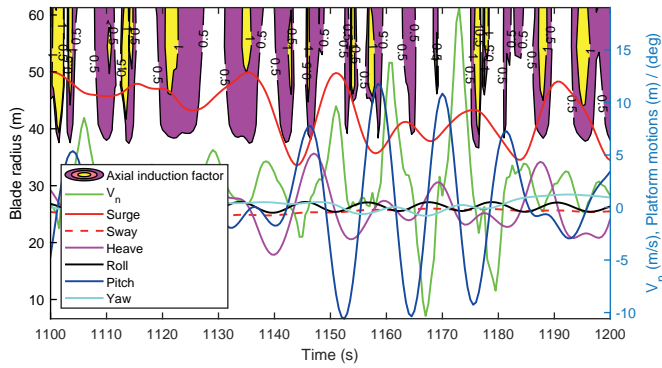


Figure 2.48: Barge with irregular waves (LC16): VRS predicted with 'a'.

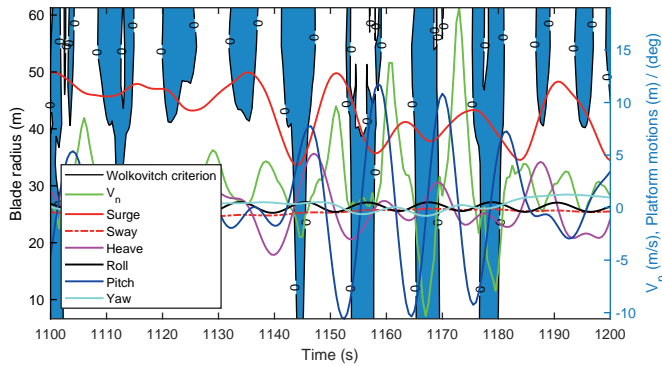


Figure 2.49: Barge with irregular waves (LC16): VRS predicted with 'w'.

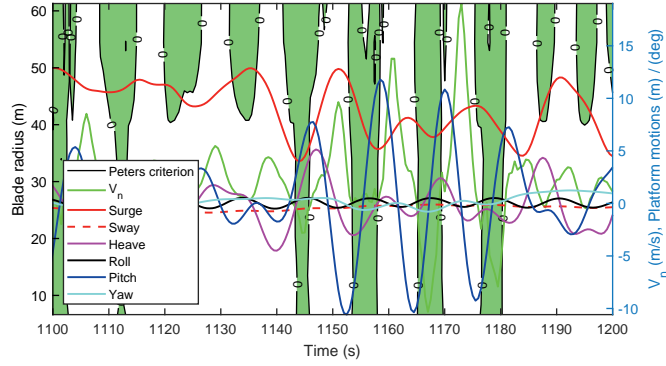


Figure 2.50: Barge with irregular waves (LC16): VRS predicted with 'p'.

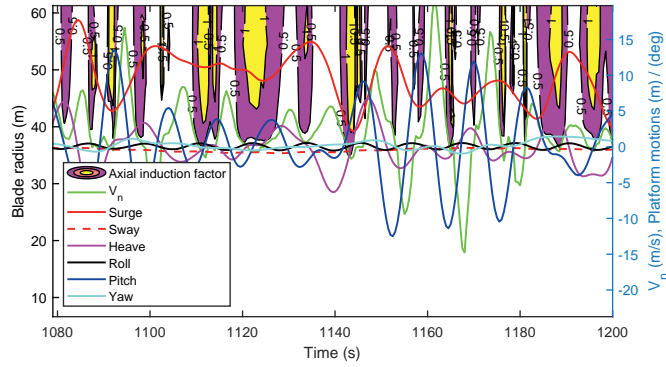


Figure 2.51: Barge with irregular waves (LC31): VRS predicted with 'a'.

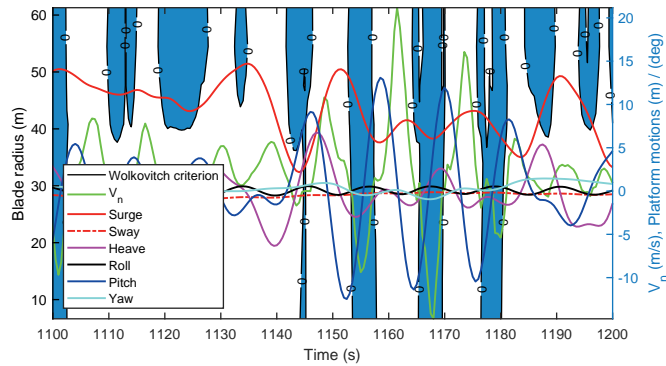


Figure 2.52: Barge with irregular waves (LC31): VRS predicted with 'w'.

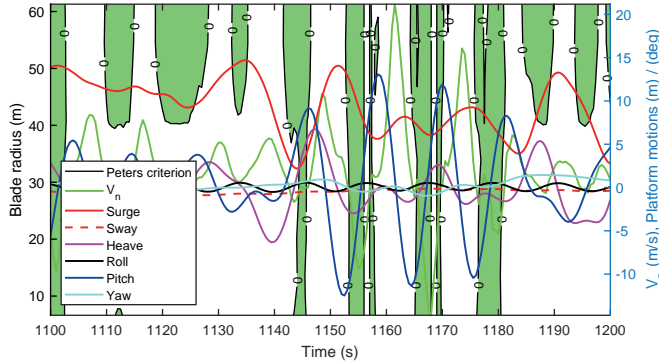


Figure 2.53: Barge with irregular waves (LC31): VRS predicted with 'p'.

### 2.6.3. NREL 5MW turbine mounted on the OC3-Hywind Spar

The examples of the VRS prediction results for the NREL 5MW turbine mounted on the OC3-Hywind Spar under irregular wave load cases are shown from Figure 2.54 to Figure 2.62. As for the TLP, the results based on the induction factor show no VRS for LC1. Based on 'w' and 'p', the percentages of occurrence of VRS are 18.07% and 53.96%, respectively. Again, the percentages increase with the load cases. Under LC16, these are 16.82%, 43.96% and 51.37% based on 'a', 'w' and 'p', respectively. For LC31, they are 21.23%, 45.05% and 52.21%, respectively. The natural periods of the surge and pitch motions for the OC3 spar are 125.0s and 29.2s, respectively, which are both larger than the wave periods of these load cases. The results show that the surge and pitch motions of the OC3-Hywind Spar platform are both sensitive to the wave loads.

### 2.6.4. Summary of the results under irregular wave load cases

Figure 2.63, Figure 2.64 and Figure 2.65 show the percentages of occurrence of the VRS for the different floaters under irregular wave state. The results show that the VRS mainly occurs for the design load cases in irregular wave states at low wind speeds. Generally speaking, for a given wind speed, the ESS 50-year load cases have a greater risk of leading to the VRS than the ESS 1-year load cases. The NSS load cases exhibit the smallest risk of VRS occurrence.

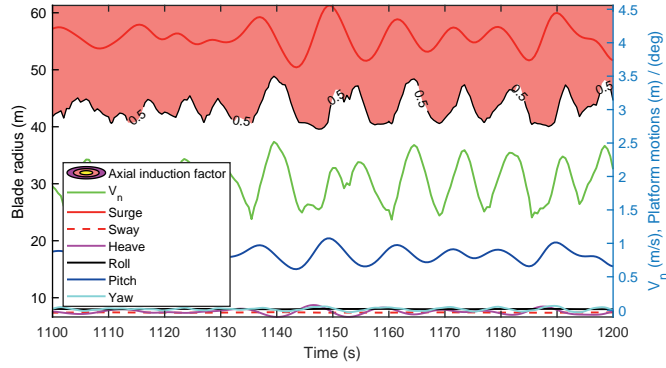


Figure 2.54: Spar with irregular waves (LC1): VRS predicted with 'a'.

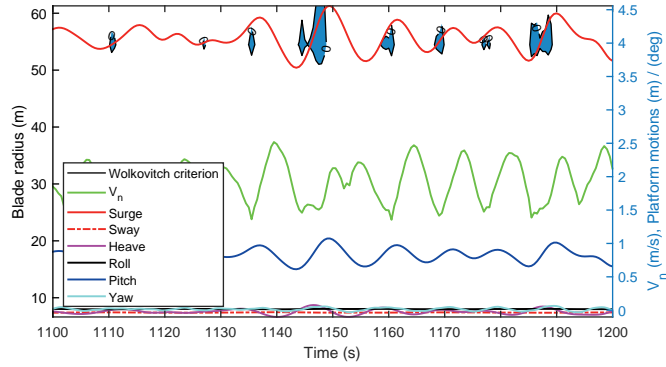


Figure 2.55: Spar with irregular waves (LC1): VRS predicted with 'w'.

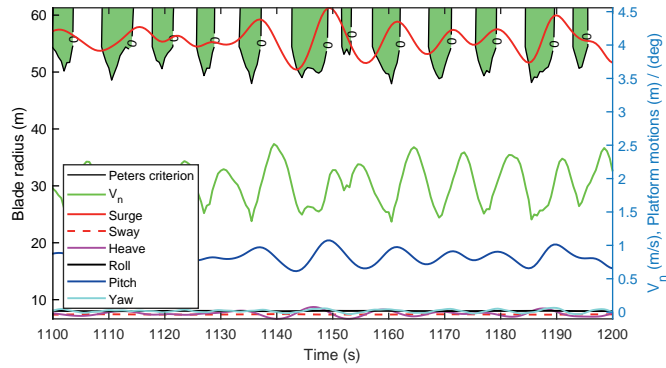


Figure 2.56: Spar with irregular waves (LC1): VRS predicted with 'p'.

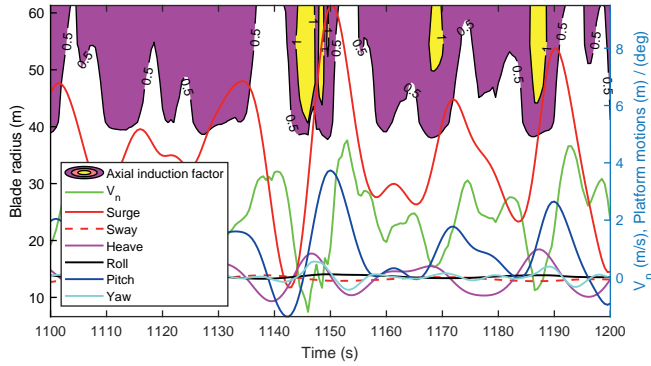


Figure 2.57: Spar with irregular waves (LC16): VRS predicted with 'a'.

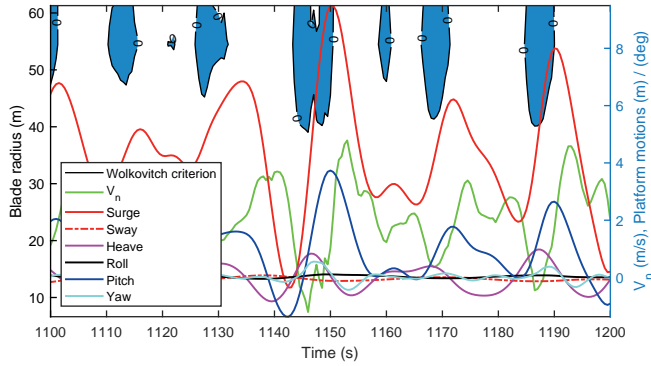


Figure 2.58: Spar with irregular waves (LC16): VRS predicted with 'w'.

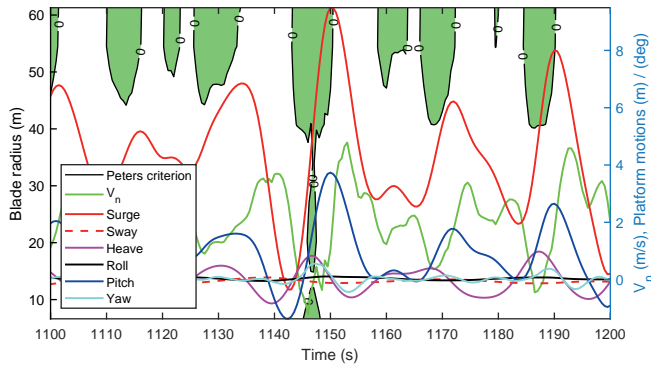


Figure 2.59: Spar with irregular waves (LC16): VRS predicted with 'p'.

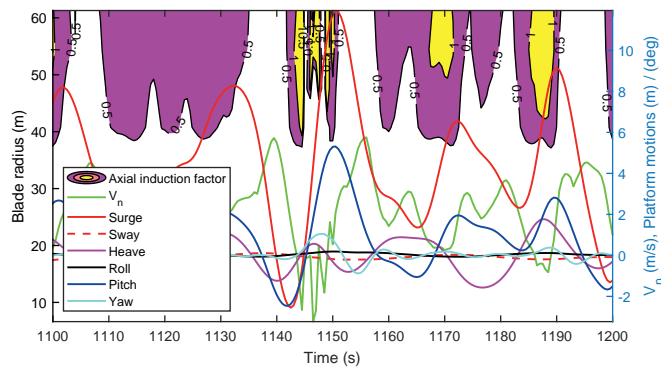


Figure 2.60: Spar with irregular waves (LC31): VRS predicted with 'a'.

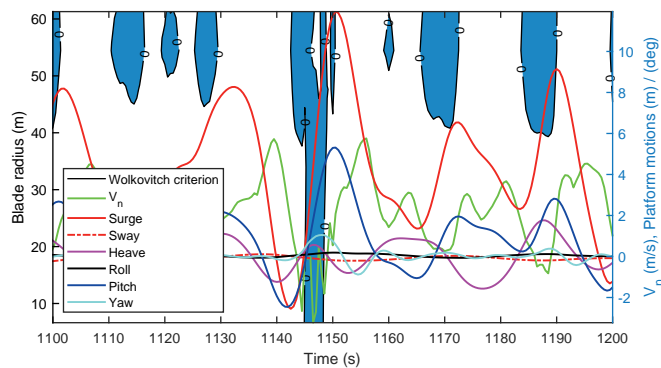


Figure 2.61: Spar with irregular waves (LC31): VRS predicted with 'w'.

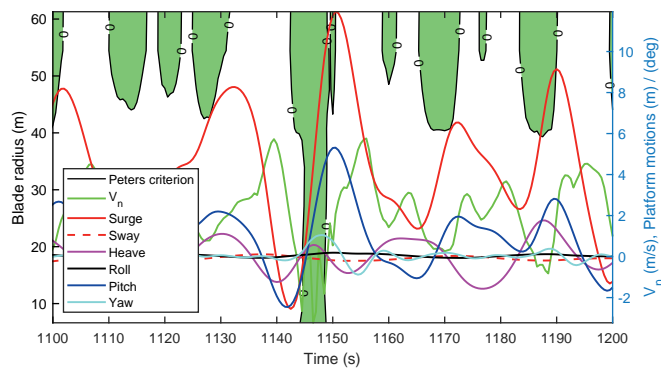


Figure 2.62: Spar with irregular waves (LC31): VRS predicted with 'p'.

Exceptions are when large  $V_n$  fluctuations occur for small wave heights. Also, the different floating foundations respond differently to the same load case. For example, the ITI Energy Barge is the most sensitive to waves, leading to a higher probability of occurrence of the VRS. By contrast, the TLP exhibits the least motion and has thus the smallest percentage of occurrence of the VRS of the three types of floating foundations. The VRS of floating offshore wind turbines is a periodic phenomenon, with an upper limit for the percentage of occurrence over time of around 50%.

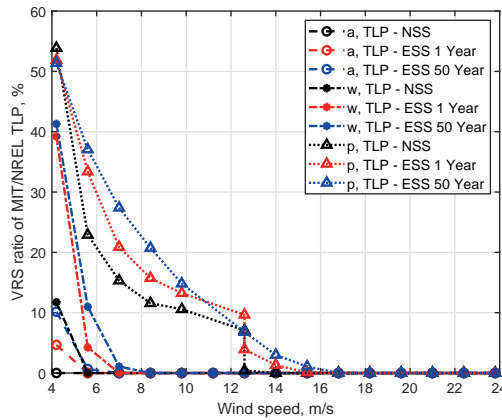


Figure 2.63: Percentages of VRS for the MIT/NREL TLP in irregular wave state.

The percentages of the VRS occurrence in operating time of OC3 wind turbine according to axial induction factor  $a$  are summarized in Table 2.8 ( $\delta = 0.007$ ) and Table 2.9 ( $\delta = 0.01$ ) for  $V_\infty = 4m/s$  to  $V_\infty = 8m/s$ , which are statistics of the data during an operation time of 1200s.

The percentages of the VRS occurrence in operating time of OC3 wind turbine according to Wolkovitch criterion are summarized in Table 2.10 ( $\delta = 0.007$ ) and Table 2.11 ( $\delta = 0.01$ ), which are statistics of the data during an operation time of 1200s.

The percentages of the VRS occurrence in operating time of OC3 wind turbine according to Peters criterion are summarized in Table 2.12 ( $\delta = 0.007$ ) and Table 2.13 ( $\delta = 0.01$ ) from  $V_\infty = 4m/s$  to  $V_\infty = 8m/s$ , which are statistics

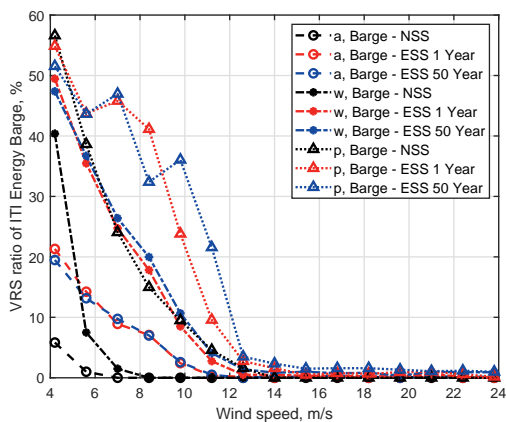


Figure 2.64: Percentages of VRS for the ITI Energy Barge in irregular wave state.

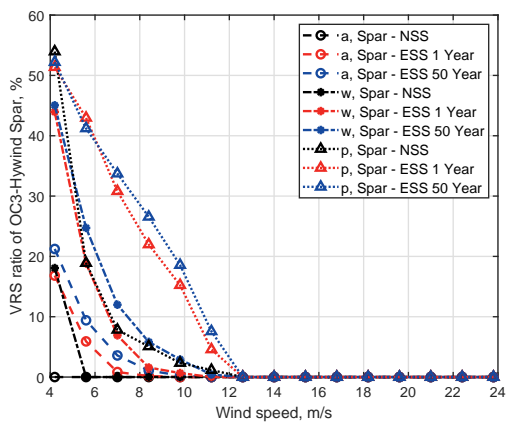


Figure 2.65: Percentages of VRS for the OC3-Hywind Spar in irregular wave state.

Table 2.8: Percentages of the VRS according to axial induction factor  $a$  with wave steepness  $\delta = 0.007$

$H$ [m]	10	9	8	7	6	5	4	3
$T$ (s)	30.50	28.89	27.24	25.48	23.59	21.54	19.26	16.68
$V_\infty$ [m/s]	The proportion of the VRS in time history (%)							
8 and above	0.00	0.00	0.00	0.00	0.00	0.00	0.00	0.00
7	0.01	1.42	0.00	0.00	0.00	0.00	0.00	0.00
6	6.58	7.91	6.49	3.50	0.00	0.00	0.00	0.00
5	13.24	16.32	15.07	12.74	3.58	3.08	0.00	0.00
4	-	-	20.87	29.48	23.56	16.07	9.33	0.00

Table 2.9: Percentages of the VRS according to axial induction factor  $a$  with wave steepness  $\delta = 0.001$

$H$ [m]	10	9	8	7	6	5	4	3
$T$ [s]	25.25	23.96	22.59	21.13	19.56	17.86	15.97	13.83
$V_\infty$ [m/s]	The proportion of the VRS in time history [%]							
9 and above	0.00	0.00	0.00	0.00	0.00	0.00	0.00	0.00
8	0.17	0.00	0.00	0.00	0.00	0.00	0.00	0.00
7	5.33	3.41	0.00	0.00	0.00	0.00	0.00	0.00
6	11.57	9.16	5.33	2.41	0.00	0.00	0.00	0.00
5	23.40	19.23	15.74	11.32	7.58	3.41	0.00	0.00
4	-	-	-	30.14	21.32	16.32	10.66	4.25

Table 2.10: Percentages of the VRS according to Wolkovitch criterion  $w$  with wave steepness  $\delta = 0.007$

$H$ [m]	10	9	8	7	6	5	4	3
$T$ [s]	30.50	28.89	27.24	25.48	23.59	21.54	19.26	16.68
$V_\infty$ [m/s]	The proportion of the VRS in time history [%]							
11 and above	0.00	0.00	0.00	0.00	0.00	0.00	0.00	0.00
10	0.25	0.83	0.00	0.00	0.00	0.00	0.00	0.00
9	2.66	4.08	3.16	1.42	0.00	0.00	0.00	0.00
8	5.83	7.49	6.66	5.66	2.16	0.00	0.00	0.00
7	10.57	12.32	12.24	9.99	7.08	3.50	0.00	0.00
6	15.57	19.65	19.73	19.07	15.49	11.99	7.66	2.25
5	27.73	27.98	32.89	34.39	41.55	25.81	20.98	15.40
4	-	-	32.15	48.88	47.13	48.04	46.13	56.04

Table 2.11: Percentages of the VRS according to Wolkovitch criterion  $w$  with wave steepness  $\delta = 0.01$

$H$ [m]	10	9	8	7	6	5	4	3
$T$ [s]	25.25	23.96	22.59	21.13	19.56	17.86	15.97	13.83
$V_\infty$ [m/s]	The proportion of the VRS in time history (%)							
11 and above	0.00	0.00	0.00	0.00	0.00	0.00	0.00	0.00
10	3.58	2.50	0.75	0.00	0.00	0.00	0.00	0.00
9	7.33	6.41	5.25	2.66	0.00	0.00	0.00	0.00
8	11.91	10.57	8.41	5.66	3.50	0.00	0.00	0.00
7	18.82	17.74	13.82	10.24	7.41	4.16	0.00	0.00
6	27.73	26.06	23.56	19.48	15.24	11.99	7.99	3.16
5	40.63	39.72	37.47	36.39	31.56	26.89	19.65	16.24
4	-	-	-	49.04	47.46	46.96	44.88	44.55

Table 2.12: Percentages of the VRS according to Peters criterion with wave steepness  $\delta = 0.007$ 

$H$ [m]	10	9	8	7	6	5	4	3
$T$ [s]	30.50	28.89	27.24	25.48	23.59	21.54	19.26	16.68
$V_\infty$ [m/s]	The proportion of the VRS in time history [%]							
12 and above	0.00	0.00	0.00	0.00	0.00	0.00	0.00	0.00
11	0.00	0.83	0.00	0.00	0.00	0.00	0.00	0.00
10	2.25	6.41	5.91	5.33	3.16	0.00	0.00	0.00
9	7.41	11.66	12.91	12.82	10.66	7.08	1.83	0.00
8	12.41	16.99	19.07	18.57	16.49	12.41	7.41	1.00
7	17.57	22.65	25.81	28.48	24.65	19.48	14.24	8.24
6	23.48	31.56	35.64	37.30	34.30	31.72	24.90	17.82
5	34.05	40.63	43.38	44.05	45.13	41.38	38.80	35.14
4	-	-	42.81	50.96	49.63	50.79	50.37	57.20

of the data during an operation time of 1200s.

### 2.6.5. Coefficient of variation analysis

The coefficient of variation,  $c_v$ , of the angle of attack (AoA) is evaluated in this section. The coefficient of variation is a dimensionless measure of dispersion of a probability distribution defined as the ratio of the standard deviation  $\sigma_v$  and the mean  $\mu_v$ , as

$$c_v = \left| \frac{\sigma_v}{\mu_v} \right|. \quad (2.21)$$

Since the change of AoA will directly change the lift and drag force on the blade, a frequent change in AoA can be related to a frequent fluctuation in aerodynamic loads on the blade. Here we discuss the load cases with wind speeds of 6m/s and 8m/s where no negative angles of attack are obtained along the whole blade of the bottom-mounted monopile wind turbine. The results are presented in Figure 2.66 for design load cases of set A and Figure 2.69-2.71 for design load cases of set B. In these figures, the prediction methods based on  $\mathbf{a}$ , Wolkovitch and Peters' criteria are denoted as ' $\mathbf{a}$ ', ' $\mathbf{w}$ ' and ' $\mathbf{p}$ ', respectively. The load cases with no VRS predicted are marked with '0'. Interesting observations can be

Table 2.13: Percentages of the VRS according to Peters criterion with wave steepness  $\delta = 0.01$ 

$H$ [m]	10	9	8	7	6	5	4	3
$T$ [s]	25.25	23.96	22.59	21.13	19.56	17.86	15.97	13.83
$V_\infty$ [m/s]	The proportion of the VRS in time history [%]							
12 and above	0.00	0.00	0.00	0.00	0.00	0.00	0.00	0.00
11	3.33	1.58	0.25	0.00	0.00	0.00	0.00	0.00
10	13.82	12.91	11.16	8.91	5.00	1.25	0.00	0.00
9	20.65	19.32	18.07	15.74	11.82	7.83	2.41	0.00
8	28.39	28.23	26.14	22.48	17.40	13.41	7.41	1.83
7	36.39	34.30	33.89	33.22	26.23	20.32	13.91	9.49
6	41.55	39.97	40.05	37.89	35.39	31.97	24.81	18.15
5	46.29	45.38	44.46	44.71	43.21	41.22	44.63	33.81
4	-	-	-	50.79	50.29	50.71	49.63	50.54

made. Firstly, the  $c_v$  of the AoA increases with the decrease in wind speed. Also, for the same wind speed, the  $c_v$  of the AoA increases with the increase in wave steepness. Secondly, with the same wind speed and wave steepness, the  $c_v$  of the AoA increases with the increase in wave height. Thirdly, the  $c_v$  of the bottom-mounted wind turbine always has a peak value in the middle of the blade (node 5), while the peak values of the  $c_v$  for the FOWT shifts to the VRS region outboard of the blade (node 6). This agrees with Leishman's finding that, during the VRS, the level of thrust fluctuations is high [16]. Fourthly, the higher the  $c_v$ , the higher the chance of occurrence of the VRS. It is found that if the VRS occurs at a certain value of  $c_v$ , then the VRS also occurs when  $c_v$  is higher than that value. In Figures 2.66-2.71, the peak  $c_v$  of load cases where the VRS occurs according to 'a', 'w' and 'p' for the first time are marked in each case.

For the load cases with  $V_\infty = 6\text{m/s}$  and  $\delta = 0.007$ , the peak of  $c_v$  for the bottom-mounted turbine is 36%, the VRS is predicted with 'a', 'w' and 'p' with the peak  $c_v$  values above 95%, 44% and 31% respectively. For the load cases with 7m/s wind speed and 0.007 wave steepness, the peak of  $c_v$  for the

bottom-mounted turbine is 16%, the VRS is predicted with 'a', 'w' and 'p' with the peak  $c_v$  values above 64%, 48% and 23% respectively. For the load cases with 8m/s wind speed and 0.007 wave steepness, the peak of  $c_v$  for the bottom-mounted turbine is 13%, the VRS is predicted with 'w' and 'p' with the peak  $c_v$  values above 46% and 26% respectively, while no VRS is predicted with 'a'. The  $c_v$  of the bottom-mounted turbine is only influenced by wind speeds. For the load cases with 6m/s wind speed and 0.01 wave steepness, the VRS is predicted with 'a', 'w' and 'p' with the peak  $c_v$  values above 97%, 45% and 31% respectively. For the load cases with  $V_\infty = 7m/s$  and  $\delta = 0.01$ , the VRS is predicted with 'a', 'w' and 'p' with the peak  $c_v$  values above 87%, 50% and 22% respectively. For the load cases with 8m/s wind speed and 0.01 wave steepness, the VRS is predicted with 'a', 'w' and 'p' with the peak  $c_v$  values above 73%, 49% and 27% respectively.

Here we can see that 'a' leads to a  $c_v$  between 64% and 97%, 'w' gives  $c_v$  between 44% and 50%, and 'p' leads to a  $c_v$  between 22% and 31%. Thus it can be concluded that the induction factor 'a' is a very conservative method for the prediction of the VRS, as the  $c_v$  for this prediction method is almost 3 to 4 times that of the bottom-mounted monopile wind turbine. However, it is a good quantity to assess when the BEM theory breaks down. By contrast, 'p' is the least conservative of the three prediction methods, and can sometimes lead to a value of  $c_v$  that is lower than that of the bottom-mounted wind turbine. Finally, 'w' shows the strongest relationship with the value of  $c_v$ , where the VRS is predicted with the peak  $c_v$  consistently above approximately 40% and is clearly different from that of the monopile wind turbine. Accordingly, Wolkovitch's criterion is the most suitable for the VRS prediction, while Peters' criterion indicates the initial aerodynamic change and is therefore more suitable for early warning of the occurrence of the VRS during the operation of FOWTs.

## 2.7. Conclusions

In this chapter, the vortex ring state prediction criteria reported in the literature for helicopter rotors are adapted to floating offshore wind turbines. In particular, three criteria are derived: the axial induction factor, Wolkovitch's criterion and Peters' criterion. These criteria are then applied to the results of

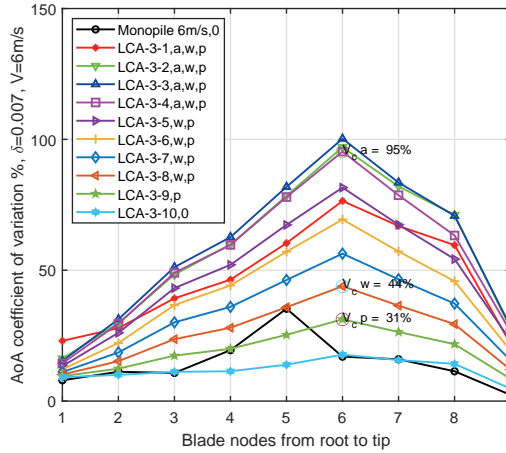


Figure 2.66: AoA coefficient of variation %,  $\delta = 0.007$ ,  $V = 6m/s$ .

a BEM model to simulate the dynamics of a floating wind turbine moving in 6 degrees-of-freedom. The results show that the type of floating foundation has a significant influence on the aerodynamic behaviour of the rotor. As expected, the TLP exhibits the least motion, and therefore, also the least probability of occurrence of the VRS. Also, the probability of occurrence of the VRS generally increases with the magnitude of the wave height, except in cases where the relative wind velocity normal to the rotor exhibits large fluctuations. However, importantly, for all the platform types, the turbine presents a risk of experiencing the vortex ring state even under normal sea states. This study demonstrates the possible occurrence of the VRS in floating wind turbines. In the following chapters, more insights will be gained on the different working states of a floating rotor using a free wake vortex ring method.

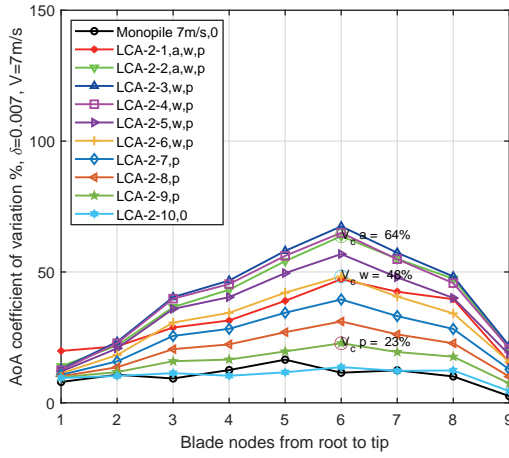


Figure 2.67: AoA coefficient of variation %,  $\delta = 0.007$ ,  $V = 7 \text{ m/s}$ .

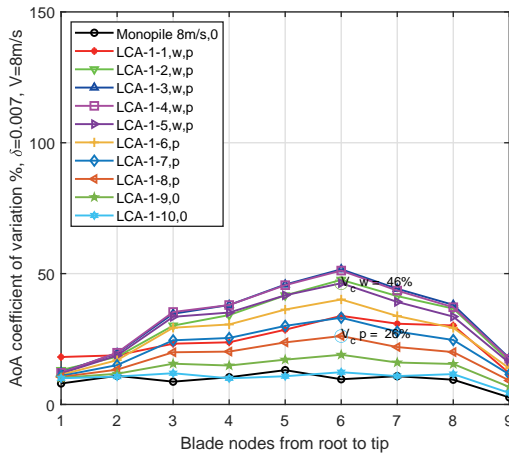


Figure 2.68: AoA coefficient of variation %,  $\delta = 0.007$ ,  $V = 8 \text{ m/s}$ .

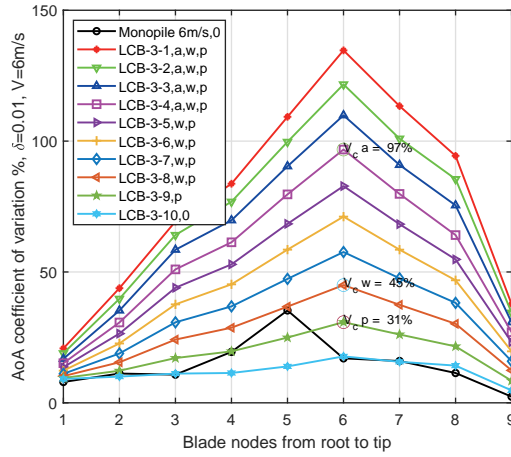


Figure 2.69: AoA coefficient of variation %,  $\delta = 0.01$ ,  $V = 6m/s$ .

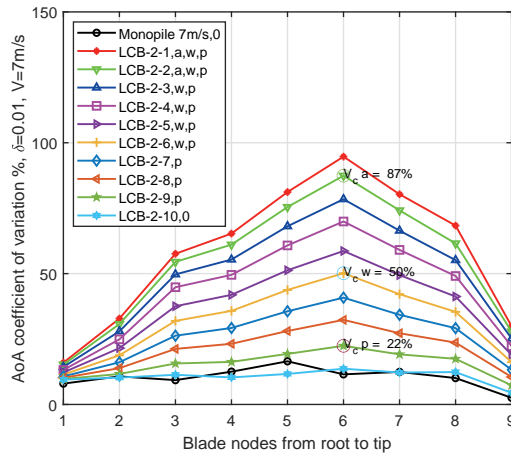


Figure 2.70: AoA coefficient of variation %,  $\delta = 0.01$ ,  $V = 7m/s$ .

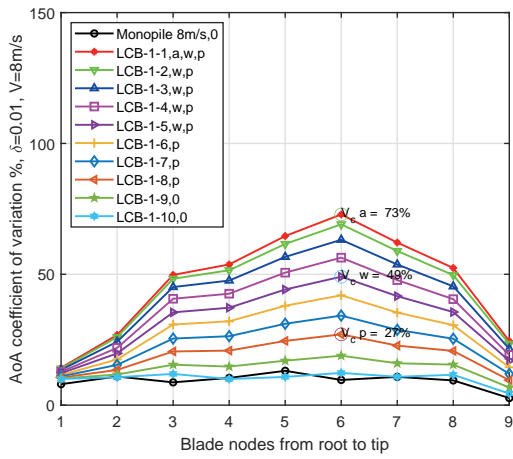


Figure 2.71: AoA coefficient of variation %,  $\delta = 0.01$ ,  $V = 8m/s$ .



# 3

## The free wake vortex ring method

工欲善其事，必先利其器。—《论语》

To do a good job, one must first sharpen one's tools.

The Analects of Confucius

A modified free-wake vortex ring model is proposed to compute the aerodynamics of floating horizontal-axis wind turbines. The model is divided into two parts. The near wake model uses a blade-bound vortex model and trailing vortex model, which is developed based on the vortex filament method. By contrast, the far wake model is based on the vortex ring method. The proposed model is a good compromise between accuracy and computational cost, for example when compared with more complex vortex methods.

### 3.1. Introduction

Simulation tools that can accurately evaluate the relationship between the aerodynamic loads on the rotor and the platform motion are required especially for off-design conditions or novel concepts. So far, the available aero-hydro coupled analysis tools are almost exclusively based on blade element momentum (BEM) theory, which is derived for steady state conditions and is believed to have limited applicability when the rotor interacts with its own wake. The previous chapter showed the existence of the VRS for floating offshore wind turbines, in agreement with earlier works on the subject, see for example Sebastian [12]. In this context, an alternative to BEM is required. One option is to use computational fluid dynamics (CFD) models that solve the Navier-Stokes equations and describe the flow physics with higher levels of detail. However, they are computationally expensive when dealing with the fully-coupled dynamics of FOWTs. Another approach, that is more accurate than momentum theory and less costly than CFD, is to use so-called vortex methods. Vorticity-based methods have a number of different formulations, ranging from simple analytical models to more advanced numerical methods (Branlard [10]). Also the computational cost of vortex models depends on the number of vortex elements and the interaction between the elements, ranging from relatively cheap models to more expensive ones (Bhagwat [49], Gohard [50]). Rotating wind turbines generate bound circulations on the blades, which in turn create vorticity in the wakes. The vorticity generated by the blade rotation is assumed to be concentrated on lifting lines, with distributed vortex strengths representing the bound circulation. The vorticity is then convected in the wake as shed and trailing vorticity. The shed vorticity is the vorticity emitted in the wake due to the time change of the bound circulation, whilst the trailing vorticity results from the spanwise change in bound circulation (Branlard [10]). Within the scope of simplified vorticity models for rotors, the wake flow can be represented by vortex filaments such as the free wake vortex filament (FWVF) method of Sebastian [51], vortex particles such as the nonlinear vortex lattice method (NVLM) method of Lee [52], or a vortex ring model. As for the vortex ring methods, the wake is modeled by vortex rings, each carrying a constant circulation determined by the aerodynamic loads on the rotor. Each ring is a vortex element which induces

velocity on both the rotor and the other rings in the field. Thus, the radius and spacing of the rings vary as the latter move downstream in the wake. This is the so-called free wake vortex ring method. In this method, the analytical solution of the induced velocity of an axisymmetric vortex ring derived from the Biot-Savart law (Newman [53], Yoon [54]) can be directly used to calculate the induced velocities in the wake as well as on the rotor. This reduces computation cost whilst retaining the basic physical properties in the wake.

The simplest vortex ring methods available in the literature represent the rotor with an actuator disc, whilst the wake is modelled as vortex rings released at the tip of the rotor (Øye [55], de Vaal [48], Yu [56]). These models are used to calculate unsteady aerodynamic loads on both fixed and moving rotors. However, some aerodynamic features such as angle of attack, and lift and drag forces on the rotor cannot be accurately reproduced due to the limitations associated with the actuator disc concept. A modeling method that represents the rotor blades with lifting lines, the near wake as a series of straight vortex lines and the far wake by vortex rings was initially suggested by Miller [57]. It relates the blade bound vortex strength with the vortex ring strength in the wake. In this case, the rotor loads are also dependent on the induced velocities from the vortex rings. Afjeh [58] and de Vaal [59, 60] adapted and improved this method to the modeling of wind turbines. Good agreement was achieved when comparing the numerical results with measurement data.

The free wake vortex ring method (FWVR) discussed in this chapter is based on that initially proposed by de Vaal [60] and is applied to the aerodynamic analysis of a horizontal-axis wind turbine. It combines the three-dimensional vortex lifting law with blade element theory, which can accurately and effectively predict the blade load using the time-evolution of the induced velocities. It also splits the wake into near wake and far wake, leading to more realistic velocities on the blade and in the far-field. However, the application of de Vaal's original method [60] can be challenging for some working states. This is for example the case of small or negative angles of attack at low wind speeds, or blade pitching motions at high wind speeds. In this chapter, we present a few modifications of the original method to overcome these challenges. Firstly, the propagation process of the vortex rings is modified and different nonlinear iter-

ation methods are tested to solve the blade bound vortex strengths. Secondly, the near-wake trailing vortex model uses finite length vortex segments instead of semi-infinite vortex lines, which makes the near wake model physically more realistic. The chapter also discusses the transition between near- and far-wake models, as well as the calculation of the self-induced velocity. The proposed free wake vortex model is validated by analyzing the aerodynamic parameters on the NREL 5MW wind turbine with a bottom-mounted monopile foundation as well as floating platforms with prescribed rigid body motions, that are typical of wave induced motions for different types of floating foundations, i.e. ITI barge, OC3-Hywind spar-buoy (OHS), and tension leg platform (TLP). Results are compared with those obtained from the blade element momentum (BEM) theory, the Reynolds-averaged Navier–Stokes (RANS) method of Sørensen [61] and two more computationally expensive vortex based aerodynamic models- the FWVF method of Sebastian [51] and the NVLM method of Lee [52].

The chapter is organized as follows. The theory of the modified free wake vortex ring method is described in Section 3.2. The numerical modeling method is described and verified in Section 3.3. The computational time efficiency of this method is evaluated in Section 3.4. Finally, conclusions are drawn in Section 3.5.

## 3.2. Vortex Ring Theory

As mentioned before, the simplified free wake vortex ring method discussed in this chapter consists of two parts: the near wake model and the far wake model. The induced velocities of the near wake model are calculated based on Biot-Savart’s law, as described in section 3.2.1. To keep a low computational cost, the far wake model is represented by the axisymmetric vortex rings as introduced in section 3.2.2.

### 3.2.1. Velocity induced by a vortex filament

The velocity  $\mathbf{V}_P$  induced by a vortex filament with a constant strength  $\Gamma$  in the field at a point  $P$  can be expressed by the Biot-Savart law as [62]

$$\mathbf{V}_P = -\frac{\Gamma}{4\pi} \int_{C(q)} \frac{\mathbf{r}_P - \mathbf{r}_q}{|\mathbf{r}_P - \mathbf{r}_q|^3} \times \frac{\partial \mathbf{r}_q}{\partial q} dq, \quad (3.1)$$

where  $\mathcal{C}(q)$  is the parametric curve which describes the path of the vortex filament,  $\mathbf{r}_P$  is the position vector of the point  $P$ ,  $\mathbf{r}_q$  is the position vector of a point  $Q$  on the filament,  $\mathbf{r} = \mathbf{r}_P - \mathbf{r}_q$  is the vector pointing from point  $Q$  to point  $P$ , and  $\frac{\partial \mathbf{r}_q}{\partial q}$  is the partial derivative of  $\mathbf{r}_q$  with respect to the filament parameter. In Eq. (3.1) the kernel of Biot-Savart operator is identified as

$$\mathbf{K}(\mathbf{r}) = -\frac{1}{4\pi} \frac{\mathbf{r}}{|\mathbf{r}|^3}, \quad (3.2)$$

and it is singular when the point  $P$  is on the vortex filament  $\mathcal{C}(q)$ . To avoid this singularity problem, a smoothing method proposed by Hoydonck et al [63] is used. It replaces the singular Biot-Savart kernel  $\mathbf{K}(\mathbf{r})$  with a desingularized kernel  $\mathbf{K}_\sigma(\mathbf{r})$ , defined as

$$\mathbf{K}_\sigma(\mathbf{r}) = -\frac{g(\sigma)}{|\mathbf{r}|^3} \mathbf{r}, \quad (3.3)$$

where  $\sigma$  is the non-dimensionalised length between the point  $P$  and a point on the filament, and  $g(\sigma)$  is a three-dimensional velocity smoothing function [63]. Here, the Rosenhead-Moore velocity smoothing function is used, i.e.

$$g(\sigma) = \frac{\sigma^3}{4\pi(\sigma^2 + 1)^{\frac{3}{2}}}. \quad (3.4)$$

This leads to the following induction velocity,

$$\mathbf{V}_P = \Gamma \int_{\mathcal{C}(q)} \mathbf{K}_\sigma(\mathbf{r}) \times \frac{\partial \mathbf{r}_q}{\partial q} dq. \quad (3.5)$$

Considering a straight line vortex filament, as shown in Fig. 3.1, the parametric curve of the filament is given by  $\mathbf{C}(q) = \mathbf{x}_1 + q(\mathbf{x}_2 - \mathbf{x}_1)$ , with  $0 \leq q \leq 1$ . Thus the desingularized kernel  $\mathbf{K}_\sigma(\mathbf{r})$  can be expressed as

$$\mathbf{K}_\sigma(\mathbf{r}) = -\frac{\mathbf{x}_P - \mathbf{C}(q)}{4\pi(|\mathbf{x}_P - \mathbf{C}(q)|^2 + r_c^2)^{\frac{3}{2}}} = -\frac{\mathbf{x}_P - (1-q)\mathbf{x}_1 + q\mathbf{x}_2}{4\pi(|\mathbf{x}_P - (1-q)\mathbf{x}_1 + q\mathbf{x}_2|^2 + r_c^2)^{\frac{3}{2}}}, \quad (3.6)$$

where  $r_c$  is the vortex core radius. Accordingly, the induced velocity  $\mathbf{V}_P$  can be expressed as

$$\mathbf{V}_P = -\Gamma \int_0^1 \frac{\mathbf{x}_P - (1-q)\mathbf{x}_1 + q\mathbf{x}_2}{4\pi(|\mathbf{x}_P - (1-q)\mathbf{x}_1 + q\mathbf{x}_2|^2 + r_c^2)^{\frac{3}{2}}} \times (\mathbf{x}_2 - \mathbf{x}_1) dq. \quad (3.7)$$

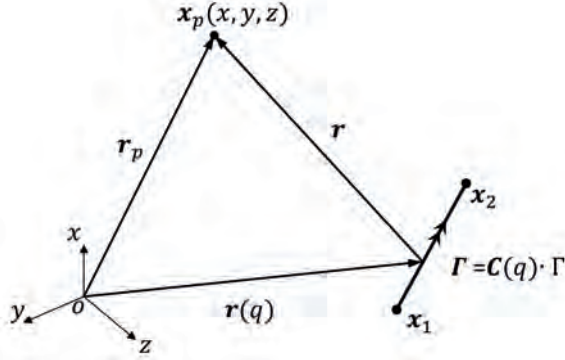


Figure 3.1: Straight line vortex filament induction.

When the point  $x_2$  extends to infinity, the straight line vortex filament becomes a semi-infinite line. In this case, the upper limit of  $q = \tilde{q}$  extends to infinity, and the induced velocity  $\mathbf{V}_p$  becomes

$$\mathbf{V}_p = -\Gamma \lim_{\tilde{q} \rightarrow \infty} f(q), \quad (3.8)$$

$$f(q) = \int_0^{\tilde{q}} \frac{\mathbf{x}_p - (1-q)\mathbf{x}_1 + q\mathbf{x}_2}{4\pi(|\mathbf{x}_p - (1-q)\mathbf{x}_1 + q\mathbf{x}_2|^2 + r_c^2)^{\frac{3}{2}}} \times (\mathbf{x}_2 - \mathbf{x}_1) dq. \quad (3.9)$$

### 3.2.2. Velocity induced by an axis-symmetric vortex ring

Considering an ideal vortex ring with radius  $R$  as shown in Fig. 3.2, its parametric curve  $C(\chi)$  as a function of an angle  $\chi$  can be expressed as

$$C(\chi) = R(\cos\chi, \sin\chi, 0), \quad \chi \in [0, 2\pi]. \quad (3.10)$$

Since the vortex ring is axis-symmetric, its local vortex ring coordinate system  $x'y'z'$  can be adjusted according to the location of the field point  $P$ . Here, the coordinates of  $P$  are  $(x'_p, 0, z'_p)$  and  $C(\chi)$  is in the  $x'y'$ -plane and centered at the origin of the  $z'$ -axis. Thus, taking the notation  $x'_p = \xi R$  and  $z'_p = \zeta R$ , we have

$$\mathbf{r}(\chi) = R(\cos\chi, \sin\chi, 0), \quad (3.11)$$

$$\mathbf{r}_p = R(\xi, 0, \zeta), \quad \xi \in (0, +\infty), \zeta \in (-\infty, +\infty). \quad (3.12)$$

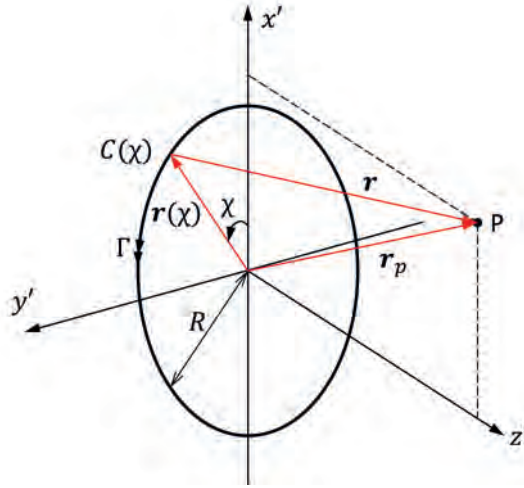


Figure 3.2: Coordinate system associated with a vortex ring.

The displacement vector  $\mathbf{r}$  is thus given by

$$\mathbf{r} = \mathbf{r}_p - \mathbf{r}(\chi) = R(\xi - \cos\chi, -\sin\chi, \zeta). \quad (3.13)$$

The velocity induced by a vortex ring at a point  $P$  is then obtained by substituting the above equations into Eq. (3.5), which yields:

$$\mathbf{V} = -\frac{\Gamma}{4\pi R} \int_0^{2\pi} \frac{(\zeta \cos\chi, \zeta \sin\chi, 1 - \xi \cos\chi)}{(1 + \xi^2 + \zeta^2 + \sigma^2 - 2\xi \cos\chi)^{\frac{3}{2}}} d\chi, \quad (3.14)$$

An analytical result of this integral has been derived as [53][54]

$$V_x = \frac{\Gamma}{2\pi RC_0} \left[ -K(m) + \frac{1 + \xi^2 + \zeta^2}{C_1^2} E(m) \right] \frac{\zeta}{\xi}, \quad (3.15)$$

$$V_z = \frac{\Gamma}{2\pi RC_0} \left[ K(m) + \frac{1 - \xi^2 - \zeta^2}{C_1^2} E(m) \right], \quad (3.16)$$

with

$$C_0^2 = 1 + 2\xi + \xi^2 + \zeta^2 + \sigma^2, \quad (3.17)$$

$$C_1^2 = 1 - 2\xi + \xi^2 + \zeta^2 + \sigma^2, \quad (3.18)$$

and the functions  $K(m)$  and  $E(m)$  being the first and second type of complete elliptic integrals, respectively, with  $m$  defined as:

$$m = \frac{4\xi}{C_0^2}. \quad (3.19)$$

It should be noted that Eqs. (3.15) and (3.16) can only be used in the local vortex ring coordinate system  $x'y'z'$ . Let us consider a global coordinate system  $xyz$ , with its origin  $O$  located at the center of the rotor disc (at the wind turbine's stable upright position), the  $x$ -axis pointing vertically upwards, opposite to gravity, the  $y$ -axis pointing to the left when looking in the nominal downwind direction, and the  $z$ -axis pointing in the nominal ( $0^\circ$ ) downwind direction. To compute the velocity induced at a control point  $P$ , with coordinate  $\mathbf{X}_P$  in the global coordinate system, a coordinate transformation needs to be applied. First, the global coordinate  $\mathbf{X}_P$  is transformed into the local coordinate  $\hat{\mathbf{X}}_P$  as

$$\hat{\mathbf{X}}_P^{xyz} = \underbrace{\mathbf{M}_{roll}(\gamma)\mathbf{M}_{pitch}(\chi)\mathbf{M}_{yaw}(\beta)}_{\text{rotation transformation}} \underbrace{(\mathbf{X}_P^{xyz} - \mathbf{X}_\delta^{xyz})}_{\text{translation transformation}}, \quad (3.20)$$

where  $\mathbf{X}_P^{xyz} = (x_P, y_P, z_P)$  is the coordinate of  $P$  in the original coordinate frame,  $\hat{\mathbf{X}}_P^{xyz} = (\hat{x}_P, \hat{y}_P, \hat{z}_P)$  is the coordinate of  $P$  in the target coordinate frame, and  $\mathbf{X}_\delta^{xyz} = (x_\delta, y_\delta, z_\delta)$  is the coordinate of the origin of the target coordinate frame  $\hat{O}$  in the original coordinate frame. Generally speaking,  $\gamma$ ,  $\chi$  and  $\beta$  are the roll, pitch and yaw angles, respectively, for the rotation transformation. The matrices  $\mathbf{M}_{pitch}(\chi)$ ,  $\mathbf{M}_{yaw}(\beta)$  and  $\mathbf{M}_{roll}(\gamma)$  for rotation transformation in pitch, yaw and roll are given as

$$\mathbf{M}_{pitch}(\chi) = \begin{bmatrix} \cos\chi & 0 & \sin\chi \\ 0 & 1 & 0 \\ -\sin\chi & 0 & \cos\chi \end{bmatrix}, \quad \mathbf{M}_{yaw}(\beta) = \begin{bmatrix} 1 & 0 & 0 \\ 0 & \cos\beta & -\sin\beta \\ 0 & \sin\beta & \cos\beta \end{bmatrix}, \quad (3.21)$$

$$\mathbf{M}_{roll}(\gamma) = \begin{bmatrix} \cos\gamma & -\sin\gamma & 0 \\ \sin\gamma & \cos\gamma & 0 \\ 0 & 0 & 1 \end{bmatrix}. \quad (3.22)$$

The induced velocity calculated in the local frame of reference then needs to be transferred back to the global frame as

$$\mathbf{V}_P^{xyz} = \mathbf{M}_{yaw}^{-1}(\beta)\mathbf{M}_{pitch}^{-1}(\chi)\mathbf{M}_{roll}^{-1}(\gamma)\hat{\mathbf{V}}_P^{xyz}. \quad (3.23)$$

### 3.2.3. Self induced velocity and induced velocity field of a vortex ring

The self induced velocity  $V_s$  of an isolated vortex ring in an unbounded medium gave by Helmholtz [64] is expressed as

$$\mathbf{V}_s = \frac{\Gamma}{4\pi R} \left[ \ln \frac{8}{a_s} - C \right] + O \left[ \frac{a_s^2}{R^2} \ln \frac{8R}{a_s} \right]. \quad (3.24)$$

where  $a_s$  is the non-dimensional core radius assuming that  $a_s \ll 1$  and  $C$  is a constant equal to  $C = 1/4$  [65].

Meanwhile, as suggested by de Vaal [60], we also evaluate the self-induced velocity from Eq. (3.16) by substituting a point on the ring with numerical values  $\xi = 1.0$  and  $\zeta = 0.0$  into Eq. (3.16) and making a series expansion which leads to

$$\mathbf{V}_s = \frac{\Gamma}{4\pi R} \left[ \ln \frac{8}{\sigma} - 1 \right] + O(\sigma^2). \quad (3.25)$$

A correction method to connect  $a_s$  and  $\sigma$  was suggested by Rosenhead [66] by defining  $a_s = \mu_s \sigma$  where  $\mu_s$  is a constant. By substituting  $a_s = \mu_s \sigma$  into Eq. (3.25) and comparing Eq. (3.24) and (3.25) (omitting high order terms), we get the expression

$$\left[ \ln \frac{8}{\sigma} - \frac{1}{4} \right] = \left[ \ln \frac{8}{\mu_s \sigma} - 1 \right], \quad (3.26)$$

which yields

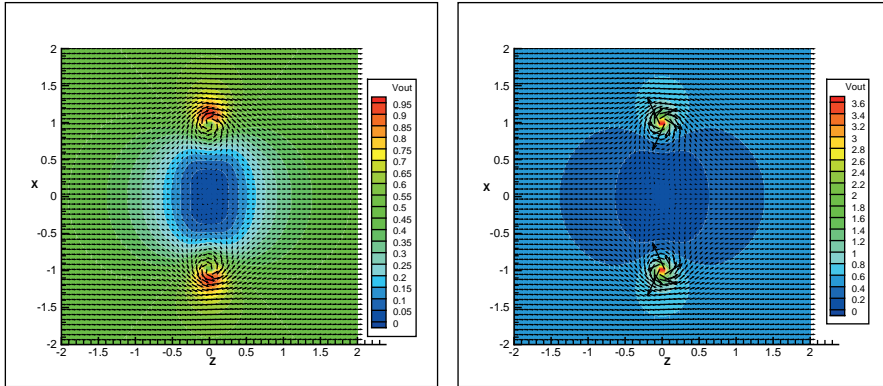
$$\mu_s = \exp(-3/4). \quad (3.27)$$

From Eq. (3.26) it can be observed that with the modified core radius  $\mu_s \sigma$ , the self-induced velocity calculated with Eq. (3.16) equals the self-induced velocity given by Eq. (3.24) with a core radius  $a$ . Moreover, Eq. (3.26) is a dynamic equilibrium equation that stipulates that each value of  $\sigma$  is associated with a value of  $a$ . Thus, theoretically Eq. (3.16) can be directly used for the calculation of the self-induced velocity of a vortex ring.

Regarding the induced velocity field of a vortex ring, it has been found that when  $\sigma = 0.0116$ , the self-induced velocity equals the induced velocity at the center of the ring, which is considered as a limiting case. When  $\sigma > 0.0116$ ,

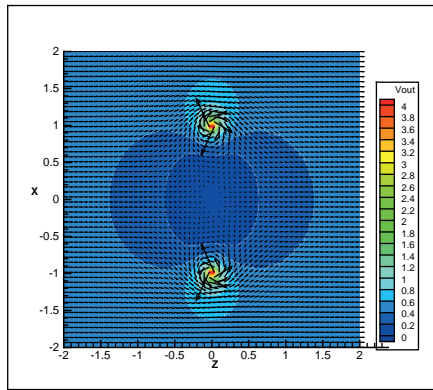
the self-induced velocity is lower than the induced velocity on the center of the ring, in which case the vortex ring is defined as a thick vortex ring and when  $\sigma < 0.0116$ , the self-induced velocity is larger than the induced velocity on the center of the ring, in which case the vortex ring is defined as a thin vortex ring [67]. Three typical induced velocity fields of the three types of vortex rings (with  $\sigma = 0.1$ ,  $\sigma = 0.0116$  and  $\sigma = 0.001$  respectively), in a cross section (XZ-plane) running through the center of the ring, are presented in Fig. 3.3. They are calculated with the parameters:  $R = 1$ ,  $\Gamma = -1$  and the normalised free stream velocity  $V_0 = 0.50$ , which is approximately equal to the value of the induced velocity on the center of the ring but with an opposite sign. It is worth mentioning that with a fixed  $R$  and a changing  $\sigma$  the induced velocity on the center of the ring remains the same while the self-induced velocity increases with a decrease of the core size. As shown in Fig. 3.3, the velocities in the center area of the vortex ring are close to zero in all three pictures because the vortex ring induced velocity compensates the free stream velocity, while the length of the velocity vectors demonstrates that a smaller vortex core will induce higher velocities at the local region around the core. By contrast, the induced velocities in the other regions away from the core are not significantly affected by the core size.

In order to further investigate the induced velocity calculated with Eq. (3.14), the induced velocity in the local region around the core center are calculated with the parameters  $\sigma = 0.0116$ ,  $R = 1$  and  $\Gamma = -1$ , as shown in Fig. 3.4, where  $V_x$  in Fig. 3.4a represents the radial induced velocity,  $V_z$  in Fig. 3.4b represents the axial induced velocity and  $V = \sqrt{V_x^2 + V_z^2}$  in Fig. 3.4c represents the resultant velocity. The results show that the radial induced velocity  $V_x$  achieves the peak value on the points  $\xi = 1$  and  $\zeta = \pm\sigma$  as shown in Fig. 3.4a and the axial induced velocity  $V_z$  reaches the peak value at the points  $\xi = 1 \pm \sigma$  and  $\zeta = 0$  on the boundary of the core, as shown in Fig. 3.4b. This conclusion is consistent with what has been found by Scully [68]. Furthermore, it can be seen from Fig. 3.4c that from the core center to the core radius  $r_c = \sigma R$ , the resultant velocity  $V$  continuously increases, and then from the core radius  $r_c$  to outside of the core the resultant velocity  $V$  continuously decreases. The resultant velocity  $V$  reaches the peak value at the points  $\xi = 1 - \sigma$  and  $\zeta = 0$  on the boundary of



(a)

(b)



(c)

Figure 3.3: Velocity field of a vortex ring in its cross section for: (a)  $\sigma = 0.1$ , (b)  $\sigma = 0.0116$ , (c)  $\sigma = 0.001$

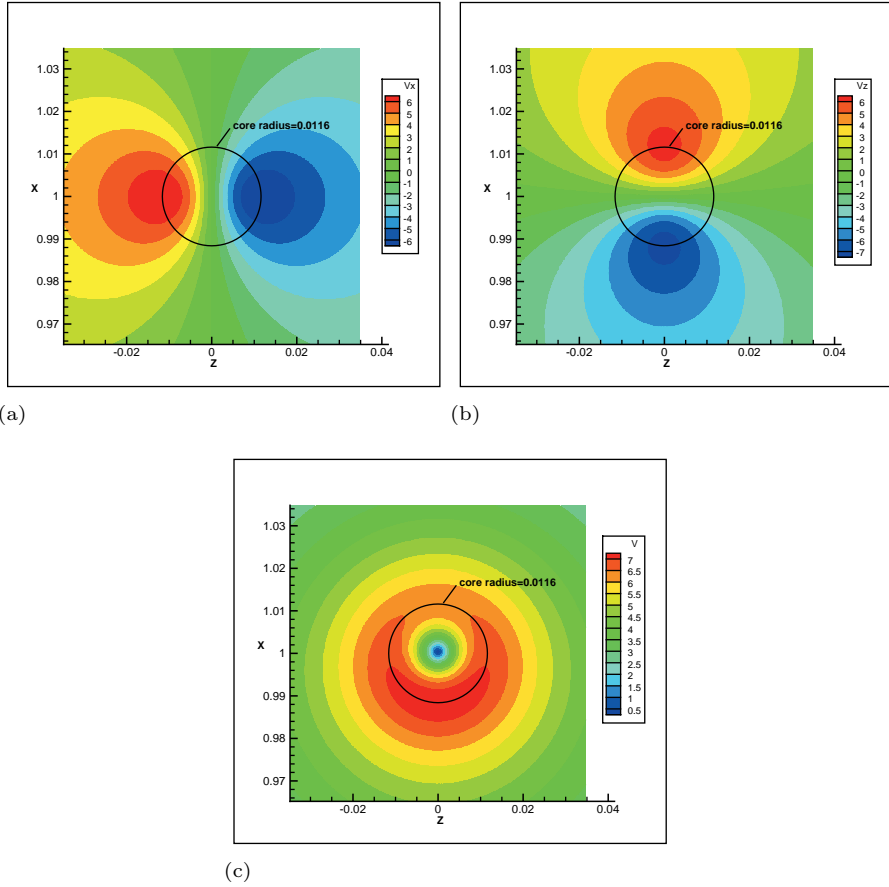


Figure 3.4: Induced velocity around a vortex core with  $\sigma = 0.01$ : (a)  $V_x$ , (b)  $V_z$ , (c)  $V = \sqrt{V_x^2 + V_z^2}$

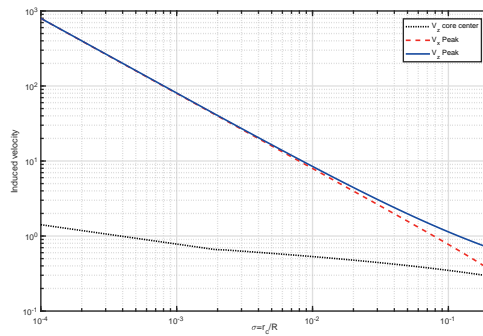


Figure 3.5: Induced velocities on the core center:  $V_z(o_c)$  and on the core radius:  $V_x(r_c)$  and  $V_z(r_c)$

the core.

Based on the discussion above, the self-induced velocity  $V_x$  and  $V_z$  should be calculated exactly on the core center with the coordinate  $\xi = 1$  and  $\zeta = 0$  from Eq. (3.15) and Eq. (3.16). The self induced velocity  $V_z(o_c)$  and the peak induced velocities on the core radius  $V_z(r_c)$  in the axial direction and  $V_x(r_c)$  in the radial direction are shown in Fig. 3.5, which all exponentially decrease with the increase of core radius factor  $\sigma$ . By contrast, the induced velocities on the core radius change much more rapidly than the self-induced velocity on the core center. It is easy to find that the self-induced velocities of an arbitrary ring given by Eq. (3.15) and Eq. (3.16) on the core center are  $V_x = 0$  and  $V_z \neq 0$ , which means that a vortex ring only induces translation velocity along the axial direction of the ring on itself while there is no contraction or expansion. But as shown in Fig. 3.5, it is clear that the induced velocity around the core center is so sensitive to the radius that a small deviation from the core center can result in a large deviation of the velocity values in either  $V_x$  or  $V_z$ . Thus from the application point of view, any numerical error can lead to an unexpected result when using Eq. (3.14) to calculate the self-induced velocity.

The vortex rings in this free wake vortex method always exist in the form of vortex ring pairs. Thus, for each vortex ring with the radius of  $R1$  and vortex strength  $\Gamma$ , there is another vortex ring with the radius of  $R2$  and vortex strength  $-\Gamma$ , which is a feature that is different with other vortex ring methods. In this method, at the initial time step the vortex ring pair emerges as concentric circles which later convect independently, which will be explained in detail in the next section. Here some basic characteristics of ideal concentric vortex rings' induced velocity are investigated and their difference from a single vortex ring is discussed. For convenience, a vortex pair of two concentric vortex rings with the parameters of the outer ring  $R1 = 1$ ,  $\Gamma1 = -1$  and of the inner ring  $R2 = 0.5$ ,  $\Gamma2 = -1$  and  $\sigma = 0.0116$  are defined as the standard vortex pair.

From Fig. 3.6a to Fig. 3.6c, the pictures show the axial induced velocity of two concentric vortex rings in the  $xy$  plane, with  $z = 0$  for the case of the standard vortex pair, and two other cases with  $R2 = 0.25$  and  $R2 = 0.75$  and the other parameters kept the same. Figure 3.6d is taken as a reference group with the induced velocity of a single outer vortex ring with  $\Gamma1 = -1$  and  $R1 = 1$ .

Figure 3.6 indicates that the outer ring induced positive velocities out of the ring and negative velocities inside the ring, while it is the other way around for the inner ring. When comparing the velocity induced by two concentric vortex rings with the velocity induced only by the outer vortex ring, it can be found that with the overlap of positive velocities from the inner ring and the negative velocity from the outer ring, positive velocities are dominant in the area of  $\bar{r} < R2$ . Also, with the overlap of negative velocities from the inner ring and the positive velocities from the outer ring, positive induced velocities are enhanced in the area  $R2 < \bar{r} < R1$ . Finally, with the overlap of negative velocities from the inner ring and the positive velocity from the outer ring, positive induced velocities are dominant in the area  $\bar{r} > R1$ . Also it can be found that the outer ring induced negative velocities on the inner ring and the inner ring induced negative velocities on the outer ring. Thus it can be inferred that the vortex ring pairs convect slower in the wake than a single outer vortex ring.

The average induced velocity  $\bar{V}(\bar{r})$  in the  $xy$ -plane with  $z = 0$  of a circular area  $S(\bar{r})$  with the same center as the vortex ring and with a normalised radius  $\bar{r}$  are calculated as

$$\bar{V}(\bar{r}) = \frac{1}{S(\bar{r})} \int_0^{S(\bar{r})} V_z dS(\bar{r}). \quad (3.28)$$

With the standard vortex pair, the average induced velocity  $\bar{V}(\bar{r})$  is calculated with  $\bar{r}$  changing between 0.05 and 3.00 as shown in Fig. 3.7. The red dashed curve represents the average induced velocity  $\bar{V}_{in}(\bar{r})$  caused by the inner ring, the black dotted curve represents the average induced velocity  $\bar{V}_{out}(\bar{r})$  caused by the outer ring and the blue solid line represents the average induced velocity  $\bar{V}(\bar{r})$  caused by the vortex pair. It can be seen from the figure that  $\bar{V}_{in}(\bar{r})$  and  $\bar{V}_{out}(\bar{r})$  have positive and negative values, respectively, and the peak value occurs when  $\bar{r}$  is equal to the radius of the ring. When the integration area  $S(\bar{r})$  is small, the trend of  $\bar{V}(\bar{r})$  is dominated by the inner ring, which also has a positive peak value at  $\bar{r} = R2$ . With the increase of the integration area  $S(\bar{r})$ , the effect of the outer ring increases. Furthermore,  $\bar{V}(\bar{r}) = 0$  when  $\bar{r} \approx 0.65$  and after that  $\bar{V}(\bar{r})$  becomes negative and reaches a peak at  $\bar{r} = R1$ . The average induced velocity  $\bar{V}(\bar{r})$  at  $\bar{r} = R1 = 1$  calculated with the  $R2 : R1$  ratio changing between 0.10 and 0.95 are shown in Fig. 3.8. It can be seen from

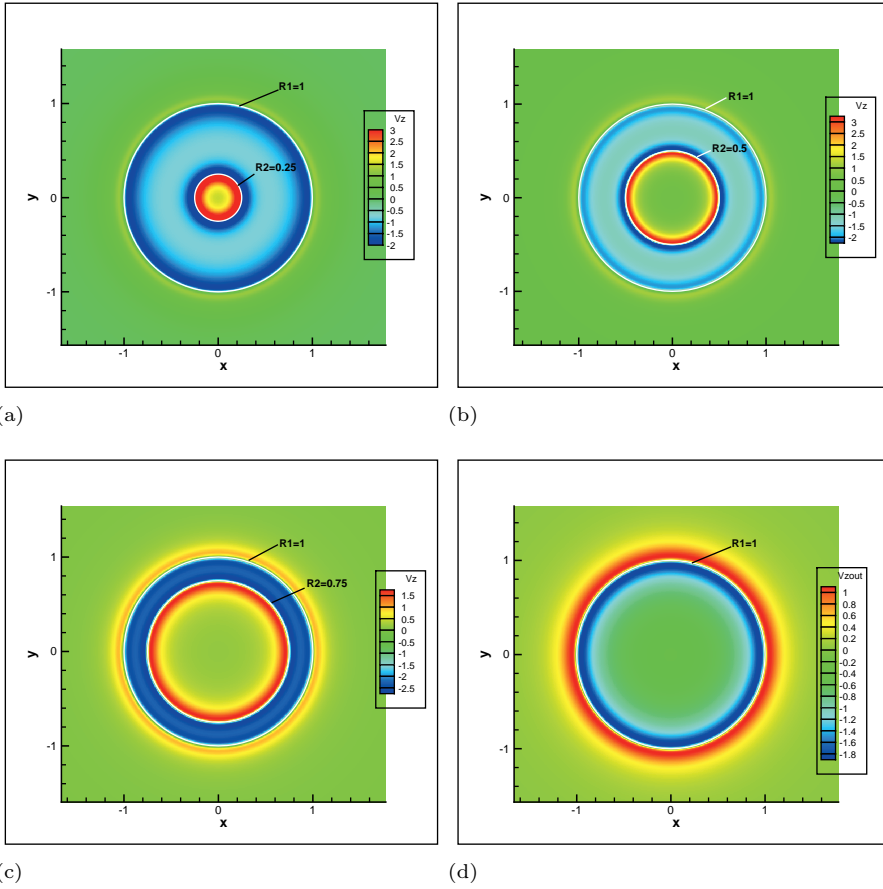


Figure 3.6: Induced velocity of two concentric vortex rings

the figure that with the increase of the  $R2 : R1$  ratio, the contribution from the inner ring increases. However, as long as  $R2$  is smaller than  $R1$ ,  $\vec{V}(\vec{r})$  is in the same direction as the induced velocity of the outer ring  $\vec{V}_{out}(\vec{r})$  while the inner ring plays a role in weakening this effect.

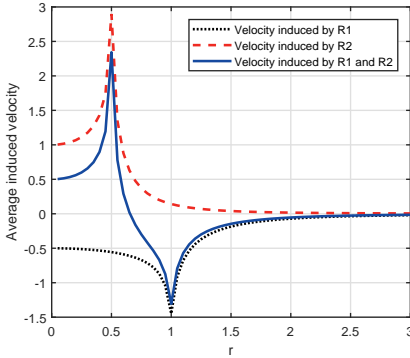


Figure 3.7: The average induced velocity  $\vec{V}(\vec{r})$  changing with  $\vec{r}$

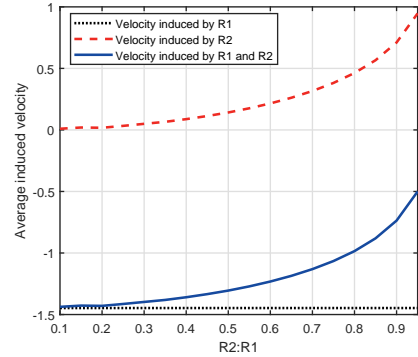


Figure 3.8: The average induced velocity  $\vec{V}(\vec{r} = R1)$  changing with  $R2:R1$  ratio.

### 3.3. Numerical discretization

The equations presented in the previous section need to be discretized in order to be solved numerically. Section 3.3.1 gives more insights into the discretization of the blades using vortex elements, while Section 3.3.2 discusses how the far wake model is implemented and how vortex rings propagate in the wake. Characteristics of the first rings shed in the wake are introduced in Section 3.3.3. The equation for the calculation of the strength of blade bound vortex is introduced in Section 3.3.4. Finally, the comparison and validation of the two trailing vortex models are given in Section 3.3.5.

#### 3.3.1. Near wake models

##### Blade bound vortex model

Figure 3.9 illustrates the blade bound vortex model for a rotor of  $N_b = 3$  blades. Each blade is discretised with a series of vortex line segments. The radial endpoints of the vortex segments are marked by red hollow points marked by  $\mathbf{t}_j$

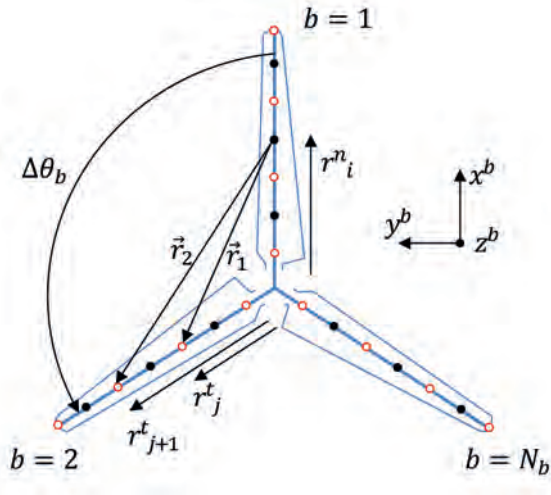


Figure 3.9: The blade bound vortex model

and the distance from the rotor center to  $\mathbf{t}_j$  is denoted by  $r_j^t$ . The control points of each vortex line segment are marked by black solid dots marked by  $\mathbf{n}_i$  and the distance from the rotor center to  $\mathbf{n}_i$  is denoted by  $r_i^n$ , where  $r_i^n = (r_j^t + r_{j+1}^t)/2$  ( $i = 1, \dots, N$  and  $j = 1, \dots, N+1$ ),  $N$  being the number of vortex segments. A local blade coordinate system  $x^b y^b z^b$  is defined. It is right-handed and centered at the rotor root. The  $x^b$ -axis is along the pitch axis and points towards the tip of the blade  $b$ , the  $y^b$ -axis points to the trailing edge of blade and is parallel to the chord line at the zero-twist blade section, and the  $z^b$ -axis is orthogonal to both  $x^b$  and  $y^b$ . In the local blade coordinate system of a blade  $b$ , the rotor lies in the  $x^b y^b$ -plane as shown in Fig. 3.9. The coordinates of a control point  $\mathbf{n}_i$  and an endpoint  $\mathbf{t}_j$  of a blade segment  $j$  are then expressed as

$$\mathbf{n}_i = \begin{Bmatrix} 0 \\ r_i^n \\ 0 \end{Bmatrix}, \quad \mathbf{t}_j = \begin{bmatrix} \cos\Delta\theta_b & -\sin\Delta\theta_b & 0 \\ \sin\Delta\theta_b & \cos\Delta\theta_b & 0 \\ 0 & 0 & 1 \end{bmatrix} \begin{Bmatrix} 0 \\ r_j^t \\ 0 \end{Bmatrix}, \quad (3.29)$$

where  $\Delta\theta_b = (bi - b)2\pi/N_b$  is the angle between blade  $bi$  and blade  $b$ ,  $b = 1, 2, \dots, N_b$ , and  $bi$  can be either the same or different from  $b$ . Assuming  $\mathbf{x}_p = \mathbf{n}_i$ ,  $\mathbf{x}_1 = \mathbf{t}_1$  and  $\mathbf{x}_2 = \mathbf{t}_2$ , and substituting Eq. (3.29) into Eq. (3.7), it can be found that the velocity induced by the segment  $x_1 x_2$  at the control point  $\mathbf{n}_i$

equals zero in both the  $x_b$ -direction and the  $y_b$ -direction. In the  $z_b$ -direction, it is equal to

$$V_{ij}^{zb} = \Gamma_j^b \frac{r_i^n \sin \Delta \theta_b [r_2 (r_j^t - r_i^n \cos \Delta \theta_b) - r_1 (r_{j+1}^t - r_i^n \cos \Delta \theta_b)]}{4\pi r_1 r_2 [r_c^2 + r_i^{n^2} - (r_i^n \cos \Delta \theta_b)^2]} = A_{ij}^b \Gamma_j^b, \quad (3.30)$$

where  $A_{ij}^b$  is the influence coefficient which only depends on the geometry and discretization of the rotor, and  $r_1$  and  $r_2$  are the lengths of the vectors  $\mathbf{x}_1 - \mathbf{x}_p$  and  $\mathbf{x}_2 - \mathbf{x}_p$  respectively, i.e.

$$r_1 = \sqrt{r_c^2 + r_i^{n^2} + r_j^{t^2} - 2r_i^n \cos \Delta \theta_b}, \quad (3.31)$$

$$r_2 = \sqrt{r_c^2 + r_i^{n^2} + r_{j+1}^{t^2} - 2r_i^n \cos \Delta \theta_b}. \quad (3.32)$$

The total induced velocity at a control point  $n_i$  is the sum of the influences of all the bound vortex segments on all  $N_b$  blades, which can be expressed as

$$V_i^{zb} = \sum_{b=1}^{N_b} \sum_{j=1}^N V_{ij}^{zb} = \sum_{b=1}^{N_b} \sum_{j=1}^N A_{ij}^b \Gamma_j^b. \quad (3.33)$$

Considering that the rotor is axis-symmetric and that all the blades' geometry and discretization are identical, the total induced velocity at all  $N$  control points on a blade  $b$ , in the local blade coordinate system, can be simplified as

$$\{V^{zb}\} = \sum_{b=1}^{N_b} \mathbf{A}^b \{\Gamma^b\}, \quad (3.34)$$

where  $\mathbf{A}^b$  is the matrix of influence coefficients of the blade bound vortex model.

### Trailing vortex model

In this section, a finite length vortex line model is introduced as opposed to the semi-infinite vortex line model proposed by de Vaal [59], as shown in Fig. 3.10a. A local blade coordinate system  $x^b y^b z^b$  is used, where the rotor lies in the  $x^b y^b$ -plane and the blade  $b$  lies along the  $x^b$ -axis. In the present model, the trailing vortex line begins from an endpoint of a blade segment on

the rotor and extends to a finite length  $l_j^t$  in the direction normal to the blade in the  $x^b y^b$ -plane. The length of a trailing vortex segment is defined as

$$l_j^t = r_j^t \theta_t, \quad (3.35)$$

which equals to the arc length of  $r_j^t$  times the angle  $\theta_t$  swept, where  $\theta_t$  is an input parameter.

The induced velocity at the control point  $n_i$  on blade  $b$  can be determined using Eq. (3.7). The coordinates of  $\mathbf{x}_p$  and  $\mathbf{x}_1$  are both given by Eq. (3.29), while the coordinates of  $\mathbf{x}_2$  can be written as

$$\mathbf{x}_2 = \begin{bmatrix} \cos\Delta\theta_b & -\sin\Delta\theta_b & 0 \\ \sin\Delta\theta_b & \cos\Delta\theta_b & 0 \\ 0 & 0 & 1 \end{bmatrix} \begin{Bmatrix} r_j^t \theta_1 \\ r_j^t \\ 0 \end{Bmatrix}. \quad (3.36)$$

Substituting Eq. (3.29) and Eq. (3.36) into Eq. (3.7), evaluating the integral and simplifying, it is found that the induced velocity of a trailing vortex segment  $x_1 x_2$  at a control point  $\mathbf{n}_i$  in the  $x_b$ -direction and the  $y_b$ -direction are both zero, and that in  $z_b$ -direction, it is equal to

$$V_{ij}^{zt} = \Delta\Gamma_j^t \frac{(r_j^t - r_i^n \cos\Delta\theta_b) [r_2' r_i^n \sin\Delta\theta_b - r_1 (r_j^t - r_i^n \sin\Delta\theta_b)]}{4\pi r_1 r_2' [r_c^2 + r_j^{t2} - 2r_i^n r_j^t \cos\Delta\theta_b - (r_i^n \cos\Delta\theta_b)^2]} = A_{ij}^t \Delta\Gamma_j^t, \quad (3.37)$$

where  $r_1$  and  $r_2'$  are the lengths of the vectors  $\mathbf{x}_1 - \mathbf{x}_p$  and  $\mathbf{x}_2 - \mathbf{x}_p$ , respectively,  $r_1$  is as given in Eq. (3.31) and  $r_2'$  can be defined as

$$r_2' = \sqrt{r_c^2 + r_i^{n2} + r_j^{t2} (1 + \theta_1^2) - 2r_i^n r_j^t (\cos\Delta\theta_b + \theta_1 \sin\Delta\theta_b)}. \quad (3.38)$$

The total velocity induced by the trailing vortex at a control point  $n_i$  is the sum of the influences of all the trailing vortex segments on all  $N_b$  blades, which can be expressed as

$$V_i^{zt} = \sum_{b=1}^{N_b} \sum_{j=1}^{N+1} V_{ibj}^{zt} = \sum_{b=1}^{N_b} \sum_{j=1}^{N+1} A_{ij}^t \Delta\Gamma_{bj}^t, \quad (3.39)$$

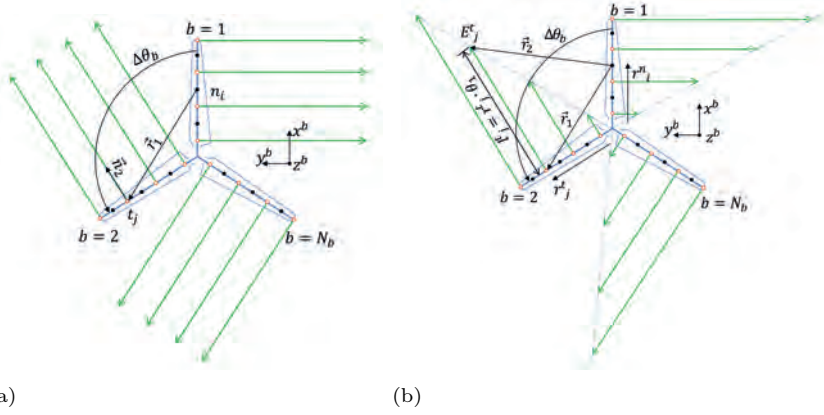


Figure 3.10: The trailing vortex models: infinite length (left), finite length (right).

where  $N + 1$  is the number of trailing vortex segments. In the local blade coordinate system of blade  $b$ , the total velocity induced by the trailing vorticity at all  $N$  control points on blade  $b$  can thus be written as

$$\{V^{zt}\} = \sum_{b=1}^{N_b} \mathbf{A}^t \{\Delta\Gamma_b^t\}, \quad (3.40)$$

where  $\mathbf{A}^t$  is the matrix of influence coefficients of the trailing vortex model.

### Total induced velocity of the near wake

The total induced velocity of the near wake on a rotor blade is the sum of the components of the blade bound vortex model given by Eq. (3.34) and the components of the trailing vortex model given by Eq. (3.40). Considering that both components have non-zero values only in the  $z_b$ -direction, the  $z_b$ -component of the near wake induced velocity  $V^{nw}$  on the rotor blade is written as

$$V^{nw} = \sum_{b=1}^{N_b} (\mathbf{A}^b \{\Gamma^b\} + \mathbf{A}^t \{\Delta\Gamma^t\}). \quad (3.41)$$

It can be seen that the near wake induced velocities only depend on the rotor geometry and the distribution of the control points.

## 3.3.2. Far wake model

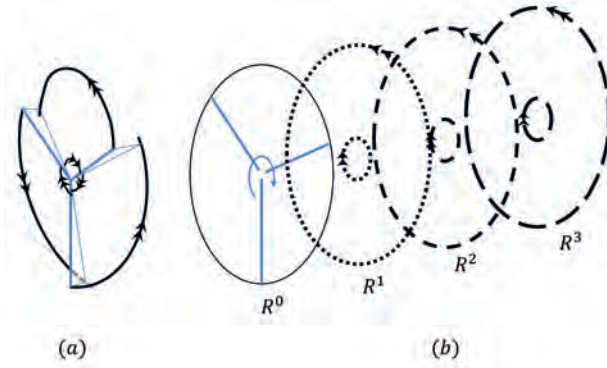


Figure 3.11: Schematic representation of a four vortex rings shed by the far wake model.

The far wake model is formulated based on the assumption that the spiral vortices in the wake of a wind turbine can be simplified into a series of vortex rings, as illustrated in Fig. 3.11. When each of the  $N_b$  blades of the wind turbine sweeps  $2\pi/N_b$  degrees, that is to say, when all the  $N_b$  blades of the wind turbine together sweep a full rotor revolution, a pair of new vortex rings  $R^1$  is shed into the wake, the outer ring being shed from the outboard part of the rotor and the inner ring being shed from the inboard part of the rotor disc. The computation of the far wake induced velocity  $\mathbf{v}_P^{fw}$  at a point  $P$  in the global coordinate system is described in Section 3.2.2. With the contribution of all  $N_R$  pairs of vortex rings, it can be expressed as

$$\mathbf{v}_P^{fw} = \sum_{k=1}^{N_R} \mathbf{v}_{in,k} + \sum_{k=1}^{N_R} \mathbf{v}_{out,k}, \quad (3.42)$$

where  $\mathbf{v}_{in,k}$  is the velocity induced by the  $k^{th}$  inner ring and  $\mathbf{v}_{out,k}$  is that induced by the  $k^{th}$  outer ring. The induced velocity at the control point of the rotor can be used to determine the thrust, torque, and other aerodynamic parameters of the wind turbine, while the induced velocity at the control point on the vortex rings is used to determine the convection of the wake.

#### The propagation of vortex rings

All the existing vortex rings in the wake convect independently downstream as time evolves. Unlike the near wake model, which only depends on the geom-

entry of the rotor, the far wake model is time-dependent. Two time scales are considered: (i) the time step for the vortex shedding defined as  $\Delta T = T_p/N_b$ , where  $T_p$  is the period of rotation of the rotor, and (ii) the time step used to compute the propagation of the vortex rings and defined as  $\Delta t = \Delta T/n_{cst}$ , where  $n_{cst}$  is a constant integer. It should be noted that since a pair of vortex ring release to the wake in every one third of the rotor rotational period, the vortex shedding causes unsteadiness to the bottom mounted turbines which should be filtered during the post-process of the numerical results.

The calculation of the propagation of vortex rings is a cyclic process which involves three steps per  $\Delta t$  at a time  $t$ :

1. Identify the control points on the vortex rings and calculate the velocities (including self-induced velocity, induced velocity from all the other rings and free stream velocity) on all the control points in the field.
2. Calculate the position of the control points both on the rotor and in the wake. The position of the control points on the rotor is determined by the position of the rotor and the azimuthal angle of the blade. The displacement of the control point in the wake is given by Euler's equation assuming an incompressible and inviscid fluid, as

$$\mathbf{S}(t + \Delta t) = \mathbf{S}(t) + \mathbf{V}\Delta t, \quad (3.43)$$

where  $V$  is the speed of a control point in the global coordinate system.

3. Update the position of the vortex rings based on the position of the control points determined in step 2.

According to the geometry characteristics of a ring, a group of geometry parameters that completely describe a vortex ring  $k$  is collected into the variable  $\mathbf{S}_k$ , as

$$\mathbf{s}_k = \begin{Bmatrix} x_{O,k} \\ y_{O,k} \\ z_{O,k} \\ R_k \\ \chi_k \\ \beta_k \\ \gamma_k \end{Bmatrix} \quad k = 1, \dots, N_R, \quad (3.44)$$

where the coordinates of the vortex ring center are denoted  $\mathbf{O}_k = (x_{O,k}, y_{O,k}, z_{O,k})$ ,  $R_k$  is the ring radius, and the roll  $\gamma_k$ , pitch  $\chi_k$  and yaw  $\beta_k$  angles are defined in Section 3.2.2. All these parameter values can change in time. Here we consider a local inertial coordinate system  $\hat{x}\hat{y}\hat{z}$  by translating the global coordinate so that its origin coincides with that of the vortex ring  $k$  without rotation. At the wind turbine's stable upright position, when the ring lies in the  $\hat{x}\hat{y}$ -plane,  $\chi_k$  and  $\beta_k$  are both zero, and when it rotates anti-clockwise around the corresponding axis according to the right-hand law, the value of the angle is defined as positive. Due to the rotational invariance property of the vortex ring, the roll angle  $\gamma_k$  around the  $\hat{z}$ -axis has no influence on the position of the ring itself but represents the azimuthal angle between the ring and the control point. In the following part of this section, the method to determine these parameters is introduced.

Consider a local vortex ring coordinate system  $x'y'z'$  defined by rotating the local inertial coordinate system  $\hat{x}\hat{y}\hat{z}$  by a pitch angle  $\chi_k$  and then a yaw angle  $\beta_k$ , so that the vortex ring lies in the  $x'y'$ -plane. During the numerical process, a vortex ring in the wake is represented by a series of control points distributed uniformly on the ring along the azimuthal angle  $\Delta\theta$ , as shown in Fig. 3.12. For convenience, each control point is assigned a number, moving anti-clockwise from the first point  $n = 1$  on the positive  $y'$ -axis to the last point  $n = N_c$ . With a total of  $N_c$  control points on a vortex ring,  $\Delta\theta = 2\pi/N_c$ . Thus the coordinate  $\mathbf{X}'_{i,k} = (x'_{i,k}, y'_{i,k}, z'_{i,k})$  of a control point  $i$  on a vortex ring  $k$  in the local vortex

ring coordinate system is given by

$$\begin{cases} x'_{i,k} = R_k \sin[\Delta\theta(i-1)] \\ y'_{i,k} = R_k \cos[\Delta\theta(i-1)] \\ z'_{i,k} = 0 \end{cases} \quad i = 1, \dots, N_c, k = 1, \dots, N_R. \quad (3.45)$$

These local coordinates need to be expressed in the global coordinate system

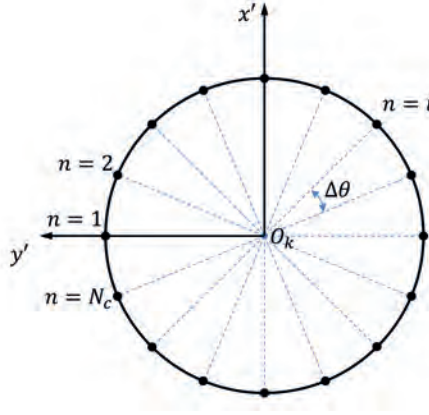


Figure 3.12: Control points on vortex ring

denoted by  $\mathbf{X}_{i,k}(t - \Delta t)$  as explained in Section 3.2.2. At each time step  $t$ , the control point velocity  $\mathbf{V}_{i,k}$  is updated according to the development of the wake. The new position of the control point denoted by  $\mathbf{X}_{i,k}(t)$  is determined by Eq. (3.43) as:

$$\mathbf{X}_{i,k}(t) = \mathbf{X}_{i,k}(t - \Delta t) + \mathbf{V}_{i,k} \Delta t. \quad (3.46)$$

Since the control points move independently, the new positions of the control points may no longer form an exact circle. This discrepancy is however very small if the time step  $\Delta t$  is small enough. Nevertheless, a new vortex ring with the geometry parameters as shown in Eq. (3.44) needs to be determined from the updated position of the azimuthal control points. Firstly, the vortex ring origin coordinate  $\mathbf{O}_k$  can be expressed by taking the average of the coordinates of all the control points as

$$\mathbf{O}_k = \frac{1}{N_c} \sum_{i=1}^{N_c} \mathbf{X}_{i,k} = \frac{1}{N_c} \sum_{i=1}^{N_c} (x_{i,k}, y_{i,k}, z_{i,k}). \quad (3.47)$$

Next, the vortex ring radius  $R_k$  is determined by taking the average of the length of the segment  $\mathbf{s}_{i,o}$  from each control point  $i$  to the center of the ring  $\mathbf{O}_k$  as

$$R_k = \frac{1}{N_c} \sum_{i=1}^{N_c} \sqrt{(x_{i,k} - x_{o,k})^2 + (y_{i,k} - y_{o,k})^2 + (z_{i,k} - z_{o,k})^2}. \quad (3.48)$$

In order to determine the pitch angle  $\chi_k$  and yaw angle  $\beta_k$  of the vortex ring  $k$ , a so-called average midline method is proposed. In this method, the rotational angles of the midlines of the ring ( $x'$ -axis for pitch and  $y'$ -axis for yaw in the local vortex ring coordinate frame respectively) in the global reference frame are taken as the rotational angles of the vortex ring as indicated in Fig. 3.13. Since the control points should be symmetric with respect to the midline axis of the ring, the coordinates of the control points on both sides of the midline are summed up to represent the coordinate of a point on the midline. To avoid obtaining a zero summation, the coordinates of the control points are summed up on the positive axis of the midline and the negative axis of the midline, respectively, and the angles are calculated separately. An average is then used as the final value. For this method to be accurate, the number of control points  $N_c$  should be even. The expressions are given by

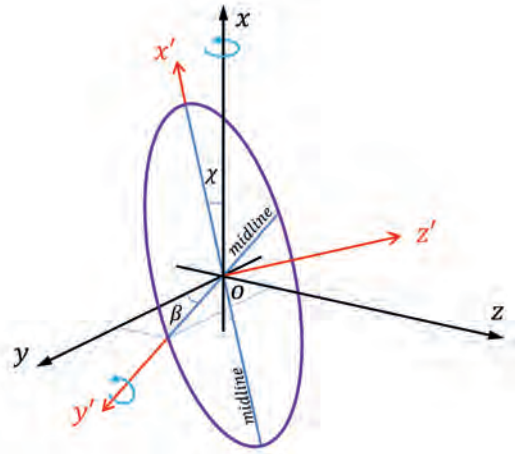


Figure 3.13: Schematic representation of the coordinate system and ring for the average midline method.

$$\begin{aligned}\chi_k &= -\frac{1}{2}\left(\arctan\frac{dz_1}{dx_1} + \arctan\frac{dz_2}{dx_2}\right), \\ \beta_k &= \frac{1}{2}\left(\arctan\frac{dz_3}{dy_1} + \arctan\frac{dz_4}{dy_2}\right),\end{aligned}\tag{3.49}$$

where  $dx_1, dx_2, dy_1, dy_2, dz_1, dz_2, dz_3$  and  $dz_4$  are defined as

$$\begin{aligned}dx_1 &= \sum_{x'_{i,k} >= 0} x'_{i,k}, & dz_1 &= \sum_{x'_{i,k} >= 0} z'_{i,k}, \\ dx_2 &= \sum_{x'_{i,k} < 0} x'_{i,k}, & dz_2 &= \sum_{x'_{i,k} < 0} z'_{i,k}, \\ dy_1 &= \sum_{y'_{i,k} >= 0} y'_{i,k}, & dz_3 &= \sum_{y'_{i,k} >= 0} z'_{i,k}, \\ dy_2 &= \sum_{y'_{i,k} < 0} y'_{i,k}, & dz_4 &= \sum_{y'_{i,k} < 0} z'_{i,k}.\end{aligned}\tag{3.50}$$

### 3.3.3. Characteristics of the first rings shed in the wake

After a certain distance behind the rotor, the trailing vortex segments of the near wake rolled up into two concentrated vortex rings in the far wake, namely the outer vortex ring and the inner vortex ring, as discussed in Section 3.3.2. The initial size and vortex strength of the vortex rings are defined in this section. The algorithm of the roll-up process is based on momentum conservation theory [69], as applied by de Vaal [59]. The location of the maximum blade bound vortex strength  $\Gamma_{max}$  is used to distinguish between inner and outer rings. In particular, the near wake trailing vortices between the location of  $\Gamma_{max}$  and the tip of the blade are rolled up into an outer ring and the near wake trailing vortices between the location of  $\Gamma_{max}$  and the root of the blade are rolled up into an inner ring in the far wake. The vortex strengths of the roll up vortex ring must be equal to the summation of the vortex strengths of the trailing vortices from which it is formed. Generally speaking, the vortex strength  $\bar{\Gamma}$  and radius  $\bar{r}$  of a vortex ring formed by the vortices trailing between blade radius  $r_1$  and  $r_2$  is given by

$$\bar{\Gamma} = - \int_{r_1}^{r_2} \frac{d\Gamma}{dr} dr, \quad (3.51)$$

$$\bar{r} = \frac{1}{\bar{\Gamma}} \int_{r_1}^{r_2} r \frac{d\Gamma}{dr} dr. \quad (3.52)$$

These equations can be used to get the expression for the inner and outer concentrated vortex strengths  $\bar{\Gamma}_{in}^b$  and  $\bar{\Gamma}_{out}^b$  and vortex ring radii  $\bar{r}_{in}^b$  and  $\bar{r}_{out}^b$  independently on each blade  $b$ , i.e.

$$\bar{\Gamma}_{in}^b = - \int_{r_1}^{r_2} \frac{d\Gamma^b}{dr} dr = \sum_{n=1}^{n_{max}} \Delta\Gamma_n^t, \quad (3.53)$$

$$\bar{r}_{in}^b = \frac{1}{\bar{\Gamma}_{in}^b} \int_{r_1}^{r_2} r \frac{d\Gamma^b}{dr} dr = \frac{1}{\bar{\Gamma}_{in}^b} \sum_{n=1}^{n_{max}} r_n \Delta\Gamma_n^t, \quad (3.54)$$

$$\bar{\Gamma}_{out}^b = - \int_{r_1}^{r_2} \frac{d\Gamma^b}{dr} dr = \sum_{n=n_{max}+1}^{N+1} \Delta\Gamma_n^t, \quad (3.55)$$

$$\bar{r}_{out}^b = \frac{1}{\bar{\Gamma}_{out}^b} \int_{r_1}^{r_2} r \frac{d\Gamma^b}{dr} dr = \frac{1}{\bar{\Gamma}_{out}^b} \sum_{n=n_{max}+1}^{N+1} r_n \Delta\Gamma_n^t. \quad (3.56)$$

Since each of the blades contributes equally to the far wake vortex ring, the final concentrated vortex strength and radius of the inner and outer ring for the whole rotor are defined as an average of the concentrated vortex strengths and radii calculated from each of the blades, that is

$$\bar{\Gamma}_{out} = \frac{1}{N_b} \sum_{b=1}^{N_b} \bar{\Gamma}_{out}^b, \quad \bar{\Gamma}_{in} = \frac{1}{N_b} \sum_{b=1}^{N_b} \bar{\Gamma}_{in}^b, \quad (3.57)$$

$$\bar{r}_{out} = \frac{1}{N_b} \sum_{b=1}^{N_b} \bar{r}_{out}^b, \quad \bar{r}_{in} = \frac{1}{N_b} \sum_{b=1}^{N_b} \bar{r}_{in}^b. \quad (3.58)$$

While the trailing model plays a function of separate the rotor and the vortex rings to avoid unrealistic local induced velocity, the program can reach a balance with a random  $z$  position of the first ring. Thus, the boundary conditions of the vortex model is not completely defined. In order to get a correct result, the first rings'  $z$  position downstream of the rotor plane need to

be determined and the program need to be calibrated based on reliable data which are already known. In this thesis, the vortex model is considered to be reliable only when both the thrust and the induced velocity are validated, which is the principle that is used to set the  $z$  position of the first ring. The induced velocity is very sensitive to the  $z$  position of the first ring, as can be seen in Fig 3.3 based on Eq. (3.14), which is not a linear relationship. Thus it is hard to develop an algorithm to determine it but maybe not impossible in the future.

### 3.3.4. Strength of the blade bound vortex

Based on the discussion above, it can be seen that both the trailing vortex strengths and the far wake vortex ring strengths are determined by the distribution of the blade bound vortex strengths. Once the blade bound vortex strengths are known, the near wake induced velocity at any point of the rotor can be determined by Eq. (3.41) and the far wake vortex ring strengths are determined at the roll-up processes and with no change during their convection in the wake. Thus the blade bound vortex strengths need to be determined as a prerequisite. A method to calculate the blade bound vortex strengths based on the three-dimensional vortex lifting law and the blade element theory is discussed below.

#### Three-dimensional vortex lifting law

The three-dimensional vortex lifting law as introduced by Phillips [70] is adopted to solve the blade bound vortex strength. Based on this theory, the lift force  $d\mathbf{F}_l$  acting on a vortex segment  $d\mathbf{l}$  can be calculated by the product of the air density  $\rho$ , the bound vortex strength  $\Gamma^b$  on the segment, and the relative wind velocity  $\mathbf{V}$ , as

$$d\mathbf{F}_l = \rho\Gamma^b\mathbf{V} \times d\mathbf{l}, \quad (3.59)$$

where the relative wind velocity  $\mathbf{V}$  includes the contribution from the free stream  $\mathbf{V}_\infty$ , the rotor rotation  $\mathbf{V}^\Omega$ , the near wake induced velocity  $\mathbf{V}^{nw}$ , the far wake induced velocity  $\mathbf{V}^{fw}$ , as well as the contribution from the motion of the turbine  $\mathbf{V}_p$  in the case of a floating offshore wind turbine. The relative wind velocity  $\mathbf{V}$  can be further decomposed into three components in the blade coordinate system as  $V_{x^b}$  in the  $x^b$ -direction, which is along the pitch axis towards

the tip of the blade, and  $V_{yb}$  and  $V_{zb}$  lie in the blade section and are normal to the blade pitch axis. Thus the relative wind velocity  $\mathbf{V}$  can be written as

$$\mathbf{V} = \mathbf{V}_\infty + \mathbf{V}^\Omega + \mathbf{V}^{nw} + \mathbf{V}^{fw} + \mathbf{V}_p = \begin{Bmatrix} V_{xb} \\ V_{yb} \\ V_{zb} \end{Bmatrix}, \quad (3.60)$$

where the velocity of a floating support structure  $\mathbf{V}_p$  is determined as [71]

$$\begin{aligned} \mathbf{V}_p &= \dot{\mathbf{x}}_p + \dot{\theta}_p \times \mathbf{x}_p \\ &= \begin{Bmatrix} x_{heave} \\ -y_{sway} \\ z_{surge} \end{Bmatrix} + \begin{Bmatrix} \dot{\theta}_{yaw} \\ -\dot{\theta}_{pitch} \\ \dot{\theta}_{roll} \end{Bmatrix} \times \begin{Bmatrix} x \\ y \\ z \end{Bmatrix} \\ &= \begin{Bmatrix} \dot{x}_{heave} + z\dot{\theta}_{pitch} - y\dot{\theta}_{roll} \\ -\dot{y}_{sway} + x\dot{\theta}_{roll} - z\dot{\theta}_{yaw} \\ \dot{z}_{surge} + x\dot{\theta}_{pitch} + y\dot{\theta}_{yaw} \end{Bmatrix}. \end{aligned} \quad (3.61)$$

Substituting Eq. (3.60) into (3.59), and given that the  $x^b$ -axis is parallel to  $d\mathbf{l}$ , it is found that only the  $V_{yb}$  and  $V_{zb}$  components contribute to the lifting force acting on the blade. Thus Eq. (3.59) can be rewritten as

$$d\mathbf{F}_l = \rho \Gamma^b \mathbf{V}^n \times d\mathbf{l}, \quad (3.62)$$

where  $\mathbf{V}^n$  is the velocity vector that has only the  $V_{yb}$  and  $V_{zb}$  components, i.e.

$$\mathbf{V}^n = \begin{Bmatrix} 0 \\ V_{yb} \\ V_{zb} \end{Bmatrix}. \quad (3.63)$$

### Blade element force

The lift force on a blade segment can also be calculated from the airfoil properties of the segment as indicated in Fig. 3.14. The lift force can be expressed as

$$d\mathbf{F}_l = \frac{1}{2} \rho |\mathbf{V}^n|^2 C_l c dl, \quad (3.64)$$

where  $\mathbf{V}^n$  is defined in Eq. (3.63),  $c$  is the chord length of the blade section, and  $C_l$  is the lift coefficient which can be obtained by means of tabulated aerodynamic parameters of the airfoil with a given angle of attack  $\alpha$ . The angle of

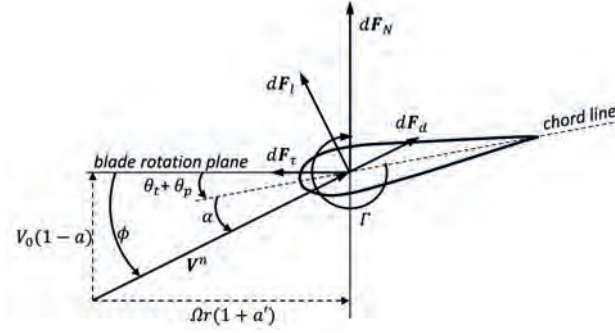


Figure 3.14: Forces acting on a blade element.

attack can be calculated with the fluid velocity around the blade section as

$$\alpha = \phi - (\theta_t + \theta_p), \quad (3.65)$$

where  $\theta_t$  is the twist angle of the blade section,  $\theta_p$  is the collective pitch angle of the blade and the angle of relative wind  $\phi$  is the angle between the wind velocity  $\mathbf{V}_n$  and the plane of the rotor disc, which can be expressed as

$$\phi = \tan^{-1} \frac{V_0(1-a)}{\Omega r(1+a')}. \quad (3.66)$$

In Eq. (3.66),  $\Omega$  is the rotor angular speed,  $a$  is the axial induction factor and  $a'$  is the angular induction factor. Similar to the lift force, the drag force  $d\mathbf{F}_d$  can be calculated from the tabulated drag coefficient  $C_d$  and the angle of attack  $\alpha$ , leading to

$$d\mathbf{F}_d = \frac{1}{2} \rho |\mathbf{V}^n|^2 C_d c dl. \quad (3.67)$$

Based on the discussion above, it is found that both Eq. (3.62) and Eq. (3.64) express the lift force of the blade segment. Thus by equating them for a blade section  $i$ , the following relation is obtained

$$\Gamma_i^b |\mathbf{V}_i^n(\Gamma_j) \times d\mathbf{l}_i| - \frac{1}{2} |\mathbf{V}_i^n(\Gamma_j)|^2 C_l(\alpha_i) c_i dl_i = 0. \quad (3.68)$$

For each blade section  $i = 1, \dots, (N_b \cdot N)$ , an equation like Eq. (3.68) can be set up. For all  $(N_b \cdot N)$  blade sections, a system of  $(N_b \cdot N)$  non-linear equations are obtained and solved for  $(N_b \cdot N)$  unknown values of the bound vortex strength  $\Gamma_i^b$ . Different methods can be used to solve the resulting set of

non-linear equations. The trust-region methods <sup>1</sup> are used here as they proved to be more stable and converge more rapidly than Newton-Raphson methods, especially for small and negative angles of attack. Accordingly, the rotor thrust  $\mathbf{F}_T$  is expressed as

$$\mathbf{F}_T = \sum_{b=1}^{N_b} \sum_{j=1}^N d\mathbf{F}_{Nb_j} = \sum_{b=1}^{N_b} \sum_{j=1}^N (d\mathbf{F}_{lb_j} \cos\phi_{bj} + d\mathbf{F}_{db_j} \sin\phi_{bj}), \quad (3.69)$$

whilst the torque  $Q$  is given by

$$Q = \sum_{b=1}^{N_b} \sum_{j=1}^N d\mathbf{F}_{Tb_j} r_{bj} = \sum_{b=1}^{N_b} \sum_{j=1}^N (d\mathbf{F}_{lb_j} \sin\phi_{bj} - d\mathbf{F}_{db_j} \cos\phi_{bj}) r_{bj}. \quad (3.70)$$

### 3.3.5. Comparison and validation of the two trailing vortex models

Based on the numerical methods discussed above, the two trailing vortex models introduced in section 3.3.1 will be compared and validated and the vortex ring pairs will be used to qualitatively evaluate the effectiveness of the trailing vortex models. Two types of rotors are used for the comparison and validation. The first one is an NEJ-rotor, which is a rotor with constant circulation along the blades. The second one is a Betz rotor with varying vortex strength along the blades. For simplification, each of the rotor have a radius  $R = 10$ , 3 blades ( $N_b = 3$ ) and 10 control points on each blade ( $N = 10$ ). The detailed parameters of these two types of rotors are given in Table 3.1, where  $n_i$  is the number of control points,  $r_i^n$  is the radial position of the control point,  $\Gamma_i^b$  is the bound vortex strength,  $r_j^f$  is the start point position of the trailing vortex line and  $\Gamma_j^f$  is the trailing vortex strength.

<sup>1</sup><https://www.mathworks.com/help/optim/ug/equation-solving-algorithms.html>

NEJ-rotor, $N_b=3$ , $N=10$ , $R=10.00$											
$n_i$	1	2	3	4	5	6	7	8	9	10	11
$r_i^n$	1.45	2.35	3.25	4.15	5.05	5.95	6.85	7.75	8.65	9.55	
$\Gamma_i^b$	10.00	10.00	10.00	10.00	10.00	10.00	10.00	10.00	10.00	10.00	10.00
$r_j^f$	1.00	1.90	2.80	3.70	4.60	5.50	6.40	7.30	8.20	9.10	10.00
$\Gamma_j^f$	10.00	0.00	0.00	0.00	0.00	0.00	0.00	0.00	0.00	0.00	-10.00

Betz-rotor, $N_b=3$ , $N=10$ , $R=10.00$											
$n_i$	1	2	3	4	5	6	7	8	9	10	11
$r_i^n$	1.45	2.35	3.25	4.15	5.05	5.95	6.85	7.75	8.65	9.55	
$\Gamma_i^b$	1.00	5.00	7.00	8.50	9.50	10.00	9.50	8.50	7.00	3.00	
$r_j^f$	1.00	1.90	2.80	3.70	4.60	5.50	6.40	7.30	8.20	9.10	10.00
$\Gamma_j^f$	1.00	4.00	2.00	1.50	1.00	0.50	-0.50	-1.00	-1.50	-4.00	-3.00

Table 3.1: Parameters for the NEJ and Betz rotors.

The induced velocity on the two types of rotor with the two trailing vortex models are given in Table 3.2, where  $f_w$  is the weight coefficient accounting for the sweeping area of the control point,  $V_{i,1}^t$  is the induced velocity on each control point calculated with the infinite length model (model 1),  $V_{i,2}^t$  is the induced velocity on each control point calculated with the finite length model (model 2), and  $V_{ind}$  is the average induced velocity on the rotor. From the result it can be seen that for both rotors, the magnitude of the average induced velocity of model 2 is larger than that from model 1 when  $\Delta\theta_b = 120^\circ$ . Also, the average induced velocity as a function  $\Delta\theta_b$ , and obtained with model 2, is given in Fig. 3.15. It can be seen that, for both rotors, when  $\Delta\theta_b < 100^\circ$ , the induced velocity changes rapidly with a change in  $\Delta\theta_b$ , whilst when  $\Delta\theta_b > 100^\circ$ , the induced velocity is rather independent of  $\Delta\theta_b$ .

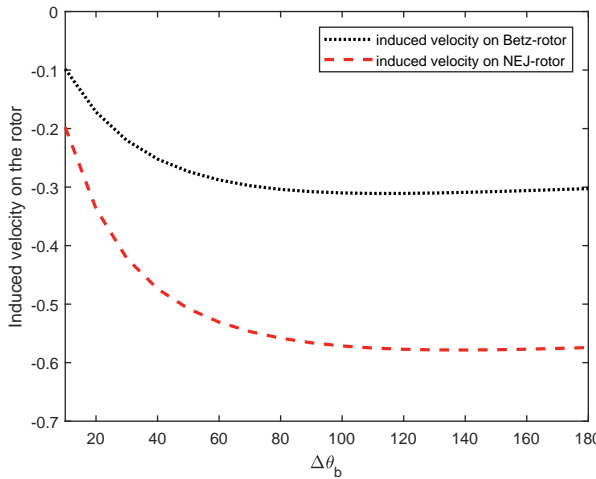


Figure 3.15: Average induced velocity on the rotor calculated with model 2 for different values of  $\Delta\theta_b$  degrees.

According to the method introduced in section 3.3.3, the near wake vortices are transformed into vortex pairs which can represent the wake during  $1/N_b$  period of rotation. The vortex strength and the radius are determined based on the principle of momentum conservation. For the NEJ-rotor, the parameters of the vortex pair are:  $\bar{\Gamma}_{in} = 10, \bar{\Gamma}_{out} = -10, \bar{r}_{in} = 1, \bar{r}_{out} = 10$ . For the Betz-rotor, the parameters of the vortex pair are:  $\bar{\Gamma}_{in} = 10, \bar{\Gamma}_{out} = -10, \bar{r}_{in} = 2.71, \bar{r}_{out} =$

NEJ-rotor, $N_b=3$ , $N=10$ , $R=10.00$ , $\Delta\theta_b = 120^\circ$					
$n_i$	$f_w$	$V_{i,1}^t$	$V_{i,2}^t$	$f_w V_{i,1}^t$	$f_w V_{i,2}^t$
1	2.61	-0.81	-0.56	-2.11	-1.45
2	4.23	-0.10	-0.24	-0.41	-1.00
3	5.85	-0.00	-0.21	-0.02	-1.22
4	7.47	-0.00	-0.22	-0.03	-1.66
5	9.09	-0.03	-0.25	-0.30	-2.24
6	10.71	-0.08	-0.28	-0.85	-3.02
7	12.33	-0.15	-0.34	-1.81	-4.14
8	13.95	-0.26	-0.43	-3.59	-6.01
9	15.57	-0.49	-0.65	-7.68	-10.12
10	17.19	-1.40	-1.53	-24.10	-26.28
sum	99.00			-40.91	-57.13
Average induced velocity on the rotor $V_{ind}$				-0.41	-0.58

Betz-rotor, $N_b=3$ , $N=10$ , $R=10.00$ , $\Delta\theta_b = 120^\circ$					
$n_i$	$f_w$	$V_{i,1}^t$	$V_{i,2}^t$	$f_w V_{i,1}^t$	$f_w V_{i,2}^t$
1	2.61	0.89	0.53	2.32	1.38
2	4.23	-0.06	-0.08	-0.24	-0.34
3	5.85	-0.17	-0.19	-0.99	-1.12
4	7.47	-0.30	-0.31	-2.22	-2.35
5	9.09	-0.40	-0.42	-3.64	-3.78
6	10.71	-0.52	-0.53	-5.53	-5.64
7	12.33	-0.46	-0.49	-5.62	-6.00
8	13.95	-0.43	-0.47	-5.96	-6.55
9	15.57	-0.50	-0.54	-7.73	-8.39
10	17.19	0.26	0.12	4.50	2.03
sum	99.00			-25.10	-30.77
Average induced velocity on the rotor $V_{ind}$				-0.25	-0.31

Table 3.2: The velocity induced on a blade by trailing vortices.

8.92. The induced velocity on the two rotors from the two trailing vortex models is given in Table 3.2. It can be found that on the NEJ-rotor the induced velocity from the first trailing model is  $-0.41$  and the induced velocity from the second trailing model with  $\theta_t = 120^\circ$  is  $-0.58$ . While on the NEJ-rotor, the induced velocity from the first trailing model is  $-0.25$  and the induced velocity from the second trailing model with  $\theta_t = 120^\circ$  is  $-0.31$ . It can be seen that, for both rotors, the second trailing model has a stronger contribution to the induced velocity, meaning that the near wake trailing model can more effectively separate the vortex rings from the rotor, which makes the local induced velocities on the rotor more realistic and accurate.

In order to further analyse the effect of the near wake trailing models, we compare induced velocities from the trailing models with those from the far wake vortex pair. Firstly, the velocities on the NEJ-rotor and Betz-rotor induced by the vortex ring pair, when the distance from the vortex ring pair and the rotor changes, are shown in Fig. 3.16.

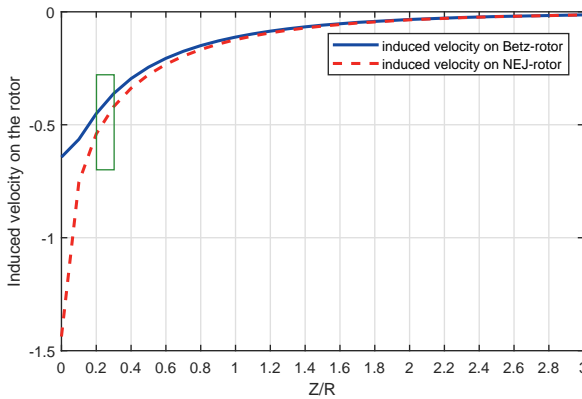


Figure 3.16: Average velocity on the rotor induced by the vortex ring pair changing with the distance between the vortex ring pair and the rotor. (The green rectangular marks the estimated induced velocity of the first vortex ring pair)

The tip speed ratio is taken as 4 for this three-blade rotor according to the suggestion given by Manwell [15]. Thus the following relationship between the free stream speed  $V_0$  and the rotor angular speed  $\Omega$  can be obtained

$$\frac{\Omega}{V_0} = \frac{\lambda}{R} = \frac{4}{R}. \quad (3.71)$$

Assuming that the shedding vortex filaments move downstream with the speed of  $V_0$  (for simplification, the induced velocity is not considered), then during a  $1/N_b$  period of rotation, the distance of the filaments should extend for  $z = 0$  to

$$z = \frac{T}{3} V_0 = \frac{2\pi}{3\Omega} V_0 = \frac{2\pi R}{3} \frac{R}{4} \approx 0.52R. \quad (3.72)$$

Thus according to Fig. 3.16, as is marked in the green rectangular, for the NEJ-rotor, the induced velocity from the vortex ring pair is about -0.48, and for the Betz-rotor, the induced velocity from the vortex ring pair is about -0.40. Accordingly, for the NEJ-rotor, the first trailing model induced velocity is equivalent to about 85% of the vortex pair induced velocity at  $z = 0.5R$ , and the second trailing model induced velocity is equivalent to about 120% of the vortex pair induced velocity at  $z = 0.5R$ . For the Betz-rotor, the first trailing model induced velocity is equivalent to about 63% of the vortex pair induced velocity at  $0.5R$ , and the second trailing model induced velocity is equivalent to about 76% of the vortex pair induced velocity at  $z = 0.5R$ .

According to the analysis above, both the first and second trailing vortex models induce the velocity in the same magnitude with the corresponding vortex pair but the effect of the second trailing vortex models is stronger than the first one. Another finding is that the induced velocities from both the trailing vortex models are stronger on the NEJ-rotor than on the Betz-rotor for both the net values and the percentages of vortex pair induced velocities. This is because, on the NEJ-rotor, the trailing vortex strengths are concentrated on both ends of the blades, which minimizes the cancellation of induced velocities.

Some more simplified vortex ring methods omit the near wake model and directly use the concentrated vortex rings to represent the wake. Such practice will lead to unrealistic local induced velocities on the rotor where it is too close to the vortex filament, even though the average induced velocity on the rotor might be good. The trailing vortex model plays a role in dispersing the vortex strength in the near wake and keeping a distance between the rotor and the far wake vortex rings, in order to avoid the effect of unrealistic local induced velocities acting on the rotor by the concentrated vortex rings. The near wake model and far wake model together induce the real velocity on the rotor. Thus, the stronger the trailing vortex model, the further away the vortex rings are from

the rotor. From this point of view, the second vortex model is more effective than the first vortex model. The exact match of the near wake model and the far wake model depends on more detailed information about the rotor and the environment.

### 3.4. Computational cost description

This simplified free wake vortex model aims at finding a compromise between physical accuracy and low computational cost. In this section, we compare the computational cost of the present method with other methods available in the literature. Table 3.3 shows the methods under consideration with computational cost and modeling capability: blade element momentum theory (BEM), actuator disc with free wake vortex ring model (AFWRV) of de Vaal [48] and Yu [56], the present free wake vortex ring model (FWVR), and two more advanced vortex methods, namely the free wake vortex filament (FWVF) method of Sebastian [51] and the nonlinear vortex lattice method (NVLM) method of Lee [52]. In Table 3.3,  $N_b$  is the number of rotor blades,  $N_\theta$  is the number of

Table 3.3: Computational time and function of different models.

Method	Computational time	Modeling capability
BEM	$C_b N_\theta N_\Omega$	Rotor aerodynamics without wake
AFWVR	$\frac{1}{3} C_a N_b^2 N_\theta^2 N_\Omega^3$	Rotor / uncoupled wake aerodynamics
FWVR	$\frac{1}{3} C_r N_b^2 N_\theta^2 N_\Omega^3 + C_\Gamma N_\theta N_\Omega$	Coupled rotor and wake aerodynamics
FWVF	$\frac{1}{3} C_f N_b^2 N_\theta^3 N_\Omega^3 + C_\Gamma N_\theta N_\Omega$	Coupled rotor and wake aerodynamics
NVLM	$\frac{1}{3} C_m N_b^2 N_\theta^3 N_\Omega^3 + C_\Gamma N_\theta N_\Omega$	Coupled rotor and wake aerodynamics

time steps per rotor rotation and  $N_\Omega$  is the number of rotor rotation to be simulated. Also,  $N_\theta N_\Omega$  represents the total number of time steps,  $C_b$  is the time cost of evaluating the induced velocity at a point in the field with BEM. It involves

the iterative solution of the BEM equations and some analytical corrections, such as Prandtl tip-loss, Prandtl hub-loss, and Pitt and Peters skewed-wake corrections when needed. Finally,  $C_a$ ,  $C_r$ ,  $C_f$  and  $C_m$  represent the time cost of evaluating the induced velocity of a vortex element (vortex rings or vortex filaments) at a point in the field with AFWVR, FWVR, FWVF and NVLM, respectively. Whether the blades are modeled or not, all the four methods are evaluated with the same number of control points on the rotor and with the same number of time steps.

The BEM theory method solves the induced velocities on the rotor based on the momentum theory and the blade element theory. The number of control points is constant and each point is considered independently. Thus the computational time has a linear relationship with the number of time steps, which is the fastest method for aerodynamic simulations. By contrast, the solution of the other four vortex methods mainly includes two parts: the calculation of the vortex element strength and the calculation of the induced velocity including self-induced velocity and mutually-induced velocity. The induced velocities are solved on the rotor as well as in the wake. The number of points where the induced velocities need to be calculated increases with the number of vortex elements in the wake (being vortex rings or vortex filaments) and each control point is induced by all the vortex elements in the field.

The vortex ring strength of AFWVR is directly determined from a prescribed thrust coefficient  $C_T$  [48], so the computational time is negligible. By contrast, the FWVR and FWVF methods first determine the blade bound vortex strength by iteratively solving the equations based on the 3D vortex lifting law and blade element theory with tabulated data of lift coefficients  $C_l$ . Then, the vortex strengths are distributed to the new generated vortex rings or vortex filaments in the wake. The computational times to determine the vortex strengths for FWVR, FWVF and NVLM methods at each time step are identical and denoted by  $C_r$ . Since  $C_r$  and  $C_b$  are both iterative processes with the same number of equations, they are considered to be of the same order of magnitude.

The computational times for evaluating the induced velocities of FWVR and FWVF are given in de Vaal [59] and van Garre [72]. Since the number of

vortex filaments is  $N_\theta$  times the number of vortex rings, the number of induced velocities that needs to be calculated at each time step for FWVR is also  $N_\theta$  times that of FWVF. Since AFWVR has the same number of control points and vortex rings than FWVR, the number of induced velocities that needs to be calculated is the same. The quantity  $C_a$  involves the analytical solution of a vortex ring induced velocity, which includes the evaluation of the elliptic integrals of the first and second kind. The quantity  $C_r$  involves the same calculation as  $C_a$  as well as the analytical solutions of near wake induced velocities at the rotor points where the time cost is very small. Thus  $C_r$  is approximately equal to  $C_a$ . Finally,  $C_f$  involves the resolution of the trigonometry functions based on Biot-Savart law, and  $C_m$  involves computing the Biot-Savart kernel functions. Thus  $C_f$  and  $C_m$  are considered to be of the same order of magnitude and slightly less expensive than  $C_r$  [59].

As expected, the above analysis shows that more physically accurate models are also more computationally expensive. BEM is the fastest model amongst those considered here. AFWVR and FWVR differ in solving the blade bound vortex strength equations, which is approximately the computational time of BEM, whilst FWVR, FWVF and NVLM differ by a factor  $N_\theta$  for the computation of the induced velocities, which can be significant. Regarding the modeling capability, BEM evaluates the rotor aerodynamics without considering the wake aerodynamics, whilst AFWVR evaluates both rotor and wake aerodynamics but uses a prescribed thrust coefficient to determine the vortex strengths. This prevents further analysis on the influence of the wake on the rotor. FWVR, FWVF and NVLM evaluate the coupled rotor aerodynamics and the wake aerodynamics, thus presenting similar capabilities, despite the fact that FWVR discretizes the wake into vortex rings. Thus Table 3.3 shows that the present simplified numerical model has low computational cost and relatively high performance compared to other reference models.

### 3.5. Conclusions

In this chapter, a simplified free wake vortex ring method for a horizontal-axis wind turbine is modified and assessed. Biot-Savart law is used for the near wake, while an analytical axis-symmetric vortex ring formulation is used for the

far wake. Different induced velocity formula are adopted for the near wake and far wake induced velocity. The self-induced velocity can also be calculated by the analytical vortex ring induced velocity formula. However, it should be noted that only the velocity on the vortex core center can be taken as self-induced velocity. If there is a small deviation from the core center, then the velocity can be much larger than it should be. It is also shown that the vortex pair convects slower than a single vortex ring, and the velocity induced by a vortex pair is also smaller than that of a single vortex ring. Finally, a new trailing vortex model with finite length vortex lines is proposed in this chapter. The results show that the new trailing vortex model can induce higher near wake velocities and more effectively reduce the unrealistic shear velocity exerted on the rotor by the vortex rings.

It should be noticed that, due to the simplification of the model, the near wake model perpendicular to the rotor axis and do not induce any velocity in the rotor plane. The far wake vortex rings convect freely and induce velocities in directions according to their own position and azimuth angles. Thus the vortex rings induce velocity in the rotor plane but not accurately represent the real conditions. Thus, the main aim of the model is a satisfactory prediction of the axial induction factor  $a$  and the thrust. The rotational induction factor  $a'$  cannot be predicted accurately due to the limitation of the model itself.

# 4

## Verification of the free wake vortex ring method

纵一苇之所如，凌万顷之茫然。—苏轼 (宋)

I row a boat as small as a leaf on the river as wide as boundless.

Su Shi (Song Dynasty)

The method presented in the previous chapter is verified on the 5 MW NREL turbine rotor subjected to different platform motions. The results are compared with other aerodynamic models for the same rotor and motions. The results show that the proposed method is reliable. In addition, the proposed method is less time consuming and has similar accuracy when compared with more advanced vortex-based methods.

## 4.1. Introduction

This chapter focuses on the validation of the free wake vortex ring method as introduced in Chapter 3. This chapter is organized as follows. First, the reference wind turbine parameters used for the validation are introduced in Section 4.2. Simulation results for a bottom-mounted wind turbine are discussed in Section 4.3, whilst the results for a floating wind turbine experiencing a single-DoF motion are shown in Section 4.4 and for multiple-DoF motion in Section 4.5. The wake structure of this model is discussed in Section 4.6. Finally, the conclusions are drawn in Section 4.7.

4

## 4.2. NREL 5MW reference turbine parameters

The aerodynamic model of the NREL 5MW reference turbine is simulated with the free wake vortex method, with rotor blades and tower assumed to be rigid. Thus the rotor motion is only due to the platform motions and the effect of tower structural distortions are not considered. The basic parameters of the turbine are shown in Table 2.1, the airfoils and aerodynamic parameters along the blade are given in Table 4.1, the rotor speed and blade pitch data corresponding to wind speed from cut-in to cut-out are given in Fig. 4.1 and other detailed information can be found in the NREL report [42].

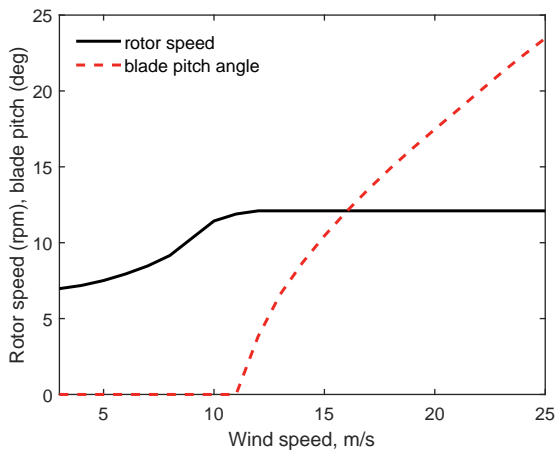


Figure 4.1: Rotor speed and blade pitch angle of NREL 5MW reference turbine

Node	RNodes	AeroTwst	DRNodes	Chord	Airfoil Table
[-]	[m]	[°]	[m]	[m]	[-]
1	2.8667	13.308	2.7333	3.542	Cylinder1.dat
2	5.6000	13.308	2.7333	3.854	Cylinder1.dat
3	8.3333	13.308	2.7333	4.167	Cylinder2.dat
4	11.7500	13.308	4.1000	4.557	DU40_A17.dat
5	15.8500	11.480	4.1000	4.652	DU35_A17.dat
6	19.9500	10.162	4.1000	4.458	DU35_A17.dat
7	24.0500	9.011	4.1000	4.249	DU30_A17.dat
8	28.1500	7.795	4.1000	4.007	DU25_A17.dat
9	32.2500	6.544	4.1000	3.748	DU25_A17.dat
10	36.3500	5.361	4.1000	3.502	DU21_A17.dat
11	40.4500	4.188	4.1000	3.256	DU21_A17.dat
12	44.5500	3.125	4.1000	3.010	NACA64_A17.dat
13	48.6500	2.319	4.1000	2.764	NACA64_A17.dat
14	52.7500	1.526	4.1000	2.518	NACA64_A17.dat
15	56.1667	0.863	2.7333	2.313	NACA64_A17.dat
16	58.9000	0.370	2.7333	2.086	NACA64_A17.dat
17	61.6333	0.106	2.7333	1.419	NACA64_A17.dat

Table 4.1: Distributed blade aerodynamic properties of the NREL 5MW reference turbine.

Firstly, in order to verify the code and show how the program works, a series of correlated parameters is outputted along the span of blade 1 with the wind speed of 8m/s, 12m/s and 15m/s after 120s of calculation time, as shown in Table 4.2, Table 4.3 and Table 4.4, respectively. In total, 20 control points are equally distributed along the blade span and the geometry parameters at these points are interpolated from Table 4.1. Furthermore, the contribution of the cylindrical part of the blade root is neglected. To simplify the process, the shaft tilt angle is set to 0, the wind speed is constant and uniform, and the rotor plane is normal to the wind direction. In the tables,  $n_i$  denotes the number of the control points and the other parameters are calculated at the control points. Additionally,  $\Gamma$  is the local blade bound circulation which is given by Eq. (3.68). Once  $\Gamma$  is known, the induced velocities can be determined, including: the near wake induced velocity in the  $z$  direction,  $V_z^{nw}$ , and the far wake induced velocities in the  $x, y$  and  $z$  directions, namely  $V_x^{fw}, V_y^{fw}, V_z^{fw}$ , respectively. The induced velocities are important parameters to determine the relative velocities  $V_n$  and  $V_r$  on the blade section, where for a fixed turbine  $V_n = V_0(1 - a)$  and  $V_r = \Omega r(1 + a')$ , as illustrated in Fig. 3.14. Knowing these two velocities, the relative wind angle  $\phi$  with respect to the rotor plane is computed from Eq. (3.66), and the angles of attack  $\alpha$  are calculated with Eq. (3.65). The values of  $\alpha$  are used to identify the tabulated data of  $C_l$  and  $C_d$  for the given airfoil polars. Using the geometry parameters from Table 4.1, the thrust on each blade segment  $dF_{Th}$  can be determined with Eq. (3.64), (3.67), and (3.69). The sum of the values  $dF_{Th}$  on all three blades is the rotor thrust. Here we can approximate the rotor thrust  $F_r$  by multiplying by a factor of three the thrust on one blade, as listed in the tables. The results are: 483kN, 715kN and 520kN respectively for the wind speed of 8m/s, 12m/s and 15m/s. From Fig. 4.2, we find that these data are in line with the rotor thrust given by NREL, as calculated using BEM theory. When retracing the parameters in the tables, it can be found that  $\Gamma$  and  $dF_{Th}$  are lowest on the root of the blade and gradually increase along the span until the maximum occurs at the outboard part of the blade and then drops at the tip. The axial induced velocity  $V_z^{fw}$  gradually decreases from root to tip. The velocity normal to the rotor  $V_n$  is mainly influenced by the free stream and the axial induced velocity. The velocity parallel to the rotor  $V_r$  is largely

Table 4.2: Aerodynamic parameters along the blade span with 8m/s wind speed

Wind speed=8m/s, tilt angle=0°, blade collective pitch=0°												
$n_i$	$\Gamma$	$V_z^{nw}$	$V_x^{fw}$	$V_y^{fw}$	$V_z^{fw}$	$V_\tau$	$V_n$	$\phi$	$\alpha$	$C_l$	$C_d$	$dF_{Tn}$
[-]	[m <sup>2</sup> /s]	[m/s]	[m/s]	[m/s]	[m/s]	[m/s]	[m/s]	[°]	[°]	[-]	[-]	[N]
1	0.70	1.54	-0.02	0.07	-0.91	-8.02	8.63	47.09	33.78	0.03	0.35	286
2	48.35	-0.59	-0.03	0.09	-0.90	-10.71	6.51	31.28	17.98	1.72	0.31	2077
3	59.65	-0.65	-0.04	0.11	-0.90	-13.40	6.45	25.73	13.26	1.71	0.04	2924
4	63.34	-0.51	-0.05	0.13	-0.89	-16.08	6.59	22.30	11.12	1.58	0.02	3701
5	63.78	-0.35	-0.06	0.16	-0.88	-18.77	6.77	19.83	9.56	1.43	0.01	4342
6	64.55	-0.29	-0.07	0.18	-0.87	-21.45	6.84	17.67	8.19	1.32	0.01	5021
7	64.84	-0.22	-0.07	0.20	-0.86	-24.14	6.92	15.98	7.31	1.23	0.01	5671
8	67.09	-0.30	-0.08	0.23	-0.85	-26.83	6.85	14.33	6.48	1.21	0.01	6521
9	68.20	-0.30	-0.09	0.25	-0.83	-29.51	6.87	13.10	6.12	1.17	0.01	7289
10	69.49	-0.31	-0.10	0.27	-0.82	-32.20	6.87	12.05	5.89	1.15	0.01	8101
11	72.06	-0.42	-0.11	0.29	-0.80	-34.89	6.78	11.00	5.64	1.16	0.01	9101
12	73.52	-0.49	-0.11	0.31	-0.77	-37.57	6.74	10.17	5.62	1.16	0.01	9999
13	74.75	-0.59	-0.12	0.33	-0.75	-40.26	6.66	9.39	5.64	1.16	0.01	10892
14	71.75	-0.43	-0.13	0.35	-0.73	-42.94	6.85	9.06	5.98	1.10	0.01	11151
15	71.61	-0.51	-0.13	0.36	-0.70	-45.63	6.79	8.46	5.94	1.10	0.01	11825
16	71.23	-0.61	-0.14	0.38	-0.67	-48.32	6.72	7.92	5.94	1.10	0.01	12452
17	70.43	-0.74	-0.14	0.39	-0.64	-51.00	6.62	7.39	5.95	1.10	0.01	12996
18	68.93	-0.97	-0.14	0.40	-0.61	-53.69	6.43	6.82	5.93	1.10	0.01	13387
19	64.77	-1.27	-0.15	0.40	-0.58	-56.38	6.15	6.23	5.84	1.09	0.01	13209
20	47.41	-0.96	-0.15	0.41	-0.54	-59.06	6.49	6.27	6.16	1.12	0.01	10131
Sum up the thrust along the blade												161076

influenced by the rotational speed of the rotor, thus it increases significantly along the blade from root to tip. These trends are in line with common sense and the final output thrusts are comparable with BEM. This gives confidence in the results obtained with the present method.

### 4.3. Results for a bottom-mounted wind turbine

The rotor thrust  $F_T$  for a bottom-mounted wind turbine on a monopile support structure in a constant free stream wind, from the cut-in wind speed of 3m/s to the cut-out wind speed of 25m/s, is calculated and shown in Fig. 4.2.

Table 4.3: Aerodynamic parameters along the blade span with 12m/s wind speed

Wind speed=12m/s, tilt angle=0°, blade collective pitch=3.823°												
$n_i$	$\Gamma$	$V_z^{nw}$	$V_x^{fw}$	$V_y^{fw}$	$V_z^{fw}$	$V_\tau$	$V_n$	$\phi$	$\alpha$	$C_l$	$C_d$	$dF_{Th}$
[-]	[m <sup>2</sup> /s]	[m/s]	[m/s]	[m/s]	[m/s]	[m/s]	[m/s]	[°]	[°]	[-]	[-]	[N]
1	1.00	2.01	0.04	0.07	-0.91	-10.60	13.10	51.02	33.88	0.03	0.35	616
2	67.56	-1.00	0.05	0.09	-0.91	-14.15	10.09	35.50	18.37	1.73	0.33	3922
3	81.73	-1.05	0.06	0.11	-0.90	-17.70	10.05	29.58	13.30	1.71	0.05	5307
4	84.65	-0.82	0.08	0.13	-0.89	-21.25	10.29	25.84	10.84	1.56	0.02	6540
5	82.68	-0.53	0.09	0.16	-0.88	-24.80	10.58	23.11	9.02	1.37	0.01	7442
6	81.54	-0.43	0.10	0.18	-0.87	-28.35	10.70	20.68	7.37	1.24	0.01	8383
7	78.85	-0.24	0.12	0.20	-0.86	-31.90	10.90	18.86	6.36	1.12	0.01	9120
8	80.79	-0.38	0.13	0.22	-0.84	-35.45	10.78	16.91	5.24	1.09	0.01	10376
9	80.34	-0.35	0.14	0.24	-0.82	-39.00	10.83	15.52	4.71	1.03	0.01	11349
10	80.17	-0.33	0.15	0.27	-0.80	-42.55	10.87	14.33	4.34	1.00	0.01	12353
11	82.11	-0.47	0.16	0.28	-0.78	-46.10	10.75	13.12	3.95	0.99	0.01	13704
12	82.70	-0.54	0.17	0.30	-0.76	-49.65	10.71	12.17	3.80	0.98	0.01	14863
13	83.13	-0.66	0.18	0.32	-0.73	-53.20	10.61	11.28	3.70	0.97	0.01	16006
14	77.51	-0.40	0.19	0.33	-0.70	-56.75	10.90	10.88	3.98	0.90	0.01	15916
15	76.32	-0.48	0.20	0.35	-0.67	-60.30	10.85	10.20	3.85	0.88	0.01	16651
16	75.14	-0.58	0.21	0.36	-0.64	-63.85	10.78	9.58	3.78	0.87	0.01	17358
17	73.75	-0.72	0.21	0.37	-0.60	-67.40	10.67	9.00	3.73	0.87	0.01	17983
18	71.74	-0.96	0.22	0.37	-0.57	-70.95	10.47	8.40	3.68	0.86	0.01	18414
19	67.00	-1.27	0.22	0.38	-0.54	-74.50	10.20	7.79	3.58	0.85	0.01	18058
20	49.01	-0.96	0.22	0.38	-0.50	-78.05	10.54	7.69	3.76	0.87	0.01	13837
Sum up the thrust along the blade												238198

Table 4.4: Aerodynamic parameters along the blade span with 15m/s wind speed

Wind speed=15m/s, tilt angle=0°, blade collective pitch=10.45°												
$n_i$	$\Gamma$	$V_z^{nw}$	$V_x^{fw}$	$V_y^{fw}$	$V_z^{fw}$	$V_\tau$	$V_n$	$\phi$	$\alpha$	$C_l$	$C_d$	$dF_{Th}$
[-]	[m <sup>2</sup> /s]	[m/s]	[m/s]	[m/s]	[m/s]	[m/s]	[m/s]	[°]	[°]	[-]	[-]	[N]
1	1.17	1.77	0.00	0.00	-0.08	-10.60	16.69	57.58	33.82	0.03	0.35	908
2	78.25	-1.40	0.00	0.00	-0.08	-14.15	13.52	43.69	19.93	1.78	0.40	4855
3	88.90	-1.21	0.00	0.01	-0.08	-17.70	13.71	37.75	14.83	1.69	0.09	5925
4	93.28	-1.14	0.00	0.01	-0.08	-21.25	13.78	32.96	11.34	1.60	0.02	7227
5	87.53	-0.76	0.00	0.01	-0.08	-24.80	14.16	29.73	9.01	1.37	0.01	7890
6	82.01	-0.55	0.01	0.01	-0.08	-28.35	14.37	26.88	6.94	1.19	0.01	8441
7	74.54	-0.26	0.01	0.01	-0.08	-31.90	14.66	24.68	5.55	1.01	0.01	8633
8	73.21	-0.39	0.01	0.01	-0.08	-35.45	14.53	22.29	3.99	0.95	0.01	9411
9	68.01	-0.25	0.01	0.01	-0.08	-39.00	14.68	20.62	3.18	0.85	0.01	9617
10	63.62	-0.15	0.01	0.01	-0.08	-42.55	14.77	19.15	2.54	0.77	0.01	9814
11	62.97	-0.30	0.01	0.01	-0.08	-46.10	14.63	17.61	1.80	0.74	0.01	10519
12	60.09	-0.29	0.01	0.02	-0.07	-49.65	14.64	16.42	1.42	0.70	0.01	10810
13	57.54	-0.35	0.01	0.02	-0.07	-53.20	14.58	15.32	1.12	0.66	0.01	11091
14	50.13	-0.09	0.01	0.02	-0.07	-56.75	14.84	14.65	1.13	0.57	0.01	10307
15	47.00	-0.12	0.01	0.02	-0.07	-60.30	14.80	13.79	0.82	0.54	0.01	10268
16	44.33	-0.17	0.01	0.02	-0.07	-63.85	14.76	13.02	0.58	0.51	0.01	10253
17	41.96	-0.24	0.01	0.02	-0.07	-67.40	14.69	12.30	0.41	0.49	0.01	10246
18	39.66	-0.36	0.01	0.02	-0.07	-70.95	14.57	11.60	0.26	0.47	0.01	10194
19	36.14	-0.52	0.01	0.02	-0.07	-74.50	14.41	10.95	0.11	0.45	0.01	9753
20	25.38	-0.32	0.01	0.02	-0.07	-78.05	14.61	10.60	0.04	0.45	0.01	7176
Sum up the thrust along the blade												173338

To validate the accuracy of the present model, the thrust force computed with different methods for the same load cases has been found in the literature, including the results from NREL [42], which are calculated using FAST-Aerodyn based on BEM theory; the results from Sørensen [61], where the Reynolds-Averaged Navier-Stokes (RANS) method was used, and the results from Lee [52], where nonlinear vortex lattice method (NVLM) was used. Figure 4.2 shows good agreement with the thrust forces of the literature. From the cut-in wind speed to the rated wind speed, the thrusts obtained with the NVLM model, RANS model and the present FWVR model are higher than the thrusts from FAST v8, while the thrusts at above-rated wind speeds from these three models are lower than the thrusts from FAST v8. However, it should be noted that the wind turbine used by the RANS model is not exactly the NREL 5MW reference turbine but a similar one, which can be a good reference. Also, the thrust forces of the NREL 5MW reference turbine released by NREL[42] are not pure aerodynamic thrusts, but also include the effects of gravity and inertial loads of the rotor<sup>1</sup>, which are significantly higher than the pure aerodynamic thrusts. From 6m/s to 15m/s, the thrust force obtained with the present vortex ring method agrees well with that given by NREL. For wind speeds smaller than 6m/s or higher than 15m/s, the thrusts deviate. The present results are lower than that given by NREL, while both RANS and NVLM didn't show the results with wind speed lower than 6m/s. According to the literature, BEM is not accurate enough in low speed regions [73] and high speed regions where flow separation occurs [74]. The results suggest that the present vortex ring method can provide better results than FAST in low and high wind speed regions.

The axial induced velocities of wind speeds 6m/s, 11.4m/s and 18m/s of the bottom-mounted wind turbine are compared with the results from FAST v8 as shown in Figure 4.3. It can be seen that the two results from 20m to 60m along the blade match well with each other. Due to the tip- and root-corrections, the inductions from FAST v8 at the tip and root of the blade are both zero. The induction from the FWVR at the tip of the blade also exhibits a drop for all the three wind speeds, which are mainly influenced by the near wake model and the outer ring of the far wake model. By contrast, at the root of the blade, the inner

<sup>1</sup><https://wind.nrel.gov/forum/wind/viewtopic.php?f=2&t=917>

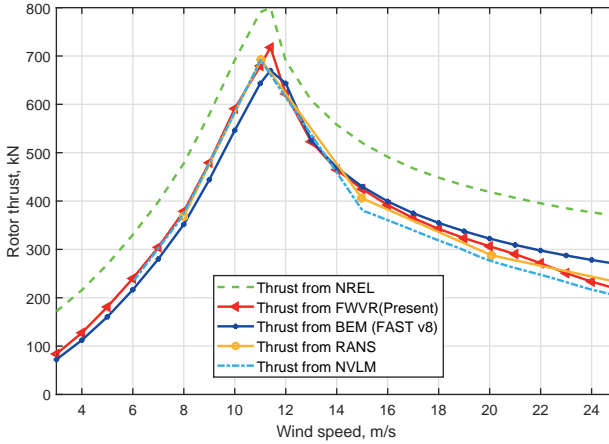


Figure 4.2: Comparison of the thrust force of monopile NREL 5MW wind turbine as a function of the wind speed.

ring of the far wake model mainly weakens the inductions while the inductions from the near wake model are still strong. With the increase of the wind speed, the effect of the near wake model becomes stronger than that of the far wake model. Thus it can be seen that, at the wind speed 6m/s, the induction drops at the root whilst it is still strong for the other two wind speeds. The axial induction factors weighted with the swept area of the three wind speeds are 0.3, 0.262 and 0.044 from FWVR and 0.305, 0.242 and 0.035 from FAST v8, respectively.

#### 4.4. Floating wind turbine under a single-DoF motion

Since the results from the present vortex ring method are shown to be reliable for a bottom-mounted wind turbine, the model is now applied to a floating offshore wind turbine with a prescribed platform motion. The platform motion is prescribed along a single degree-of-freedom (either translational or rotational) using a sine function with motion amplitude ( $A_i$ ) and frequency ( $f_i$ ),  $i = 1, 2$ , i.e.

$$X(t) = A_1 \sin(2\pi f_1 t). \quad (4.1)$$

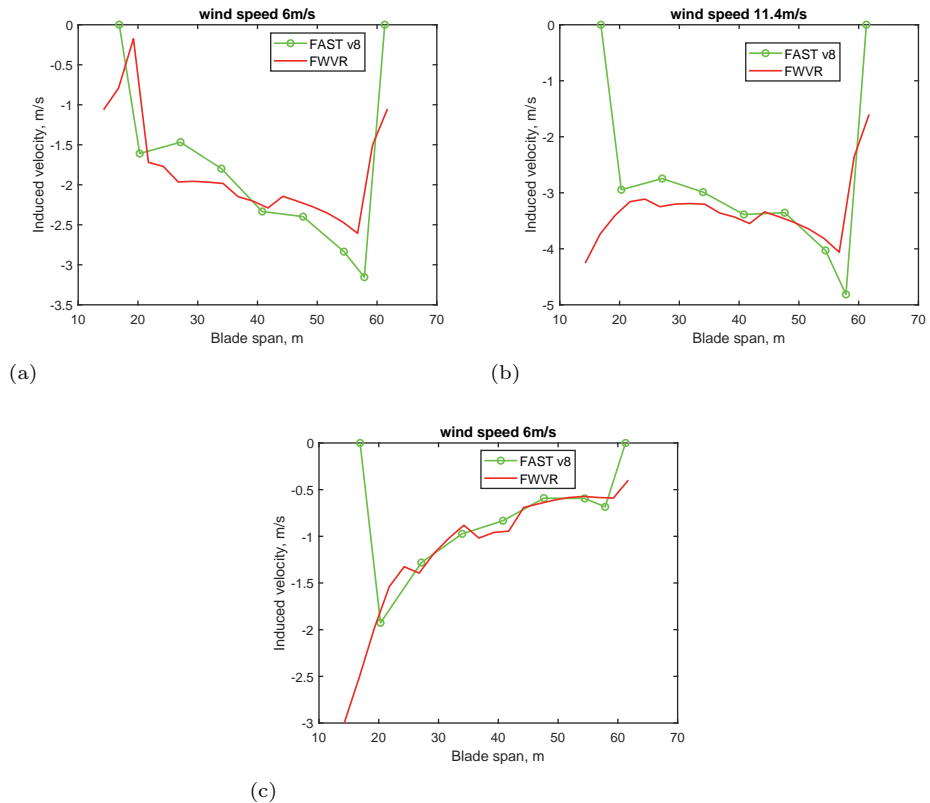


Figure 4.3: The axial induced velocities at wind speeds 6m/s, 11.4m/s and 18m/s

The associated values of the thrust force are calculated and compared with those of Lee [52] for a wind speed of 8m/s, a rotor speed of 9.16 rpm, and under the motion amplitudes and frequencies listed in Table 4.5.

Motion	Amplitude $A_i$ [m or °]	Frequency $f_i$ [Hz]
Translation (surge, sway, heave)	4	0.1
Rotation (roll, pitch, yaw)	4	0.05
surge	4,8,12	0.03
pitch	2,4,6	0.03

Table 4.5: Amplitude and frequency of the prescribed single-DoF motions [52]

The results of the thrust force with individual translations and rotations of the floating platform are shown in Fig. 4.4 and compared with the NVLM method [52]. Fig. 4.4a shows the thrust curves with individual surge, sway and heave motions, whilst Fig. 4.4b shows the thrust force with individual yaw, pitch, and roll motions. All these motions have been imposed separately, as this study is restricted to a one DoF system. The thrust for a fixed rotor is also provided for comparison. For a moving rotor, the thrust forces obtained from both methods have similar amplitude and frequency, which are both consistent with the thrusts shown in Fig. 4.2.

Figure 4.4 shows that the thrust under translational platform motions is most sensitive to surge, and the thrust under rotational platform motions is most sensitive to pitch, for the reason that these motions are in the wind direction, which can significantly influence the relative wind speed normal to the rotor disc. When the rotor has a leeward speed, the relative wind speeds are reduced on the blades and the angles of attack are smaller, which leads to a lower thrust load than average. When the rotor has a windward speed, the situation is reverse and the thrust load is larger than average. It is also observed that the heave and sway motions of the same amplitude and frequency theoretically

have equivalent influence on the rotor thrust. The heave and sway motions can change the relative tangential wind speed on the airfoils, which either increases or decreases the angle of attack according to the azimuthal angle of the blade, thus increasing or decreasing the thrust. However, this influence is relatively small as the change of tangential wind speed is much smaller than the tangential speed coming from the rotor rotation. Figure 4.4a shows that with the present FWVR method, the thrust force under heave and sway motions almost overlap and slightly fluctuate around the thrust value of the bottom-mounted turbine, which is deemed to be reasonable.

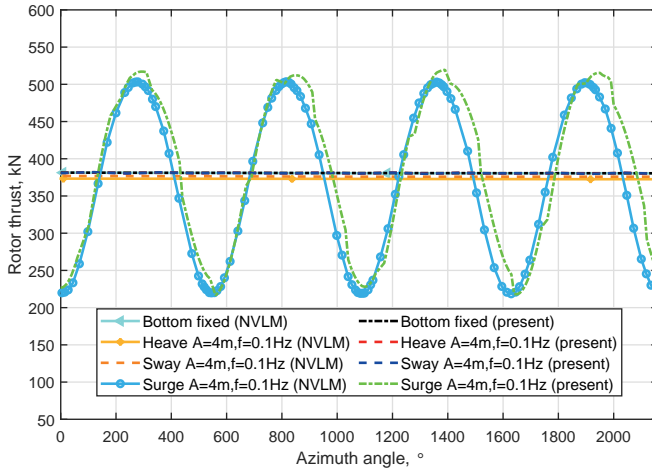
The effect of the roll motion on the thrust is similar to that of the heave and sway motions, which mainly influence the relative tangential wind speed and the wake induced velocity on the rotor. The yaw motion can reduce the overall wind area of the rotor, hence reducing the thrust load compared to the bottom-mounted turbine, as obtained for both NVLM and FWVR.

The effect of the surge and pitch motions with different amplitudes are further analyzed and compared with the results of Lee [52] in Fig. 4.5. Figure 4.5a compares the thrust with surge motions with the amplitude of 4m, 8m, 12m and the frequency of 0.03Hz, whilst Fig. 4.5b compares the thrust with pitch motions with the amplitude of 2°, 4°, 6° and the frequency of 0.03Hz. Since the amplitudes of the platform motions are small and the frequency is relatively low, the thrusts change linearly with platform motions for both surge and pitch.

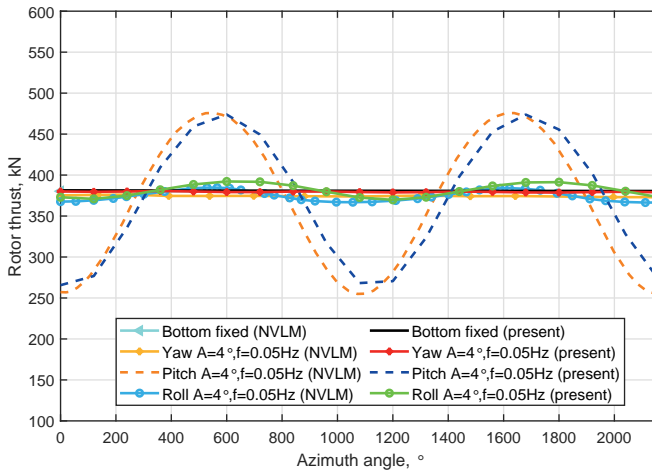
The angles of attack are calculated and compared with the literature at the following operating and environmental conditions taken from Sebastian [51] and de Vaal [59]:

1. below-rated:  $V_\infty = 6.0m/s$ ,  $\lambda = 9.63$ ,  $H_s = 1.83m$ ,  $T_p = 12.72s$ ,
2. at rated:  $V_\infty = 11.4m/s$ ,  $\lambda = 7.00$ ,  $H_s = 2.54m$ ,  $T_p = 13.35s$ ,
3. above-rated:  $V_\infty = 18.0m/s$ ,  $\lambda = 4.43$ ,  $H_s = 4.09m$ ,  $T_p = 15.33s$ ,  $\theta_p = 15^\circ$ .

The platform motions in the time domain are synthesised as sinusoidal series at the first two dominant frequencies  $f_1$  and  $f_2$  extracted from the simulation [51]. Thus the time-varying platform motion is determined as

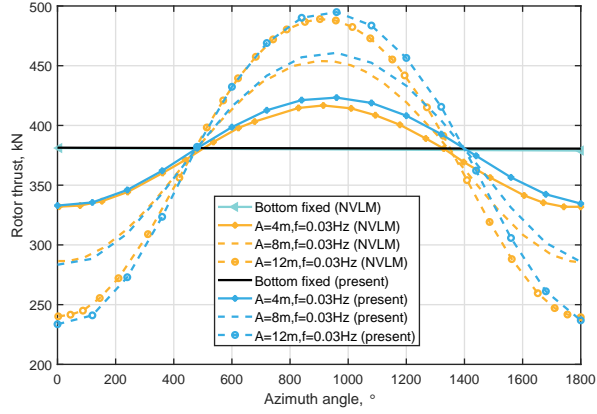


(a)

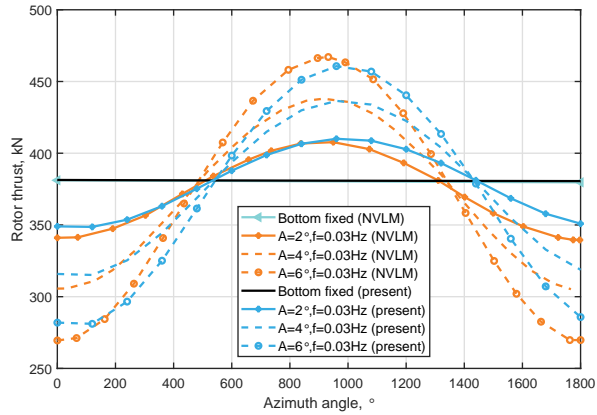


(b)

Figure 4.4: Variation in the thrust of wind turbine in (a) translational motions ( $A=4m$ ,  $f=0.1Hz$ ) and (b) rotational motions ( $A=4^\circ$ ,  $f=0.05Hz$ )



(a)



(b)

Figure 4.5: Variation in the thrust of wind turbine in (a) surge ( $A=4\text{m}, 8\text{m}, 12\text{m}$ ,  $f=0.03\text{Hz}$ ) and (b) pitch ( $A=2^\circ, 4^\circ, 6^\circ$ ,  $f=0.03\text{Hz}$ )

$$X(t) = X_0 + A_1 \sin(2\pi f_1 t + \phi_1) + A_2 \sin(2\pi f_2 t + \phi_2), \quad (4.2)$$

where the mean value  $X_0$ , amplitudes  $A_i$ , frequencies  $f_i$  and phase angles  $\phi_i$  are given in Table 4.6.

Oper.	Platf.	Mode	$X_0$ [m]/[°]	$A_1$ [m]/[°]	$f_1$ [Hz]	$\phi_1$ [rad]	$A_2$ [m]/[°]	$f_2$ [m]/[°]	$\phi_2$ [rad]
1	ITI	surge	13.602	0.725	0.007	-1.163	-0.442	0.078	2.609
1	ITI	heave	-0.130	0.318	0.078	1.303	0.254	0.108	2.702
1	ITI	pitch	0.591	1.475	0.078	-0.066	1.630	0.083	1.816
1	OHS	pitch	1.580	-0.084	0.066	1.930	-0.116	0.077	3.113
1	OHS	yaw	-0.021	0.091	0.108	1.983	-0.036	0.120	3.429
1	TLP	surge	1.206	0.436	0.016	-0.831	-0.222	0.077	3.018
2	ITI	pitch	1.722	-0.637	0.065	-0.381	1.677	0.077	1.835
3	ITI	pitch	0.939	1.518	0.066	2.132	2.979	0.078	6.863
3	OHS	pitch	3.324	11.961	0.029	0.420	0.000	0.000	0.000
3	OHS	yaw	-0.222	2.000	0.029	-0.359	3.185	0.058	3.385

Table 4.6: Parameters of platform motions [51] for a floating offshore wind turbine with different floater types.

The mean  $\mu_\alpha$  and standard deviation  $\sigma_\alpha$  of  $\alpha$  on the outboard 2/3 of the blade are compared with those from the work of Sebastian [51] and de Vaal [59], as shown in Table 4.7. The current numerical results are presented in the column titled 'FWVR2, tilt=0°', without shaft tilt angle. It is shown that  $\mu_\alpha$  and  $\sigma_\alpha$  have the same trend as that observed in the literature. In particular,  $\mu_\alpha$  is rather independent of the platform motion, for a given wind speed. The bottom-mounted monopile presents the smallest value of  $\sigma_\alpha$  compared with floating support structures at the same wind speed. This can be explained by the fluctuations of the induced velocities caused by the turbine motion in the floating case. The value of  $\sigma_\alpha$  increases with an increase in platform motion. Also, the pitch motions of the platform tend to have more effect on the value of  $\sigma_\alpha$  than the surge motions, because the pitch motions generate non-perpendicular wind velocities on the rotor. The values of  $\mu_\alpha$  are smaller than the reference results throughout and the difference are within 1°, which is considered to be acceptable. The column 'FWVR2, tilt=5°' shows the results in the design condition of the NREL 5MW turbine with a nonzero tilt angle. It can be seen that the values of  $\mu_\alpha$  are slightly smaller than for the case with a zero tilt angle, which is mainly because the total wind area is smaller on the rotor with tilt. Moreover,  $\sigma_\alpha$  is significantly influenced by the tilt angle in all the cases because the latter can generate fluctuating wind speeds especially on the outboard part of the blades.

Operation	Platform	Mode	WInDS [51]		FWVR1 [59]		FWVR2, tilt=0°		FWVR2, tilt=5°	
			$\mu_\alpha$ [°]	$\sigma_\alpha$ [°]						
1	Monopile	-	3.95	0.23	3.86	0.48	3.82	0.15	3.71	3.23
1	ITI	surge	3.95	0.40	3.87	0.53	3.78	0.23	3.64	3.23
1	ITI	pitch	3.99	2.21	3.90	1.5	3.89	1.92	3.84	3.85
1	OHS	pitch	3.94	0.32	3.84	0.49	3.66	0.25	3.84	3.21
1	TLP	surge	3.95	0.27	3.86	0.49	3.64	0.23	3.70	3.23
2	Monopile	-	6.76	0.37	6.66	0.69	5.84	0.35	5.76	3.35
2	ITI	pitch	6.78	1.67	6.67	1.30	5.82	1.09	5.73	3.47
3	Monopile	-	-0.10	0.80	-0.31	2.24	-0.59	0.05	-0.61	2.91
3	ITI	pitch	-0.08	2.26	-0.28	2.88	-0.59	1.87	-0.61	3.39
3	OHS	pitch	-0.45	3.59	-0.52	3.09	-0.83	2.40	-0.85	3.57

Table 4.7: Mean and standard deviation of  $\alpha$  at the outboard 2/3 part of the blade.

The thrust force on the rotor for a bottom-mounted monopile at rated wind speed and three floating support structures in below-rated, rated and above-rated conditions are evaluated in the time domain (Fig. 4.6) and frequency domain (Fig. 4.7). Figure 4.6 shows that the thrust curves fluctuate around their mean values, after an initial transient. The latter is due to the fact that a certain time is needed for the far-wake vortex rings to develop. Thus, initially, only the near wake mostly contributes to the values of induced velocities. After about 50 seconds, a steady-state is reached and results can be considered reliable. Figure 4.7 highlights the dominant frequencies in the rotor thrust. For a bottom-mounted turbine on a monopile at rated wind speed, the first dominant frequency is at about 0.6Hz, which corresponds to the vortex rings shedding frequency, which is a numerical effect. Higher frequencies are multiples of the first one. Also, when the induced velocity reaches a peak value, the thrust force reaches a minimum value, and vice versa. For the three FOWTs, without exception, the frequencies of the platform motions dominate in the frequency of the thrust force. This is because the velocities induced by the platform motions are larger than the induced velocities from the vortex rings.

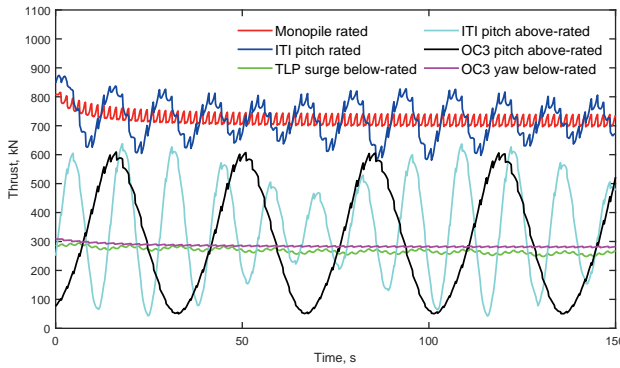


Figure 4.6: Time evolution of the thrust force on the rotor for different turbine configurations.

Finally, we evaluate the blade-bound vortex strength  $\Gamma$  and its relationship with other parameters. As explained before, the value of  $\Gamma$  is obtained by equating the lift forces calculated from the 3D vortex lifting law to that from

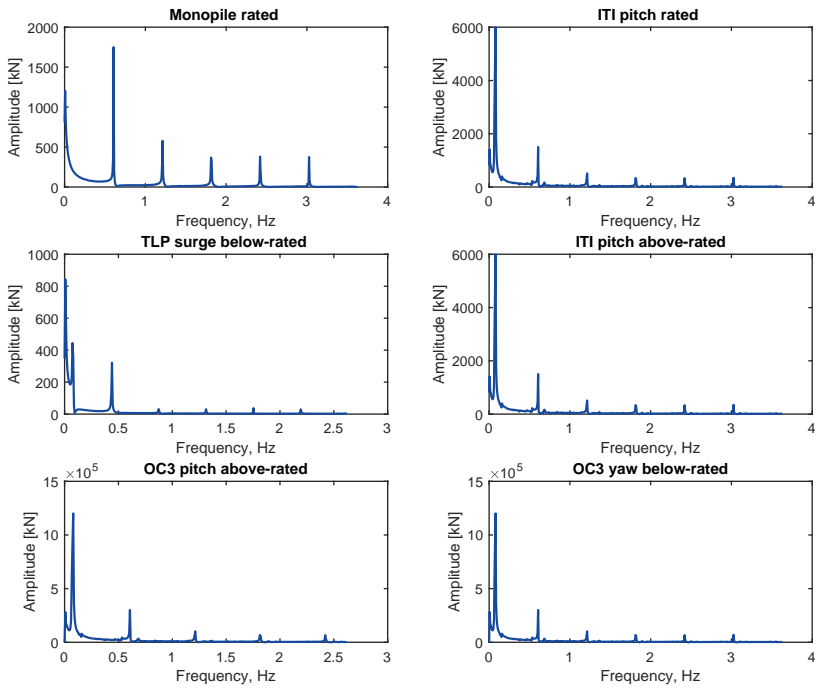


Figure 4.7: Frequency content of the thrust force on the rotor for different turbine configurations.

blade element theory (Eq. (3.68)) This leads to:

$$\Gamma = \frac{c}{2} C_l(\alpha) V^n, \quad (4.3)$$

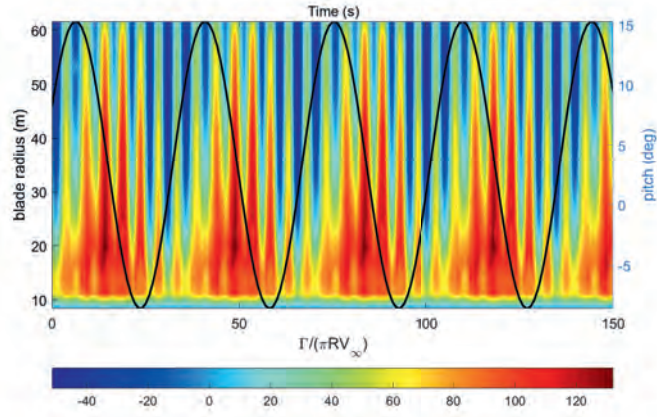
where  $c$  is the constant chord length,  $C_l$  is the lift coefficient and  $V^n$  is the normal wind speed. The time evolution of  $\Gamma$ ,  $V^n$ ,  $C_l$  and  $\alpha$  are shown in Fig. 4.8 and Fig. 4.9, for the case of a floating wind turbine (OHS) above rated power. In each figure, the continuous line shows the platform pitching motion. The non-dimensional blade bound vortex strength  $\Gamma/(\pi R V_\infty)$  (Fig. 4.8a) fluctuates regularly with the platform pitch motion. Also, the high-frequency oscillation with the period of about 4.96s is due to the rotor tilt angle. It can be seen that on the outboard part of the blade, there are negative values of  $\Gamma$ , which is consistent with the negative values of  $\alpha$  and  $C_l$  observed in the same conditions (Figs. 4.9a and 4.9b). The normal relative wind speed  $V^n$  (the relative velocity without the component along the blade) is less influenced by the platform motion and the rotor tilt, its main fluctuations coming from the constant rotation of the rotor.

## 4.5. Floating wind turbine under multiple-DoF motion

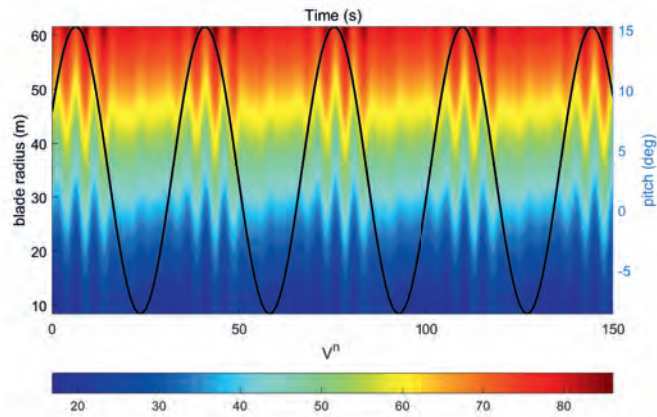
Three multiple-DoF operating conditions are also considered for the NREL 5MW turbine, combining the properties listed in Table 4.6. The aerodynamic performance of a bottom fixed wind turbine is also presented here for comparison. The following conditions are presented.

1. below-rated: The ITI Energy barge with platform surge, heave, and pitch DoFs,
2. below-rated: The OC3-Hywind spar-buoy with platform pitch and yaw DoFs, and
3. above-rated: The OC3-Hywind spar-buoy with platform pitch and yaw DoFs.

The multiple-DoF motion thrust values of the ITI Energy barge and the OC3-Hywind spar with the below-rated operating conditions, as well as the

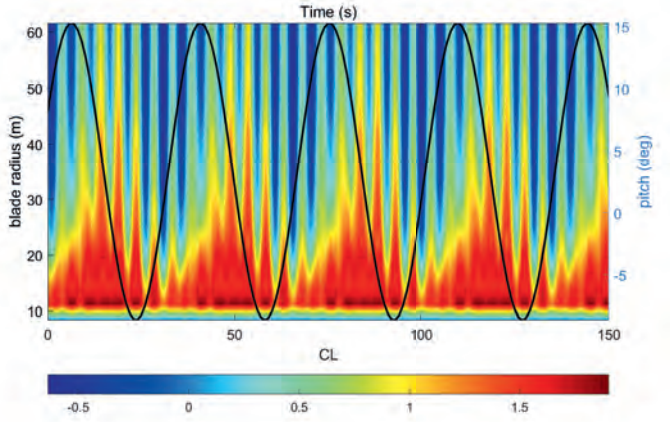


(a)

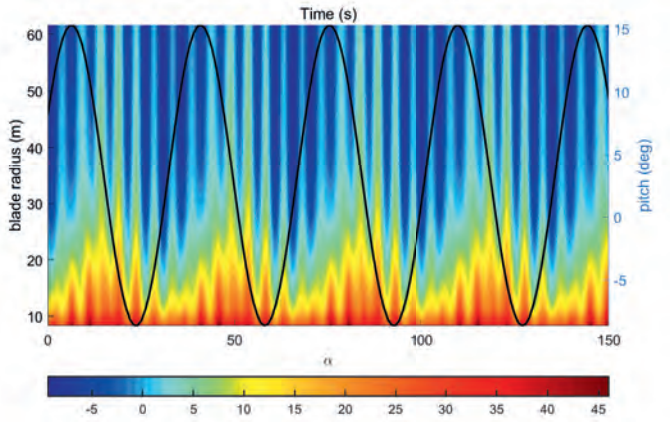


(b)

Figure 4.8: Time evolution of: (a)  $\Gamma/(\pi RV_\infty)$  and (b)  $V^n$  as a function of the location on the blade. The continuous line shows the pitching motion of the platform. Results are shown for the OHS above rated conditions.



(a)



(b)

Figure 4.9: Time evolution of: (a)  $C_t$  and (b)  $\alpha$  as a function of the location on the blade. The continuous line shows the pitching motion of the platform. Results are shown for the OHS above rated conditions.

bottom fixed thrust values, are shown in Fig. 4.10 and compared with those of Lee [52]. It should be noted that the start time of the platform motions in the NVLM code and the present FWVR code are different. The platform motions start at a zero azimuth angle in the FWVR code while it starts approximately after one rotation of the rotor in the NVLM code, which can be seen in the figure. In order to compare the thrusts of these two methods more clearly, the thrust force from the present FWVR method is therefore shifted by  $+360^\circ$  along the Azimuth angle-axis, so that it coincides with the thrust force from the NVLM method. It can be found that the bottom fixed thrust calculated with the present FWVR method is higher than the bottom fixed thrust calculated with the NVLM method, which is consistent with what has been observed in the previous section. The thrust amplitudes and frequencies of both the ITI Energy barge and the OC3-Hywind spar platform are comparable between these two methods. The large oscillation with a long time period envelope is consistent with the fluctuation of relative wind velocity normal to the rotor disc led by the 3-DoF platform motions.

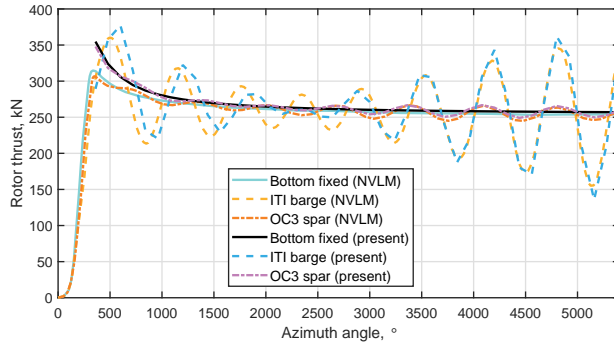


Figure 4.10: Variation in the thrust of 5MW NREL wind turbine in multiple-DoF motions

The wake induction at the rotor as a function of the downstream distance of the vortex rings is computed as a percentage of the total induced velocity at the rotor, which is compared with Sebastian [51] in Fig. 4.11 for the ITI energy barge and in Fig. 4.12 for the OC3-Hywind spar-buoy. The blue dashed lines represent the contribution of the induced velocities from each section along the wake given by the FWVF method and the red lines represent the same parameter from

the present FWVR method. The red circles on the line indicate the position of the vortex rings. The black lines and the green dotted lines represent the accumulated percentage of the induced velocities along the wake given by the FWVF method and the FWVR method, respectively. The induced velocity data output from the present FWVR method is captured at the operating time of 150s, when a steady-state is reached. Since the downstream convection of the vortex rings is a dynamic process, the induced velocity does vary slightly with time.

In general, the induced velocities are comparable between the two methods. Figure 4.11 shows that the accumulated percentage of the induced velocity decreases as the distance from the rotor increases. For example, the percentage at one diameter downwind (1D) is about 84.1% for FWVF and 86.2% for FWVR (discrepancy of 2.3%), at 2D it is about 94.2% for FWVF and 96.1% for FWVR (discrepancy of 2.1%), at 3D it is about 97.6% for FWVF and 98.6% for FWVR (discrepancy of 1.0%), and finally at 4D the percentages with both methods are above 99%. The induced velocities from each section along the wake from these two methods show similar trends with large fluctuations, which are mainly influenced by the platform motions, particularly from the pitch motion. In Fig. 4.12a, the accumulated percentage of the induced velocity at 1D is about 82.2% for FWVF and 85.1% for FWVR (discrepancy of 2.4%); at 2D it is about 93.5% for FWVF and 95.5% for FWVR (discrepancy is 2.1%); at 3D it is about 97.9% for FWVF and 98.5% for FWVR (discrepancy of 0.6%), and finally at 4D both percentages are above 99%. The induced velocities from each section along the wake obtained with these two methods show similar trends, namely a decrease with the increase of distance downstream. Also, the influence of the pitch and yaw platform motions are relatively small, and no significant fluctuation of the induced velocities are visible with both methods. In Fig. 4.12b, the accumulated percentage of the induced velocity at 1D is about 84.4% for FWVF and 92.7% for FWVR (discrepancy is 9.8%); at 2D it is about 91.2% for FWVF and 95.6% for FWVR (discrepancy is 4.8%); at 3D it is about 95.4% for FWVF and 96.3% for FWVR (discrepancy is 0.9%); and at 4D they are both close to 99%. The induced velocities from each section along the wake obtained with these two methods both decrease with an increase of distance downstream

and the influence of the pitch and yaw platform motions are relatively small. Also, no significant fluctuations are apparent in the induced velocities for both methods. The present FWVR method predicts significantly larger contributions of the induced velocity from the vortex rings up to 1D distance downstream. This is mainly because the vortex rings convect faster with an increase in wind speed and the density of rings decreases at higher wind speed. Because the induced velocity is very sensitive to the distance between the control point and the vortex ring, as apparent from Eq. (3.30), the contribution to the induced velocity from the front rings is much larger than that from the rings far away from the rotor.

There are several differences between the wake induction of these two methods. The first one is that the induced velocities of the wake given by the FWVF method are output for each vortex segment in the wake, while the induced velocities obtained with the present FWVR method are output for each vortex ring. As explained in Section 3.4 there are fewer vortex rings than vortex segments in the wake, thus the induced velocities in the wake from the FWVF method are relatively constant compared to those from the FWVR method. The second difference is that, due to the different modeling properties, the induced velocities obtained with the FWVF method start from a position very close to the rotor, while the induced velocities from the present FWVR method start from the position of the first vortex ring. Also, the induced velocity at the rotor from the near wake model is not accounted for here. Lastly, the induced velocities close to the rotor (blue line) given by FWVF are all truncated to below 20%, while the peak values are not shown, which might affect the comparison and conclusion in this section.

## 4.6. Discussion on the wake structure

The wake structures of the bottom-fixed wind turbine with the specified below-rated operating condition, as well as the FOWTs with the three multiple-DoF platform motions, are shown in Fig. 4.13 at the operating time of 150s. The inner and outer rings are distinguished with red and blue colors, respectively. The vectors indicate the directions of motion of the control points. The wake structures of the below-rated operating conditions as shown in Fig. 4.13a,

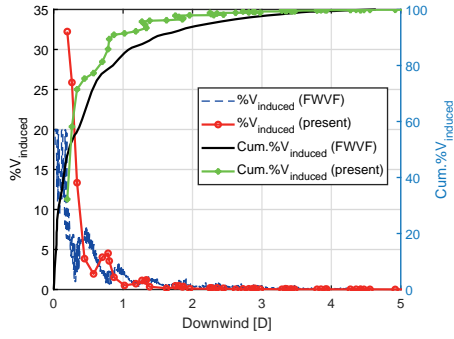


Figure 4.11: Wake induced velocity at the rotor for the NREL-5MW turbine + ITI Energy barge under platform surge, heave, and pitch for below-rated operating conditions.

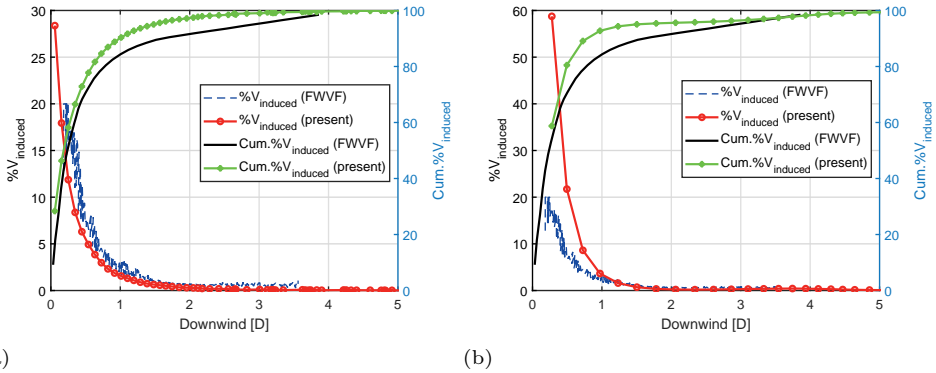
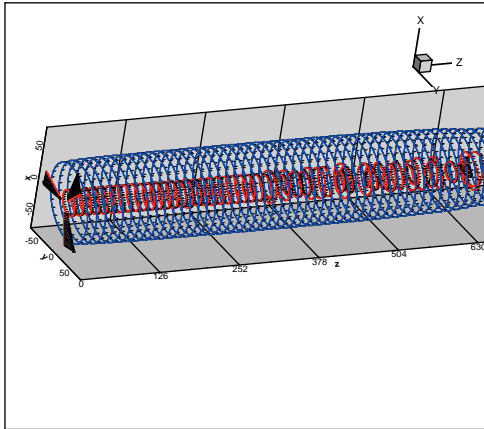


Figure 4.12: Wake induced velocity at the rotor for the NREL-5MW turbine + OC3-Hywind spar-buoy under platform pitch and yaw. (a) Below-rated; (b) Above-rated

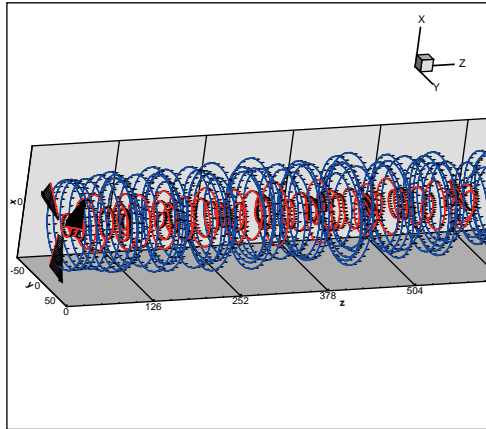
Fig. 4.13b and Fig. 4.13c are found to be more compact than those in the above-rated operating conditions as shown in Fig. 4.13d. This is due to the fact that the vortex rings are convected at higher speed when the free stream velocity increases. It is also clear that the vortex ring radii are constant along the wake as the blade bound vortex strengths are constant. By contrast, the wake structures vary in the wake of FOWTs because both the blade bound vortex strengths and the rotor position change with time, thus affecting the roll-up process in the wake model. Additionally, the vortex rings of different radii and strengths interact with each other which causes additional disturbances. This is particularly true below-rated conditions, for which the downstream vortex rings are relatively close to one another, as seen in Fig. 4.13b and Fig. 4.13c.

## 4.7. Conclusions

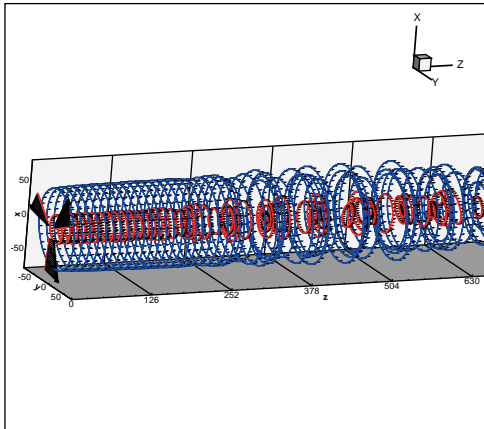
In this chapter, the NREL 5MW wind turbine is used to verify the free-wake vortex model developed in this work. The rotor thrust force associated with a fixed monopile wind turbine was calculated with the present free wake vortex ring method and compared with the result from BEM theory. The results show a good agreement between the two approaches for a large range of wind speeds. At low and high wind speeds, the results suggest that the present free wake vortex ring method is more reliable than BEM theory when calculating the rotor thrust. The method was also applied to floating offshore wind turbines at below-rated, rated, and above-rated conditions. It was found that the mean and standard deviations of the angles of attack at the outboard 2/3 part of the blade are comparable with the literature. Also, the rotor tilt angle seems to significantly influence the standard deviation of the angle of attack. The analysis of the thrust force on the rotor shows that its first dominant frequency for a monopile support structure is dominated by the vortex shedding frequency, whilst its first dominant frequency for a floating support structure is driven by the platform motion. Also, the latter influences the lift coefficient on the rotor, and hence, the blade bound vortex strength. To conclude, the modified free wake vortex ring method proposed here is considered to be effective and reliable when predicting the aerodynamic loads on horizontal-axis wind turbines, both on fixed and floating support structures. It can be used to calculate conditions



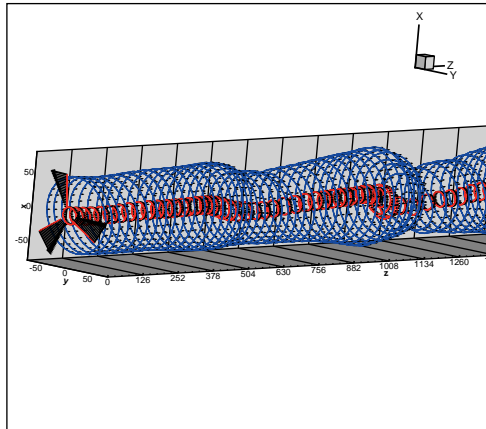
(a)



(b)



(c)



(d)

Figure 4.13: Wake structures of the NREL 5MW turbine: (a) Bottom fixed below-rated; (b) ITI barge below-rated; (c) OHS below-rated; (d) OHS above-rated.

leading to small angles of attack at low wind speeds, small angles of attack due to blade pitch motion at high wind speeds, and varying angles of attack due to unsteady wind flows in the context of floating offshore wind turbines. In the next chapter, the method will be further applied to the detailed analysis of wake-rotor interactions under a prescribed surge motion of the turbine.

# 5

## Working states of a floating offshore wind turbine in surge motion

行成于思，毀于隨。—韓愈 (唐)

Action is successful because of thought and failing because of following.

Han Yu (Tang Dynasty)

In this chapter, the free wake vortex method developed in Chapter 3 is used to simulate the different working states of a floating offshore wind turbine under a prescribed surge motion. First, the focus is on the vortex ring state (VRS) and good agreement is shown with the CFD analysis of Kyle et al [21]. Second, the results are analysed for a full cycle of the surge motion where onsets of the windmill state and propeller state are also highlighted. Finally, it is shown that a continuous pitching of the blade during the surge motion can be used to

mitigate the negative effects associated with the vortex ring state and propeller working state.

## 5.1. Introduction

As discussed in Chapter 2, floating offshore wind turbines can experience larger unsteady loads than bottom-fixed turbines during operation. The range of working states experienced by the rotor are also different. In particular, the literature highlights four possible rotor working states for FOWTs. In this work, three of them are identified for a wind turbine rotor undergoing a prescribed surge motion. First, the onset of the vortex ring state (VRS), and its influence on the aerodynamic performance of FOWTs, are shown. This is done by using the free wake vortex ring method [75] introduced in Chapter 3, in combination with the VRS prediction criteria defined in Chapter 2. The results are compared with those of Kyle [21] that were obtained using a CFD method. Second, one surge cycle is investigated in more details to highlight the occurrence of other working states under steady free stream wind conditions.

In this chapter, the following questions are answered:

1. How do the results obtained with the present free vortex ring model compare with those obtained by Kyle [21] using a CFD method? In particular:
  - How do the thrust forces and angles of attack compare with the CFD values?
  - Are the vortex ring state and propeller working state identified for the same load cases using both methods?
  - Using the free vortex ring model, does the propeller working state also occur after the onset of the vortex ring state, as in the CFD analysis from Kyle [21]?
2. What are the effects of the change of working state on the rotor? In particular:
  - How can the boundaries between the propeller working state and the vortex ring state be identified?
  - What is the influence of the change of working states on the aerodynamic performance of the rotor, and can it be mitigated?

This chapter is organized as follows. Firstly, the problem description is outlined in Section 5.2, including the turbine coordinate system and load cases. The results under a prescribed surge motion are shown in Section 5.3. In particular, the thrust force and angles of attack at the rotor are compared with Kyle's model. Additionally, the percentage of occurrence of VRS is given and more insights in the velocity and thrust along the blade span are presented. The wake structure is also shown. Overall, results are first discussed for multiple periods of the surge motion. Then, the focus is on one period of the surge motion, in order to better analyse the boundaries between the various working states. In this context, the occurrence of both windmill state and propeller state, in addition to VRS, is highlighted. Insights are provided into the velocity field through and around the rotor, the angles of attack, the thrust coefficient, and the aerodynamic load associated with the change in working state. Finally, conclusions are drawn in Section 5.4.

## 5.2. Coordinate systems and load cases

### 5.2.1. Floating offshore wind turbine coordinate systems

In order to compare the results with Kyle et al. [21], the same configuration and load cases are adopted here. Thus, the NREL 5MW reference wind turbine [42] with a  $5^\circ$  shaft tilt angle and the basic parameters shown in Table 2.1 were chosen here. The inertial reference coordinate system  $S$  marked in red and the rotor-fixed reference coordinate system  $S'$  marked in green are shown in Fig. 5.1. The inertial reference coordinate system is defined as:

- The origin fixed on the ground.
- $x$  axis pointing vertically upward in the opposite direction to gravity.
- $y$  axis pointing to the right when looking in the nominal downwind direction.
- $z$  axis pointing in the nominal ( $0^\circ$ ) downwind direction.

The rotor-fixed reference coordinate system is defined as:

- The origin is fixed on the rotor center, translating and rotating with the tower.

- $x'$  axis orthogonal with the  $y'$  and  $z'$  axes such that they form a right-handed coordinate system.
- $y'$  axis pointing to the right when looking from the tower toward the nominally downwind end of the nacelle.
- $z'$  axis pointing along the (possibly tilted) shaft in the nominally downwind direction.

In this research, the inertial reference coordinate system is applied when describing the platform and rotor motions, while the rotor-fixed reference coordinate system is applied when describing the flow field around the rotor and the load perceived by the rotor.

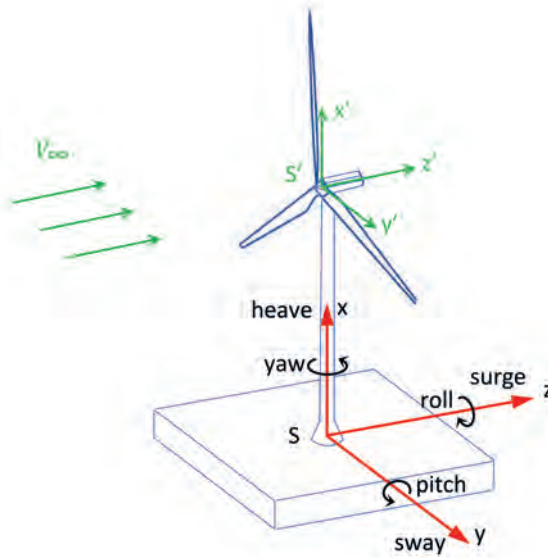


Figure 5.1: Inertial reference system and rotor-fixed reference system.

### 5.2.2. Load cases

Two load cases are considered here and the results are compared with those of Kyle et al. [21]. The load cases are designed in such a way that the VRS and propeller state occur under a surge motion of the rotor and for a below-rated wind speed of 7m/s. In this case, the flow velocity at the rotor minus

the surge velocity is negative, as shown in table 2 of Kyle et al. [21]. Table 5.1 summarizes the load cases labeled as RF, RS, BF, and BS, where 'R' represents 'Rated' wind speed, 'B' represents 'Below' rated wind speed, 'F' represents 'Fixed' and 'S' represents 'Surge'.  $A_s$  denotes the amplitude of the sinusoidal surge motion. Two values of the free stream velocity  $V_\infty$  are considered: the below-rated value of 7m/s and the rated value of 11.4m/s. Both a fixed and moving rotor (under a prescribed surge motion) are considered.

Table 5.1: Rated and below-rated load cases.

Lable	Rotation rate [rpm]	$V_\infty$ [m/s]	$A_s$ [m]	Surge period [s]
RF	12.10	11.4	–	–
RS	12.10	11.4	9.4	8.1
BF	8.47	7.0	–	–
BS	8.47	7.0	9.4	8.1

In the prescribed surge motion, the surge displacement,  $\chi_s$ , is defined as:

$$\chi_s = A_s \sin(\omega_s t), \quad (5.1)$$

where  $\omega_s$  is the surge frequency in rad/s and  $t$  is time in seconds. Accordingly, the surge velocity of the rotor is given by:

$$u_s = \frac{d\chi_s}{dt} = A_s \omega_s \cos(\omega_s t). \quad (5.2)$$

The surge motion angle is defined as [76]:

$$\theta_s = \omega_s t. \quad (5.3)$$

The rotor axial displacement and velocity of the load cases RS and BS are shown in Fig. 5.2. The  $0^\circ$  surge motion angle corresponds to the maximum surge velocity  $u_s$  (going downwind).

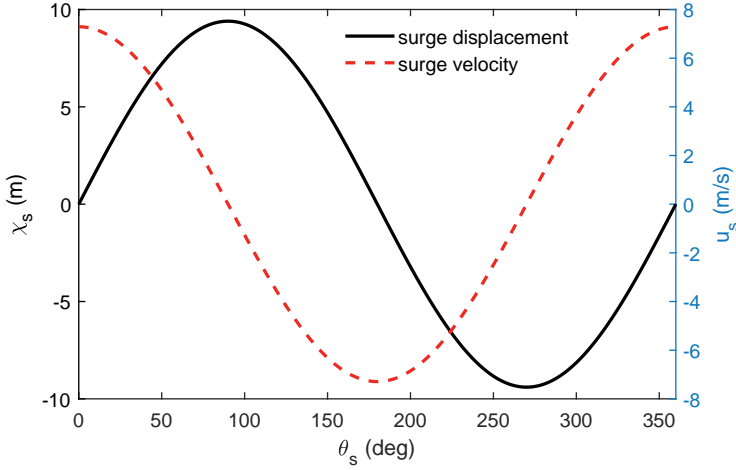


Figure 5.2: The rotor surge displacement and velocity of the load cases RS and BS

The original design of this set of load cases is formulated according to the response amplitude operator (RAO) which predicts the surge motion of the whole wind system, with the assumption that the 5MW NREL reference wind turbine is mounted on a barge platform. The translational RAO is defined as:

$$RAO_i(\omega) = \left| \frac{\Xi_i(\omega)}{A_{wave}} \right| \quad i = 1, 2, 3, \quad (5.4)$$

where  $\omega$  is the wave frequency,  $\Xi$  is the system response amplitude,  $A_{wave}$  is the wave amplitude, and  $i = 1, 2, 3$  corresponds to the surge, heave and sway degrees of freedom, respectively. The barge surge RAO amplitude is taken as 5. In order to get the VRS from a pure surge motion of the platform, the wave condition selection is: wave height  $A_{wave} = 1.87m$  and wave period of  $T = 8.1s$ , which leads to a platform surge amplitude of 9.4m and surge period of 8.1s. It is worth mentioning that the surge period is quite low, which leads to only a short period during the surge cycle for the onset and development of VRS (approximately 2s as mentioned in the literature). This surge period is much smaller than what is expected in reality for floating wind turbines, as presented in Chapter 2. However, these values are identical to those investigated by Kyle et al. [21], and therefore, enable a direct comparison with their CFD results. It is also worth noting that according to our previous research results [77], the

5MW NREL reference wind turbine mounted on a barge platform is indeed very sensitive to the wave loads, and the VRS is more likely to occur than with spar or tension-leg platform under the same wind and wave conditions.

### 5.3. Results and discussion

Each load case is simulated for 150 seconds, and the data are shown after 50s when the wake structure is sufficiently developed. The time step  $\Delta t$  for the cases 'RF' and 'RS' equals 0.1377s, whilst for the cases 'BF' and 'BS', it equals 0.1968s.

As discussed before, the results are compared to those of Kyle [21], where the VRS occurs when the turbine pitches or surges downwind at a velocity similar to the convection velocity of the wake. Kyle [21] used a finite volume discretisation of the incompressible Reynolds-Averaged Navier-Stokes equations in OpenFOAM. In this work, the free-wake vortex model as presented in chapter 3 is used and compared with Kyle's CFD method. The criteria used to identify the VRS differ from Kyle's work. In Kyle [21], the propeller state is first identified when the surge velocity exceeds the flow velocity at the rotor. Then, the VRS is identified during the propeller state event when the blade vortex interaction at the tip and the strong flow recirculation at the root are visible. In this work, the two criteria outlined in Chapter 2 are used instead.

#### 5.3.1. Thrust coefficients on the rotor

The thrust coefficient  $C_T$  acting on the rotor is compared with those from the literature [21, 77].

Firstly, the values of  $C_T$  acting on fixed rotors (RF and BF) are compared with both Kyle's results and the output from FAST [77, 78], as shown in Fig. 5.3 and Fig. 5.4. The figures show that, both at rated wind speed (RF) and below rated wind speed (BF), the present values of  $C_T$  fluctuate closely around the output of FAST. The fluctuations are due to the periodic release of vortex rings into the wake. Also, the results from Kyle are slightly higher than the values obtained by FAST and the present method.

Figure 5.5 and Fig. 5.6 show a comparison between the present results and Kyle's results [21] when the rotor is experiencing a prescribed surge motion

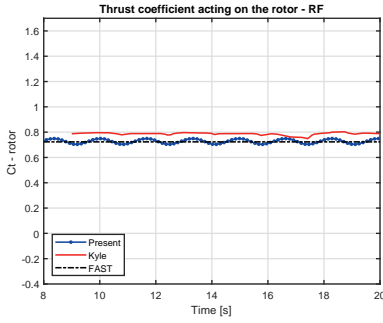


Figure 5.3: Thrust coefficient for a fixed rotor at rated wind speed (RF).

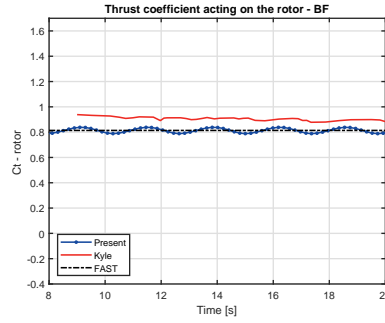


Figure 5.4: Thrust coefficient for a fixed rotor below rated wind speed (BF).

(cases RS and BS). The figures show that the two  $C_T$  curves match well with one another. They both fluctuate with the same period (the phases being adjusted to facilitate the comparison). Their average values and the amplitudes of the fluctuations are also found to be identical. In the load case 'BS', negative values of  $C_T$  are apparent for times between 121.7s and 129.7s, while in the load case 'RS', only positive values are obtained. In addition, the curves from the present vortex ring method become flatter when they reach the peaks and become sharper when they reach the troughs, which is also the case in the CFD results from Kyle [21]. The main difference between the two methods is the presence of fluctuations in the CFD results near the peak values of  $C_T$ . This is due to the higher resolution used in the CFD simulations compared to the present vortex ring cases. Despite these differences, the results from both methods are considered to be comparable and in good agreement.

### 5.3.2. Prediction of VRS and associated rotor characteristics

The VRS boundaries are predicted for the load cases with a prescribed surge motion. The results of the load cases 'RS' and 'BS' according to the axial induction factor 'a' and the Wolkovitch's criterion 'w', respectively, are shown from Fig. 5.7 to Fig. 5.10, where  $V_n$  is the relative wind speed normal to the rotor taken from the middle of a blade and 'surge' is the surge displacement at the rotor center. The figures are plotted based on the results of one of the three blades of the rotor. The horizontal axis represents time and the vertical

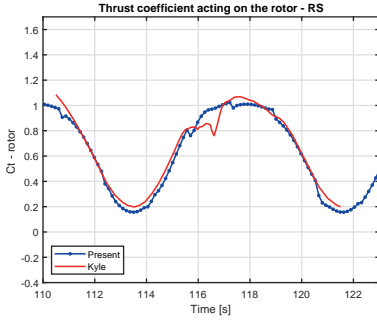


Figure 5.5: Thrust coefficient for a moving rotor (in surge) at rated wind speed (RS).

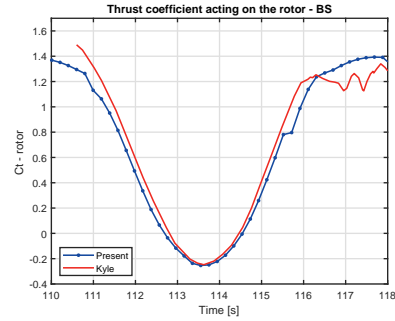


Figure 5.6: Thrust coefficient for a moving rotor (in surge) below rated wind speed (BS).

axis represents the blade span. Figure 5.7 and Fig. 5.8 show that at rated wind speed (case 'RS'), the criteria based on  $a \geq 1$  leads to narrow VRS areas, whilst the regions predicted by Wolkowitch's criterion ('w') are wider. In particular, the total percentage of the occurrence of the VRS is 4% based on 'a' and 23.2% based on 'w', respectively. In Kyle's analysis for the 'RS' case, the VRS is not significant enough to be observed. Figure 5.9 and Fig. 5.10 show that below rated wind speed (case 'BS'), the VRS areas appear periodically with the motion of the rotor, and correspond to times at which  $V_n$  is small and when the rotor moves downwind with the surge motion. It can also be seen that the VRS area is very small at the tip of the blade, where the relative velocity is large, as also apparent in Kyle's analysis for the 'BS' case. Similarly to the 'RS' case, the VRS areas predicted with 'a' are smaller than those predicted with 'w'. The total percentage of the occurrence of the VRS is 27.4% based on 'a' and 35.3% based on 'w', respectively, which means that the average duration of the VRS during each surge period is  $8.1s \times 27.4\% = 2.2s$  based on 'a' and  $8.1s \times 35.3\% = 2.8s$  based on 'w'. This is comparable to the value of 2s obtained in the literature [21] and it is associated with negative values of the relative velocity at the rotor. This shows that the present method is capable of predicting this phenomenon quantitatively with the results consistent with the qualitative analysis. The fact that the VRS period predicted by 'w' is slightly larger than in the literature can be explained by the fact that the Wolkowitch criterion identifies the VRS onset before  $V_n$  becomes negative. The total period of the VRS phenomenon is

therefore larger with 'w' than it is based on 'a'.

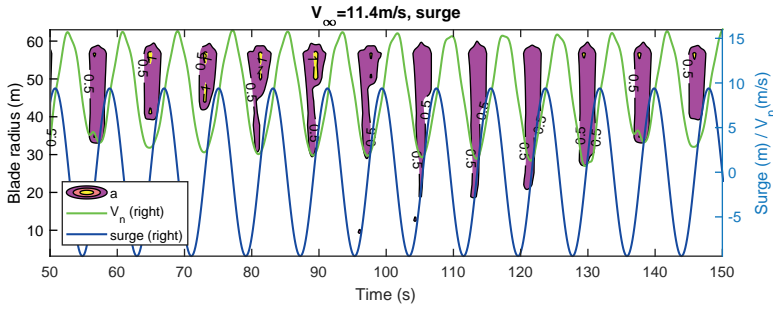


Figure 5.7: Regions of VRS predicted with 'a' (in yellow) with  $V_n$  and surge motion (RS)

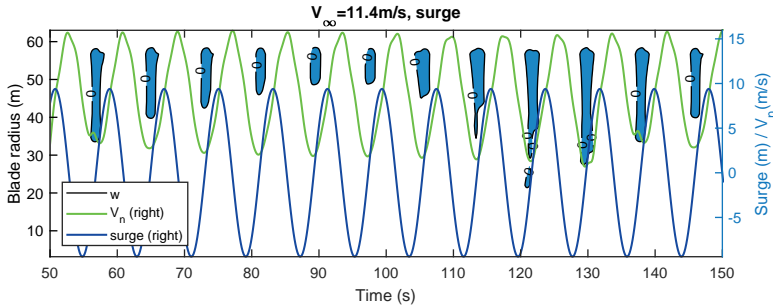


Figure 5.8: Regions of VRS predicted with 'w' (in blue) with  $V_n$  and surge motion (RS)

### 5.3.3. Velocity field around the rotor

In order to assess whether the propeller working state (PWS) occurs, the velocity fields around the rotor are further examined. This is done by plotting the velocity fields around the rotor, in a longitudinal section in the center plane of the rotor in the rotor-fixed reference frame. In these plots, the horizontal axis points downwind and the vertical axis points upward (both have the unit of [m]), and the rotor position is marked with a black line. Firstly the velocity field of the fixed rotor 'BF' is plotted for reference, as shown in Fig. 5.11. The typical windmill state is observed with small velocity gradients in front of the rotor, a significant drop of velocity behind the rotor, and the stream lines expansion from the rotor downwind. For comparison, Fig. 5.12 to Fig. 5.22 show the flow velocity fields at different instants in the surge motion. The value of  $\theta_s$  is

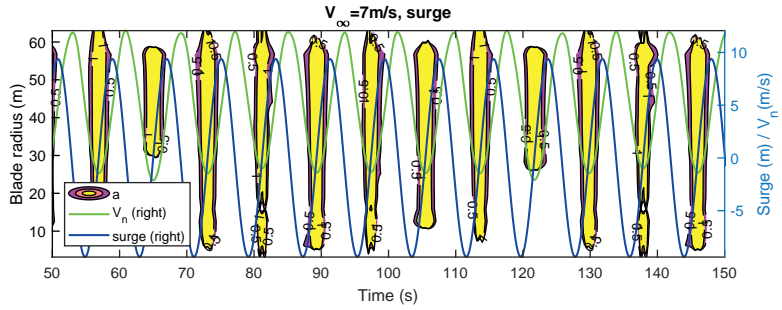


Figure 5.9: Regions of VRS predicted with 'a' (in yellow) with  $V_n$  and surge motion (BS)

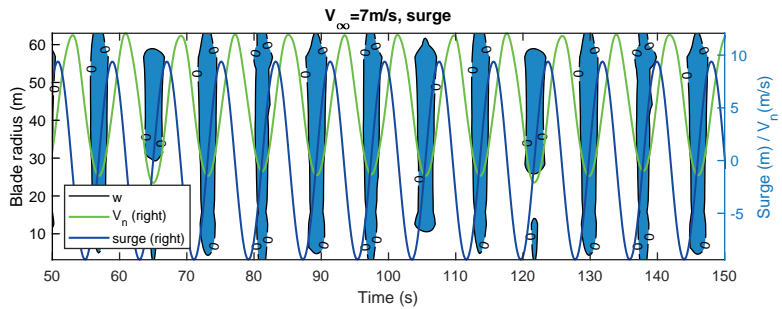


Figure 5.10: Regions of VRS predicted with 'w' (in blue) with  $V_n$  and surge motion (BS)

marked in the figures, which represents the position and velocity of the rotor during surge motion. From the shape of the stream lines and the contour plots of the relative velocity normal to the rotor, it can be seen that the velocity experienced by the rotor changes dramatically in a short period of time. At 111.583s in Fig. 5.12, the rotor is in the windmill state, and then, at 111.977s in Fig. 5.13, the vortices begin to accumulate downstream. At 112.371s in Fig. 5.14 and 114.535s in Fig. 5.19, the vortices accumulate near the rotor and the velocities at the rotor are very small. At 112.567s in Fig. 5.15 and 114.339s in Fig. 5.18, the rotor is engulfed by the vortices and the velocity at the rotor changes sign, which indicates that the rotor experiences the VRS. At 113.158s in Fig. 5.16 and 113.551s in Fig. 5.17, the stream lines cross the rotor from downwind to upwind, which indicates that the rotor operates in the propeller working state (PWS). From 114.732s in Fig. 5.20 to 114.929s in Fig. 5.21, the rotor goes back to the windmill state. And at 117.487s in Fig. 5.22, the windmill working state with the highest velocity around the rotor is identified.

This analysis leads to the following observations. Firstly, in this load case, the sequence of working states in one cycle of the surge motion is: windmill working state, vortex ring state, propeller working state, vortex ring state again, and finally windmill working state. Secondly, the VRS itself is a dynamic process, where the vortices start to accumulate in the far wake, then near the rotor, with the rotor being engulfed by them, before the rotor moves away from them. Thirdly, the PWS is identified by the characteristics of the streamlines in this particular load case. But it is worth mentioning that the PWS does not necessarily always happen after the VRS. This depends on the actual relative velocity perceived by the rotor.

#### 5.3.4. Angles of attack on the blade

The angles of attack (AoA) are also compared with Kyle's model, as shown in Fig. 5.23 and Fig. 5.24 for the four load cases: RF and RS at rated wind speed, and BF and BS at below-rated wind speed. In the figures, the AoA curves of 'Present - RF' and 'Present - BF' are the time-average AoAs (taken between 50s and 150s) of the fixed rotor, which compare with the AoA curves of 'Kyle - RF' and 'Kyle - BF', respectively. It is shown that the results match

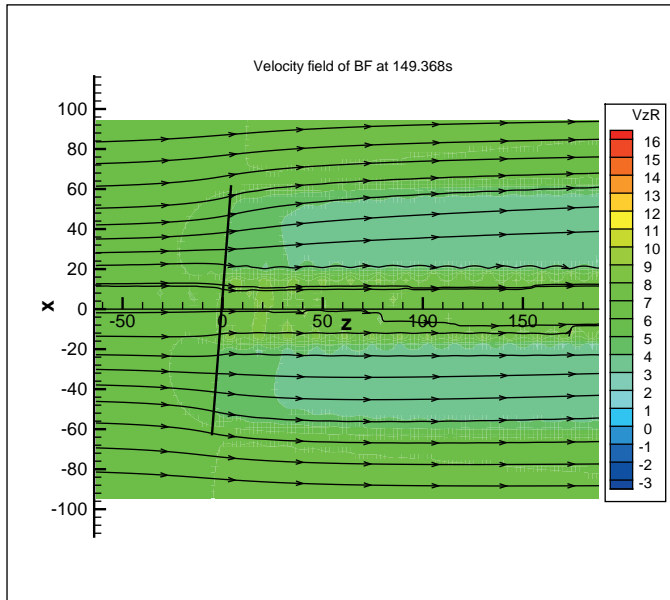
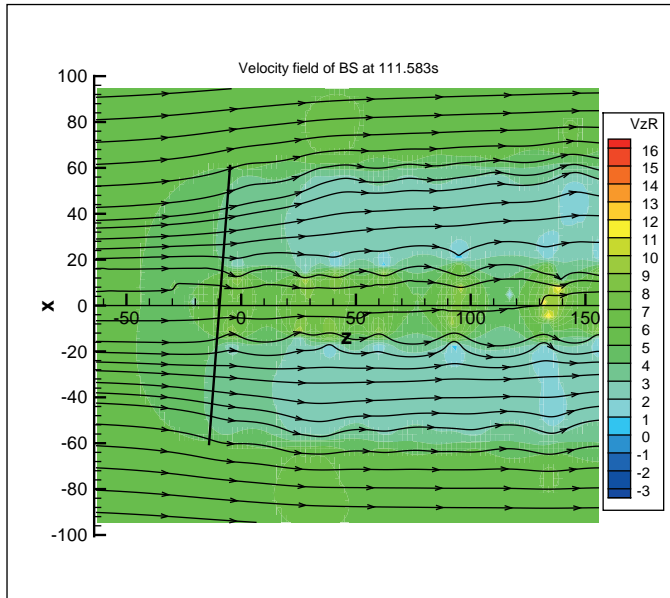


Figure 5.11: The velocity field around the rotor at 149.368s (BF)

Figure 5.12: The velocity field around the rotor at 111.583s,  $\theta_s = 279^\circ$  (BS)

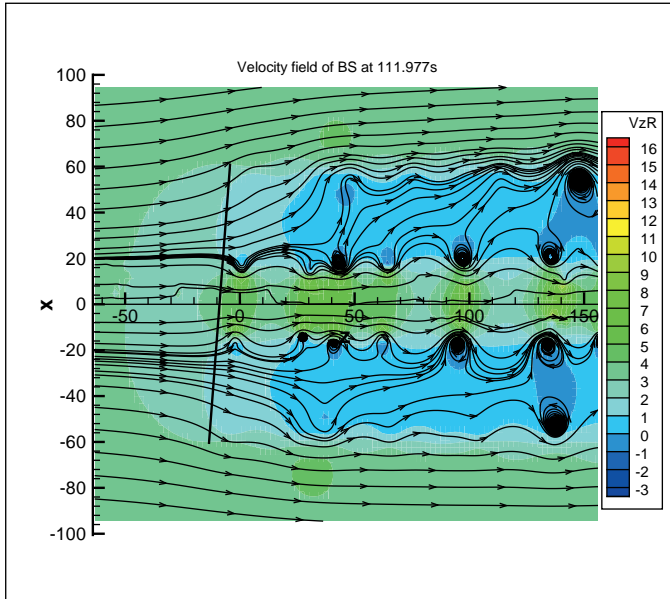


Figure 5.13: The velocity field around the rotor at 111.977s,  $\theta_s = 297^\circ$  (BS)

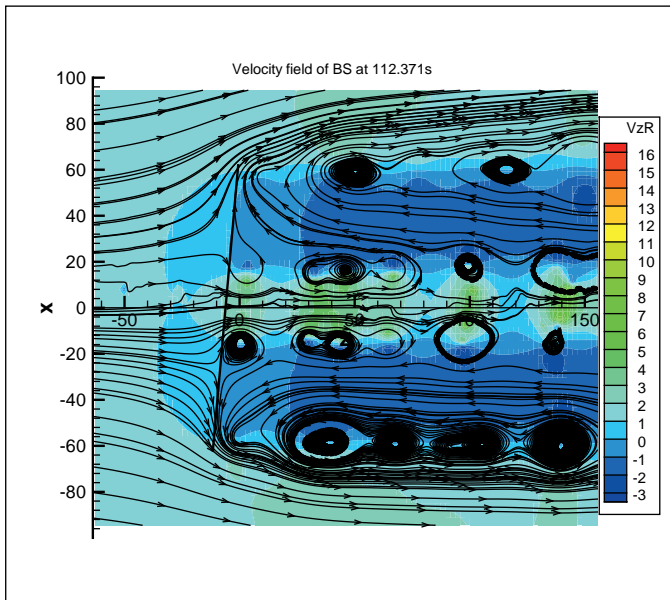


Figure 5.14: The velocity field around the rotor at 112.371s,  $\theta_s = 314^\circ$  (BS)

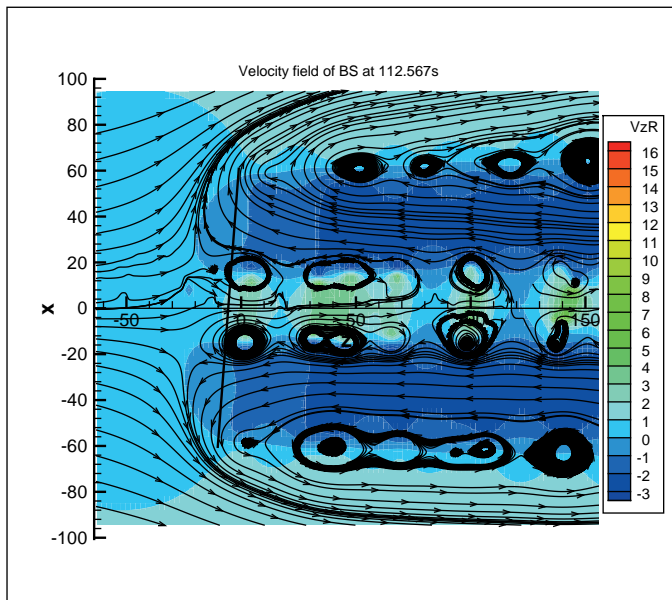


Figure 5.15: The velocity field around the rotor at 112.567s,  $\theta_s = 323^\circ$  (BS)

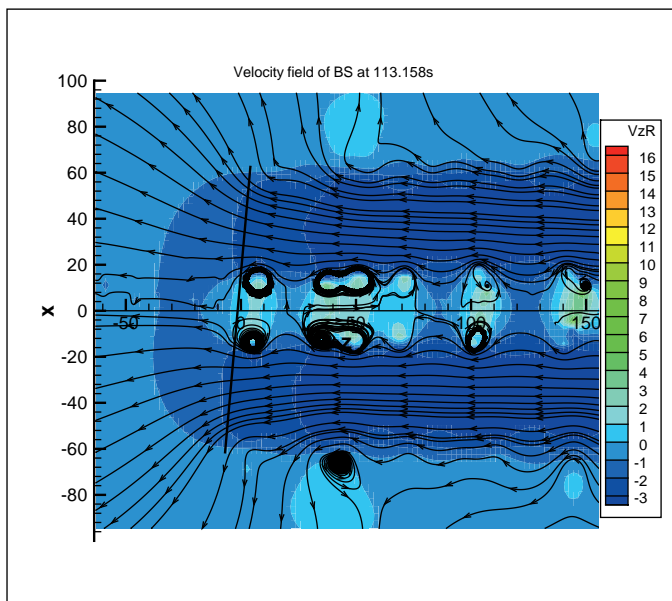


Figure 5.16: The velocity field around the rotor at 113.158s,  $\theta_s = 349^\circ$  (BS)

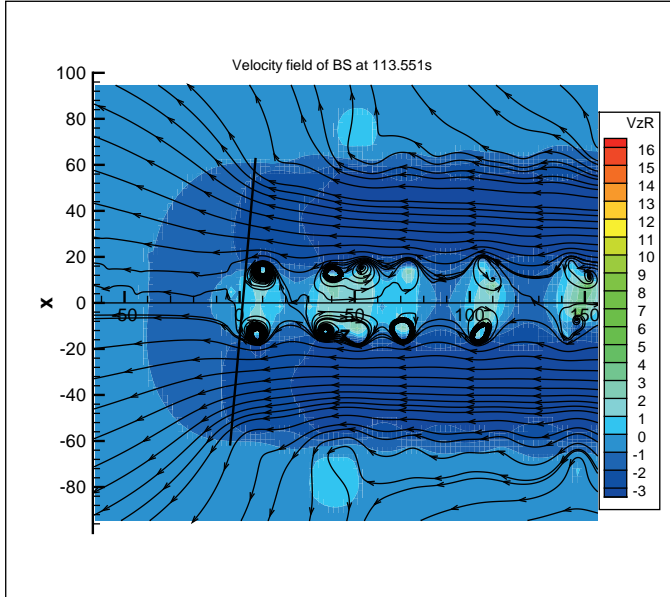


Figure 5.17: The velocity field around the rotor at 113.551s,  $\theta_s = 7^\circ$  (BS)

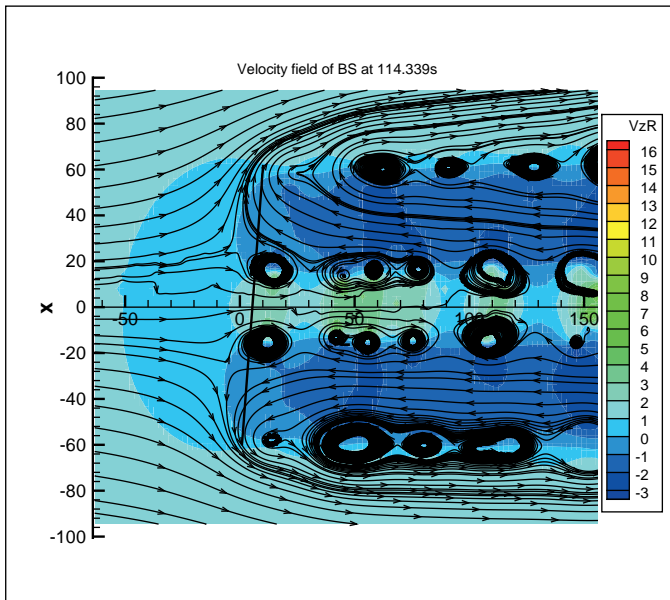


Figure 5.18: The velocity field around the rotor at 114.339s,  $\theta_s = 42^\circ$  (BS)

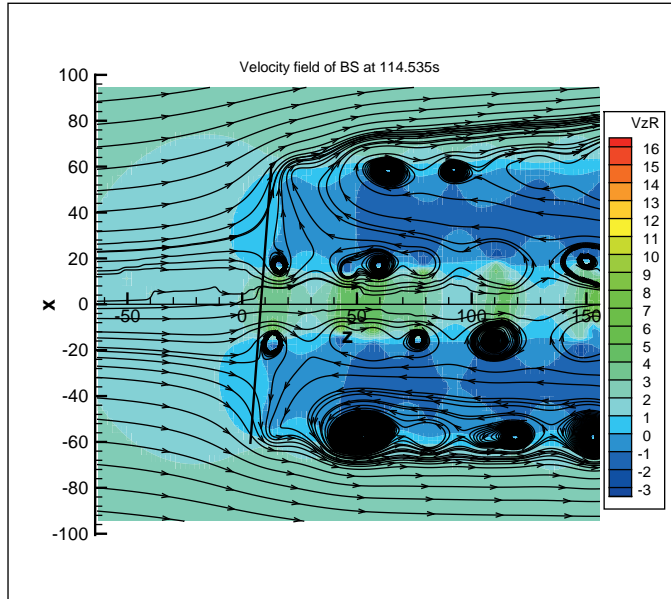


Figure 5.19: The velocity field around the rotor at 114.535s,  $\theta_s = 50^\circ$  (BS)

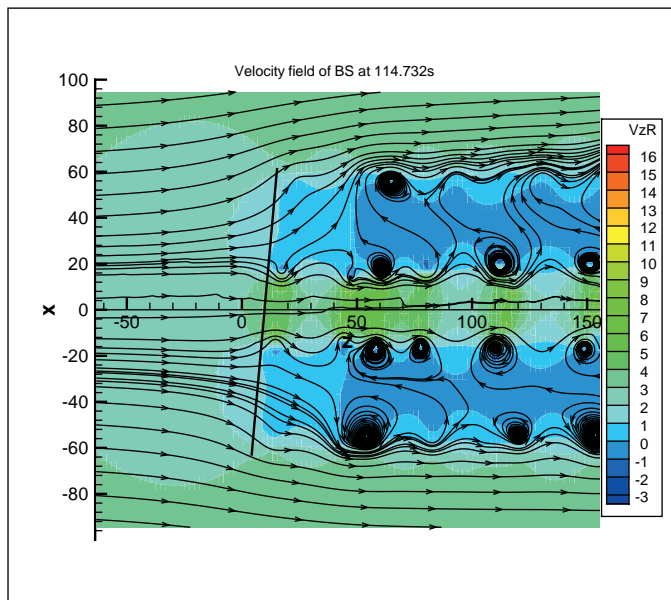


Figure 5.20: The velocity field around the rotor at 114.732s,  $\theta_s = 59^\circ$  (BS)

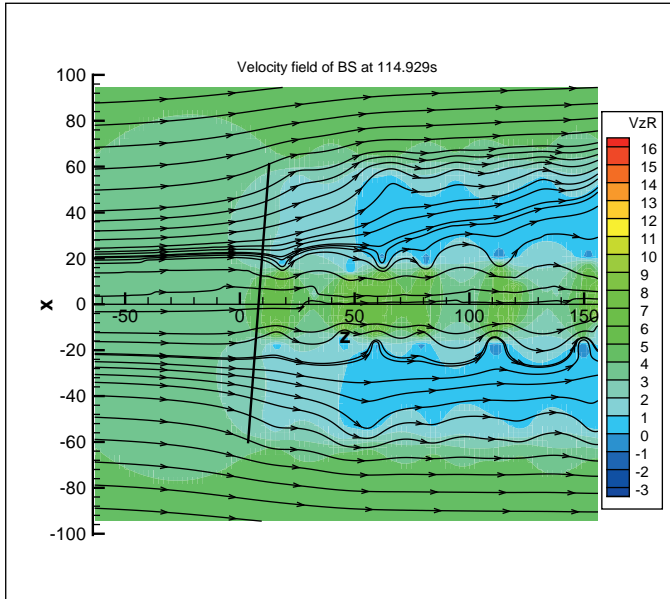


Figure 5.21: The velocity field around the rotor at 114.929s,  $\theta_s = 68^\circ$  (BS)

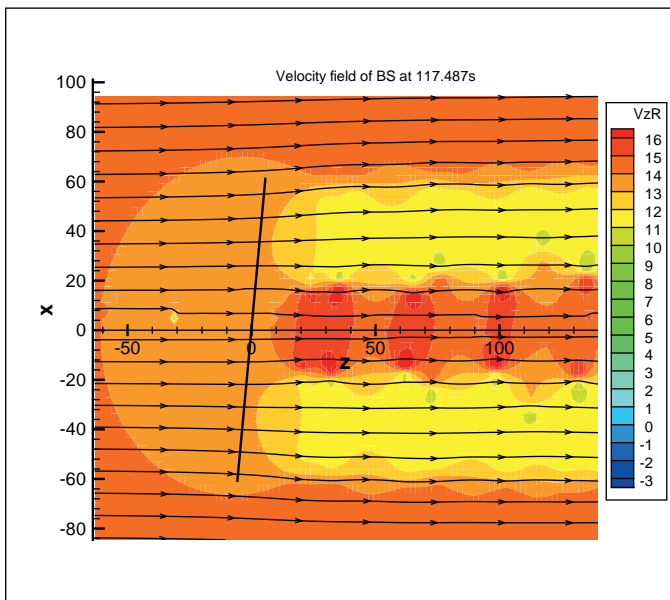


Figure 5.22: The velocity field around the rotor at 117.487s,  $\theta_s = 181^\circ$  (BS)

well with one another. The AoA curves of 'Present high - RS', 'Present high - BS' are the AoAs output with the  $C_T$  value (highest  $C_T$ ) at a time  $t = 16s$  in the literature and they are compared with the ones of 'Kyle - RS' and 'Kyle - BS', respectively. It is shown that the results match well with one another. In these figures, we also output the AoA curves when the  $C_T$  reaches its lowest value, which are marked as 'Present low - RS' and 'Present low - BS'. It can be seen that they are all negative values. Taking the negative twist angle 'Blade twist' as a reference it can be found that the AoAs of 'Present low - RS' are higher than the negative twist angles, thus, the lowest  $C_T$  is above zero as shown in Fig. 5.5. By contrast, the AoAs of 'Present low - BS' are lower than the negative twist angles along the span, which explains why the lowest  $C_T$  is negative as shown in Fig. 5.6.

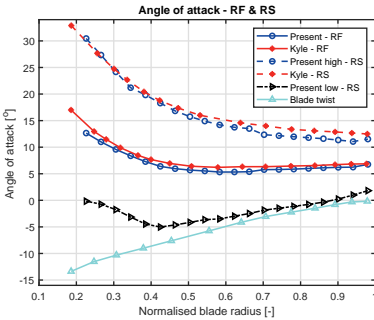


Figure 5.23: Angle of attack along the blade at a rated wind speed of 11.4m/s.

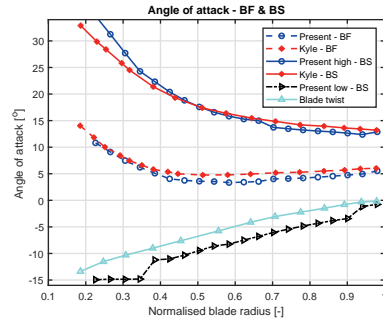


Figure 5.24: Angle of attack along the blade for the below rated wind speed of 7m/s.

From the above analysis in section 5.3.3 it can be seen that in the typical VRS, the airflow goes upwind from the inboard part of the blade and goes downwind from the outboard part of the blade. By contrast, during the typical PWS, the airflow goes upwind uniformly all along the blade. The airflow direction significantly influences the angles of attack, and therefore, the latter can be used to quantitatively indicate the boundary between VRS and PWS. Accordingly, the angles of attack (AoAs) denoted by  $\alpha$  at different time steps are evaluated and compared with the negative twist angles denoted by  $\theta_{-twist} = -\theta_t$ , which represents the AoAs when the relative wind velocity  $V_0(1 - a)$  is zero, assuming that the collective pitch angle  $\theta_p$  of the blades is zero as illustrated in Fig. 5.25.

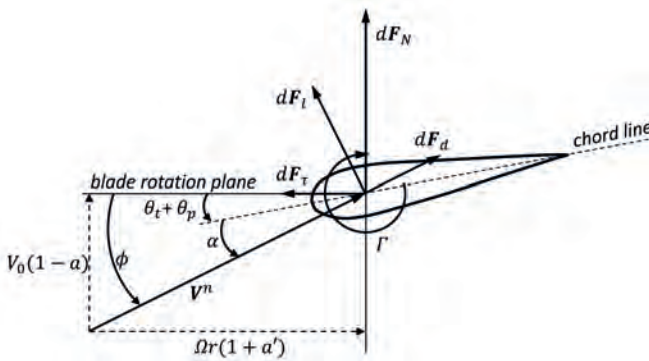


Figure 5.25: Forces acting on a blade element [75].

The values of AoAs along the blade in a time span from 111.780s to 115.126s are shown in Fig. 5.26, where it can be seen that when the working state changes from the windmill working state to the propeller working state as analyzed in Section 5.3.3, the AoAs along the blade gradually drop from positive to negative values. From 112.961s to 114.142s, the AoAs along the blade are well below the negative twist angles  $\theta_{-twist}$ . Also, it can be seen that the time instants corresponding to the onset of the PWS, which can be visually identified in Fig. 5.16 and Fig. 5.17, exactly fall in this region when AoAs are smaller than  $\theta_{-twist}$ . On the other hand, when the working state is visually seen as typical VRS as shown in Fig. 5.15 and Fig. 5.18, the AoA curve and the  $\theta_{-twist}$  curve intersect. Thus, it is concluded that the boundary between VRS and PWS can be predicted by the condition when  $\alpha$  becomes smaller than  $\theta_{-twist}$  all along the blade. For this particular surge cycle of the load case 'BS', the boundaries between the VRS and PWS are identified at 112.961s and 114.142s.

### 5.3.5. Velocity and thrust along the blade

In order to see more clearly the characteristics of the FOWTs during the vortex ring state, the velocity and thrust along the blade span at different time steps of the load case 'BS' are plotted and analyzed. From Fig. 5.27 to Fig. 5.32, specific times within a cycle of the platform motion are shown. In these figures,  $V_n$  is the relative velocity normal to the rotor disc,  $V_i$  is the induced

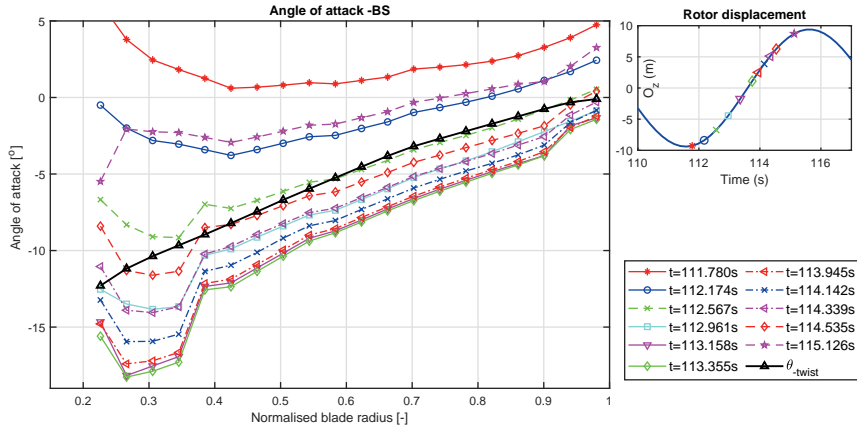


Figure 5.26: Angle of attack along the blade at different time instants (one curve corresponds to one time instant). The inset on the right shows the time instants in the surge period.

velocity which includes two components in this vortex model: the near wake induced velocity  $V_{I-n}$  and the far wake induced velocity  $V_{I-f}$ .  $V_{I-n}$  is determined by Eq. (3.41), thus its direction is related to the direction of the blade bound circulation. By contrast, the component  $V_{I-f}$  is determined by Eq. (3.42), which is determined by the vortex rings in the wake. Additionally,  $V_{plfm}$  is the velocity of the platform motion, which is constant along the blade at each time step considering that there is only a surge motion. Finally, 'Thrust' is the force normal to the rotor disc on each segment of the blade.

As a reference, Figure 5.33 and Figure 5.34 indicate two typical instances corresponding to the occurrence of the windmill state. In this state, the values of the thrust force along the blade are all positive,  $V_n$  is larger than the cut-in wind speed, and  $V_I$ ,  $V_{I-n}$  and  $V_{I-f}$  are all negative along the blade. By contrast, Fig. 5.27 and Fig. 5.31 show that, at the boundaries of the VRS according to the Wolkovitch's criterion, the thrust from inboard to about two-third of the blade drops below zero,  $V_n$  becomes smaller than the cut-in wind speed and  $V_{I-n}$  at the inboard part of the blade becomes positive. This indicates that the blade-bound circulation changes sign. In Fig. 5.28 and Fig. 5.30, when  $C_T$  is zero, it can be seen that a larger part of the thrust becomes negative, a larger part of  $V_{I-n}$  becomes positive and  $V_n$  drops to zero. And in Fig. 5.29, at the

lowest  $C_T$ , it can be seen that the thrust,  $V_n$  and  $V_{plfm}$  all reach their lowest values, whilst  $V_{I-n}$  reaches its highest value. Also the thrust in the middle of the blade experiences larger variations than at the tip and root of the blade, and the overall thrust is influenced significantly by  $V_{plfm}$ . It can also be noticed that the change of  $V_I$  with the rotor surge motion is not significant, thus its influence on the thrust is small. Therefore, it can be inferred that the large change in the axial induction factor 'a', as shown in Fig. 5.9, is mainly due to the change in the inflow velocity component  $V_{plfm}$ , while the influence of  $V_I$  is relatively small during the whole process.

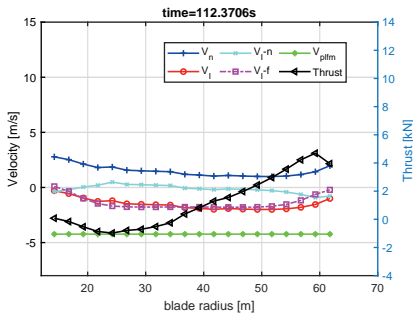


Figure 5.27: Relative velocity, induced velocity, and thrust force along the blade when the rotor enters VRS based on 'w'

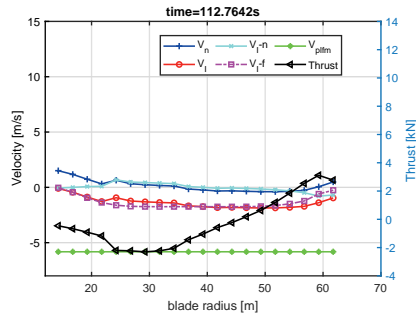


Figure 5.28: Relative velocity, induced velocity, and thrust force along the blade when  $C_T$  decreases towards zero

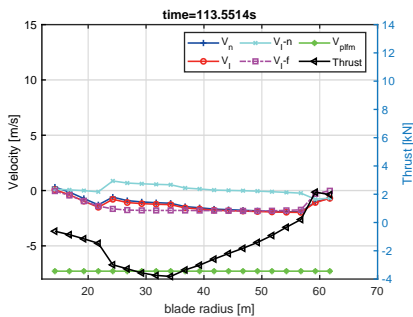


Figure 5.29: Relative velocity, induced velocity, and thrust force along the blade when  $C_T$  reaches its lowest value

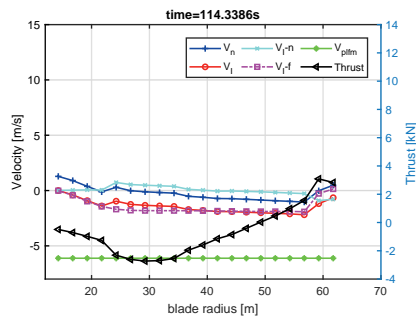


Figure 5.30: Relative velocity, induced velocity, and thrust force along the blade when  $C_T$  is negative but increasing towards zero.

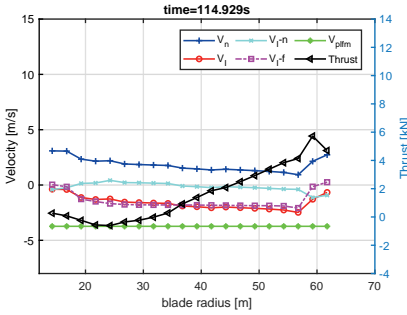


Figure 5.31: Relative velocity, induced velocity, and thrust force along the blade when the rotor exits VRS based on 'w'

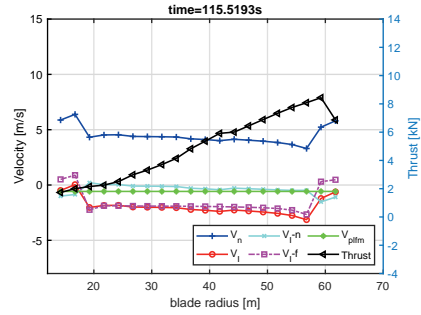


Figure 5.32: Relative velocity, induced velocity, and thrust force along the blade when the platform velocity is close to zero

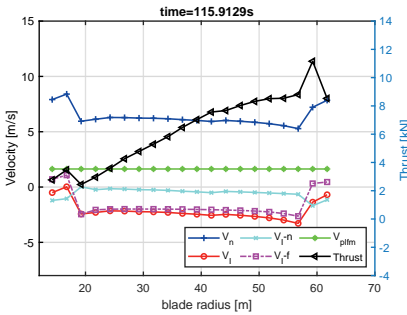


Figure 5.33: Relative velocity, induced velocity, and thrust force along the blade when the platform velocity increases and is positive

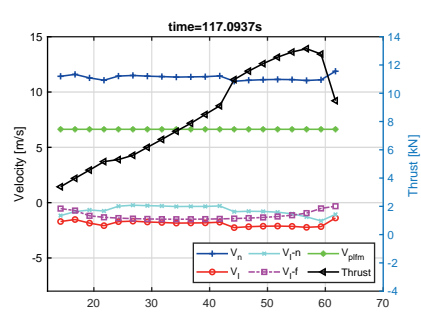


Figure 5.34: Relative velocity, induced velocity, and thrust force along the blade when  $C_T$  reaches its highest value

5.3.6. Working states within one surge period

The VRS boundaries are shown more clearly in Fig. 5.35 and Fig. 5.36 for one period in the surge motion (shown on the right axis) and below rated wind speed (case 'BS'). The prediction from the axial induction factor 'a' is shown by the yellow area, while those from Wolkovitch's criterion 'w' are shown in blue. Again, the results are plotted based on one of the three blades, the horizontal axis represents the time line and the left vertical axis represents the blade span. For this particular surge period, the duration of the VRS according to 'a' is 2.1s (from 112.6s to 114.7s) and according to 'w', the duration of VRS in this cycle is 2.6s (from 112.4s to 115.0s).

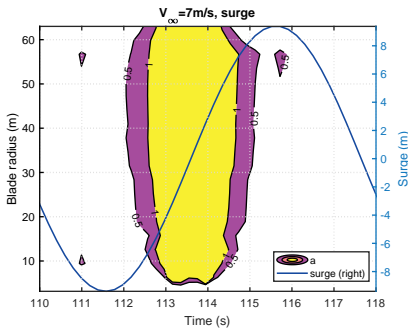


Figure 5.35: The VRS predicted with 'a' under a surge motion and below rated wind speed (case 'BS')

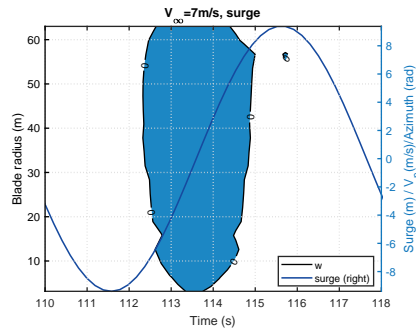


Figure 5.36: The VRS predicted with 'w' under a surge motion and below rated wind speed (case 'BS')

The time evolution of the thrust coefficient  $C_T$  within one period of the surge motion is plotted in Fig. 5.37, where the corresponding working states are also shown. In the figure, w1 and w2 represent the boundaries between windmill working state and VRS according to Wolkovitch criterion; and P1 and P2 represent the boundaries between the VRS and PWS. The time instants at which  $a = 0.5$  and  $a = 1$  are highlighted on the graph. These instants are determined based on the boundaries of the purple region and the yellow region, respectively, on both side of Fig. 5.35, which correspond to the time instants the wake becomes chaotic and the time instants of the VRS. The time instants of w1 and w2 are taken from the boundaries of the blue region on both side of Fig. 5.36. And the time instants of P1 and P2 are identified according to the relationship between the angle of attack and the negative twist angle as shown

in Fig. 5.26.

The regions dominated by the windmill working state, VRS and PWS, respectively, are shown in the figure. It can be seen that, in this load case, the rotor works in the windmill state for most of the time. However, the VRS occurs when  $C_T$  is positive (according to either the criterion 'a' or 'w') and extends until  $C_T$  becomes negative, while the PWS occurs only when  $C_T$  is well below zero. It is also worth mentioning that the turbulent wake state did not occur in this simulation, because based on the definition, during the turbulent wake state, the thrust should be high. But the thrust increase is not seen even through the chaotic flow occurs before the vortex ring state. This can be due to the fact that the potential flow assumption is used here, as well as the fact that the surge motion of the rotor is imposed and the floater velocity regularly changes sign. The results of this study show that the VRS is not necessarily an outcome of the development of the turbulent wake state, but can appear directly after the windmill working state. However, higher-fidelity models that do not rely on the potential flow assumption should be used to confirm this observation.

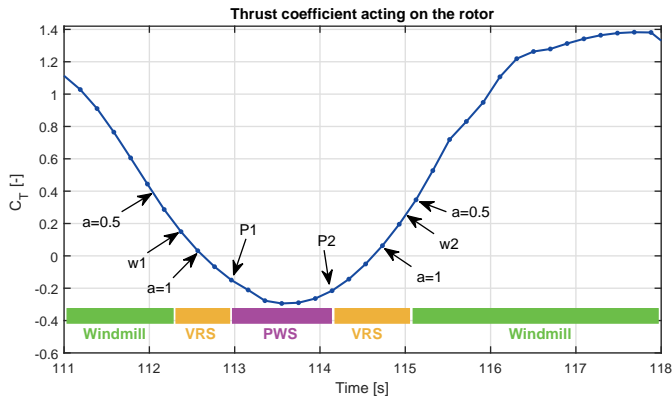


Figure 5.37: Thrust coefficient acting on fixed rotor (BS)

In order to further investigate the aerodynamics of the FOWT during the change of working state, the time evolution of the aerodynamic load on the blade sections  $dF_N$  normal to the rotor disc is shown in Fig. 5.25, for the load case 'BS'. In order to evaluate the behaviour of  $dF_N$ , the following parameters are introduced: the mean value  $\mu$ , standard deviation  $\sigma$  and coefficient of variation

$C_v$  defined by Eq. (2.21).

In order to assess the fluctuations of  $dF_N$  in different working states, the parameters above are calculated, at every five consecutive time steps (i.e. every 0.984s), as:

$$\mu(n_t) = \sum_{i=n_t-2}^{n_t+2} dF_N(i), \quad (5.5)$$

where  $n_t$  is the current time step. Figure 5.38 to Fig. 5.43 show the time evolution (between 108s and 117s) of the values of  $\mu$ ,  $\sigma$  and  $C_v$  for  $dF_N$  at different locations along the blade (one figure per location, the radial location being indicated on the figure title), from root to tip. The time span shown here covers the working states from windmill to propeller. Firstly, as expected, in each figure the mean value  $\mu$  has its peak value in the windmill working state and its minimum value in the PWS. Also it can be seen that the difference between the maximum and minimum values of  $\mu$  monotonically increases as we move from the inboard part of the blade (e.g.  $r=16.75\text{m}$  in Fig. 5.38) to the outboard part (e.g.  $r=51.75\text{m}$  in Fig. 5.42), and then it decreases again at the tip (i.e.  $r=61.75\text{m}$  in Fig. 5.43). Also, the lowest value of  $\mu$  occurs in the middle of the blade, as shown in Fig. 5.40. Secondly, in each figure the standard deviation  $\sigma$  changes regularly, namely it gradually increases from the region of windmill working state to the VRS, and then it gradually decreases from the VRS to PWS. Additionally, it can be seen that the maximum value of  $\sigma$  occurs in the middle of the blade (in the VRS region), see Fig. 5.40. Thirdly, it is found that in each figure the coefficient of variation  $C_v$  has two peak values (except on the tip of the blade), both occurring around the VRS boundaries 'w1' and 'w2' as shown in Fig. 5.37. At these instants,  $\mu$  is close to zero and  $\sigma$  is relatively large.

### 5.3.7. Wake structure

The wake structures of 'BS' are exhibited from Fig. 5.44 to Fig. 5.47, which correspond to four of the time instants considered in Section 5.3.5. To show the relative position of the rotor and the far wake vortex rings more clearly, the  $z$  coordinates of the rotor center  $Z_{o,c}$  and the center of the first ring in the wake

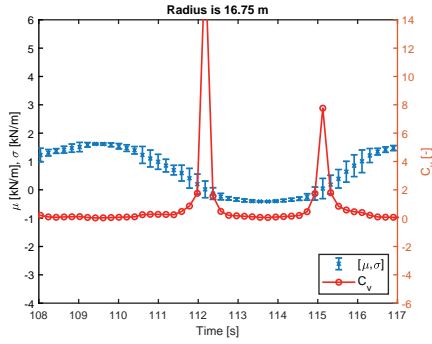


Figure 5.38: The  $\mu$ ,  $\sigma$  and  $C_v$  of  $dF_N$  at  $r=16.75\text{m}$

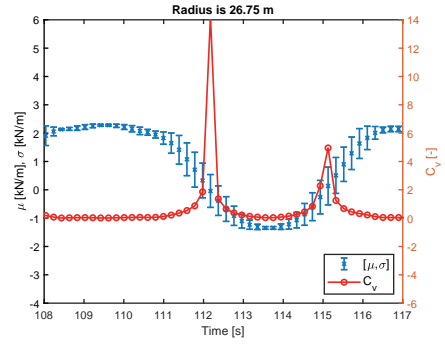


Figure 5.39: The  $\mu$ ,  $\sigma$  and  $C_v$  of  $dF_N$  at  $r=26.75\text{m}$

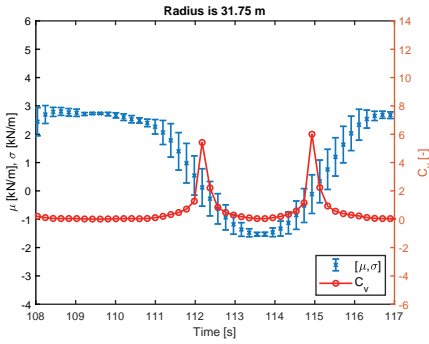


Figure 5.40: The  $\mu$ ,  $\sigma$  and  $C_v$  of  $dF_N$  at  $r=31.75\text{m}$

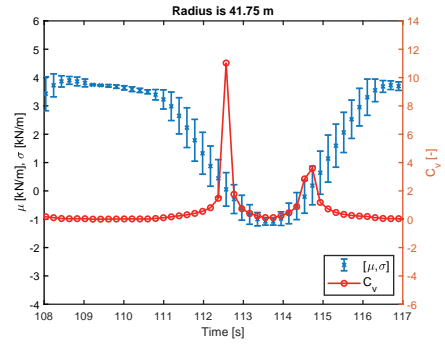


Figure 5.41: The  $\mu$ ,  $\sigma$  and  $C_v$  of  $dF_N$  at  $r=41.75\text{m}$

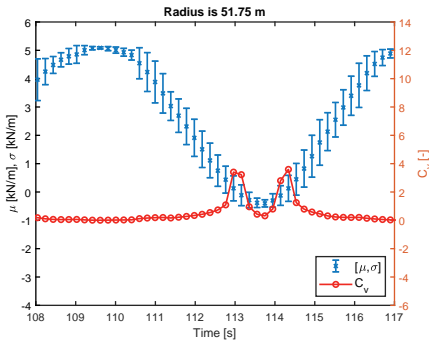


Figure 5.42: The  $\mu$ ,  $\sigma$  and  $C_v$  of  $dF_N$  at  $r=51.75\text{m}$

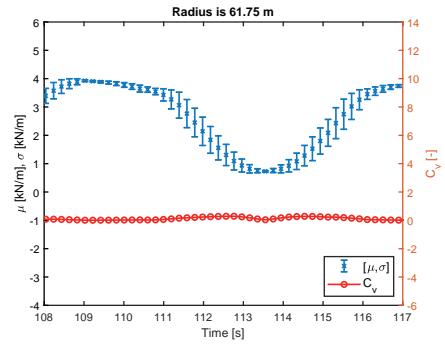


Figure 5.43: The  $\mu$ ,  $\sigma$  and  $C_v$  of  $dF_N$  at  $r=61.75\text{m}$

$Z_w1$  in the inertial reference coordinate system are given in the caption of the figures. In these figures, the blade-bound circulation strength and vortex ring strength are shown, where red represents positive values and blue represents negative ones. It can be seen that in all these figures the inner ring vortex strengths have positive values and the outer ring vortex strengths have negative values. Figure 5.44 represents a typical windmill state of the rotor, where the blade-bound circulation strength is positive. Figure 5.45 to Fig. 5.47 describe the process from the VRS boundary predicted with 'w' (i.e. at 112.371s) to the time at which  $C_T$  reaches its lowest value (i.e. at 113.551s). It can be seen that the rotor gradually approaches the vortex rings and, during this process, the blade-bound circulation strength along the blade gradually changes from positive to negative values, from root to tip of the blades. More precisely, from the relative position of  $Z_0c$  and  $Z_w1$ , it can be seen that the rotor gradually approaches the far wake, and at 113.551s, it catches up with the first vortex ring. Note that there are still near wake blade-bound and trailing vortex models not explicitly shown in these figures, thus the intersection between the rotor and the far wake vortex rings as shown does not represent the exact moment of the onset of VRS.

This phenomenon, together with the direction change of the thrust force, represents the unsteady flow around the blade during VRS. It can also be seen that the far wake vortex ring strengths are always in the same direction, thus their accumulated induction is relatively stable, which explains why the induced velocity  $V_i$  is relatively stable during the rotor surge motion as discussed in section 5.3.5.

## 5.4. Conclusion

In this chapter, a simplified free wake vortex ring method is used to simulate the aerodynamic performance of a floating wind turbine rotor under a prescribed surge motion. The results are compared with those from the literature, where a CFD model is used. In this research, the thrust coefficient and angles of attack are found to be comparable with those obtained using a CFD method. The vortex ring state boundaries are predicted with the axial induction factor and the Wolkovitch's criterion, and the duration of the VRS is found to be in

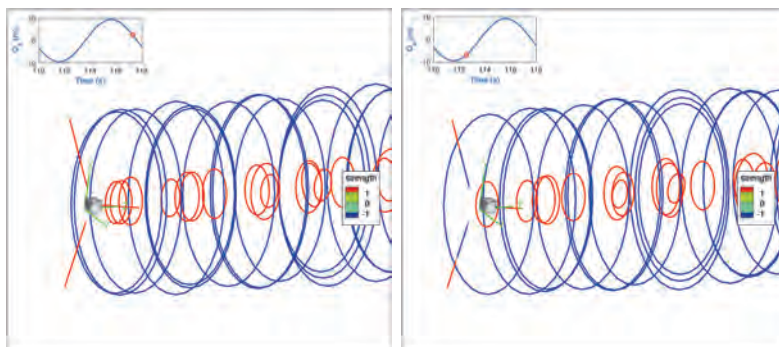


Figure 5.44: The wake structure at 117.094s,  $Z_{oc} = 2.565m$ ,  $Z_{w1} = 21.116m$  Figure 5.45: The wake structure at 112.371s,  $Z_{oc} = -6.733m$ ,  $Z_{w1} = 4.300m$

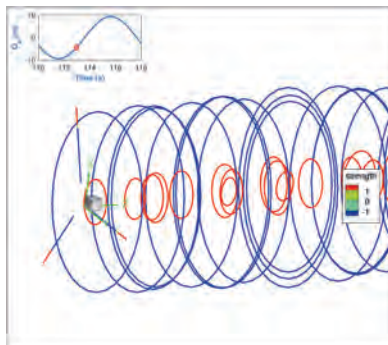


Figure 5.46: The wake structure at 112.764s,  $Z_{oc} = -4.450m$ ,  $Z_{w1} = 6.904m$

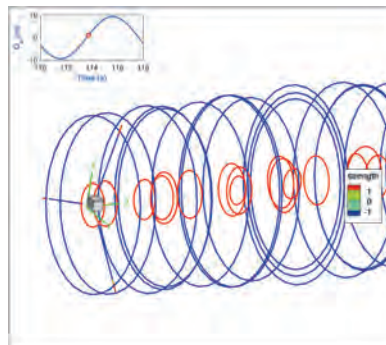


Figure 5.47: The wake structure at 113.551s,  $Z_{oc} = 1.101m$ ,  $Z_{w1} = 1.019m$

agreement with a higher fidelity CFD model in the literature. The velocity and the force along the blade are analyzed, and the corresponding wake structures are evaluated. It can be found that during the whole cycle of the rotor motion, and in conditions where VRS occurs, the thrust changes significantly. These changes are mostly due to the rotor surge velocity, while the induction influence is small. During the VRS, the unsteady blade bound circulation are captured.

This work also investigates the changes of working state that the rotor experiences during its surge motion. Firstly, the vortex ring state boundary of the rotor is predicted using both the Wolkovitch's criterion and the axial induction factor. Then, the velocity field perceived by the rotor, and the associated flow streamlines, are visualised for one surge period. Three different working states are clearly identified. The value of the thrust coefficient in these three states is also highlighted. Furthermore, the boundary between the vortex ring state and the propeller working state is identified by comparing the angle of attack with the twist angle of the blade. Finally, the aerodynamic loads on the blade are evaluated by analyzing their mean value, standard deviation and coefficient of variation during successive short time intervals. It is found that the largest load fluctuations occur at the vortex ring state boundaries (according to Wolkovitch's criterion), while the fluctuations of the thrust are not significant in the windmill working state and the propeller working state.

This chapter demonstrates the usefulness of a free wake vortex model in better understanding the complex aerodynamics of FOWTs, a topic that is still relatively new for the wind energy community.



# 6

## Conclusion and Recommendations

一切过往，皆为序章。—莎士比亚《暴风雨》

What's past is prologue.

Shakespeare, *The Tempest*

This is a concluding chapter summarising the answers to the research questions defined in Chapter 1. Problems remain or exposed by this work are reflected and recommendations for further research are also presented in this chapter.

## 6.1. Conclusions

The work presented in this thesis aimed to improve the understanding of rotor-wake interactions for floating offshore wind turbines, with a specific focus on the vortex ring state. This goal was achieved through three main steps, dealing respectively with: (i) the prediction of the occurrence of the vortex ring state, (ii) the development of an aerodynamic model based on a free wake vortex method to simulate a floating rotor, and (iii) the simulation of both the vortex ring state and other working states of a floating offshore wind turbine. This chapter summarizes the main contributions and conclusions of this thesis according to the research objectives, with an outlook towards recommended further research.

### 6.1.1. Objective 1: Prediction of the vortex ring state

The primary question answered by this research was to find out whether, and to what extent, the vortex ring state is experienced by floating offshore wind turbines. It is because that before this research, the existence of the vortex ring state of floating offshore wind turbines is briefly outlined in the literature. However, there was no criterion or standard that exactly defining this problem.

- to improve the physical understanding of the rotor-wake interactions for floating offshore wind turbines, with a specific focus on the vortex ring state, paving the way to better design and large-scale development of floating offshore wind turbines.

To achieve this objective, three prediction criteria were proposed, two of them being adapted from the helicopter community. These criteria are based on various methods, including momentum theory, experiments, model tests, field tests, and numerical simulations. They give boundaries for the occurrence of the vortex ring state according to the horizontal and vertical velocities at a rotor. The three criteria considered here are: the axial induction factor, which is given by the definition of the vortex ring state situated between the turbulent wake state and the propeller working state; Wolkovitch' s criterion and Peters' criterion which are both derived from momentum theory. The criteria were

applied to the fully-coupled simulation of a floating wind turbine, for different floating support structures and environmental conditions (with both regular and irregular waves). The analysis was conducted using the open source aero-hydro-servo-elastic coupled analysis tool FAST/OpenFAST <sup>1</sup>.

This work systematically demonstrated the possibility of occurrence of the vortex ring state, even under normal sea states, for each of the main three concepts of floating platforms: spar-buoy, semi-submersible, and tension-leg platform. The results show that the type of floating foundation has a significant influence on the aerodynamic characteristics of the rotor. For example, a tension leg platform exhibits the least motion, and therefore, also the least probability of occurrence of the VRS. Also, the probability of occurrence of the VRS generally increases with the magnitude of the wave height, except the cases in which the velocity normal to the rotor has large fluctuations.

### 6.1.2. Objective 2: Develop an aerodynamic model for the simulation of rotor-wake interactions

Engineering aerodynamic models for floating offshore wind turbines are still mostly based on blade element momentum (BEM) theory. However, the use of BEM is questionable when the rotor moves into its own wake and is subjected to unsteady flows. Also because it only solves the problem on the rotor disc, while the velocity field in the wake cannot be considered. By contrast, computational fluid dynamics methods can deal with complex flows but are often very time consuming.

A key research objective is therefore:

- to develop an aerodynamic model for the rotor-wake interactions problems of FOWTs, which can do the kinematic analysis for both the rotor and the wind field around it with considerable accuracy and computational efficiency.

In this context, a mid-fidelity free wake vortex ring method was developed to provide a compromise between accuracy and computational efficiency. The model includes a near wake model based on straight vortex filaments and a far

<sup>1</sup><https://www.nrel.gov/wind/nwtc.html>

wake model that uses an analytical axis-symmetric vortex ring formulation. A new trailing vortex model with finite length vortex lines was also proposed in this thesis. The results showed that it can induce higher near wake velocities and reduce more effectively the unrealistic shear velocity on the rotor from the vortex rings comparing with the semi-infinite trailing vortex model. Also the average mid-line method was proposed for the calculation of the rotational angles of the vortex rings.

6 Simulations were run using the NREL 5MW wind turbine. Firstly, the rotor thrust force on a bottom-mounted monopile wind turbine was calculated with the proposed free wake vortex ring method and compared with the results from BEM theory. The results showed a good agreement between the two approaches for a large range of wind speeds. Secondly, the method was applied to floating offshore wind turbines at below-rated, rated and above-rated conditions and compared with other vortex based methods. It was found that the mean and standard deviations of the angle of attack were comparable with the literature. The analysis of the thrust force on the rotor showed that its first dominant frequency for a bottom-mounted monopile foundation is largely driven by the vortex shedding frequency, whilst the first dominant frequency for floating support structures is driven by the platform motion. Also, the latter influences the lift coefficient on the rotor, and hence, the blade bound vortex strength.

To conclude, the modified free wake vortex ring method proposed here is considered to be effective and reliable when solving the aerodynamic load around horizontal-axis wind turbines, both on fixed and floating support structures. It can be used to calculate conditions of small angles of attack at low wind speeds, small angles of attack due to blade pitch motion at high wind speeds, and varying angles of attack due to unsteady wind flows in the context of floating offshore wind turbines.

### 6.1.3. Objective 3: Analyze the characteristics and impact of the rotor-wake interactions on the performance of floating offshore wind turbines

Finally, the proposed free wake vortex ring method was used to simulate the aerodynamic performance of a wind turbine rotor subjected to prescribed surge motions. The vortex ring state was identified by using the axial induction factor and Wolkovitch's criterion. Its duration was found to be in agreement with that from a CFD model in the literature. Two research objectives were identified as:

- How is the turbine performance affected by the vortex ring state?
- What is the impact of a change in working state during the whole cycle of the platform motion?

In order to assess the effect of VRS on the turbine aerodynamic performance, various diagnostics were extracted from the simulations. It can be found that during the vortex ring state, the thrust drops significantly. This is mostly due to the rotor surge velocity, while the influence of the induction is small. During the vortex ring state, the unsteady blade bound circulation is seen. The blade bound circulation strength along the blade gradually changes from positive to negative, from root to tip of the blades.

When zooming into one period of the surge motion, the work highlighted the possible occurrence of three working states: windmill working state, vortex ring state, and propeller working state. It was shown that the thrust coefficient reaches the peak level during the windmill working state, is close to zero during the vortex ring state, and is negative during the propeller working state. The largest load fluctuation occurs at the vortex ring state boundaries (as predicted by Wolkovitch's criterion), while it is not significant in the windmill working state and the propeller working state. Thus, the vortex ring state could be critical for the fatigue loading on the blades and the associated turbine lifetime.

This research demonstrates the occurrence of the vortex ring state phenomenon for a floating offshore turbine undergoing surge. Additionally, both the windmill state and propeller state also occur during the surge cycle. All

these results were obtained using the free wake vortex model, which is believed to be a good compromise between accuracy and computational cost for these types of analyses.

## 6.2. Outlook

This section discusses potential topics for which it is worth conducting additional research.

### 6.2.1. Prediction of the vortex ring state

Further work is required to accurately predict the vortex ring state. Firstly, the prediction criteria for the vortex ring state introduced here originate from the literature on helicopters. In the future, it would be helpful to use test or measurement data to compare with the present numerical results. Secondly, so far, the vortex ring state prediction criteria are exclusively functions of the relative wind speeds normal and parallel to the rotor, which are convenient for the quantitative prediction of the onset of the working state. However, the drawback is that different criteria lead to different envelopes of the boundaries associated with the vortex ring state. It would be convenient to have a unique criterion to predict the occurrence of the vortex ring state which is applicable for both helicopters and floating offshore wind turbines.

### 6.2.2. Improvements in the numerical model

In this thesis, a free wake vortex ring method is used to simulate the aerodynamic performance of a rotor. This method is a simplified method, which calculates the pure aerodynamic load on a rotor with prescribed platform motions and a fixed-speed rotor rotation. This simplification has two shortcomings. Firstly, it leads to a loss of fidelity when analysing the aerodynamic performance of a moving rotor, because the rotor rotational speed is prescribed whilst, in reality, it could change with the thrust variations. A change in the rotational speed of the rotor influences the blade bound circulation strengths, and hence the induced velocity of the wake. Therefore, a wind turbine controller could be included in order to adjust the rotor rotational speed with the real-time

torque. Moreover, in this aerodynamic model only steady uniform wind speeds are considered. To simulate more accurately the operating environment of wind turbines, variations in the inflow should be considered, such as shear and turbulence intensity. The stall and dynamic stall corrections should also be included in the model for more extensive application.

### 6.2.3. Working state change of a moving rotor

In this thesis, the aerodynamic performance of the rotor during the change of working state is discussed. However, this study is limited to a surge motion. Future work should look at other motions, such as a pitch motion and a combination of multiple degrees of freedom. Also, it would be worth discussing ways to mitigate the negative effects of the changes of working state during the turbine motions, considering that the vortex ring state causes large load fluctuations on the rotor and that the propeller working state leads to a loss in efficiency. Finally, higher fidelity models should be used to further investigate if such motions do lead to the occurrence of the turbulent wake state.

## 6.3. Final remarks

This thesis has filled a gap in the research on the aerodynamics of floating offshore wind turbine rotors. In particular, it addressed the prediction, simulation and aerodynamic characteristics of rotor-wake interactions for a moving rotor. This thesis contributes to timely research in this area and paves the way towards better understanding of the unsteady aerodynamics of floating offshore wind turbines.



# Bibliography

- [1] YC Leung Dennis and Y Yuan. “Wind Energy Development and Its Environmental Impact: A Review”. In: *Renewable and Sustainable Energy Reviews* 16.1 (2012), pp. 1031–1039. ISSN: 1364-0321. DOI: <https://doi.org/10.1016/j.rser.2011.09.024>.
- [2] IRENA. *30 Years of Policies for Wind Energy: Lessons from 12 Wind Energy Markets*. 2nd ed. Abu Dhabi, United Arab Emirates: GWEC, 2012.
- [3] S Laskow. “Hope Floats for a New Generation of Deep-Water Wind Farms”. In: *Good Environment* (2011). URL: <https://www.good.is/articles/hope-floats-for-a-new-generation-of-deep-water-wind-farms>.
- [4] W Musial et al. “2019 Offshore Wind Technology Data Update”. In: NREL/TP-5000-77411 (2020).
- [5] FG Nielsen. “Offshore Wind Seminar Floating Foundations”. In: Geophysical Institute, UiB (2017).
- [6] D Matha. *Model Development and Loads Analysis of an Offshore Wind Turbine on a Tension Leg Platform, with a Comparison to Other Floating Turbine Concepts*. Tech. rep. NREL/SR-500-45891. NREL, 2010.
- [7] Butterfield S et al. *Engineering Challenges for Floating Offshore Wind Turbines*. Tech. rep. NREL/CP-500-38776. NREL, 2007.
- [8] WF Durand et al. “A General Review of Progress, Under a Grant of the Guggenheim Fund for the Promotion of Aeronautics”. In: Springer: Berlin (1935).
- [9] Y Zhang. “Wind Turbine Rotor Aerodynamics The Iea Mexico Rotor Explained”. Thesis for the degree of Philosophiae Doctor. Delft: TU Delft, 2017.

- [10] E Branlard. *Wind Turbine Aerodynamics and Vorticity-Based Methods, Fundamentals and Recent Applications*. Springer, 2017.
- [11] O Apata and DTO Oyedokun. “An Overview of Control Techniques for Wind Turbine Systems”. In: *Scientific African* 10 (2020), e00566. ISSN: 2468-2276. DOI: <https://doi.org/10.1016/j.sciaf.2020.e00566>.
- [12] T Sebastian and M Lackner. “Characterization of the Unsteady Aerodynamics of Offshore Floating Wind Turbines”. In: *Wind Energy* 16 (2013), pp. 339–352. DOI: [10.1002/we.545](https://doi.org/10.1002/we.545).
- [13] G de Bothezat. *The General Theory of Blade Screws*. Report 29. NACA, 1919.
- [14] JG Leishman, MJ Bhagwat, and S Ananthan. “The Vortex Ring State as a Spatially and Temporally Developing Wake Instability”. In: *Journal of the American Helicopter Society* 49 (Apr. 2004), pp. 160–175. DOI: [10.4050/JAHS.49.160](https://doi.org/10.4050/JAHS.49.160).
- [15] JF Manwell, JG McGowan, and AL Rogers. *Wind Energy Explained: Theory, Design and Application*. 2nd ed. Chichester, U.K: Wiley, 2009.
- [16] JG Leishman. *Principles of Helicopter Aerodynamics*. Cambridge: Cambridge University Press, 2006.
- [17] T Tran and DH Kim. “The Platform Pitching Motion of Floating Offshore Wind Turbine: A Preliminary Unsteady Aerodynamic Analysis”. In: *Journal of Wind Engineering and Industrial Aerodynamics* 142.C9 (2015), pp. 65–81. DOI: [10.1016/j.jweia.2015.03.009](https://doi.org/10.1016/j.jweia.2015.03.009).
- [18] T Tran, DH Kim, and J Song. “Computational Fluid Dynamic Analysis of a Floating Offshore Wind Turbine Experiencing Platform Pitching Motion”. In: *Energies* 7.8 (2014), pp. 5011–5026. DOI: [10.3390/en7085011](https://doi.org/10.3390/en7085011).
- [19] M Jeon, S Lee, and S Lee. “Unsteady Aerodynamics of Offshore Floating Wind Turbines in Platform Pitching Motion Using Vortex Lattice Method”. In: *Renewable Energy* 65.2-3 (2014), pp. 207–212. DOI: [10.1016/j.renene.2013.09.009](https://doi.org/10.1016/j.renene.2013.09.009).

- [20] R Kyle. “Alleviation of the Vortex-ring State for Floating Offshore Wind Turbines using a Modified Blade-tip Shape”. In: ETP Conference, Wind session (2017).
- [21] R Kyle, YC Lee, and W-G Früh. “Propeller and Vortex Ring State for Floating Offshore Wind Turbines During Surge”. In: *Renewable Energy* 155 (2020), pp. 645–657. ISSN: 0960-1481. DOI: <https://doi.org/10.1016/j.renene.2020.03.105>.
- [22] S Mancini et al. “Characterization of the Unsteady Aerodynamic Response of a Floating Offshore Wind Turbine”. In: *Wind Energy Science Discussions* 2020 (2020), pp. 1–26. DOI: [10.5194/wes-2020-94](https://doi.org/10.5194/wes-2020-94).
- [23] P Basset et al. “Prediction of Vortex Ring State Boundary of a Helicopter in Descending Flight by Simulation”. In: *Journal of the American Helicopter Society* 53 (Apr. 2008), pp. 139–151. DOI: [10.4050/JAHS.53.139](https://doi.org/10.4050/JAHS.53.139).
- [24] JM Drees and WP Hendal. *Airflow through Helicopter Rotors in Vertical Flight*. Tech. rep. NLL Report V. 1535. National Aeronautical Research Institute, 1949.
- [25] K Washizu et al. “Experiments on a Model Helicopter Rotor Operating in the Vortex Ring State”. In: *Journal of Aircraft* 3.3 (1966), pp. 225–230. DOI: [10.2514/3.43729](https://doi.org/10.2514/3.43729).
- [26] H Xin and Z Gao. “A Prediction of the Vortex-Ring State Boundary Based on Model Tests”. In: *Transactions of Nanjing University of Aeronautics and Astronautics* 11.2 (1994), pp. 159–194.
- [27] MD Betzina. “Tiltrotor Descent Aerodynamics: A Small-Scale Experimental Investigation of Vortex Ring State”. In: *Washington: American Helicopter Society 57th Annual Forum Proceedings*, 2001.
- [28] J Wolkovitch. “Analytical Prediction of Vortex-Ring Boundaries for Helicopter in Steep Descents”. In: *Journal of the American Helicopter Society* 17 (July 1972), pp. 13–19. DOI: [10.4050/JAHS.17.13](https://doi.org/10.4050/JAHS.17.13).

- [29] DA Peters and SY Chen. “Momentum Theory, Dynamic Inflow, and the Vortex-Ring State”. In: *Journal of the American Helicopter Society* 27.3 (1982), pp. 18–24. DOI: [10.4050/JAHS.27.18](https://doi.org/10.4050/JAHS.27.18).
- [30] JG Leishman, MJ Bhagwat, and S Ananthan. “Free-Vortex Filament Methods for the Analysis of Helicopter Rotor Wakes”. In: *Journal of Aircraft* 39 (Sept. 2002), pp. 759–775. DOI: [10.2514/2.3022](https://doi.org/10.2514/2.3022).
- [31] S Newman et al. “Predicting the Onset of Wake Breakdown for Rotors in Descending Flight”. In: *Journal of the American Helicopter Society* 48.1 (2003), pp. 28–38. ISSN: 2161-6027. DOI: [doi:10.4050/JAHS.48.28](https://doi.org/10.4050/JAHS.48.28).
- [32] A Taghizad et al. “Experimental and Theoretical Investigation to Develop a Model of Rotor Aerodynamics Adapted to Steep Descent”. In: *Canada: American Helicopter Society 58th Annual Forum Proceedings, 2002*.
- [33] RE Wilson and PBS Lissaman. *Applied aerodynamics of wind power machines*. NASA STI/Recon Technical Report N. July 1974.
- [34] JM Jonkman and ML Buhl. *FAST User’s Guide*. Tech. rep. NREL, 2005.
- [35] PJ Moriarty and AC Hansen. *AeroDyn theory manual*. Tech. rep. NREL, 2005.
- [36] K Sivalingam, S Martin, and AA Singapore Wala. “Numerical Validation of Floating Offshore Wind Turbine Scaled Rotors for Surge Motion”. In: *Energies* 11.10 (2018). ISSN: 1996-1073. DOI: [10.3390/en11102578](https://doi.org/10.3390/en11102578).
- [37] S Mancini et al. “Characterization of the Unsteady Aerodynamic Response of a Floating Offshore Wind Turbine to Surge Motion”. In: *Wind Energy Science* 5.4 (2020), pp. 1713–1730. DOI: [10.5194/wes-5-1713-2020](https://doi.org/10.5194/wes-5-1713-2020).
- [38] W Yu. “The wake of an unsteady actuator disc”. Thesis for the degree of Philosophiae Doctor. Delft: TU Delft, Apr. 2018.
- [39] K Boorsma and M Caboni. “Numerical Analysis and Validation of Unsteady Aerodynamics for Floating Offshore Wind Turbines”. In: *TNO, Petten* (2020). URL: <https://repository.tno.nl//islandora/object/uuid:10b69f85-dd5a-4f74-ac68-fdc62c01ead3>.
- [40] DM Eggleston and FS Stoddard. *Wind Turbine Engineering Design*. New York: Van Nostrand Reinhold Company, 1987.

- [41] J Jonkman and M Sprague. NWTC Information Portal (OpenFAST). Tech. rep. NREL, 2018. URL: <https://nwtc.nrel.gov/OpenFAST..>
- [42] J Jonkman et al. Definition of a 5-MW Reference Wind Turbine for Offshore System Development. Tech. rep. NREL, 2009.
- [43] J Jonkman and D Matha. “A Quantitative Comparison of the Responses of Three Floating Platforms”. In: European Offshore Wind 2009 Conference and Exhibition (2009). NREL/CP-500-46726.
- [44] JMJ Journée and WW Massie. Offshore Hydromechanics (First Edition). Delft University of Technology, 2001.
- [45] DNV and GL. Environmental Conditions and Environmental Loads. Tech. rep. Recommended practice, DNVGL-RP-C205. DNV GL, 2017.
- [46] IEC 61400–3. Wind Turbines –Part 3: Design Requirements for Offshore Wind Turbines. Switzerland: International Electrotechnical Commission (IEC), 2009.
- [47] JM Jonkman. Dynamics Modeling and Loads Analysis of an Offshore Floating Wind Turbine. Tech. rep. NREL/TP-500-41958. NREL, 2007.
- [48] JB de Vaal, MOL Hansen, and T Moan. “Validation of a Vortex Ring Wake Model Suited for Aeroelastic Simulations of Floating Wind Turbines”. In: Journal of Physics: Conference Series (2014). DOI: [10.1088/1742-6596/555/1/012025](https://doi.org/10.1088/1742-6596/555/1/012025).
- [49] MJ Bhagwat and JG Leishman. “Transient Rotor Inflow Using a Time-Accurate Free-Vortex Wake Model”. In: AIAA, Aerospace Sciences Meeting and Exhibit (2001). DOI: [10.2514/6.2001-993](https://doi.org/10.2514/6.2001-993).
- [50] J-C Gohard. Free Wake Analysis of Wind Turbine Aerodynamics. Technical Report. MIT, 1978.
- [51] T Sebastian and M Lackner. “Analysis of the Induction and Wake Evolution of an Offshore Floating Wind Turbine”. In: Energies 5 (2012), pp. 968–1000. DOI: [10.3390/en5040968](https://doi.org/10.3390/en5040968).

- [52] H Lee and D-J Lee. “Effects of Platform Motions on Aerodynamic Performance and Unsteady Wake Evolution of a Floating Offshore Wind Turbine”. In: *Renewable Energy* 143 (2019), pp. 9–23. ISSN: 0960-1481. DOI: <https://doi.org/10.1016/j.renene.2019.04.134>.
- [53] SJ Newman. *The Induced Velocity of a Vortex Ring Filament*. AFM Technical Reports 11/03. University of Southampton, School of Engineering Sciences, 2011.
- [54] S Yoon and S Heister. “Analytical Formulas for the Velocity Field Induced by an Infinitely Thin Vortex Ring”. In: *International Journal for Numerical Methods in Fluids* 44 (2004), pp. 665–672. DOI: [10.1002/flid.666](https://doi.org/10.1002/flid.666).
- [55] S Øye. “A simple vortex model”. In: In Proc. of the third IEA Symposium on the Aerodynamics of Wind Turbines, ETSU, Harwell (1990).
- [56] W Yu et al. “Verifying the Blade Element Momentum Method in Unsteady, Radially Varied, Axisymmetric Loading Using a Vortex Ring Model”. In: *Wind Energy* 20.2 (2017), pp. 269–288. DOI: <https://doi.org/10.1002/we.2005>.
- [57] RH Miller. *Simplified Free Wake Analysis for Rotors*. Technical Report. Aeronautical Research Inst. of Sweden, Stockholm.; National Aeronautics and Space Administration, Washington, DC, 1982.
- [58] A Afjeh. *Wake Effects on the Aerodynamic Performance of Horizontal Axis Wind Turbines*. Tech. rep. NASA contractor report, Sept. 1984.
- [59] JB de Vaal, ML Hansen, and T Moan. “Influence of Rigid Body Motions on Rotor Induced Velocities and Aerodynamic Loads of a Floating Horizontal Axis Wind Turbine”. In: ASME. *International Conference on Offshore Mechanics and Arctic Engineering 9B: Ocean Renewable Energy* (2014). DOI: [10.1115/OMAE2014-24227](https://doi.org/10.1115/OMAE2014-24227).
- [60] JB de Vaal. “Aerodynamic Modelling of Floating Wind Turbines”. Thesis for the degree of Philosophiae Doctor. Trondheim: NTNU, June 2015.

- [61] N Sørensen and J Johansen. “UPWIND, Aerodynamics and Aero-Elasticity Rotor Aerodynamics in Atmospheric Shear Flow”. In: Invited presentation. Published at the web. Denmark: European Wind Energy Conference& Exhibition, EWEC, 2007.
- [62] A Leonard. “Computing Three-Dimensional Incompressible Flows with Vortex Elements”. In: *Annual Review of Fluid Mechanics* 17.1 (1985), pp. 523–559. DOI: [10.1146/annurev.fl.17.010185.002515](https://doi.org/10.1146/annurev.fl.17.010185.002515).
- [63] W van Hoydonck, M Gerritsma, and M van Tooren. “On Core and Curvature Corrections used in Straight-Line Vortex Filament Methods”. In: submitted for review to the *Journal of the American Helicopter Society* (Apr. 2012), p. 34.
- [64] H Helmholtz. “Über Integrale der hydrodynamischen Gleichungen, welche den Wirbelbewegungen Entsprechen”. In: *Journal für die reine und angewandte Mathematik* 55 (1858), pp. 25–55. DOI: [10.1515/crll.1858.55.25](https://doi.org/10.1515/crll.1858.55.25).
- [65] WM Hicks. “Researches on the Theory of Vortex Rings. Part II”. In: *Philosophical Transactions of the Royal Society of London* 176 (1885), pp. 725–780. DOI: <https://doi.org/10.1098/rstl.1885.0015>.
- [66] PG Saffman. *Vortex Dynamics*. Cambridge University Press, 1992.
- [67] VV Meleshko, AA Gourjii, and TS Krasnopolskaya. “Vortex rings: History and state of the art”. In: *Journal of Mathematical Sciences* 187.4 (2012), pp. 772–808. DOI: [10.1007/s10958-012-1100-0](https://doi.org/10.1007/s10958-012-1100-0).
- [68] M. Scully. “Computation of Helicopter Rotor Wake Geometry and Its Influence on Rotor Harmonic Airloads”. Thesis for the degree of Philosophiae Doctor. Massachusetts Institute of Technology. Dept. of Aeronautics and Astronautics, 1975.
- [69] A Betz. *Behavior of Vortex Systems*. Technical Reports NACA-TM-713. National Advisory Committee for Aeronautics, 1993.
- [70] WF Phillips and DO Snyder. “Modern Adaptation of Prandtl’s Classic Lifting-Line Theory”. In: *Journal of Aircraft* 34.4 (2000), pp. 622–670. DOI: [10.2514/2.2649](https://doi.org/10.2514/2.2649).

- [71] OM Faltinsen. *Sea Loads on Ships and Offshore Structures*. Cambridge University Press, 1993.
- [72] A van Garrel. “Requirements for a Wind Turbine Aerodynamics Simulations Module - Version 1”. In: (Jan. 2001).
- [73] J Vaz, J Pinho, and A Mesquita. “An extension of BEM method applied to horizontal-axis wind turbine design”. In: *Renewable Energy* 36 (2011), pp. 1734–1740. DOI: <https://doi.org/10.1016/j.renene.2010.11.018>.
- [74] T Knudsen and T Bak. “Simple Model for Describing and Estimating Wind Turbine Dynamic Inflow”. In: *American Control Conference* (2013), pp. 640–646. DOI: [10.1109/ACC.2013.6579909](https://doi.org/10.1109/ACC.2013.6579909).
- [75] J Dong et al. “A Modified Free Wake Vortex Ring Method for Horizontal-Axis wind Turbines”. In: *Energies* 12.20 (Oct. 2019). ISSN: 1996-1073. DOI: [10.3390/en12203900](https://doi.org/10.3390/en12203900).
- [76] X Shen et al. “Study of the Unsteady Aerodynamics of Floating Wind Turbines”. In: *Energy* 145 (2018), pp. 793–809. ISSN: 0360-5442. DOI: <https://doi.org/10.1016/j.energy.2017.12.100>.
- [77] J Dong and A Viré. “Comparative Analysis of Different Criteria for the Prediction of Vortex Ring State of Floating Offshore Wind Turbines”. In: *Renewable Energy* 163 (2021), pp. 882–909. ISSN: 0960-1481. DOI: <https://doi.org/10.1016/j.renene.2020.08.027>.
- [78] B Jonkman and J Jonkman. FAST v8.15.00a-bjj. Tech. rep. NREL, 2016.

# Acknowledgement

My PhD experience is like a box of chocolates. I did know what I was going to get. It let me experienced a lot and gave me a lot of stories to tell. In any event, this thesis will not be finished without the help of many people. At this moment, I would like to thank all their support during my doctoral study.

Firstly, I would like to thank Xiaoli, who noticed me of my research talent and through Gabriel they formally invited me to TU Delft with CSC funding. Secondly, I would like to thank René and Mirek, who I worked together with for a short period but greatly enhanced my skill of designing research proposals. And then I will thank Axelle my supervisor, who accept me as a PhD student in wind energy group and supported me during this four years of study, and Gerard, who gave me valuable guidance during the first two years of my PhD and was always been able to exactly point out my advantages and wakenesses with his sharp eye. Next I will thank Carlos for his challenge which enhanced my understanding of many scientific problems. And then I will thank Simon my promoter, who support me to the very end of this PhD journey and corrected my entire thesis with precise English expressions. For these, I am eternally grateful.

Particularly, I would like to give a lot of thanks to Cees, Mascha and Pieter, who selflessly gave me the warmest care and support to overcome all kinds of difficulties.

Further more, I would like to say many thanks to Jacobus de Vaal, who supported me a lot during the development of the vortex ring method by means of sending me his PhD thesis from Norway. My cordially thanks also extends to Jason Jonkman, who guided and enlightened me a lot at some key points of my research.

I want to thank our secretary Sylvia for her efficiency and patience. Besides, I would like to express my appreciation to all my colleagues: Gijs, Dominic,

Damiano, Daniele, Roland, Nando, Francesco, Wim, Delphine, Wei, Michiel, Ricardo, Carlos Baptista, Vinit, Livia, Jaco, Ashwin, Bedassa, Leandro, Sebastian, Mikko, Manoel, Yunusi, Sharif, Chihoon, Bruce, Jingna, Ming, Navi, Mark, Julia, Christopher, Juan, Kiran and Paul. Thank you all for interesting conversation and all kinds of help.

I also want to thank my friends Sun Fulin, Sun Jiayao, Li Ang, Wang Junyi, Li Na, Zhang Yanan, Zeng Qinqin, Ye Qingqing, Wang Zi, Chen Guangming, Zeng Qingsong, Hu Qv, Ma Wenbin, Ye Jun, Qin Yanxin, Zou Tao and Zhang Xiaobo, for all your accompany.

Particular thanks will be given to Qu Wenhua, who concerned me a lot during the final stage of my PhD defence.

I would like to say a special thank to Shen Gufei, a great teacher who I followed for years to enter the door of business analysis and investment, which entirely fresh my mind and providing me a new angle of seeing the world.

I am grateful to Mirjam, Huiwen, Mrs Qiu and Meeling, from whom I have learned not only a lot of biblical knowledge but also faith, hope and love. My gratitudes also to Buddhist Master Jingkong, who help me a lot to find my inner peace, forgiveness and wisdom.

Many thanks go to my parents and my family, An Gang, Dong Chunxiao, Dong Chunming, An Hui, Pan Surong, Li Guobin, Li Zhangrui and Anan for their endless support, encouragement, accompany and love.

Jing Dong

Delft, Aug 2021

# Curriculum Vitæ

Jing DONG

16-01-1986      Born in Beipiao, China.

## Education

2004–2008	Bachelor Naval Architecture and Ocean Engineering Dalian University of Technology
2008–2011	Master Naval Architecture and Ocean Engineering Dalian University of Technology
2017–2021	PhD. Wind Energy Delft University of Technology



# List of Publications

## JOURNALS

4. J. Dong, A. Viré, C. Ferreira, Z. Li, G. van Bussel, A Modified Free Wake Vortex Ring Method for Horizontal-Axis Wind Turbines, [Energies 12, 3900 \(2019\)](#).
3. J. Dong, A. Viré, Comparative analysis of different criteria for the prediction of vortex ring state of floating offshore wind turbines, [Renewable Energy, 163 \(2021\)](#).
2. J. Dong, A. Viré, The aerodynamics of floating offshore wind turbines in different working states during surge motion, Submitted to Renewable Energy.
1. J. Dong, A. Viré, Z. Li, Analysis of the vortex ring state and propeller state of floating offshore wind turbines and verification of their prediction criteria by comparing with a CFD model, Submitted to Renewable Energy.

## CONFERENCE PROCEEDINGS

2. J. Dong, A. Viré, C. Ferreira, Z. Li, G. van Bussel, A modified free-wake vortex ring model for the aerodynamics of floating offshore wind turbines., [Proceedings of the ASME 2019 2nd International Offshore Wind Technical Conference](#) St. Julian's, Malta. November 3–6, 2019. ASME..
1. J. Dong, A. Viré, Predicting the occurrence of the vortex ring state for floating offshore wind turbines, [Journal of Physics: Conference Series 1618. \(Torque2020\)](#).



